

**Applications of Genetic Algorithms to  
Problems in Seismic Anisotropy**

by

Stephen A. Horne

B.Sc.(Hons.) Physics 1991

University of Surrey.

Thesis submitted for the  
degree of Doctor of Philosophy  
Department of Geology and Geophysics  
University of Edinburgh

1995



I hereby declare that this thesis has been composed by myself and that the work described is entirely my own unless explicitly stated in the text

Stephen Horne

## **ABSTRACT**

The primary concern of this thesis is to develop inversion methods which may be applied to observations of seismic anisotropy. I achieve this through the implementation of a non-linear global optimization scheme known as a Genetic Algorithm. I apply this technique to the inversion of quasi-compressional velocities obtained from laboratory measurements and shear-wave splitting observations measured from an azimuthal VSP experiment and two near-offset VSPs. These VSP experiments were conducted at the Conoco Borehole Test Facility, Oklahoma which presents an ideal setting due to its geological and structural simplicity and the availability of a-priori information, for example from borehole televiewer images, core samples and logging information. I compare the information derived from these sources with the results obtained from the inversion of shear-wave birefringence measurements. Comparative studies of this type are important in establishing the relation between the observed seismic anisotropy and equivalent media systems due to such phenomena as aligned fractures or fine layering.

The inversion results for the azimuthal VSP and near-offset VSPs are in good agreement with each other and also with the a-priori data. The azimuthal VSP inversion allowed the identification of a significant feature associated with shear-wave propagation in anisotropic media known as a shear-wave singularity. Another significant inversion result is the suggestion that the observed seismic anisotropy is due to a sub-vertical fracture system. This result is supported through the analysis of shear-wave observations obtained from the near-offset VSP experiments. I suggest that fracture dip may be determined using appropriate acquisition geometries such as an opposite azimuth VSP for which two VSPs are recorded with sources located diametrically opposite each other about the well.

A significant correlation is observed to exist between the lithology at the Conoco Borehole Test Facility and the degree of shear-wave birefringence. Specifically it

appears that the shear-wave birefringence is most pronounced for wave propagation through the sandstone formations which are known to be heavily fractured. Correlations of this type are important if any confidence is to be placed in the interpretation of shear-wave birefringence in terms of fracture systems.

Although the Genetic Algorithm is shown to be a useful tool, several problems are identified with such schemes. The most significant of these is the sensitivity to the choice of parametrization scheme employed. This may prove to be critical to the success of this method. Further problems arise from the lack of any rigorous framework by which the genetic operators and their associated control parameters can be optimally determined. Perhaps the most restrictive feature of Genetic Algorithms is the substantial number of models that need to be sampled during the search. Thus the function evaluation must be sufficiently fast for the search to be economical. Nonetheless satisfactory results could be obtained despite the considerable simplifications necessary to efficiently implement the forward modelling used in the function evaluation.



## **ACKNOWLEDGEMENTS**

I gratefully acknowledge Elf (GRC) for their financial support of this work and also the sponsors of the Edinburgh Anisotropy Project. I especially wish to thank Conoco Inc. for releasing the Azimuthal VSP and near-offset VSP datasets to me. In relation to this John Queen, Bill Rizer and Dale Cox provided essential information and discussions regarding the Conoco Borehole Test Facility, Oklahoma. The British Geological Survey very kindly provided me with additional funding between October 1994 to December 1994 and also funded my attendance at the United Kingdom Geophysical Assemblies held at Edinburgh, Oxford and Liverpool. Blackwell science allowed me to reproduce a paper published in *Geophysical Prospecting* which I have included in the back of this thesis.

I am very pleased to have the opportunity to thank my supervisor Colin MacBeth. From my conversations with other postgraduate students I suspect that I have been very fortunate in having been supervised by him. He has always been available for discussions and has encouraged me to develop my own ideas. In addition to Colin I must also thank the many people who spared their valuable time to review my thesis - they must have had better things to do. These reviewers include: Bruce Hobbs (Chapters 1, 2, 3, 4, 5 and 6), Peter Leary (Chapter 4), Xiang-Yang Li (Chapter 3), Enru Liu (Chapters 4 and 5), Colin MacBeth (Chapters 1, 2, 3, 4, 5 and 6), Colin Slater (Chapter 5) and Xinwu Zeng (Chapter 2).

I must express gratitude to my friends and colleagues at the British Geological Survey who have provided much needed relief in the tedium that has accompanied much of my studies. Many thanks then to; Brian Baptie, Heng-Chang Dai, Gordon Holmes, Aphrodite Karnassopoulou, Yun Liu, Helen Rowlands, Colin Slater, Gareth Yardley and Xinwu Zeng. I also wish to thank Phil Wild, Willie Velzian and Paul Henni for their assistance with various computational aspects of this work

I would like to thank my parents and Nguyễn Thi Cát for their continual encouragement and support. I also wish to thank Jean Carriay for encouraging me to continue my education.

Final thanks must go to some very good friends of mine. Adrian Patterson and Gordon Holmes have been extraordinarily kind to me and it is difficult for me to express how grateful I am to both of you.

## CONTENTS

### CHAPTER 1

A REVIEW OF SEISMIC ANISOTROPY .....	1
1.1 INTRODUCTION .....	1
1.2 DEFINITION OF SEISMIC ANISOTROPY .....	1
1.3 SHEAR-WAVE BIREFRINGENCE .....	5
1.4 POSSIBLE CAUSES OF SEISMIC ANISOTROPY .....	9
1.5 DETECTION OF ANISOTROPY .....	11
1.6 THE POTENTIAL USE OF SEISMIC ANISOTROPY .....	12
1.7 OPTIMIZATION SCHEMES AND SEISMIC ANISOTROPY .....	13
1.8 OVERVIEW OF THIS THESIS .....	14

### CHAPTER 2

#### ESTIMATION OF SHEAR-WAVE SPLITTING

USING GENETIC ALGORITHMS .....	17
2.1 INTRODUCTION .....	17
2.2 IMPLEMENTATION OF THE GA .....	19
2.3 PARAMETRIZATION OF SHEAR-WAVE SPLITTING .....	36
2.4 SENSITIVITY TO GA PARAMETERS. ....	38
2.5 APPLICATION TO SYNTHETIC DATA .....	47
2.6 RESULTS OF COMPARISON TEST .....	49
2.7 APPLICATION TO FIELD DATA .....	52
2.8 SUMMARY .....	54

## CHAPTER 3

INVERSION FOR LABORATORY *QP*-WAVE

VELOCITY MEASUREMENTS .....	56
3.1 INTRODUCTION .....	56
3.2 EXPERIMENTAL ARRANGEMENT .....	56
3.3 INVERSION PROCEDURE .....	60
3.4 PARAMETRIZATION SCHEMES .....	65
3.5 INVERSION RESULTS .....	70
3.6 DISCUSSION AND CONCLUSIONS .....	82

## CHAPTER 4

## AZIMUTHAL VSP INVERSION .....

83

4.1 INTRODUCTION AND OVERVIEW .....	83
4.2 REVIEW OF THE CBTF EXPERIMENT .....	84
4.3 AVSP PROCESSING .....	90
4.4 JUSTIFICATION OF HOMOGENEITY ASSUMPTION .....	99
4.5 INVERSION PROCEDURE .....	108
4.6 INVERSION RESULTS: HEXAGONAL SYMMETRY .....	114
4.7 FULL-WAVEFORM MODELLING .....	126
4.8 INVERSION RESULTS: ORTHORHOMBIC SYMMETRY ..	129
4.9 CONCLUSIONS AND DISCUSSION .....	136

## CHAPTER 5

## NEAR-OFFSET VSP INVERSION .....

142

5.1 INTRODUCTION .....	142
5.2 FORWARD MODELLING TECHNIQUES .....	142
5.3 RAY TRACING .....	145
5.4 VERIFICATION OF RAY TRACING METHOD .....	148

5.5	APPLICATION TO FIELD DATA .....	155
5.6	NEAR-OFFSET VSP ACQUISITION GEOMETRIES .....	156
5.7	PROCESSING SEQUENCE APPLIED TO SHEAR-WAVE DATA .....	161
5.8	STRATIGRAPHIC CORRELATION WITH SHEAR-WAVE BIREFRINGENCE .....	174
5.9	INVERSION PROCEDURE .....	177
5.10	INVERSION RESULTS .....	181
5.11	COMPARISON OF AVSP AND NEAR-OFFSET VSP INVERSION RESULTS .....	208
5.12	CONCLUSION .....	211

## CHAPTER 6

SUMMARY AND CONCLUSIONS .....	213
-------------------------------	-----

6.1	INTRODUCTION .....	213
6.2	GENETIC ALGORITHMS .....	213
6.3	FRACTURE CHARACTERIZATION AT THE CONOCO BOREHOLE TEST FACILITY .....	214
6.4	SHEAR-WAVE ANISOTROPY .....	215
6.5	SUGGESTIONS FOR FUTURE WORK .....	216

## APPENDIX A

DERIVATION OF SLOWNESS EQUATIONS FOR MONOCLINIC MEDIA .....	218
----------------------------------------------------------------	-----

REFERENCES .....	223
------------------	-----

## ATTACHED TO BACK COVER

HORNE, S., MACBETH, C. 1994. Inversion for seismic anisotropy using genetic algorithms. *Geophysical Prospecting* 42 953-974.

If our eye could penetrate the earth and see its interior from pole to pole, from where we stand to the antipodes, we would glimpse with horror a mass terrifyingly riddled with fissures and caverns.

Thomas Burnet, *Telluris Theoria Sacra*, Amsterdam, Wolters, 1694, p38.

## CHAPTER 1

### A REVIEW OF SEISMIC ANISOTROPY

#### 1.1 INTRODUCTION

In this Chapter I will review some of the underlying concepts that are essential to the understanding and development of this thesis. This will entail a mathematical description of seismic anisotropy and a discussion of possible sources of this phenomenon. Seismic anisotropy will be discussed within the context of its potential usefulness to the hydrocarbon industries.

#### 1.2 DEFINITION OF SEISMIC ANISOTROPY

Anisotropy is defined to be the 'variation of a physical property depending on the direction in which it is measured' (Sheriff 1984). Therefore when we refer to seismic anisotropy we are referring to the directional variation of a material's response to the passage of elastic waves. Mathematically this is described using the equations of motion for an elastic solid and the generalised Hooke's Law, which are respectively

$$c_{ijkl} u_{k,lj} - \rho \ddot{u}_i = 0; \quad (1.1a)$$

and

$$\sigma_{ij} = c_{ijkl} u_{k,l}; \quad (1.1b)$$

where  $\sigma$  is a second rank tensor describing the stress,  $\rho$  is the density and  $u_{ij}$  is the displacement component in the  $i$  th direction partially differentiated with respect to the  $j$  th direction, that is,  $u_{ij} = \partial u_i / \partial x_j$ . This quantity is a measure of strain and is also commonly written as the second rank tensor  $\epsilon_{ij} = (u_{ij} + u_{ji})/2$ . Hooke's law relates these second rank tensors of stress and strain by the fourth order tensor of elastic

constants or stiffnesses,  $c_{ijkl}$ . Since each index of this tensor may take values between 1 and 3 this implies that a total of 81 elastic constants may be required to specify the elastic response of a material. However, by consideration of arguments related to the symmetry of the stress and strain tensors and energy constraints, the number of independent tensorial elements reduces to 21. The stiffness tensor may be conveniently condensed by replacing the 4 suffixes,  $ijkl$ , with 2 suffixes,  $mn$ , defined such that,

$$ij(ji) \text{ or } kl(lk) = 11 \rightarrow 1 \quad 22 \rightarrow 2 \quad 33 \rightarrow 3 \quad 23 \rightarrow 4 \quad 13 \rightarrow 5 \quad 12 \rightarrow 6$$

This notation is often referred to as the Voigt notation and allows the elastic tensor to be written as a symmetric 6 by 6 matrix

$ij \quad kl \rightarrow$	11	22	33	23	13	12
$\downarrow$						
11	$c_{11}$	$c_{12}$	$c_{13}$	$c_{14}$	$c_{15}$	$c_{16}$
22	.	$c_{22}$	$c_{23}$	$c_{24}$	$c_{25}$	$c_{26}$
33	.	.	$c_{33}$	$c_{34}$	$c_{35}$	$c_{36}$
23	.	.	.	$c_{44}$	$c_{45}$	$c_{46}$
13	.	.	.	.	$c_{55}$	$c_{56}$
12	.	.	.	.	.	$c_{66}$

All 21 elastic constants are required in the case that the material possesses no other symmetries other than those already mentioned. Materials of this type are said to possess triclinic symmetry, the lowest class of symmetry. At the opposite end of the range of symmetries are materials with the highest symmetry system in which every plane is a plane of symmetry. These materials are isotropic and only two independent elastic constants are required to define the elastic tensor. Between these two extremes there exist several other symmetry classes (Figure 1.1). Perhaps the most commonly considered symmetry class in the study of seismic anisotropy is that of hexagonal materials. For these materials there is a single rotational symmetry axis so that in



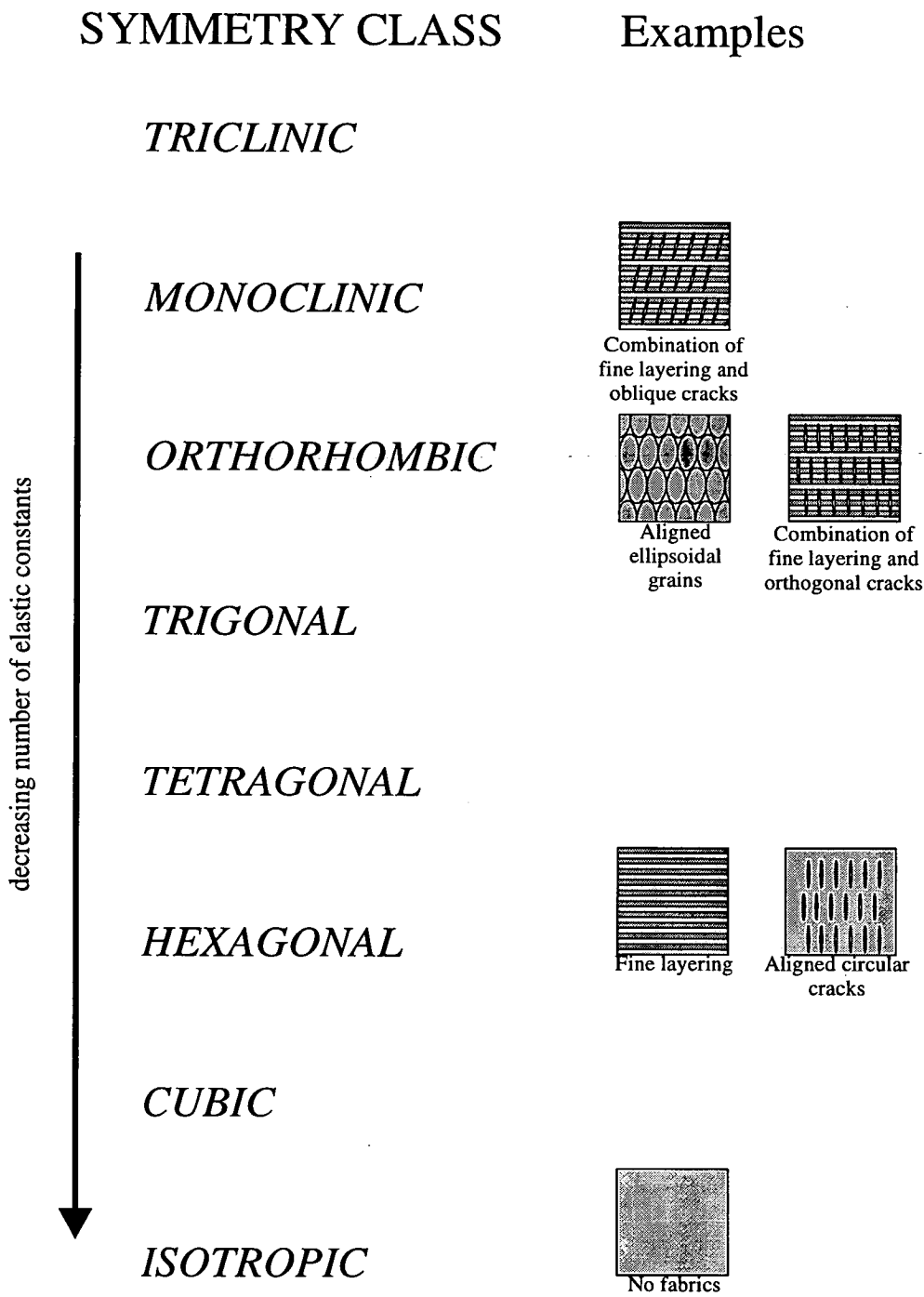


Figure 1.1 - This figure shows the symmetry classes from the lowest symmetry system of triclinic increasing to the highest symmetry system of isotropy. Icons shown to the right indicate possible mechanisms which result in the corresponding symmetry class shown to the left.

directions perpendicular to this the material's properties appear directionally invariant. For this reason materials of this type are commonly described as being 'Transversely Isotropic' (TI). Hexagonal materials are defined in terms of five independent elastic constants. Other symmetry classes which are also relevant to this thesis are the orthorhombic and monoclinic systems. Orthorhombic materials possess three mutually orthogonal planes of symmetry and are defined using nine independent elastic constants. Monoclinic materials possess a single plane of symmetry and require at most thirteen independent elastic constants to define the stiffness tensor.

The seismic response of an anisotropic material may be investigated by substitution of a plane wave solution into the wave equation (which may be derived from equations 1.1a and 1.1b) of the form

$$\mathbf{u}(\mathbf{n}, t) = \mathbf{U}(\mathbf{n}) e^{i\omega(t - \frac{\mathbf{n} \cdot \mathbf{x}}{V(\mathbf{n})})}; \quad (1.2)$$

where  $\mathbf{u}$  is the displacement vector for a wave propagating with phase velocity  $V$  at the position  $\mathbf{x}$ . The propagation direction is defined by the unit vector  $\mathbf{n}$  and  $\mathbf{U}$  is a constant polarisation vector. Substitution of equation 1.2 into the wave equation yields the Kelvin-Christoffel equation

$$\det | C_{ijkl} n_j n_l - \rho V^2 \delta_{ik} | = 0. \quad (1.3)$$

A solution of this equation generally yields three eigen values and three corresponding eigen vectors. The eigen vectors are equal to the polarisation vectors,  $\mathbf{U}^i(\mathbf{n})$ , and the eigen values,  $e^i$ , are related to the phase velocities as,  $V^i(\mathbf{n}) = (e^i / \rho)^{1/2}$ , where the superscript identifies the different eigen solutions. An alternative construction of the Kelvin-Christoffel equation is based upon the rewriting of the plane wave equation in terms of the slowness components,

$$\mathbf{u}(\mathbf{n}, t) = \mathbf{U}(\mathbf{n}) e^{i\omega(t - \mathbf{p} \cdot \mathbf{x})}, \quad (1.4)$$

where  $\mathbf{p}$  is the slowness vector which is defined as  $\mathbf{p} = \mathbf{n} / V(\mathbf{n})$ . This gives the

Kelvin-Christoffel equation in the alternative form

$$\det | C_{ijkl} p_j p_l - \rho \delta_{ik} | = 0. \quad (1.5)$$

These two forms of the Kelvin-Christoffel equation, given in equations 1.3 and 1.5, allow the seismic properties to be calculated as a function of either the propagation direction or the slowness vector, respectively. The choice of which form of the Kelvin-Christoffel equation is to be used will depend on the problem being addressed. For example, if problems involving ray tracing are to be solved then the Kelvin-Christoffel equation written in terms of the slowness components may be more appropriate since the problem involves the conservation of slowness components across interfaces. Both forms of the Kelvin-Christoffel equation will be used in this thesis.

### 1.3 SHEAR-WAVE BIREFRINGENCE

Perhaps the most significant difference between isotropic and anisotropic wave propagation is the general existence of three distinct body waves which form an orthogonally polarised set. This compares with an isotropic material in which only two body waves exist, that is a compressional wave ( $P$  wave) polarised parallel to the direction of propagation and a shear-wave ( $S$  wave) which may be polarised in any direction in a plane perpendicular to the direction of propagation. In the anisotropic case the three body waves are commonly described in terms of a quasi-compressional wave ( $qP$ ) and two quasi-shear waves ( $qS$ ). The term quasi is introduced to emphasise that these waves are not strictly polarised in the directions normally associated with  $P$  and  $S$  waves. For example, in the case of  $qP$  waves there is a small displacement component in the plane perpendicular to the propagation direction. The two  $qS$  waves are mutually orthogonal and polarised in the plane perpendicular to the  $qP$ -wave polarization direction. These  $qS$  waves are often distinguished by referring to the faster and slower quasi-shear waves which are denoted  $qS1$  and  $qS2$  respectively. Alternative forms of notation may be adopted in the case that propagation occurs within a symmetry plane (Crampin 1981). It is the existence of these two quasi-shear

waves which leads to the phenomenon known as shear-wave birefringence or shear-wave splitting which is illustrated in Figure 1.2. In this figure a shear-wave is schematically shown propagating through an anisotropic cube embedded in an isotropic medium. As the shear-wave passes from the surrounding isotropic material into the anisotropic region two quasi-shear waves are excited. These continue to propagate through the anisotropic region with distinct velocities and polarisations which are fixed by the propagation direction and the medium's properties. This leads to a separation between the two quasi-shear waves so that a time delay accumulates between the two different arrivals.

As already described above there are in general two quasi-shear waves. However, there exist certain 'special' directions which correspond to degeneracies in the solution of the Kelvin-Christoffel equation. These directions are known as singularities and in these directions only two solutions exist for the body waves instead of the usual three. These two solutions correspond to a quasi-compressional wave and a single quasi-shear-wave which may be polarised in any direction orthogonal to the  $qP$ -wave polarisation vector. Thus for these directions the phenomenon of shear-wave splitting does not occur. It is important to notice that upon crossing these shear-wave singularities the time delays approach zero and there is an abrupt change in the faster shear-wave polarisation. It has been suggested that the identification of these features in shear-wave surveys may be important in constraining the interpretations of shear-wave splitting (MacBeth *et al.* 1993, Bush 1990).

A further complication involving wave propagation in anisotropic media is presented when group and phase velocities are considered. The reason for this difference can easily be described using the schematic illustration shown in Figure 1.3. This figure shows wave propagation in isotropic and anisotropic homogeneous media for a point source exciting only one arbitrary wave mode. In the case of the isotropic material the wavefronts are spherical and centred about the point source. A later wavefront may be constructed using either Huygens' principle or by the superposition of plane waves (Helbig 1994). It can be seen that this latter construction is simple since the

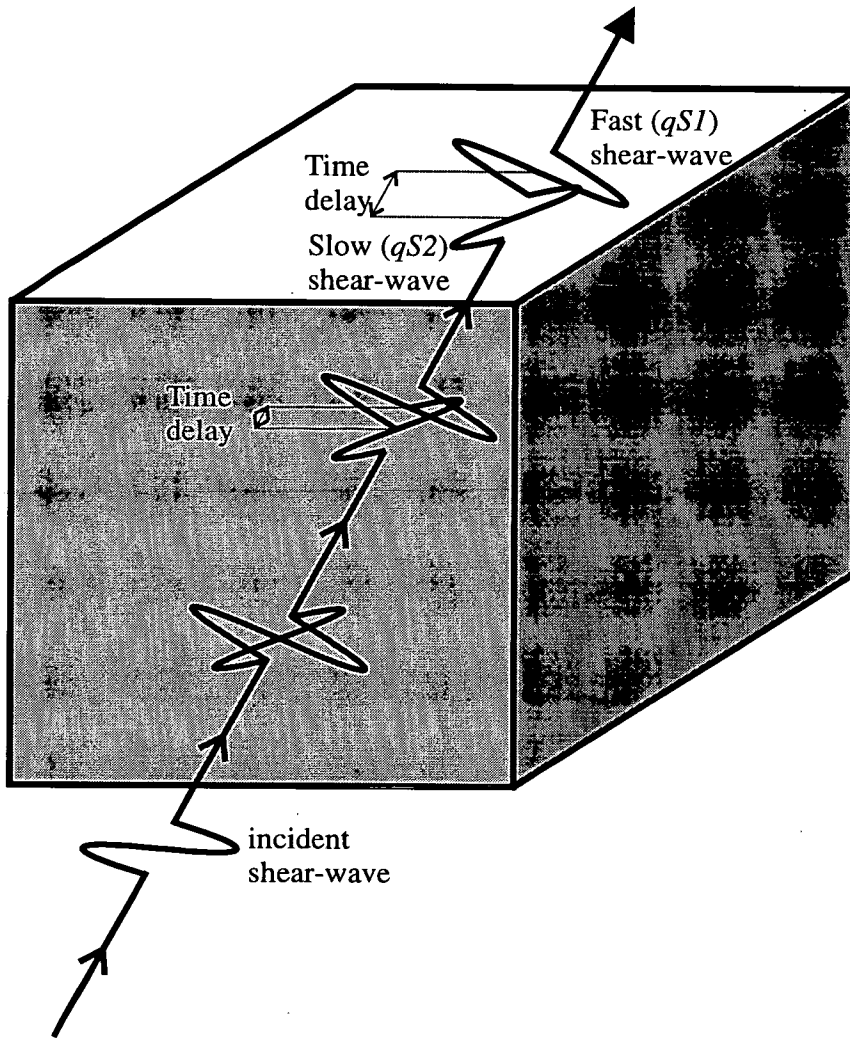
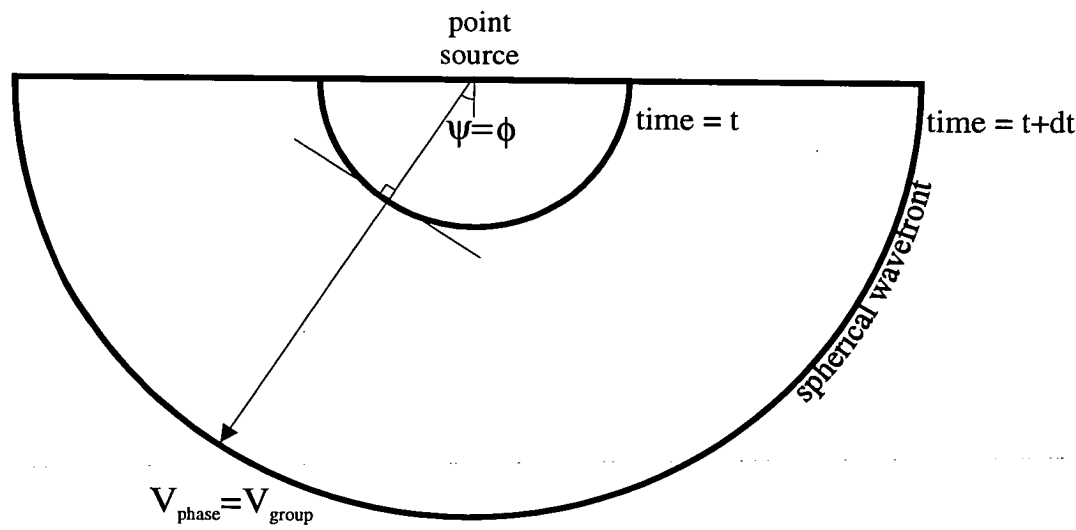


Figure 1.2 - A schematic illustration showing a shear wave propagating from an isotropic region into an anisotropic region shown as a shaded cube. As the shear-wave enters the anisotropic region two shear-waves may be excited which propagate with different velocities and polarisations. As these waves continue to propagate through the medium the two shear waves separate leading to a time delay between the two arrivals. This effect is known as shear-wave birefringence or shear-wave splitting (after Crampin 1985.)

a)

# ISOTROPIC



b)

# ANISOTROPIC

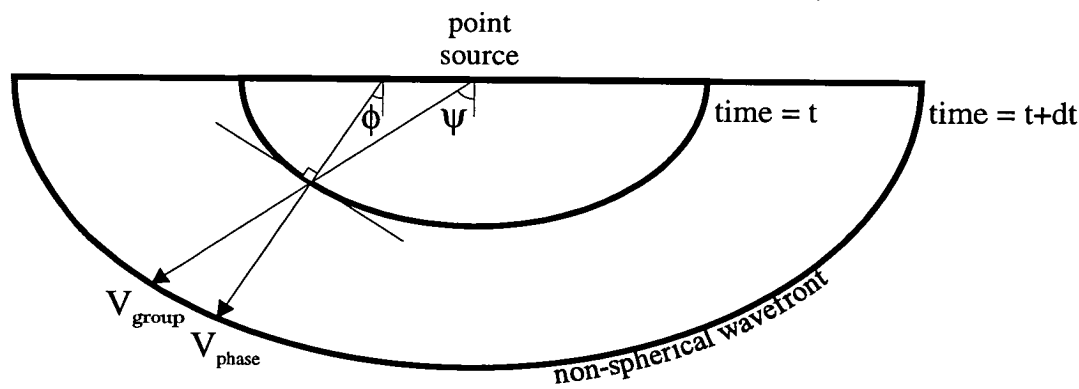


Figure 1.3 - A graphical example showing the difference between phase and group velocities, denoted  $V_{\text{phase}}$  and  $V_{\text{group}}$  respectively, for wave propagation in a) isotropic and b) anisotropic media. The group velocity corresponds to the angle  $\psi$  and is associated with the propagation of energy. The phase velocity corresponds to the angle  $\phi$  and is associated with the plane wave locally perpendicular to the wavefront (after Thomsen 1986).

plane waves propagate in a straight line connecting the source and the two points on the successive wavefronts. Thus the group velocity, associated with the propagation of energy, and the phase velocity, associated with the advance of plane wavefronts, are the same, in the absence of any frequency dispersion effects. This is not the case for wave propagation in anisotropic media. In this case the wavefronts are not spherical and the directions associated with energy transport and plane waves are no longer coincident (Figure 1.3.)

#### 1.4 POSSIBLE CAUSES OF SEISMIC ANISOTROPY

Crystalline materials, such as calcite and olivine, are anisotropic because of the ordered lattice arrangement of their constituent atoms. The seismic response of such materials corresponds to the underlying symmetry of the atomic lattice arrangement as described by Neumann's principle (Musgrave 1970). These types of materials are often referred to as 'intrinsically anisotropic'. However, this distinction is unclear in the sense that the measured anisotropy is dependent upon the scale length at which the material is observed (Helbig 1994). At wavelengths small enough to resolve atomic structures these crystalline materials will appear to be inhomogeneous. However, at larger wavelengths the discrete nature of the atomic lattice will not be resolved and the material is observed to be homogeneous and anisotropic. This relation between the observed anisotropy and the scale length is a fundamentally important concept which has come to be known as 'equivalent media' theory. Equivalent media theory allows the replacement of an ordered ensemble of inhomogeneous elements, which may be isotropic or anisotropic, with an equivalent homogeneous anisotropic material which possesses an equivalent response when measured at wavelengths greater than the constituent heterogeneities.

Seismological measurements span wavelengths between 100 km for teleseismic observations to a few centimetres for laboratory ultrasonic experiments. In this range there may be various forms of ordered heterogeneity leading to observations of seismic anisotropy (MacBeth 1995). Perhaps the most obvious of these arises from the fine

layering of materials with different elastic properties which may be expected in sedimentary sequences. Finely layered media usually possess a rotational axis of symmetry in a direction perpendicular to the layering. Thus equivalent media of this type are transversely isotropic about this axis. If this fine layering is horizontally stratified so that the symmetry axis is vertical then the equivalent anisotropic medium is said to be Transversely Isotropic with a Vertical (TIV) axis of symmetry. This form of equivalent medium has long been recognised as a possible source of seismic anisotropy and is well documented (Backus 1962, Helbig 1994, Schoenberg and Muir 1989).

Associated with fine layering anisotropy is 'depositional' anisotropy where the individual constituent particles are preferentially aligned. This introduces a fabric within the rock. For example, in some sandstones the approximately ellipsoidal sand particles tend to align themselves so that the long axis is in the horizontal plane (Helbig 1994). This resulting equivalent anisotropic medium will depend on the average shape of the particles and the degree of alignment. In the case that the particles are approximately ellipsoidal with the two minor axes equal, so that the major axis is a symmetry axis, then the anisotropy exhibited will be that of transverse isotropy. In the case that the two minor axes are not equal then the equivalent medium will belong to the orthorhombic symmetry class. This is illustrated in Figure 1.1.

Much of the recent interest in seismic anisotropy involves equivalent media based upon crack and fracture systems. Such information is of particular interest to the oil and gas industries for which the knowledge of fracture systems may well prove to be critical to the successful development of a field (Mueller 1992, Cooke-Yarborough 1994). The simplest equivalent medium of this type can be constructed from a set of aligned circular cracks. The class of symmetry exhibited by this type of system is that of transverse isotropy (hexagonal) with the symmetry axis aligned perpendicular to the crack face. It has been suggested that because of the subsurface stress regime within the Earth crack systems will be vertically aligned with the crack strike parallel to the



direction of the maximum compressive stress (Crampin 1994). If this is the case then fracture based equivalent media will exhibit transverse isotropy with a horizontal axis of symmetry.

More complicated symmetry systems can easily be constructed from the combination of different types of equivalent media. For example, vertical cracks embedded into a horizontally finely layered medium results in an orthorhombic medium.

## **1.5 DETECTION OF ANISOTROPY**

Until recently the seismic industry has been primarily concerned with the acquisition, processing and interpretation of results obtained from compressional wave reflection surveys. For these experiments the assumption of an isotropic earth is appropriate for two reasons. Firstly, the angular coverage used in reflection surveys is limited so that the directional variation introduced by anisotropic effects is negligible. Secondly the compressional wave is relatively insensitive to the effects of wave propagation in anisotropic media (Crampin 1985). This is not the case for shear waves where the phenomenon of shear-wave birefringence marks a significant departure from isotropic wave propagation. It should not then be surprising that interest in seismic anisotropy has been closely coupled with the increasing use of shear-wave surveys and its associated technology, in particular the use of three-component receivers and polarized sources (Tatham and McCormack 1991). Observations from such surveys showed misties between reflection depth estimates when recorded using different source polarizations, non-hyperbolic reflection events and, perhaps most significantly, shear-wave birefringence (Helbig 1994). Of particular importance to the recognition of seismic anisotropy was the introduction of the survey technique known as the Vertical Seismic Profile (VSP) during the 1970s (Gal'perin 1974). This surveying method generally employs downhole receivers and source on the surface. The wavefield is then measured as a function of depth by locking the receiver at a series of levels in the well and recording the wavefield generated by the repeated activation of the source for every depth level. There are many variations on this basic VSP technique, such

as the Reverse VSP (RVSP) where the locations of source and geophone are exchanged, so that the source is located downhole and the receivers are located on the surface. If the intention of a VSP survey is to characterise the anisotropic response of the sub-surface, then some angular variation of the earth should be investigated (Helbig 1994). This may be achieved using multi-offset or multi-azimuthal acquisition geometries. Furthermore, if the anisotropy is to be analysed in terms of shear-wave birefringence the source should ideally excite both quasi-shear waves. This may be ensured by employing at least two orthogonally polarized shear-wave sources. Thus a typical VSP experiment to investigate shear-wave birefringence utilises multiple sources polarized in different directions and three-component receivers to record the full wavefield. Such a dataset is often referred to as a multicomponent survey.

## **1.6 THE POTENTIAL USE OF SEISMIC ANISOTROPY**

The existence of anisotropy can be viewed in terms of two opposing opinions. Firstly, anisotropy can be viewed in the negative sense in that it introduces distortion into conventional seismic imaging which generally assumes an isotropic earth. The converse attitude is that observations of seismic anisotropy contain information which may be meaningfully extracted to give estimates on subsurface properties which may be beyond the resolution of conventional seismic techniques (MacBeth 1995). Information which may be coded into these anisotropic attributes may include details of fine layering and fracture systems. This second approach is pursued in this thesis and some examples of the successful application of shear-wave birefringence analysis are now given. Recently there have been several studies of multicomponent shear-wave reflection data. Shuck, Benson and Davis (1993) present results from such a survey which was intended to map the variation in the shear-wave birefringence over a coal bed methane reservoir near Cedar Hills, New Mexico. The anisotropy was successfully correlated with the fracture/cleat system in the coal seams and the productivity rates from producing wells over the surveyed region. A further success in the application of shear-wave anisotropy was reported by Mueller (1992). In this study anomalies in shear-wave reflection amplitudes for the fast and slow reflection

sections from the Austin Chalk formation were analysed. Lateral changes in these sections were interpreted in terms of local fracture swarms. On the basis of these results a horizontal borehole was directionally drilled so that the well perpendicularly intersected the supposed fracture swarms. Subsequent productivity from this horizontal well was reported to be significantly higher in comparison with surrounding wells. A further case study, again associated with the Austin Chalk formation, was presented by Li (1992). In this case a correlation was identified between the time delays measured along three reflection lines and the degree of productivity reported from existing producing wells in the vicinity of the surveys. Such correlations between productivity and time delays have also been reported from VSP surveys, for example Client *et al.*, (1991), Bates, Lynn and Layman (1995).

## 1.7 OPTIMIZATION SCHEMES AND SEISMIC ANISOTROPY

Many of the problems encountered in seismology can be posed in terms of an optimization problem. Of particular interest is the inverse problem for which a model is to be derived on the basis of a set of physical observations. However, due to the complicated non-linear nature of the seismic anisotropy inverse problem few studies have addressed this problem. Some exceptions have included the works of Arts, Rasolofosaon and Zinszner (1991), Brodov *et al.*, (1991) and MacBeth (1991). However, in order to solve the inverse problem these studies have often involved local search strategies or simplifications in the forward modelling schemes, such as the assumption of phase velocity measurements.

Inversion is usually cast into a minimization problem where the difference between synthetic data, generated for a known model, and the observed data is to be minimized. Minimization schemes can be broadly classified as being either local or global schemes. Local schemes usually proceed from an initial point in the model space in a direction which leads 'downhill' towards the minimum. Global schemes are designed to search the entire model space to ensure that the minimum found

corresponds to the global solution. In the case that the model space is a unimodal function a local scheme can be implemented very efficiently. However, in practice inversion problems deal with observations which may be noisy, insufficient and inconsistent. For these types of problem the model space is likely to be multi-modal with many local minima. Thus the application of a local optimization scheme will be critically sensitive to the initial starting model. Therefore, for practical inversion problems the application of global optimization methods is desirable. However, because of their global nature these types of schemes are usually expensive since they necessarily entail a more thorough search of the model space than is achieved by local schemes. The ideal optimization scheme is required to be robust, efficient and of a global nature. Recently, reports of algorithms which appear to satisfy these criteria have appeared and are based upon the methods of Simulated Annealing (SA) and Genetic Algorithms (GA). For both methods analogues exist with minimization processes that occur naturally. In the case of SA the optimization scheme is analogous to the energy minimization that occurs during the cooling of melts to form crystalline structures. GA's attempt to model the process of evolution by which biological organisms adapt through reproduction and 'survival of the fittest'.

## 1.8 OVERVIEW OF THIS THESIS

In this thesis I implement a global optimization scheme, known as a GA, which is applied to various problems encountered in the analysis of seismic observations in the presence of anisotropy. As discussed previously the primary purpose of this work is to develop inversion methods which may be applied to seismic anisotropic observations. In the next Chapter of this thesis, I describe how a GA may be applied to the problem of estimating shear-wave splitting attributes obtained from a single source. The purpose of this chapter is to introduce the concept of the GA, its construction and its application to a practical problem encountered in shear-wave anisotropy. Inversion is the subject of Chapters 3, 4 and 5. In Chapter 3  $qP$ -wave velocity measurements, derived from laboratory travel time experiments, are inverted. The remaining two Chapters, 4 and 5, are concerned with the inversion of shear-wave

splitting data obtained from various VSP experiments conducted at the Conoco Borehole Test Facility, Oklahoma. A brief summary of each chapter is now reported.

Chapter 2 - In this chapter I apply the GA to the problem of estimating the shear-wave splitting parameters of time delays and  $qS1$ -wave polarizations for shear waves generated using a single source. Although many more practical methods have been devised for this problem this application serves as a suitable problem to investigate the characteristic behaviour of a GA. The GA's performance is tested with respect to 'advanced' genetic operators and also control parameters. The GA is applied to both synthetic and field data to determine shear-wave splitting estimates.

Chapter 3 - I apply the GA to the inversion of  $qP$ -wave velocities measured from travel time measurements over a wide variety of directions for two different spherical samples. Since GA's may be critically sensitive to different model representations three different parametrization schemes are used to investigate the GA's behaviour.

Chapter 4 - This is a case study in which shear-wave splitting estimates measured from an Azimuthal VSP experiment are inverted and interpreted. The results suggest that a shear-wave singularity is illuminated by the survey and also that the observed anisotropy may be interpreted in terms of a sub-vertical fracture system or a combination of vertical cracks embedded into finely layered media.

Chapter 5 - The previous inversions presented in Chapters 3 and 4 assume a homogeneous anisotropic medium. For more practical applications a spatial variation of the anisotropy needs to be considered. Therefore, in this chapter a forward modelling scheme based upon ray tracing methods is used. A comparison of ray tracing with full wave form synthetics shows good agreement. The inversion method is applied to shear-wave splitting estimates measured from two near-offset VSP experiments conducted at the same site as the Azimuthal VSP discussed in Chapter 4. An interesting correlation between lithology and shear-wave birefringence is observed. The near-offset VSP inversion results support the interpretation of a sub-vertical

fracture system suggested by the inversion results given in Chapter 4. This study emphasizes the need for careful interpretation of shear-wave splitting estimates and also the need for multi-azimuthal measurements of shear-wave splitting if confidence is to be placed on the results of such experiments.

Chapter 6 - In the final chapter of my thesis I discuss the implications of this thesis with respect to the interpretation of shear-wave splitting. The importance of seismic anisotropy due to sub-vertical fracturing is discussed. The inclusion of multi-azimuthal observations for the resolution of dipping fractures is emphasized as a potentially important use of seismic anisotropy.

## CHAPTER 2

### ESTIMATION OF SHEAR-WAVE SPLITTING USING GENETIC ALGORITHMS

#### 2.1 INTRODUCTION

In this chapter I will introduce the GA in the context of a tool by which shear-wave splitting may be quantified. This will serve as an example to illustrate the behaviour of a GA applied to a practical problem encountered in shear-wave anisotropy. I will use this problem to show the sensitivity of the optimization method to various parameters and processes controlling the GA search. Although this work is only intended to demonstrate the GA as a search mechanism it will be shown that the GA is comparable to other existing estimation techniques in both accuracy and reliability of the results.

An active research area in seismic anisotropy is the automation of the detection and quantification of shear-wave splitting. This research is intended to eliminate both the subjectivity and time consuming process that is involved in the examination of hodograms (particle-motion diagrams). Several techniques have been developed such as the numerical rotation analysis of Alford (1986) which I will now briefly describe in the role of an optimisation scheme. In the case of the Alford rotation the three-component seismograms are recorded using at least two source orientations, this arrangement is conveniently displayed in a multi-component plot (see Figure 2.1). These seismograms may be numerically rotated so that the source is effectively polarized into the in-line and cross-line directions aligned parallel to the radial and transverse geophone components respectively. In the case of an isotropic material, for which there is no shear-wave splitting, there is no energy in the off-diagonal elements. This is because an in-line source does not excite energy on the transverse geophone component and a cross-line source does not excite energy on the radial geophone component. In the case of an anisotropic material this is not generally the case since

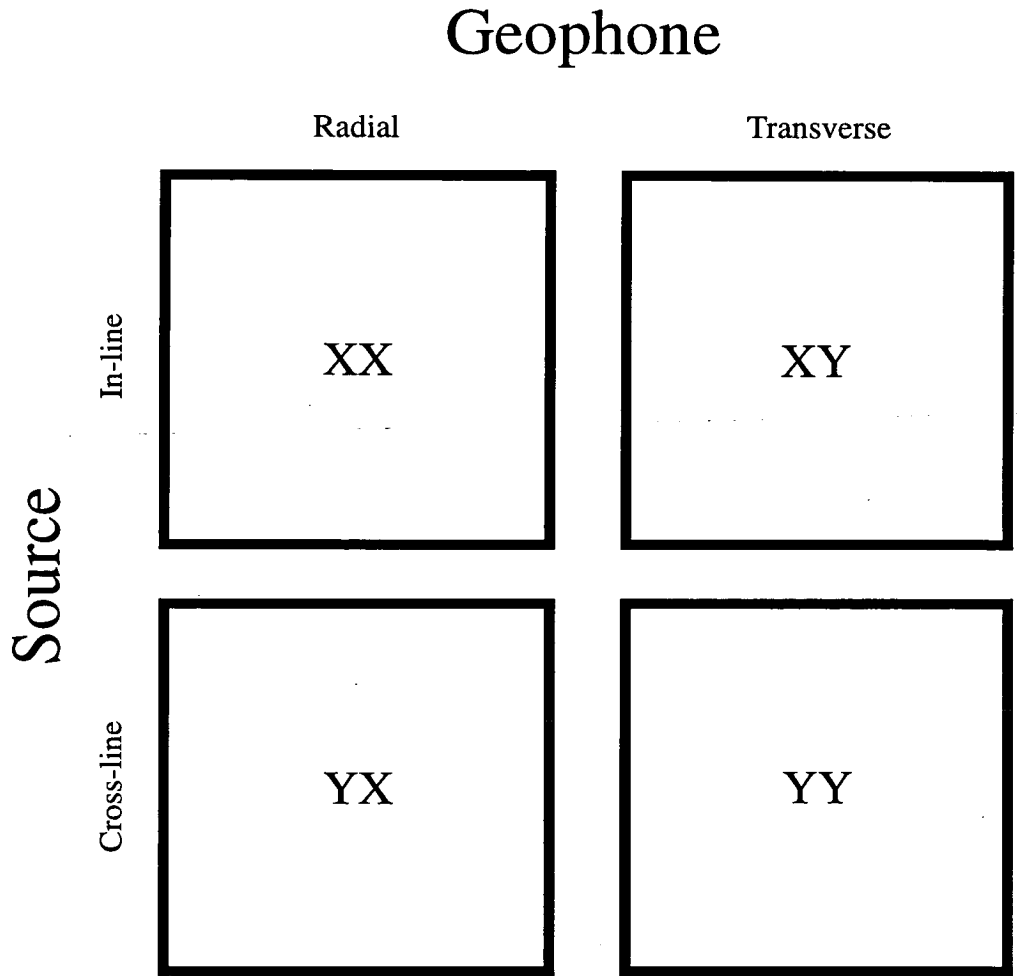


Figure 2.1 - The four component representation of multi-component data commonly used to display shear-wave data recorded from multiple source orientations. In the general case that the source and geophone orientations do not coincide with a symmetry direction shear-wave energy will be present in the off-diagonal elements XY and YX. Alford's method of estimating the *qSI*-wave polarization is to numerically rotate the data matrix to minimise this off-diagonal energy effectively aligning the source and geophone components with the fast and slow shear-wave polarizations.



the shear-wave polarizations are fixed by the propagation direction relative to the symmetry axis. In the case that the in-line and cross-line shear-wave source polarizations do not coincide with a symmetry direction, so that the quasi-shear waves do not decouple into pure  $SH$  or  $SV$  modes, energy appears in the off-diagonal elements of the multi-component representation. Alford's method numerically rotates the seismograms aligning the fast and slow shear-wave polarizations with the source and geophone components. In this co-ordinate frame the energy is maximized on the diagonal elements and minimised on the off-diagonal elements of the multi-component representation. Alford's rotation method can then be viewed in terms of an optimization process whereby the goal function is to minimize the sum of energy on off-diagonal components or alternatively to maximize energy on the diagonal components. I develop an original anisotropic estimation technique which will use a GA as the optimization method.

## 2.2 IMPLEMENTATION OF THE GA

Genetic algorithms attempt to simulate evolution by the implementation of analogues of genetic processes which act upon chromosomal representations of a suite of models known as a population. These methods are relatively new and their existence dates to the 1970's when researchers in artificial intelligence were attempting to model evolution (Holland 1975). The use of these methods has seen increasing popularity in many diverse fields for which optimization using traditional approaches has proved to be unsuccessful. A schematic comparison of some popular search methods is presented in Figure 2.2. This illustrates the search mechanisms associated with Monte Carlo (MC), Simulated Annealing (SA), GA and local gradient search methods. Local search methods are usually efficient in the case that gradient information can be easily obtained for an essentially unimodal objective function. Unfortunately for many of the problems encountered in geophysics this requirement is often violated due to non-uniqueness, overparametrization and noise (Smith, Scales and Fischer 1992). In such cases local schemes may be critically dependent upon the starting model from which

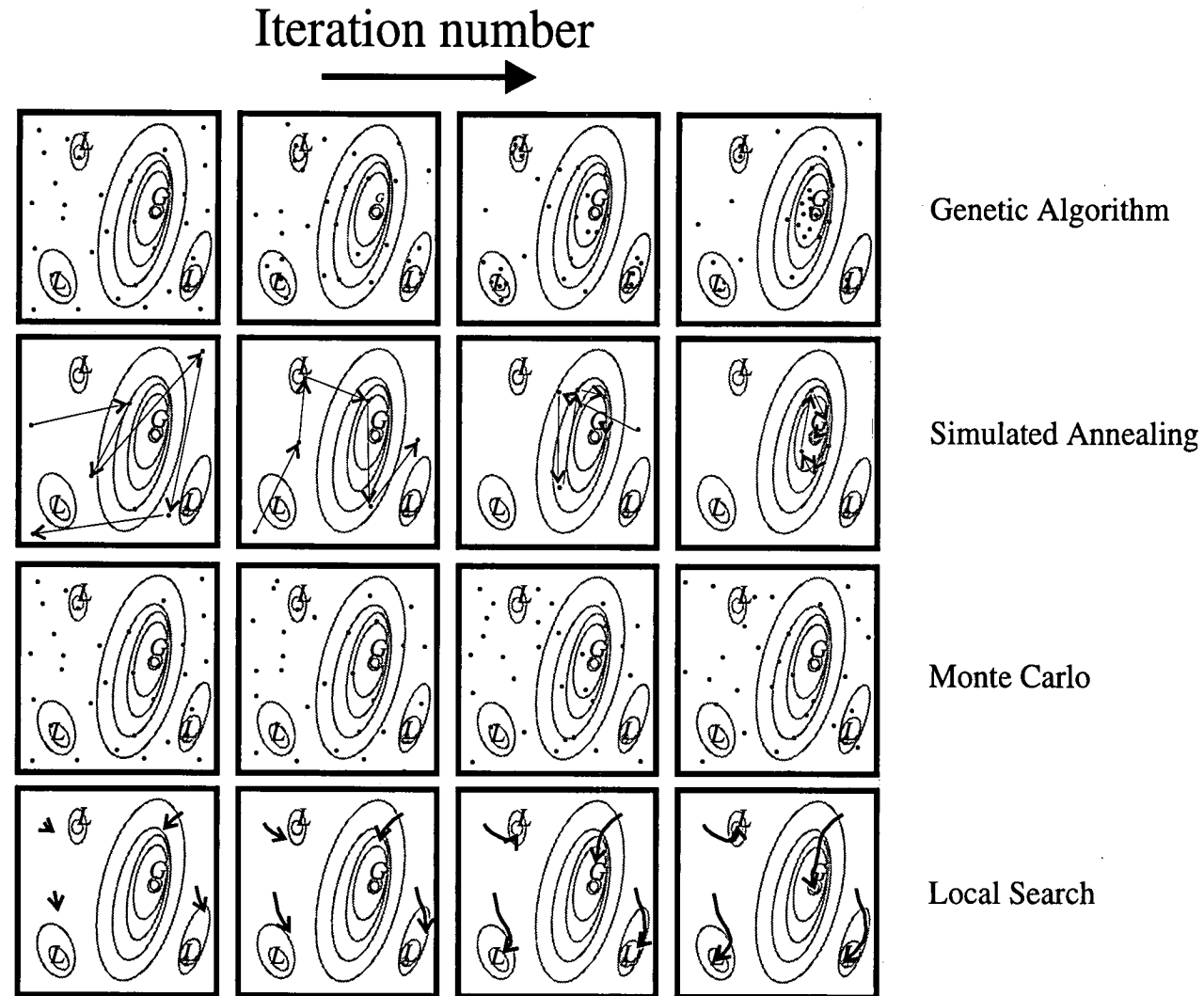


Figure 2.2 - A schematic illustration showing the characteristic methods associated with some optimization methods. The G and L denote global and local maxima respectively. The black dots indicate models sampled by the algorithms and the arrows the search direction.

the search proceeds. A search method is required that is robust, reliable, efficient and global. One of the simplest methods that satisfies these criteria is an enumerative search which searches the entire discretized model space. This method is impractical for all but the smallest of model spaces and is typically useless for realistic problems that are addressed in geophysical applications. Another popular approach has been the use of MC schemes. True MC searches are undirected, memoryless random walks through the model search space. Models are sampled at random until a sufficiently good number of solutions have been found from which a statistical estimate can be made of the optimal solution (Tarantola 1987). As might be expected these methods are extremely inefficient due to the absence of any underlying search mechanism. SA and GAs can both be considered as directed MC searches in that both are stochastic methods. SA attempts to simulate the energy minimization that occurs during the crystallization of melts. During the initial stages of SA the system is 'hot' and large variations in the model parameters are allowed allowing a wide exploration of the model space. As the system is 'cooled' these jumps become progressively smaller and models are statistically accepted such that models nearer the optimal solution are more likely to be sampled. Although SA is a popular optimization scheme within the geophysics industry, problems exist with the design of a suitable annealing schedule (Basu and Frazer 1990). Just as SA is analogous to crystallization, GAs are analogous to biological systems which are subject to evolution.

The underlying processing power of a GA is thought to lie in the use of a 'chromosomal' representation of a model rather than the actual model parameters. This chromosomal representation is usually chosen to be a single string (known as a haploid) consisting of a binary representation of the model parameters. For example, consider a model which may be represented as the vector (5,2,1,3) this can be translated, using a regular binary coding, into the binary string (101,10,1,11). These strings, or chromosomes, are then manipulated using stochastic operators such that sub-strings, known as schemata, within the 'better' models are more likely to be propagated into successive generations. Such behaviour is reminiscent of the 'survival

of the fittest' whereby favourable genetic qualities are passed into successive generations depending on the 'usefulness' of the particular trait. The implementation of this process within GAs can be mathematically described using the Schema (or schemata) Theorem or the Fundamental Theorem of Genetic Algorithms (Goldberg 1989),

$$m(H,t+1) \geq m(H,t) \cdot \frac{f(H)}{f_{avg}} \left[ 1 - p_c \cdot \frac{\delta(H)}{(l-1)} - p_m \cdot O(H) \right]. \quad (2.1)$$

This equation describes an upper bound on the number,  $m(H,t)$ , of schemata  $H$  in generation  $t$ , which can be expected to be propagated into the subsequent generation  $t+1$ . The 'fitness', the quantity being optimized, for the schemata  $H$  is given as  $f(H)$  and  $f_{avg}$  is some average fitness for the entire population of chromosomes within the current population. The terms  $p_m$  and  $p_c$  refer to probabilities associated with the mutation and crossover operations which are described in detail later. As already mentioned schema are similarity templates which, for a binary representation of a model, consist of the alphabet  $\{0,1,*\}$  where  $*$  represents a wildcard. A model represented by a chromosome of  $l$  bits contains a total of  $3^l$  schemata, where  $l$  is the length of the chromosome. Some examples of schemata contained within my earlier example chromosome are  $H_1=\{1*11****\}$  and  $H_2=\{***10*11\}$ . Schemata are usually referred to in terms of their order,  $O(H)$ , and their defining length,  $\delta(H)$ . The order of a schemata is the number of bits that are fixed within the schemata. Thus for my first example schemata the order is  $O(H_1)=3$  since the first,third and fourth positions are fixed, similarly  $O(H_2)=4$ . The defining length of a schemata is the distance between the first and last fixed positions within the schema. So for the two example schemata shown the defining lengths are  $\delta(H_1)=3$  and  $\delta(H_2)=4$ . The role of schemata processing by GAs will now be discussed with reference to the genetic operators used within the GA.

GAs work using operators which are applied to a suite of models, analogous to a population, in such a way that new models are generated which are on average nearer

to the optimal solution. These new models, the offspring, are constructed from existing models in the population, the parents, in such a way that they inherit characteristics from the parent models. The simplest implementation of a GA requires only three operators - the *reproduction*, *crossover* and *mutation* operators (Goldberg 1989).

(i) *Reproduction* selects an individual from the current population of models in a probabilistic fashion determined by that individuals 'fitness' - the quantity being optimised. This feature is analogous to the Darwinian process of natural selection or the 'survival of the fittest'. A useful image of the reproduction operator can be visualised by considering a biased roulette wheel comprised of sectors. Each individual within the population is assigned a sector on the wheel in such a way that the size of each sector is proportional to that individual's fitness. Individuals are now selected by picking a point at random along the wheels circumference (see Figure 2.3a). Clearly the fitter individuals, that are assigned a larger sector of the roulette wheel, are more likely to be selected. This operation accounts for the first term in equation 2.1,

$$m(H,t) \cdot \frac{f(H)}{f_{avg}} . \quad (2.1a)$$

Thus models containing schemata of above average fitness are more likely to be propagated into the next population.

(ii) *Crossover* is applied to the individuals previously selected by the reproduction operator. The purpose of the crossover operator is to combine information from separate individuals, the parents, to create new individuals, the offspring. These new offspring will inherit characteristics associated with the parents. Crossover may be achieved by taking two of the individuals, previously selected by the reproduction operation, selecting a point at random along their string representation and swapping their chromosomal representations thereby creating two new offspring. This is shown

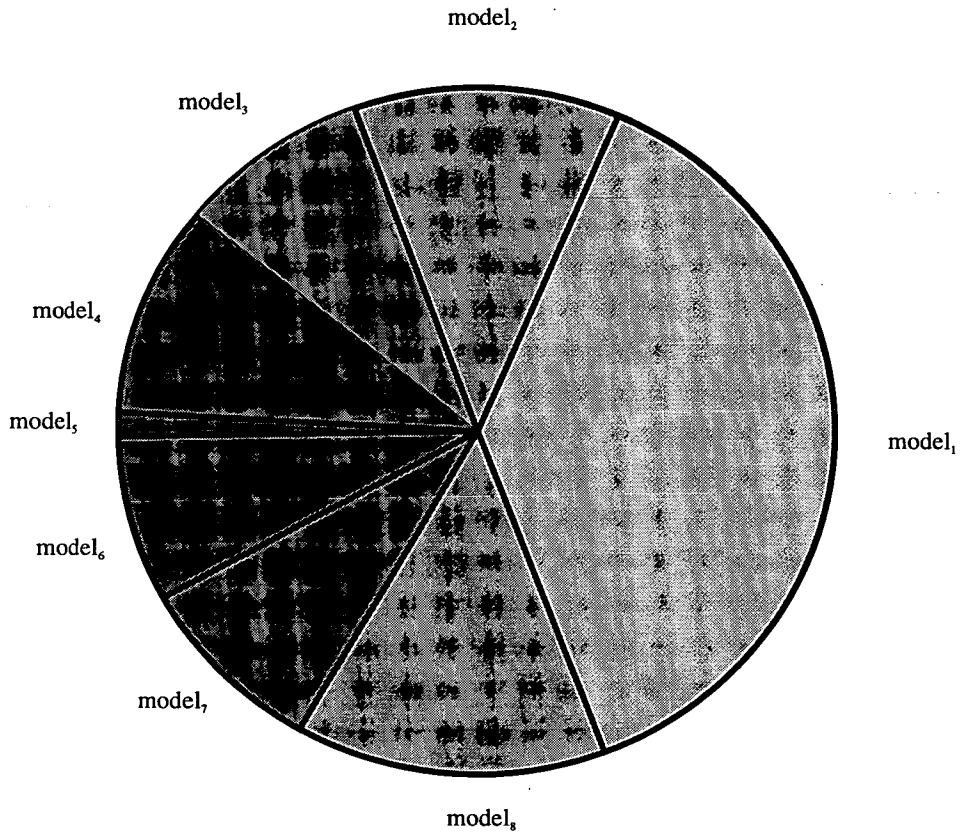


Figure 2.3a - A schematic illustration of roulette wheel selection that is used in the genetic operation of reproduction. Models are assigned a sector whose size is dependent on the models fitness. Fitter models are assigned a larger area and are more likely to be selected (after Goldberg 1989).

in Figure 2.3b. Crossover is an operation that disrupts schemata of long defining length. For example, the schemata (\*1\*\*\*0\*) of defining length 4 is more likely to be destroyed during crossover than the schemata (\*\*\*11\*\*\*) which is of defining length 1. This is because there are four positions in the first example schemata, compared with only one position in the second, for which crossover may destroy the schemata. This is described in the second term of the fundamental theorem,

$$-m(H,t) \frac{f(H)}{f_{avg}} p_c \frac{\delta(H)}{(l-1)} . \quad (2.1b)$$

Some authors suggest that the success of GAs is due to the propagation of highly fit schemata of short defining length from generation to generation (Davis 1991, Goldberg 1989). This idea is often referred to as the 'building block hypothesis' or 'implicit parallelism'.

(iii) *Mutation* is a low probability operator which is applied to prevent the permanent loss of any genetic information from the population which may be essential in constructing fitter individuals in later generations. Each element of an individuals chromosomal content is altered with a small probability. For a GA employing a binary representation the mutation operation will alter a point at random along the individuals binary string from a 0 to 1 and vice versa (see Figure 2.3c). The disruption caused by the mutation operator to schemata is proportional to the order of the schemata. This accounts for the third term in equation 2.1,

$$-m(H,t) \frac{f(H)}{f_{avg}} p_m O(H) . \quad (2.1c)$$

These operators, and their variants, are fundamental to the operation of a GA but they do not form a comprehensive set. There exist many more advanced operators and techniques which have been shown to have varying degrees of success in improving a GA's performance. I include some of these advanced operators and will now

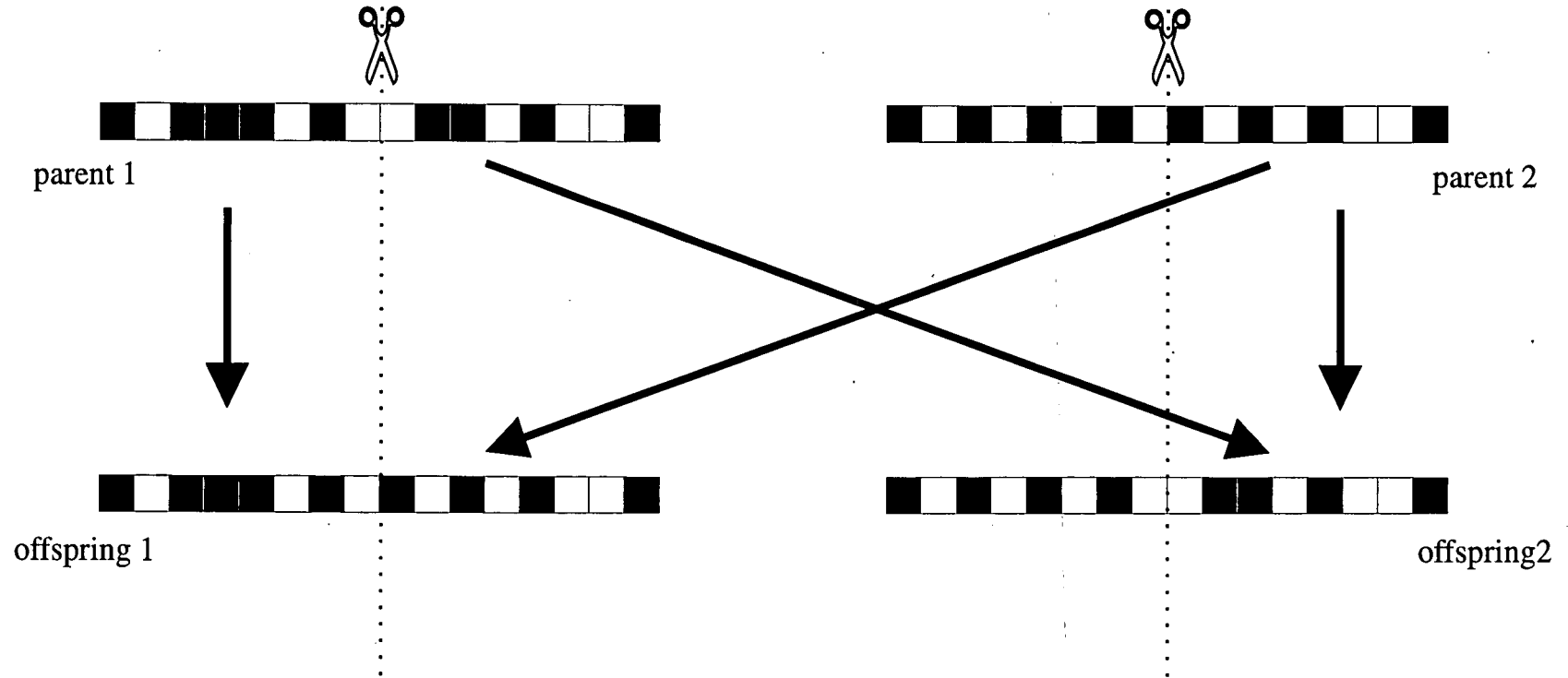


Figure 2.3(b) - A schematic illustration of the crossover operator applied to binary representations of two selected models. A point is selected at random along the binary string as shown by the dotted lines. The sub strings from either side of the crossover site are then exchanged between the two models. Two new individuals are formed by the crossover operation which have characteristics of both the parents.



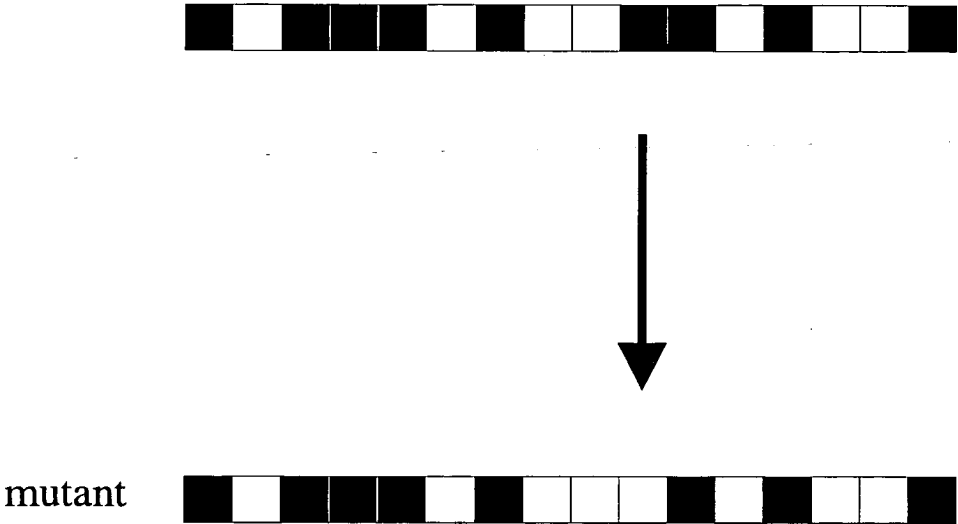


Figure 2.3(c) - A schematic illustration showing the mutation operator applied to a binary representation of a model. A bit is randomly altered from its initial state, shown here as black, to another value, represented here as white.

describe these extensions and their purpose.

*Inversion* - This does not have the same meaning as that used in geophysics whereby model parameters are to be derived from a set of observations. The inversion operator is a reordering mechanism whereby the chromosomal representation of a model is scrambled. Its purpose is to construct the low order 'building blocks' which are essential to the success of a GA search. In a regular coding scheme the separate parameters describing an individual model are typically mapped into sub-strings which are then concatenated to form the individual's chromosome (see Figure 2.3d). The position of each of these sub-strings within the individual's string is then fixed. This can cause problems if important schemata are of a high defining order since they are likely to be disrupted by the application of the crossover operator. The inversion operator is designed to circumvent this problem by attempting to construct an ordering of genetic information which is more favourable to the operation of the GA. Inversion selects two points along an individual's length and reverses the ordering of the genetic information (see Figure 2.3e). This reordering implies that extra coding describing the position of the chromosome's elements must also be stored for use in decoding the scrambled chromosome. Before the crossover operator is applied the chromosomal representations must be reordered so that the strings are compatible or homologous. There are several choices to ensure homologous crossover (Goldberg 1989) I choose to use 'best pattern matching'. In this case the inferior individual chromosome is remapped to the same representation of the fitter individual. It is important to note that the inversion operator does not affect an individual's fitness since the model parameters remain unchanged.

*Elitism* - The construction of a new population may not preserve the best individual from the previous population. The best or 'fittest' individual is taken to be the model nearest the optimal solution. Elitism combats this by simply replacing the worst individual in the current population with the best individual from the previous population.

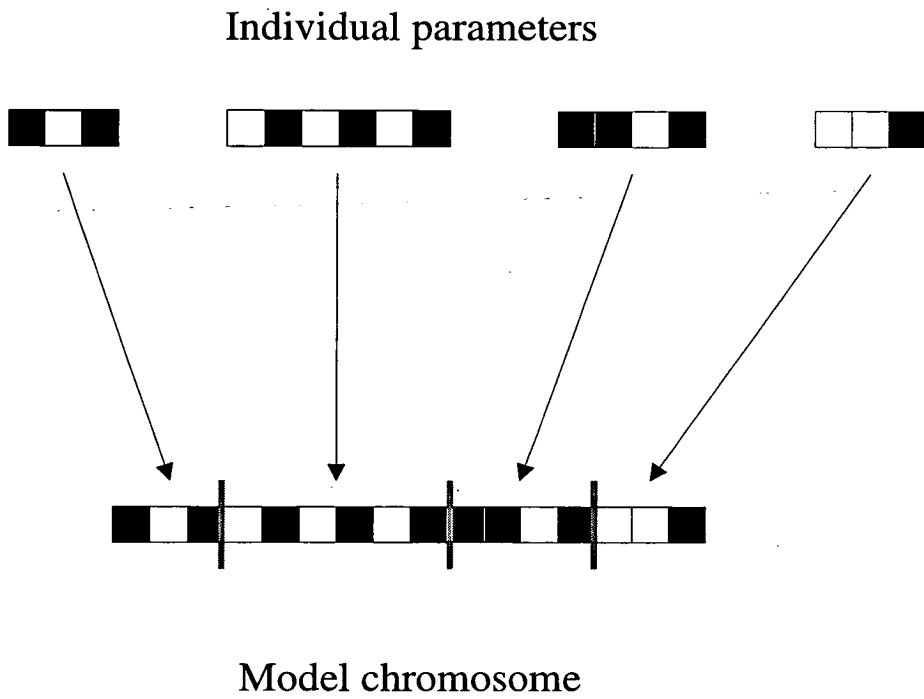


Figure 2.3(d) - A schematic illustration showing the construction of an individuals chromosome for a multi-parameter model. For each component within the model a sub-string is constructed. These sub-strings are then joined to form a string which defines the model.

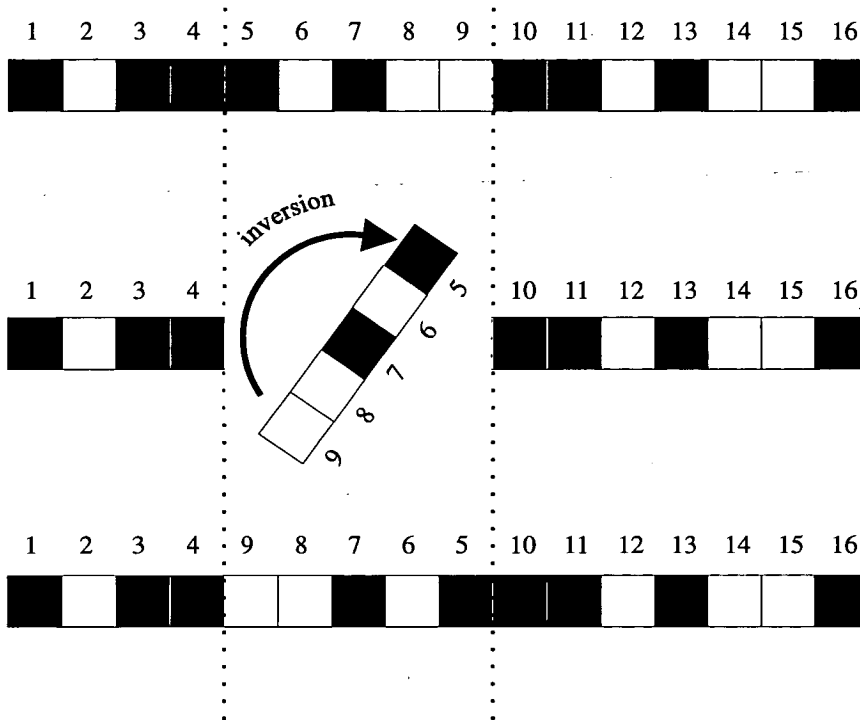


Figure 2.3(e) - A schematic illustration showing the inversion operator applied to a binary representation of a model. The upper frame shows the original string with a sequence of bits indicated by the numbers over each box. Two sites are selected at random along the string, indicated by the dotted lines. The sub-string lying between these positions is then 'flipped' so that the bit ordering is reversed as shown in the lower frame.

*Gradient-bit improvement* - This is equivalent to the numerical evaluation of the local gradient function. Each parameter in the current population's best individual is allowed to move randomly either up or down one discretization interval whilst keeping all the other parameters constant (Goldberg 1989). A trial evaluation may then be made at a point in the model space along the direction of steepest ascent or descent. If this fails to produce a fitter individual the initial model may still be replaced with any of the fitter individuals evaluated during the construction of the gradient vector. This operation implies that the implemented GA is a hybrid optimization scheme employing both local and global search strategies.

*Sharing* - If a GA is applied to the problem of searching a multi-modal space it will tend to cluster models about the optimal solution whilst ignoring many of the sub-optimal solutions (see Figure 2.4). The populations will increasingly tend to include very similar models about the optimal solution so that diversity decreases as the GA converges. This feature also occurs naturally and is known as genetic drift. This behaviour is an unattractive feature for many geophysical optimization problems where the model space is unlikely to be unimodal. For example, it is well known that an overparametrized model space is multi-modal with many optima of near equal fitness (Sen and Stoffa 1992). This problem may be alleviated by the formation of sub-populations, known as 'niches', which 'inhabit' different portions of the model space. These niches can be constructed using sharing, the technique that I use, or by constructing a parallel GA with isolated subpopulations as described by Sen and Stoffa (1992). Sharing is an operation that encourages the formation of sub-populations, or niches, within the main population. Thus sharing maintains diversity within the population whilst also maintaining a representative sample of the most significant points about local optima. Sharing derates an individual's fitness depending on the individual's similarity to all the other individuals within the current population. For a binary system of chromosomes this similarity between individuals can be measured in terms of the Hamming distance. The Hamming distance is defined to be the number of different bits between two binary codings normalised by the strings length,

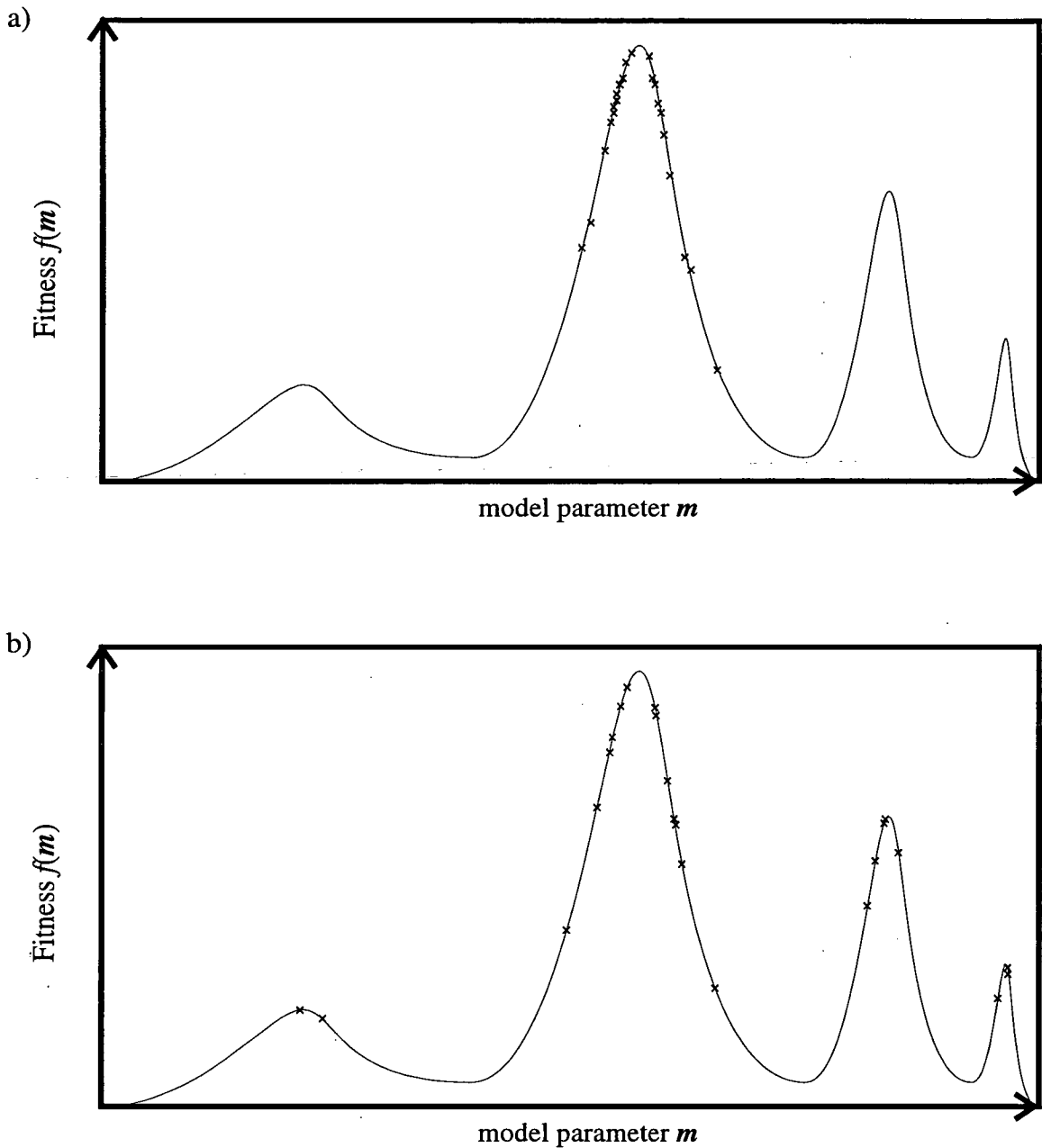


Figure 2.4 - A schematic illustration showing the behaviour of a GA applied to a multi-modal maximization problem with a) no sharing and b) sharing, solutions sampled by the GA are indicated by crosses. When sharing is included solutions are distributed about both the local and global maxima, with the approximate solution density proportional to the relative amplitudes of the peaks.

for example the Hamming distance between the two binary codes 010010 and 011001 is 0.5. The fitness of an individual within a population is derated according to the function (Goldberg 1989),

$$f_{share}(m_i) = \frac{f(m_i)}{\sum_{j=1}^{N_{pop}} s(d(m_i, m_j))} \quad (2.2)$$

where  $f_{share}$  is the derated fitness of an individual  $m_i$  with fitness  $f$ , the Hamming distance between two individuals  $m_i$  and  $m_j$  is given by the function  $d$  and  $N_{pop}$  is the total number of individuals in the current population. The function  $s$  controls the degree of sharing and is defined to be directly inversely proportional to the Hamming distance with boundary conditions  $s(0.0) = 1.0$  and  $s(1.0) = 0.0$ .

A schematic flowchart indicating the sequence in which these operators are applied in the hybrid GA is shown in Figure 2.5. The GA proceeds by selecting an initial population of  $N_{pop}$  models at random from the parametrized model space. For each of these models the fitness function is evaluated and is then used to construct the roulette wheel used in reproduction. The selection probability,  $p_s$ , that I choose is a linear function designed to suppress the undesirable effects of any individual model with an unusually high fitness which would otherwise dominate the subsequent generation. The function used is (Sambridge and Drijkoningen 1992)

$$p_s(m_i) = \frac{a f(m_i) + b}{\sum_{j=1}^{N_{pop}} p_s(m_j)} \quad (2.3a)$$

$a$  and  $b$  are calculated as,

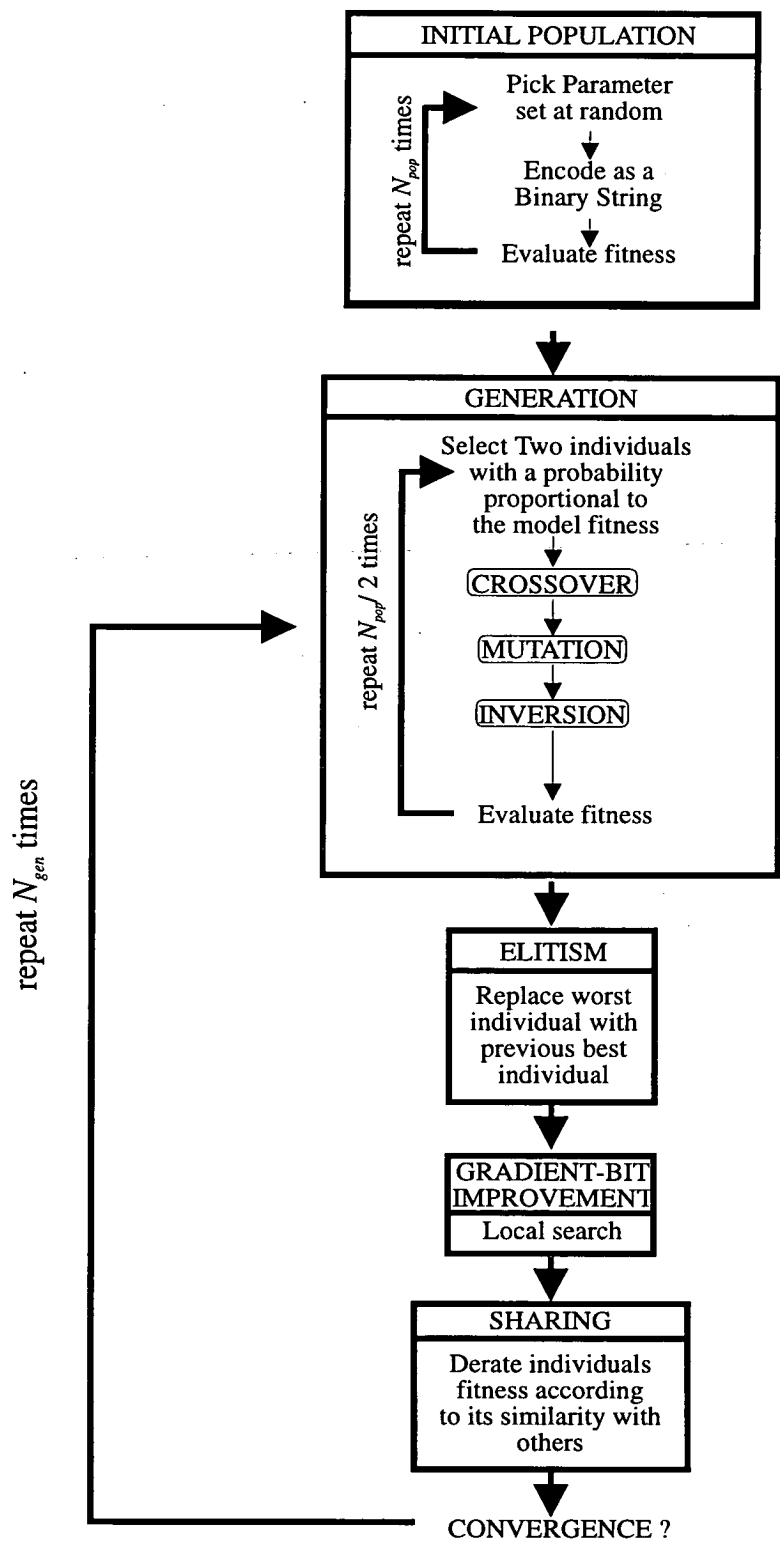


Figure 2.5 - A flowchart describing the sequence of operations that are implemented in the GA.



$$a \geq b f_{max}$$

$$b = \frac{1}{N_{pop}(f_{max} - f_{avg})} \quad (2.3b)$$

where  $f_{max}$  and  $f_{avg}$  are the maximum and average mean fitnesses within the current population of  $N_{pop}$  individuals. The reproduction process is applied to construct the next generation by selecting two parents at random using roulette wheel selection. The crossover operator is then applied to these two individuals with a probability  $p_c$  thereby creating two offspring. These are then mutated with probability  $p_m$  and the resulting two mutated offspring are inserted into the next generation. The individual's coding is then reordered with a probability  $p_i$  by application of the two point inversion operator. Population statistics are calculated for this new generation and the fittest and worst individuals identified. Elitism is applied when the fittest individual in the current population is found to be inferior to the fittest individual in the previous generation. At this stage a local search is performed about the best individual, using a Gradient-Bit search, and replaced if a fitter individual is found. Sharing is now applied so that an individual's fitness will be derated in proportion to the number of similar models in the population. This sequence of operations is repeated for a maximum of  $N_{gen}$  generations or until some other stopping criteria is satisfied. After each generation the individual model parameters and their associated fitnesses are written to a file which allows a statistical analysis of the models sampled during the GA search.

It is important to recognise that the random number generator used in determining the application of genetic operations is only pseudo-random with a finite cycle length of approximately  $10^{17}$  (Press *et al.*, 1992). GAs typically require of the order of  $N_{pop} \cdot N_{string} \cdot N_{gen}$  random numbers, where  $N_{string}$  is the length of the string defining the model. For the problems addressed in this thesis it is unlikely that the periodic nature of the random number generator will become apparent. The statistical nature underlying the pseudo-random number generator has a uniform distribution.

### 2.3 PARAMETRIZATION OF SHEAR-WAVE SPLITTING

One of the most characteristic features of seismic wave propagation through an anisotropic medium is the phenomenon of shear-wave splitting. In general two shear waves can be excited which propagate with distinct velocities and polarizations that are determined by the direction of propagation. As a result a time delay accumulates between the two shear waves which is proportional to the path length and the difference in the reciprocal of the velocities (slowness). Shear-wave splitting is frequently quantified in terms of the polarization of the leading split shear-wave (*qS1*) and the time delay between the faster and slower shear waves. A formal model of shear-wave splitting can be mathematically written as (Campden 1990),

$$\begin{aligned} x(t) &= A_1 s(t) \cos(\theta) - A_2 s(t - \delta t) \sin(\theta) ; \\ y(t) &= A_1 s(t) \sin(\theta) + A_2 s(t - \delta t) \cos(\theta) ; \end{aligned} \quad (2.4)$$

where  $x$  and  $y$  are orthogonal components of a wave motion recording unit (usually horizontal components of a three-component geophone),  $\delta t$  is the time delay between the *qS1* and *qS2* shear waves,  $\theta$  is the polarization angle of the *qS1*-wave measured from the  $x$ -axis towards the  $y$ -axis (Figure 2.6).  $A_1$  and  $A_2$  are the amplitudes of the *qS1* and *qS2* wave modes and  $s(t)$  is the source wavelet function. The two amplitude parameters can be replaced by a single parameter  $A = A_2 / A_1$  by normalization,

$$\begin{aligned} x'(t) &= s(t) \cos(\theta) - A s(t - \delta t) \sin(\theta) ; \\ y'(t) &= s(t) \sin(\theta) + A s(t - \delta t) \cos(\theta) . \end{aligned} \quad (2.5)$$

The parameters that I use to quantify the shear-wave splitting in the GA Technique (GAT) are,

- (i)  $\delta t$ , the time delay between the faster and slower split shear waves,
- (ii)  $\theta$ , the polarization direction of the *qS1*-wave,
- (iii)  $A$ , the relative amplitude of the *qS2* to the *qS1*-wave,

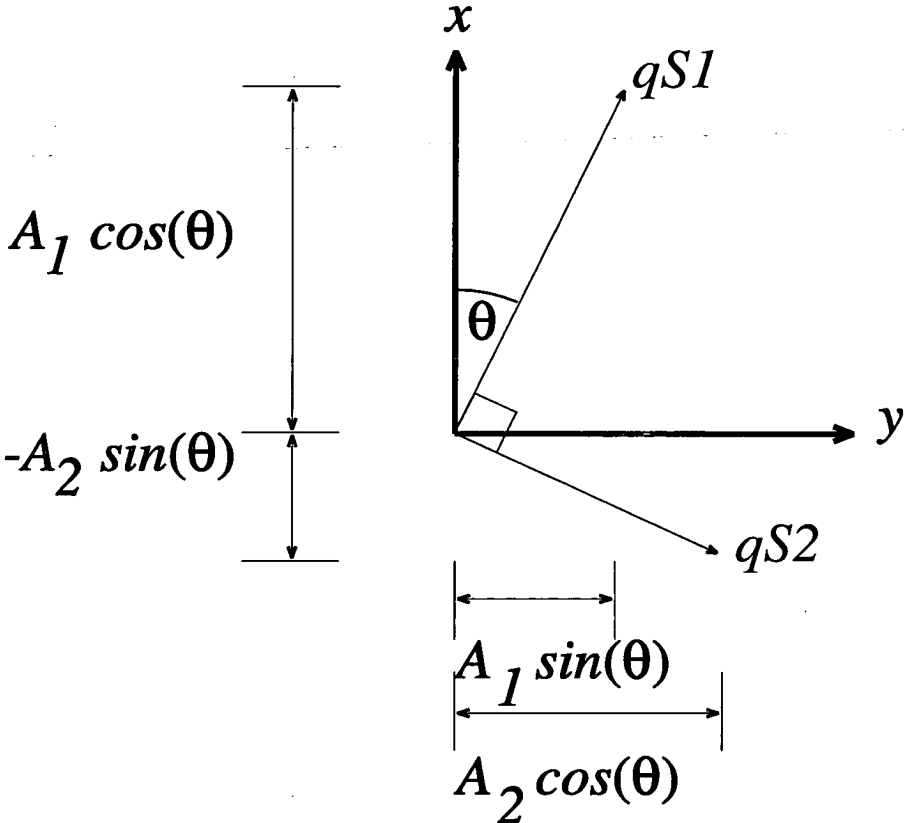


Figure 2.6 - An illustration showing the co-ordinate systems used in the shear-wave splitting model described in equation 2.4.

(iv)  $n$  and  $d$ , parameters defining the source function  $s_{n,d}(t)$ ,

$$s_{1,d}(t) = e^{-\frac{\omega t}{d}} \sin(\omega t) ; \quad (2.6a)$$

$$s_{2,d}(t) = t^2 e^{-\frac{\omega t}{d}} \sin(\omega t) ; \quad (2.6b)$$

with  $t > 0$ . These functions are based on the ANISEIS (Taylor 1990) pulse functions and define impulsive functions with the degree of damping controlled by the parameter  $d$ .

These five parameters are used to define the model space for the estimation of shear-wave splitting and are discretized according to the scheme shown in Table 2.1.

The objective function which is to be maximised by the GA is a normalized correlation coefficient between the modelled and observed waveforms denoted  $d_m(t)$  and  $d_o(t)$  respectively (Kanasewich 1981),

$$f(d_o, d_m) = \text{Re} \frac{\sum d_m(t) d_o(t)^*}{\left( \sum d_m(t) d_m(t)^* \sum d_o(t) d_o(t)^* \right)^{1/2}} ; \quad (2.7)$$

the two time series may be conveniently defined as complex quantities with the real and imaginary parts representing the  $x$  and  $y$  geophone components defined in equation (2.5).

## 2.4 SENSITIVITY TO GA PARAMETERS.

In the implementation of a GA some experimentation is required to find a suitable set of control parameters. Although some guidelines and suggestions are available for the choice of these parameters the effect will be dependent on the particular application.

Parameter		$P^L$	$P^U$	$N_{int}$
Pulse number	$n$	1	2	2
Damping	$d$	1.0	8.0	8
$qSI$ -wave polarization	$\theta(\text{deg})$	0.0	180.0	256
Time delay	$\delta t(\text{ms})$	0.0	80.0	128
Amplitude ratio	$A$	0.7	1.4	8

Table 2.1 - Discretization applied to the problem of shear-wave splitting estimation. The second and third columns indicate the lower,  $P^L$ , and upper,  $P^U$ , values for the parametrization range and the last column the number of discretization intervals,  $N_{int}$ , in this range. The number of intervals is chosen to be a multiple of 2 so that there are no redundant bits in the binary coding that is used in the GA's model representation. In total this parametrization defines  $4.2 \times 10^6$  ( $2^{22}$ ) models which may be represented as a binary string of 22 bits.

In Table 2.2 I summarise a selection of recently published papers describing GAs applied to various geophysical problems and the parameter values chosen by the authors. It can be seen that there is a considerable variance in the choice of the GA search parameters and some tuning is usually required to allow an efficient search of the model space. In this section I will demonstrate the GA's sensitivity to the following parameters and operators,

- (i) Population size,  $N_{pop}$
- (ii) Probability of Crossover,  $p_c$
- (iii) Probability of Mutation,  $p_m$
- (i) Inversion
- (v) Gradient-Bit search
- (vi) Sharing.

The GA will be applied to the estimation of shear-wave splitting for a synthetic seismogram using a source function defined by the parameters given in equation 2.6 as  $n = 2$ ,  $d = 2$ ,  $A = 1.0$ ,  $\theta = 50^\circ$  and  $\delta t = 10$  ms with an angular frequency of  $\omega = 20\pi \text{ rad s}^{-1}$  (10 Hz). Since GAs are of a stochastic nature the results that I show are the average results from a suite of searches which are initialised from different starting populations.

#### (i) Population Size $N_{pop}$

The size of the population must be chosen such that there is a sufficiently large 'gene' pool from which the optimal model may eventually be constructed (Berg 1991). This statement suggests that larger populations are more favourable to the operation of a GA but obviously a compromise is required because of the computational expense incurred for large populations. Conversely for populations that are too small there will be an insufficient diversity in the initial population resulting in premature convergence where many similar sub-optimal individuals are created in the later generations. Further improvement in these situations will proceed largely by the application of the

Author	$N_{pop}$	$p_c$	$p_m$	$N_{gen}$	Application
Stoffa, Sen, Varela, Chunduru 1994	50	0.6	0.01	100	Reflection profile inversion
Stoffa, Sen 1991	200	0.6	0.01	200	Seismic waveform inversion
Sambridge, Drijkoningen 1992	50	0.6 - 1.0	0.03 - 0.001	160	Seismic waveform inversion
Nolte, Frazer 1994	50	0.9	0.01	300	VSP waveform inversion
Jin, Madariaga 1993	20	0.95	0.01	900	Reflection profile inversion
Gallagher, Sambridge, Drijkoningen 1991	26 - 100	1.0 - 0.6	0.025 - 0.01	85-330	Seismic waveform inversion
Sen, Stoffa 1992	100	0.6	0.01	40	Seismic waveform inversion

Table 2.2 - A selected review of recently published research of GAs applied to different geophysical problems. This table gives the reported values of the different primary control parameters of population size,  $N_{pop}$ , crossover rate,  $p_c$ , mutation rate,  $p_m$  and number of generations,  $N_{gen}$ , used in the different implementations of the GA.

mutation operator and the benefits of the GA's schema processing will not be exploited. This effect is demonstrated in Figure 2.7a showing the convergence curves for a suite of GA runs using different population sizes. As expected the curve for the smaller populations of  $N_{pop}=10$  and  $N_{pop}=20$  individuals show premature convergence to sub-optimal values whereas the larger populations show improved convergence characteristics and converge to a higher correlation coefficient at earlier generations. It should be noted that the GAs using smaller populations have sampled fewer models than those with a larger populations at the same generation. Nonetheless, it is possible to compare points on the separate convergence curves according to the number of models sampled which is simply given by the product of the population size and the generation number. For example, it is possible to compare the fitness for the separate runs after 600 individuals have been sampled, this corresponds to the 60 th generation for  $N_{pop}=10$ , the 30 th generation for  $N_{pop}=20$ , the 15 th generation for  $N_{pop}=40$  and the 10 th generation for  $N_{pop}=60$ . At these points it can be seen that the larger population sizes have sampled individuals which are fitter than those with the smaller population sizes. The results for the two largest population sizes of 40 and 60 are not significantly different and a population size of 40 is subsequently used in the following trials. The optimum population size is likely to be linked to the size of the model space so that larger populations may be required for larger model spaces.

## (ii) Crossover Probability $p_c$

The crossover operator can be viewed as a defining feature of a GA since it is this operator which manipulates schemata which are fundamental to the operation of a GA. Previous studies have shown that GAs are relatively insensitive to the crossover probability provided that it is relatively high, with reported values ranging from between 0.6 to the upper limit of 1.0 (Table 2.2). Tests with crossover probabilities of  $p_c=0.5$ ,  $p_c=0.6$ ,  $p_c=0.8$  and  $p_c=0.95$  support this observation and in subsequent applications I use a crossover probability of  $p_c=0.9$ . Results from these tests are shown in Figure 2.7b.



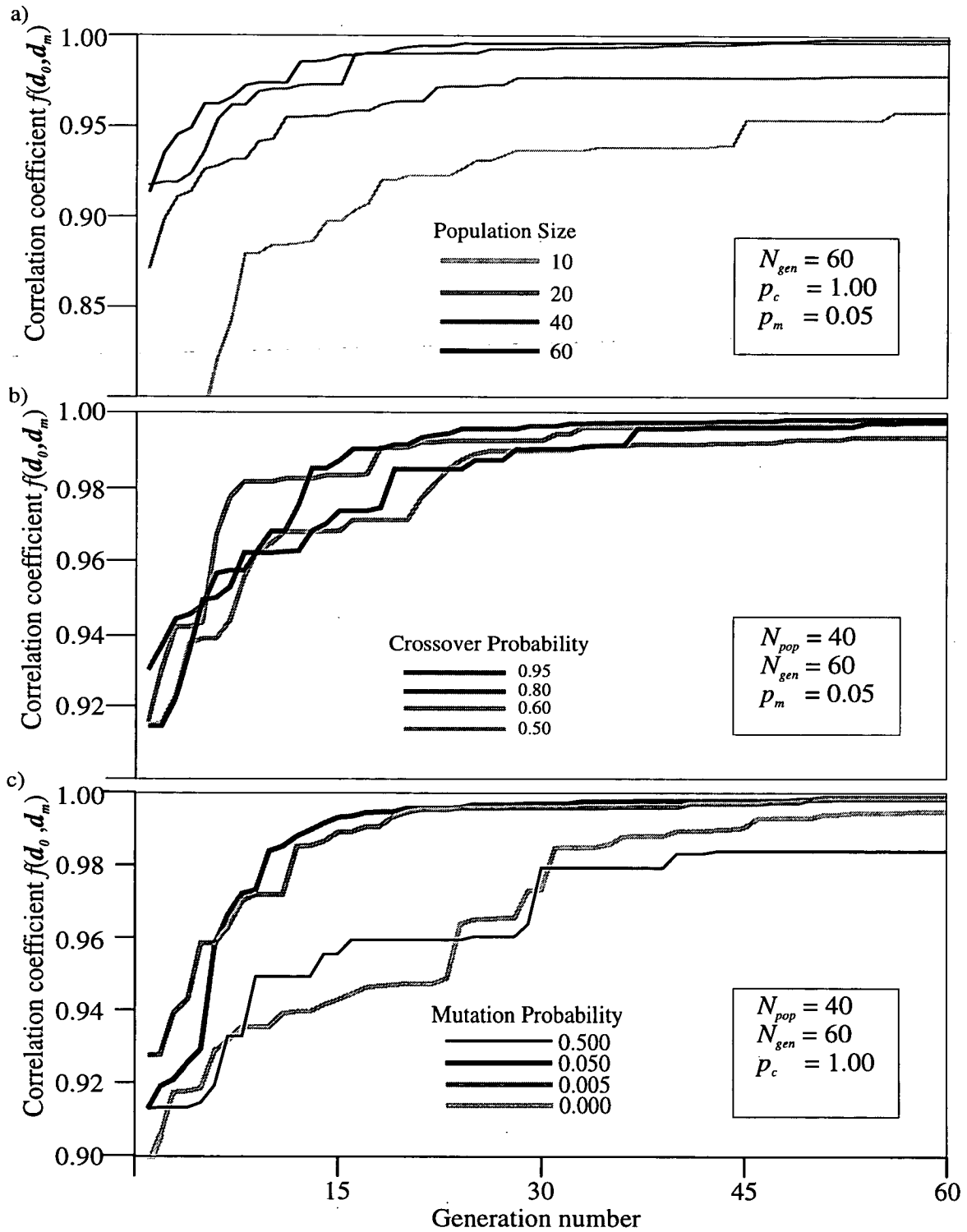


Figure 2.7 - Convergence curves showing the effect of changing a) the population size b) the crossover probability and c) the mutation probability.

### iii) Mutation Probability $p_m$

Mutation is typically applied to between 1 in every 100 to 1000 bits. An upper limit of  $p_m = 0.5$  corresponds to an entirely random search (Monte Carlo). Figure 2.7c shows the effect of the mutation rate on the convergent behaviour of the GA. The two extremes of  $p_m = 0.5$  and  $p_m = 0.0$  do not lead to satisfactory convergence whereas the curves for  $p_m = 0.05$  and  $p_m = 0.005$  are not significantly different to each other and converge to approximately the same near-optimal solution correlation after 50 generations. The effectiveness of GA search over a MC type search is clearly shown in Figure 2.7c. An alternative means of illustrating this is shown in Figure 2.8. In this diagram solutions sampled by the GA are shown as a scatter plot of the models correlation coefficient against a 'distance'. This distance is calculated from the five parameters defining the shear-wave splitting model. These can be reduced to a single (non-unique) value corresponding to a normalized vector magnitude (Tarantola 1987),

$$D(\mathbf{m}) = \left( \sum_{i=1}^{N_p} \left[ \frac{(m_i - P_i^L)}{(P_i^U - P_i^L)} \right]^2 \right)^{1/2}; \quad (2.8)$$

where  $m_i$  is the  $i$  th component of the model vector  $\mathbf{m}$ ,  $P_i^L$  and  $P_i^U$  are the lower and upper bounds for the  $i$  th parameter and  $N_p$  is the number of model parameters. Thus  $D(\mathbf{m})$  lies in the region,  $0 < D(\mathbf{m}) < N_p^{1/2}$ . The GA scheme has a higher sample density about the optimal regions of the model space compared with the MC search with many models clustered about the local and global optima so that the GA has effectively searched the more significant portions of the model space (Figure 2.8). This property makes the choice of a GA search attractive since estimates can be made for both the non-uniqueness and the variance about the best solution.

### (iv) Inversion

The inclusion of this reordering operation appears to accelerate the initial convergent behaviour of the GA although the final model fitness values are very similar (Figure 2.9a). This is in accordance with other studies (Goldberg 1989).

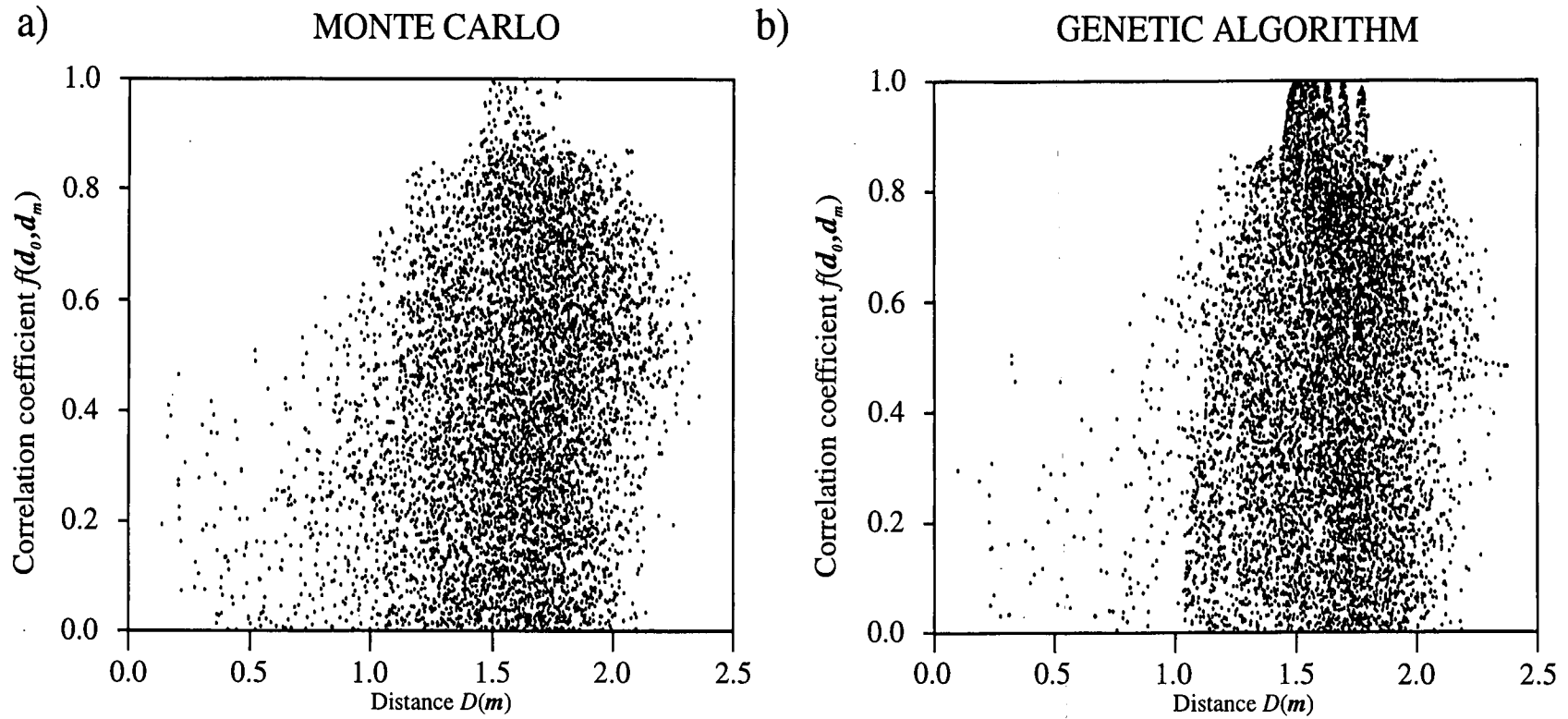


Figure 2.8 - A distance-fitness scatter plot showing correlation coefficients as a function of the model distance corresponding to models sampled by a) a Monte Carlo and b) a GA scheme.

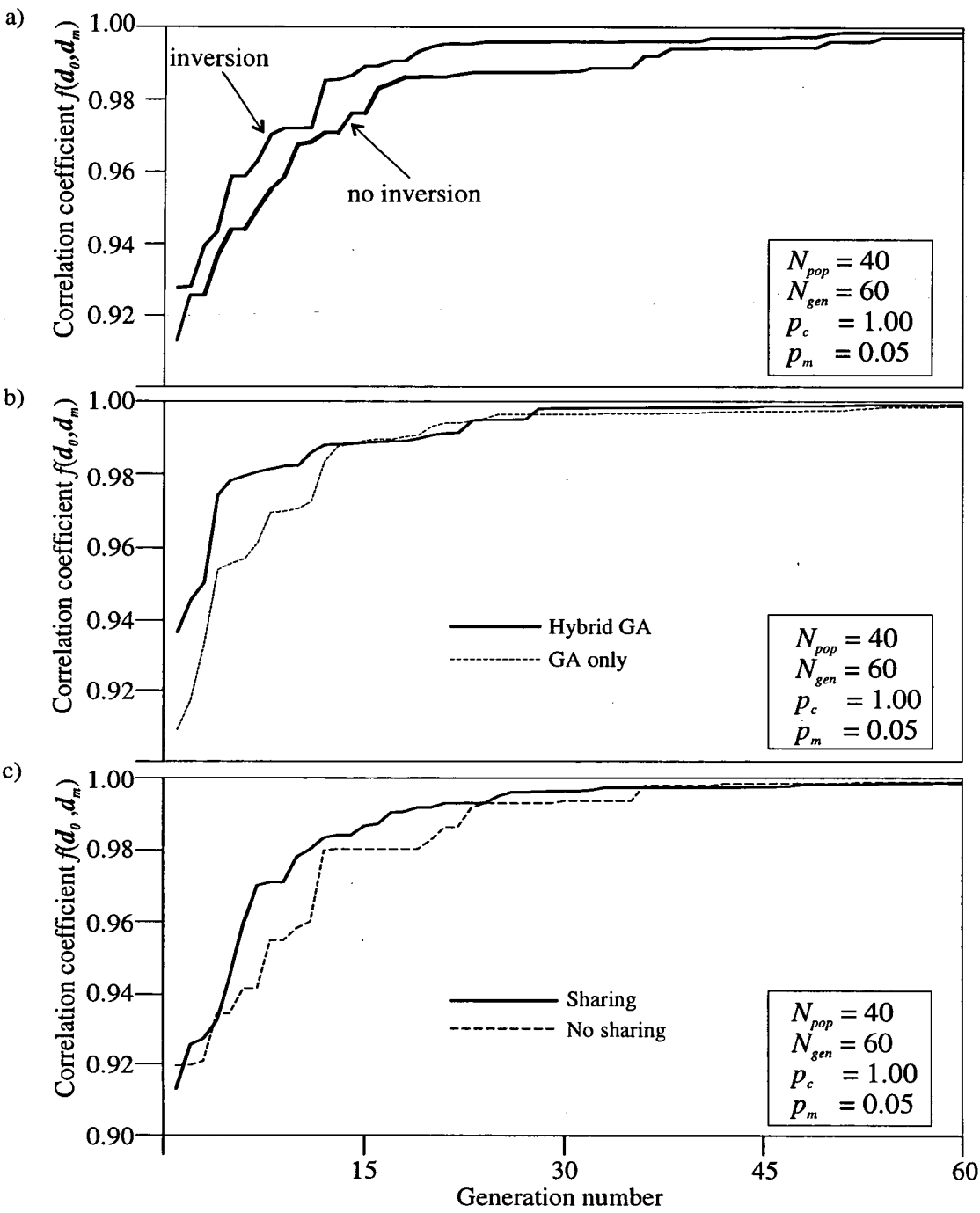


Figure 2.9 - Convergence curves showing the effect of including a) inversion b) gradient-bit improvement and c) sharing.

**(v) Gradient-Bit Improvement**

The addition of a local search operation to the GA does not produce a clear improvement (Figure 2.9b). The curve defining the hybrid scheme shows that, in general, the search produces fitter models except for a region between generations 15 and 30.

**(vi) Sharing**

The inclusion of sharing is not intended to improve the convergence of the GA search but Figure 2.9c shows that this does occur. This is probably because the sharing operation maintains diversity within later populations which would otherwise stagnate. To illustrate the success of the sharing operation in establishing sub-populations about local optima a comparison is made in Figure 2.10 of a GA with and without sharing in terms of a distance-fitness scatter plot. This figure clearly shows that the effect of sharing is to distribute more points about both the global and local optima. It should also be noted that there are considerably more samples within the window for the GA with sharing than without, implying that sharing improves the search so that the more significant 'volumes' of the model hyperspace are being sampled more intensively.

**2.5 APPLICATION TO SYNTHETIC DATA**

To test the GAT, I construct full-waveform synthetic seismograms using the ANISEIS package (Taylor 1990) to simulate vertical incidence shear-wave propagation through an anisotropic region. The acquisition geometry that I use is a zero offset VSP with sixteen geophone levels. The geophone spacing and shear-wave anisotropy are chosen so that the time delay between each successive geophone is 2 ms. This is achieved with geophones spaced every 100 m in a hexagonally anisotropic medium with a horizontal symmetry axis. This is simulated using the equivalent-media formulations of Hudson (1980) to model saturated vertical cracks of crack density 0.03 in a homogeneous isotropic halfspace of  $V_p = 3.0 \text{ km s}^{-1}$ ,  $V_s = 2.0 \text{ km s}^{-1}$  and

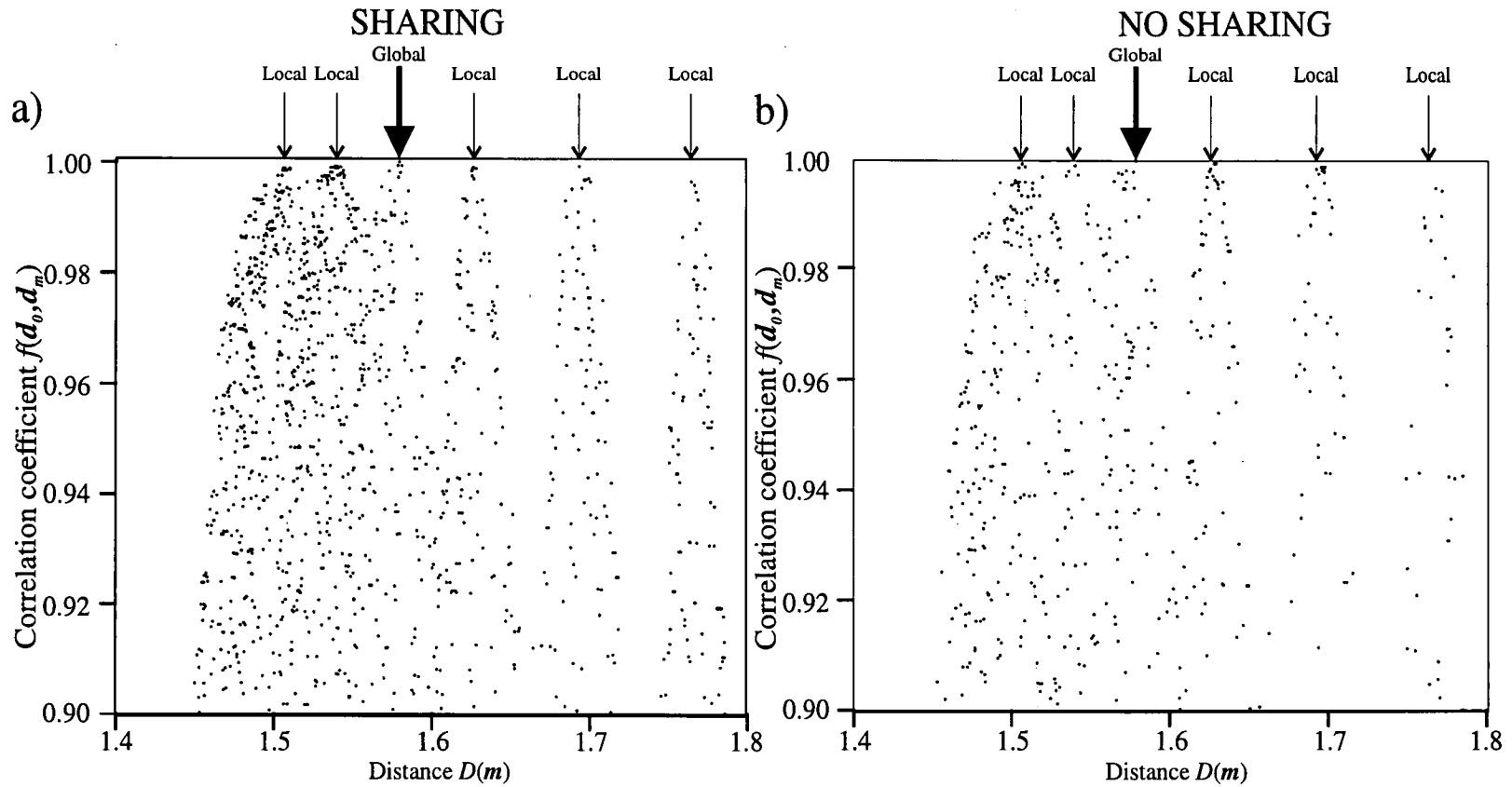


Figure 2.10 - A distance-fitness scatter plot of the correlation coefficients corresponding to models sampled by the GA when a) sharing and b) no sharing is included. The arrows indicate local and global optima.

density,  $\rho = 2.0 \text{ g cm}^{-3}$ . The first geophone level is located so that a 2 ms time delay exists between the fast and slow split shear waves. The seismic source is modelled using an impulsive horizontal source orientated at  $45^\circ$  to the fast shear-wave polarization. This source orientation ensures that both shear waves are excited with equal amplitudes. The pulse chosen is given in equation 2.6b with a damping factor of  $d=4$  and a peak frequency of  $\omega=20\pi \text{ rad s}^{-1}$  (10 Hz).

Windowed seismograms of the radial and transverse geophone components and particle motion diagrams at every fourth geophone level are shown in Figure 2.11. For split shear waves with a sufficiently large time delay the  $qSI$ -wave polarizations can be measured directly from the particle motion diagrams as the direction of the initial linear onset, as indicated by the arrows in Figure 2.11.

To evaluate the relative performance of the GAT I compare the estimation results with another commonly used single source technique, the Direct Time Series algorithm (DTS) (Campden 1990). The DTS method is an enumerative search over a grid of  $qSI$ -wave polarization angles and time delays. The geophone records are rotated and time shifted and numerically compared to evaluate a similarity function between the components. The estimated shear-wave splitting is taken to be the rotation and time shift parameters which maximize the similarity between the two recorded time series. I chose DTS from a number of possible single source techniques since experience has shown it to be one of the more reliable techniques (Liu, E., British Geological Survey, personal communication).

## 2.6 RESULTS OF COMPARISON TEST

The results of the application of the two single source techniques to the synthetic seismograms are shown in Figure 2.12. The grey lines indicate the expected values of time delay and  $qSI$ -wave polarization for the shear-wave splitting. The results for DTS show that for shear waves with small time delays the technique overestimates

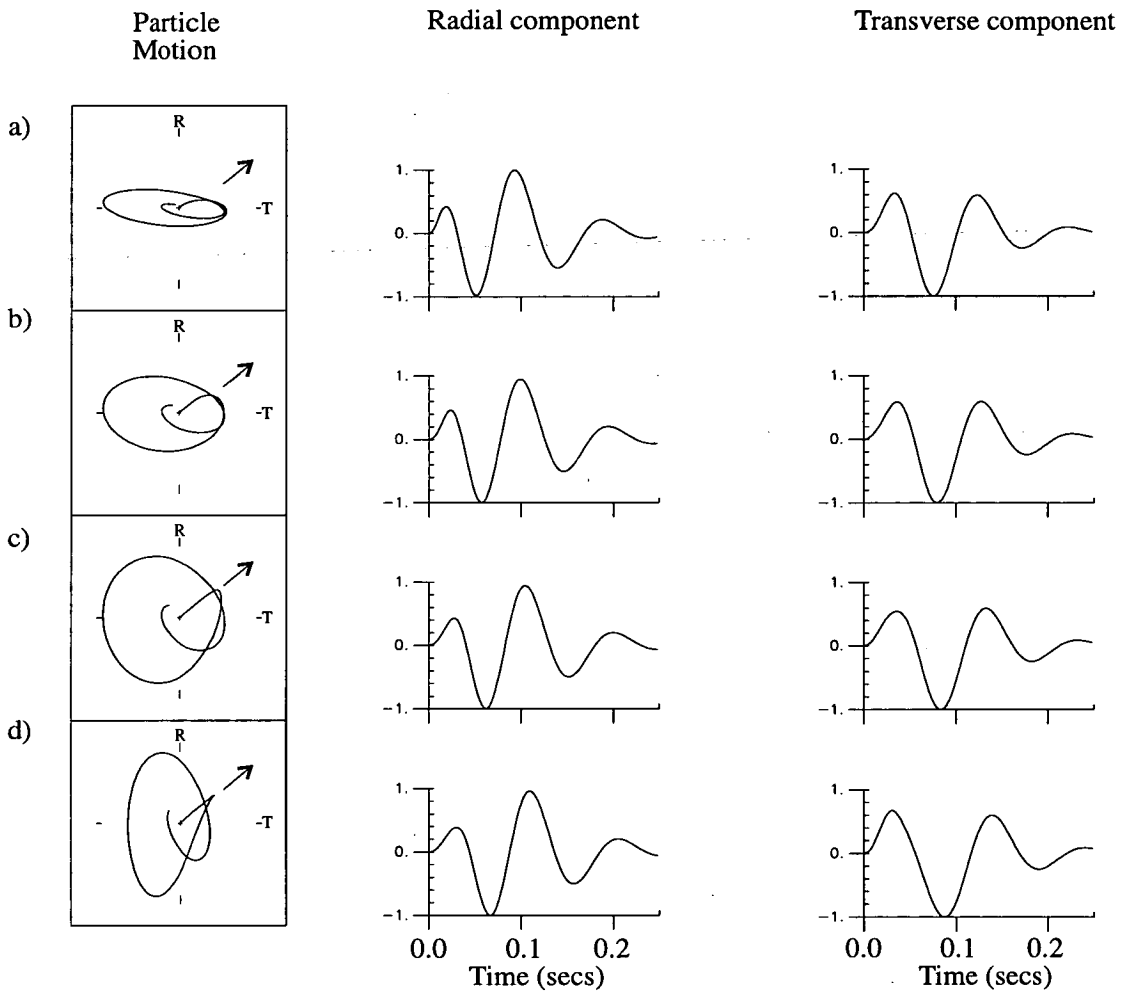


Figure 2.11 - Particle motion diagrams and windowed seismograms showing the shear-wave splitting for time delays of a) 8 ms, b) 16 ms, c) 24 ms and d) 32 ms. The arrows shown in the particle motion diagrams indicate the polarization direction of the  $qSI$  shear-wave.



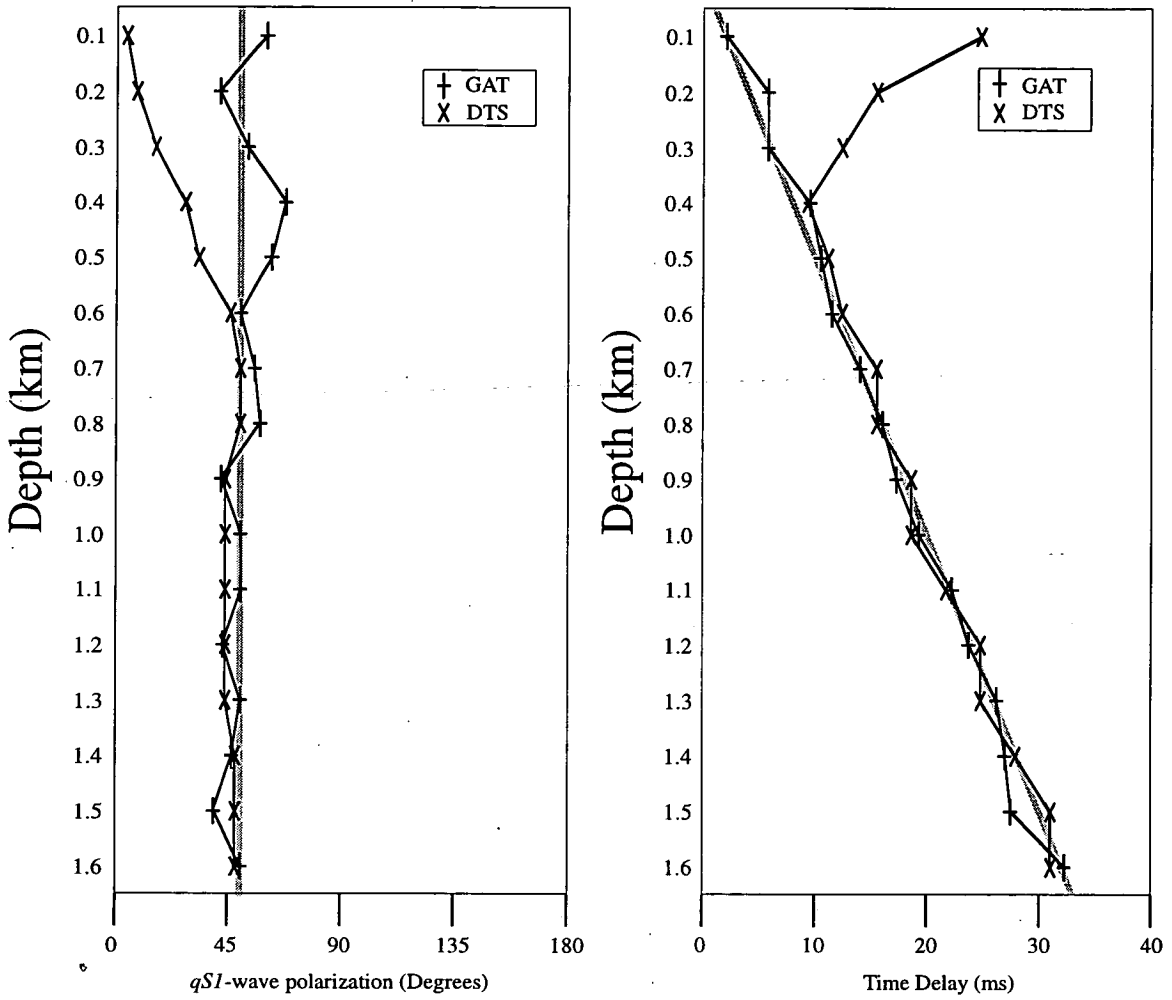


Figure 2.12 - A comparison of two single source shear-wave estimation techniques applied to synthetic data. Results from the GA and the DTS technique are shown as + and X respectively. The expected values for the  $qS1$ -wave polarization and time delays are indicated by the shaded lines.



the time delays and underestimates the fast shear-wave polarization but converges to the correct values as the time delay increases. The GA based technique does not show such systematic behaviour and estimates for both the time delays and fast shear-wave polarization are distributed about the expected value. The mean error for the estimation of the time delays for DTS and GA is, respectively, 3.3 ms and 0.7 ms and for the  $qSI$ -wave polarizations  $12.5^\circ$  and  $5.9^\circ$ . These results indicate that the GAT compares favourably with existing techniques in terms of reliability and accuracy.

## 2.7 APPLICATION TO FIELD DATA

I now apply the GAT to field data from a near-offset shear-wave VSP from the Lost Hills, Kern County, California. The experiment used an omnipulse multi-mode shear-wave generator located 155 m to the west of the wellhead. Forty-two three component geophones were approximately equally spaced between depths of 1.1 km and 2.4 km. The geophone tool included a gyroscopic instrument allowing rotation of the geophone records into a known co-ordinate frame. Selected seismograms and hodograms recorded on horizontal components with the omnipulse operating in  $SV$  mode are shown in Figure 2.13. The seismograms are of high quality with a high signal to noise ratio and clearly display significant shear-wave splitting. Previous studies (Yardley and Crampin 1990) determined the fast shear-wave polarization to be  $N55^\circ E$  with time delays of approximately 45 ms which tend to decrease with depth.

Shear-wave arrivals were identified using an interactive graphical picking routine and a time window of 260 ms applied to isolate the shear-wave time series on the horizontal geophone components. The GA parameters and the discretization scheme applied is the same as that used in the synthetic study.

Time delays,  $qSI$ -wave polarizations and the correlation coefficient corresponding to

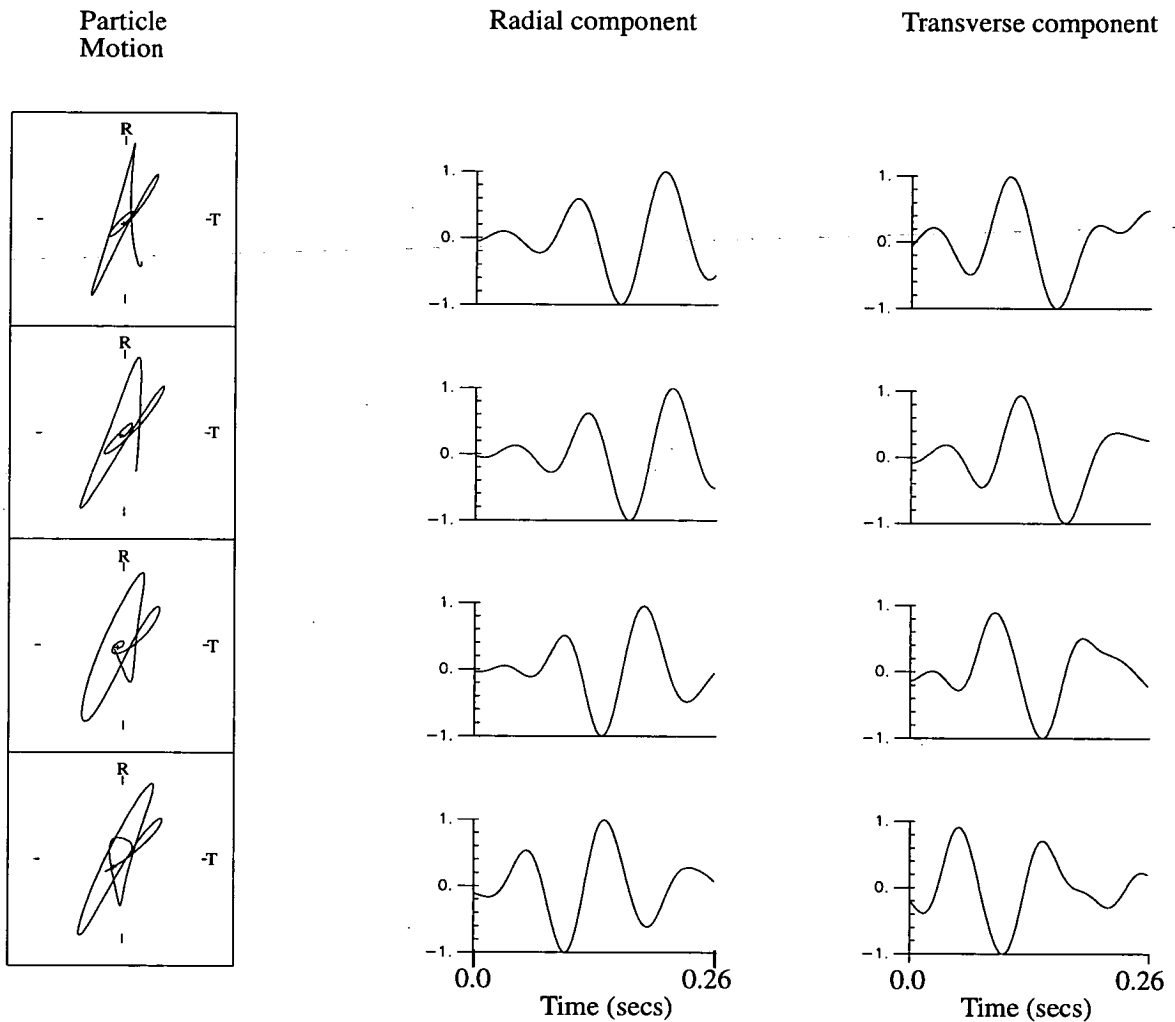


Figure 2.13 - Particle motion diagrams and windowed seismograms showing the shear-wave arrival on the horizontal geophone components for the Lost hills data set. Data is shown for every tenth geophone. The time window is defined to encompass the shear-wave arrival over 260 ms.

the best model found by the GAT are shown as a function of depth in Figure 2.14. Also shown are results from a dual source estimation technique based on the Alford rotation (Zeng and MacBeth 1993) which is expected to produce more reliable results than a single source technique. The GAT results are in good agreement with the results of Yardley and Crampin (1990) and also the dual source technique results. The high correlation coefficients for the best models show that the split shear-wave can be appropriately modelled using the parametrization scheme chosen.

## 2.8 SUMMARY

I have shown in this chapter how a GA can be applied to the problem of estimating shear-wave splitting. This method has been successfully applied to both synthetic and field data and compares favourably with single- and dual-source estimation techniques. This chapter is intended as an introduction to demonstrate how a GA performs as an optimization process. I have reviewed the implemented operators used in the GA and have shown the sensitivity of the search to different parameters. These tests have shown that the search processes associated with GAs can be improved if advanced operators are included and also that, in general, GAs are not critically sensitive to the control parameters. The superiority of GA to MC searches has been discussed and results show that whilst GAs are considerably more efficient than MC they still retain the characteristics of a global search. This is of particular importance in problems where estimates of non-uniqueness and uncertainties in model parameters are required. This type of problem is addressed in subsequent chapters where the inversion of anisotropic seismic data is discussed.

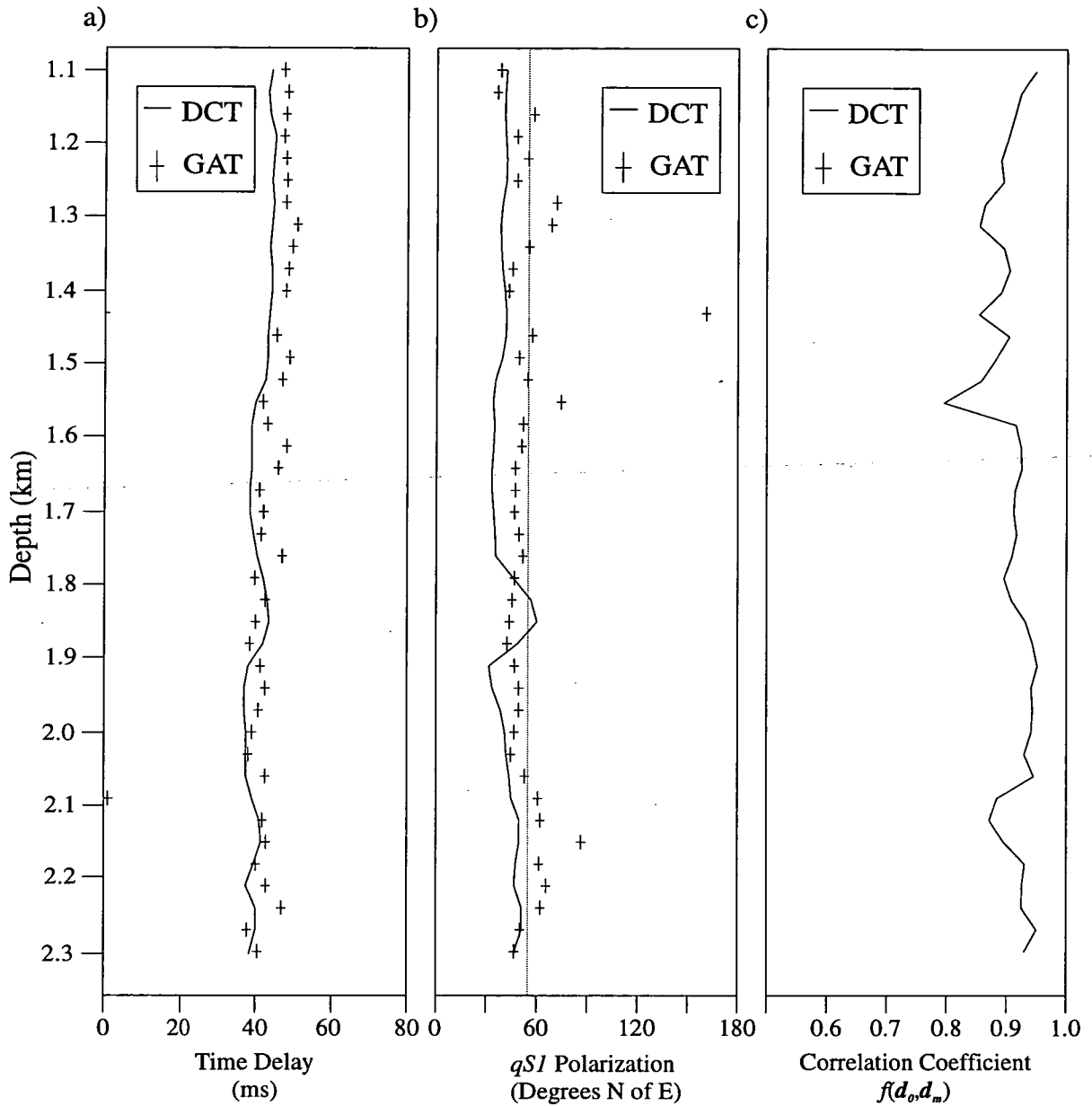


Figure 2.14 - Comparison of shear-wave splitting estimates from two different techniques applied to the Lost Hills VSP data set. The graphs show a) the time delay and b) the  $qSI$ -wave polarization estimates using the GAT (+ symbol) and from DCT (solid line). The shaded line in b) indicates the direction of N55°E reported by Yardley and Crampin 1990. Figure c) shows the normalized correlation coefficient obtained by the GAT for the best model of shear-wave splitting found by the genetic

## CHAPTER 3

### INVERSION FOR LABORATORY *QP*-WAVE VELOCITY MEASUREMENTS

#### 3.1 INTRODUCTION

In this Chapter the GA is used in an inversion role to invert *qP*-wave velocities measured in small scale laboratory experiments for parameters characterising the anisotropy. The experimental data that is used has been previously published by Thill, Willard and Bur (1967) (which I hereafter abbreviate to TWB). The purpose of these experiments was to examine the correlation between the *qP*-wave velocities and the structural subfabrics within specimens of Salisbury granite and Yule marble. The velocity variations are inverted using the GA to minimise the difference between theoretically calculated velocities from a model vector defining an anisotropic model and the experimentally measured velocities. As discussed in Chapter 1 GA's rely upon the manipulation of low-order schemata so that the success of the inversion scheme may be critically dependent upon the parametrization scheme that is used to define the model vector. This dependence is investigated using different parametrization schemes. The inversion results are compared with the petrophysical results reported by TWB. A summary of TWB's experimental procedures, results and interpretations is now described.

#### 3.2 EXPERIMENTAL ARRANGEMENT

Specimens of Salisbury granite and Yule marble were ground to spheres of diameter 50 mm enabling a wide range of propagation directions to be sampled in the travel-time experiments. Each specimen was loaded into a cradle which rigidly held the specimen with respect to the transducers. This arrangement allowed an extensive coverage of both azimuth and incident angles along 73 unique propagation directions

distributed along 7 great circles over a hemisphere of the sample. A schematic diagram showing the directional sampling distribution used in the experiments is shown in Figure 3.1. As indicated in the diagram, a right handed co-ordinate system is used with the  $z$  axis pointing downwards. This co-ordinate system is different to the one used by TWB and is used to facilitate the comparison between models. A piezo-electric transducer pair operating in an expansion mode at a frequency of 750 kHz was used to excite  $qP$  waves from which transit times were measured using a triggered digital timing system. Several measurements were taken for each propagation direction so that statistical measurements of both the transit time and experimental error could be calculated. A petrophysical analysis of the specimens was also conducted to determine the orientation and distribution of any fabric or inclusions.

The experimental results show that both the Salisbury granite and Yule marble samples possess considerable seismic anisotropy which can be correlated with mineral orientation, pore and fracture orientations. I will now consider the results for each of the samples.

### *Salisbury Granite*

The  $qP$ -wave velocity measurements indicate that the sample possessed an orthorhombic symmetry with an  $qP$ -wave anisotropy of 12 % (defined to be  $[V_{max}^{qP} - V_{min}^{qP}] / V_{max}^{qP}$ ). Approximate planes of mirror symmetry can be identified in the velocity variations aligned in the  $xy$  plane and in the planes aligned at  $\pm 10^\circ y$  and  $\pm 190^\circ y$  which are indicated in Figure 3.2(a). The measured  $qP$ -wave velocity variations are shown in Figure 3.2 as contour plots plotted in an equal angle cylindrical projection (Liu, Crampin and Booth 1989). These plots show velocity variations over an entire hemisphere of propagation directions which is achieved by assuming reciprocal raypaths. The orientations of these symmetry planes coincide with two sets of micro-cracks within the quartz crystals of the granite. The first set of micro-cracks was well developed with the crack normals aligned sub-parallel to the  $x$ -axis. The second set comprised of ill-defined, discontinuous and dilute micro-

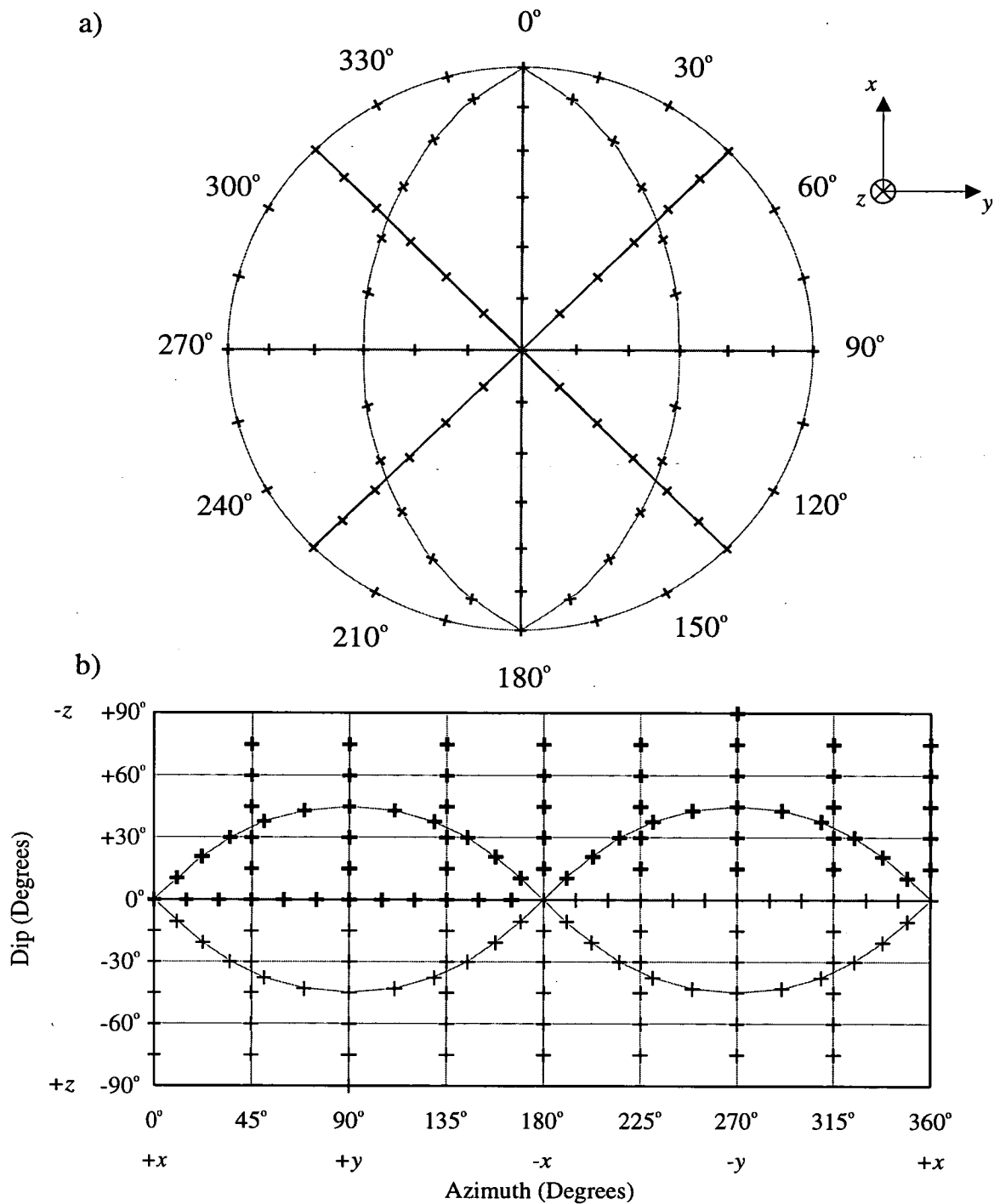


Figure 3.1- Plots showing the propagation directions, indicated by crosses, along which *qP*-wave velocity measurements were made for the Salisbury granite and Yule marble specimens. The upper plot a) shows an upper hemisphere equal-area polar plot and b) a cylindrical equal-angle projection for an entire sphere of propagation directions with the reciprocal raypaths shown as light crosses.



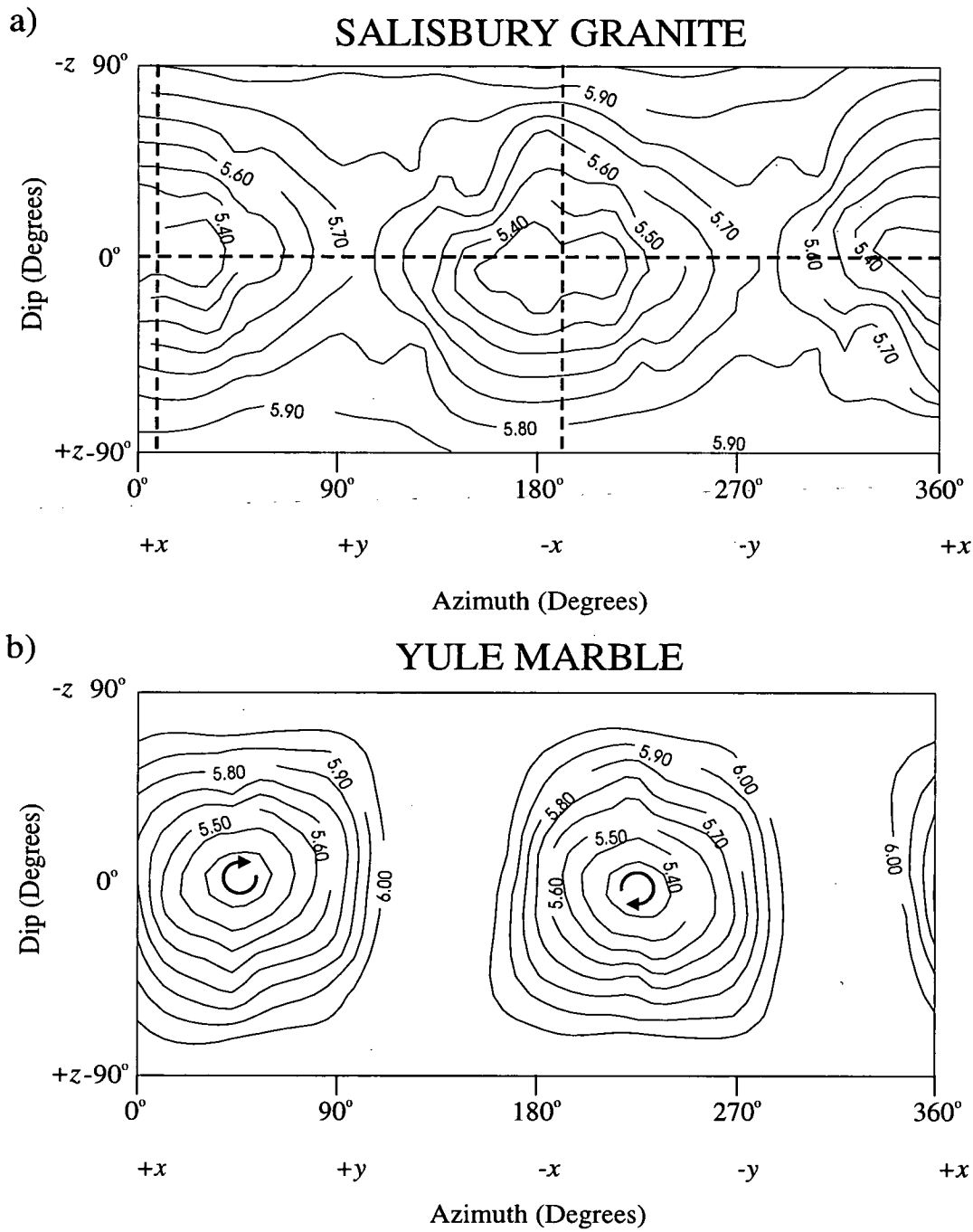


Figure 3.2 - Cylindrical equal-angle projections of the measured *qP*-wave velocity variations for a) the Salisbury granite and b) the Yule marble specimens. Approximate planes of symmetry in the Salisbury granite specimen are indicated in (a) by the dashed lines. The approximate location of the symmetry axis for the Yule marble specimen is indicated in (b) by the curved arrows. Reciprocal raypaths are assumed to allow for a complete hemispherical coverage of propagation directions.

cracks lying in the  $xy$  plane.

#### *Yule Marble*

The velocity measurements suggest that this specimen possesses hexagonal symmetry with the symmetry axis lying in the  $xy$  plane at  $x45^\circ y$ , as indicated in Figure 3.2(b). Thin section analysis showed this direction to be coincident with the preferential orientation of the constituent calcite crystals. Calcite is an intrinsically anisotropic crystal with trigonal symmetry. The percentage anisotropy is calculated to be 16%.

The petrophysical analysis indicates that both samples are homogeneous with respect to the seismic wavelength,  $\sim 10$  mm, used in the travel time experiments.

### 3.3 INVERSION PROCEDURE

#### *Objective Function*

In order to invert the  $qP$ -wave velocity observations of TWB I apply the GA in the minimization of a least-squares quantity defined by,

$$f(v_o, v_m) = \frac{1}{N} \sum_{i=1}^N \frac{(v_{o,i} - v_{m,i})^2}{\delta_i^2}; \quad (3.1)$$

where  $v_o$  and  $v_m$  are  $N$  column vectors of the observed and predicted  $qP$ -wave velocities respectively.  $N$  is the number of observations to be inverted which in this case is  $N=73$ . The subscript  $i$  identifies the vector component corresponding to a particular propagation direction.  $\delta_i$  are the estimated experimental errors. The experimental errors used in the inversions are those given by TWB which for the Salisbury granite and the Yule marble specimens are 1.4 % and 1.3% respectively. The objective function,  $f(v_o, v_m)$ , is also referred to as the misfit so that a lower misfit corresponds to a better 'goodness of fit'. The objective function is normalized by the number of observations,  $N$ , so that a misfit of less than 1.0 indicates that, on average, all the predicted and observed velocities agree to within the estimated errors.

### *Phase and Group Velocity*

Before proceeding further an important decision is required as to whether the experimental procedure adopted by TWB measured the phase or group velocities. In the case that the source can be represented as a point then the experiments will have measured the group velocities whereas if the source excites plane waves then the measurements will be of the phase velocities. A simple calculation indicates that the transducer can be considered to be a point source. Hooke's law may be used to calculate the expected compression of the sample under the applied coupling pressure used in the experiment, from which an estimate of the contact area between the source and specimen can be made. In the case of the granite specimen, under a coupling pressure of  $105 \times 10^3 \text{ Nm}^{-2}$ , as reported by TWB, then the radius of the contact area is of the order of  $10^{-3} \text{ mm}$ , assuming a value of 50 GPa for Young's modulus. Assuming an isotropic velocity of  $V_p = 5.5 \text{ kms}^{-1}$  then the *qP*-wave wavelength is approximately 10 mm. This suggests that the transducer is effectively a point source and the measured velocities are the group velocities. However, this is not a general result and other experimental arrangements may well record the phase velocities as shown by Dellinger and Vernik (1992).

The common assumption that phase and group velocities are the same for 'weak' anisotropy, as has been made in some studies (Arts *et al.* 1991, Sayers 1988), is now investigated. The maximum and average percentage differences between the group and phase velocities are calculated for a range of hexagonally anisotropic materials characterised by a (non-unique) percentage anisotropy defined by  $(V_{\max} - V_{\min}) / V_{\max}$ . These results are plotted in Figure 3.3 for two anisotropic solids with similar isotropic properties to those of granite and marble. As is expected the assumption is valid only for weak anisotropy and becomes increasingly worse as the anisotropy increases. For the samples used in this study the maximum errors associated with this assumption are at least as large as the experimental errors, and it is invalid to assume that the deviation of the phase from the group velocity is insignificant. These phase and group velocity deviations may become more significant for the quasi-shear waves for which singularities and cuspidal features may exist.

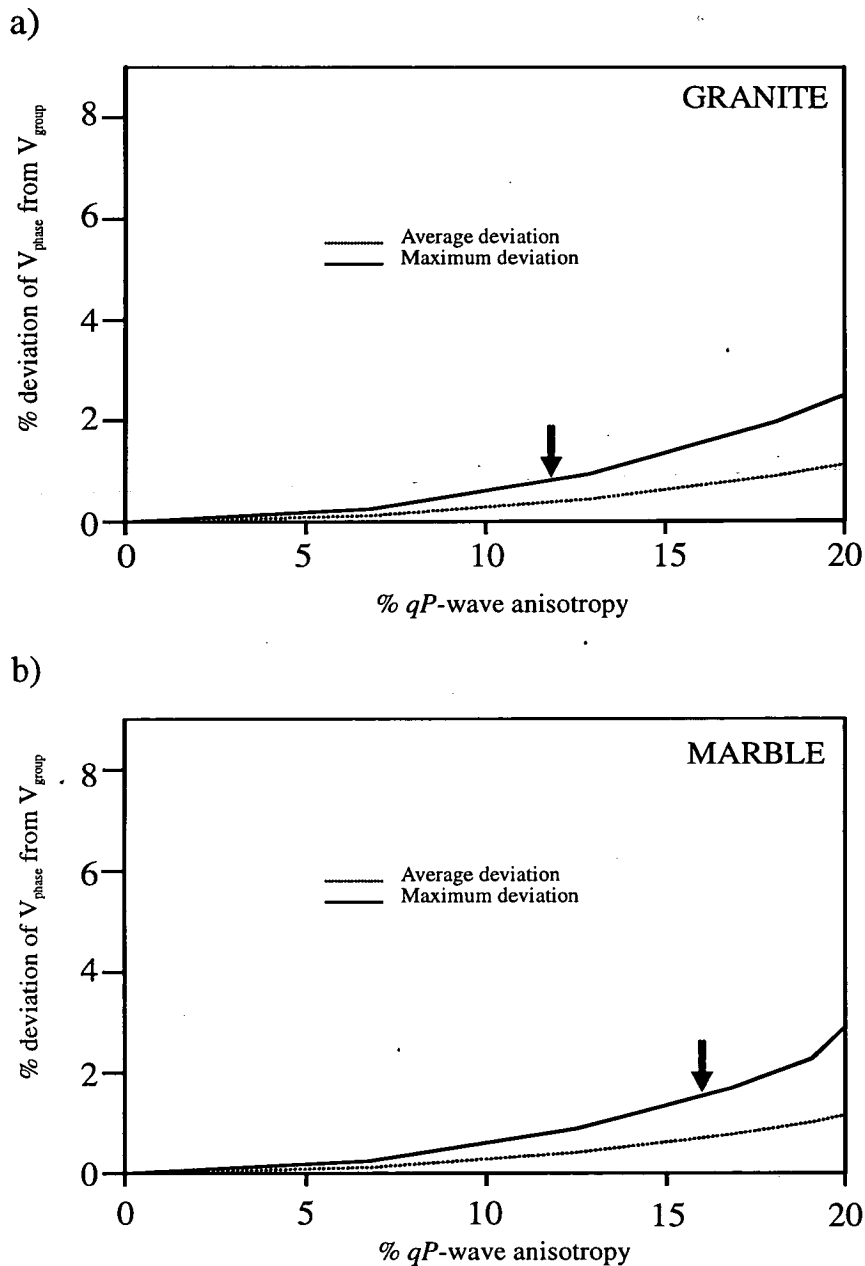


Figure 3.3 - The percentage deviation of the group velocity from the phase velocity in the group direction as a function of the % *qP*-wave velocity anisotropy (defined as  $V_{\text{max}} - V_{\text{min}} / V_{\text{max}}$ ) for a) granite and b) marble. The solid line indicates the maximum % difference and the dotted line the average deviation found by searching over a quadrant of a hexagonal material. Arrows indicate the measured anisotropy of the samples as reported by TWB.

The calculation of the phase velocities and the associated polarizations may be obtained by the solution of the Kelvin-Christoffel equation (Musgrave 1970), as discussed in Chapter 1 (equation 1.3),

$$|\mathbf{\Gamma} - \rho v^2 \mathbf{I}| = 0 ; \quad (3.2a)$$

where

$$\Gamma_{ik} = c_{ijkl} n_j n_l . \quad (3.2b)$$

$\mathbf{\Gamma}$  is the 3x3 Kelvin-Christoffel matrix which is a function of the elastic constants and the propagation direction cosines,  $n_i$ , and  $\mathbf{I}$  is the identity matrix. As discussed in Chapter 1 the solution of this equation yields three eigen values,  $e^i$ , which are related to the phase velocities as  $v^i = (e^i / \rho)^{1/2}$  where  $i$  is used to indicate the different eigen solutions. The eigenvectors correspond to the polarization directions of the three wavetypes and necessarily form a mutually orthogonal set since the Kelvin-Christoffel Matrix is symmetric. In addition to this property the Kelvin-Christoffel matrix must also be positive definite to ensure that the eigen values are real and positive. The positive definite nature of the Kelvin-Christoffel matrix is necessary to satisfy energy considerations (Helbig 1994). To ensure that all materials satisfy this criterion a check is made using the inequality given by Hearmon (1961)

$$\det \begin{vmatrix} c_{11} & \cdot & c_{1m} \\ \cdot & \cdot & \cdot \\ c_{m1} & \cdot & c_{mm} \end{vmatrix} \geq 0$$

where  $m$  is an integer within the range  $1 < m < 6$ . This step is required since some of the parametrization schemes employed in the GA may define materials that violate stability constraints.

The calculation of the group velocity for a given propagation direction is not so simple. The group velocity vector may be calculated for a given phase velocity

direction by constructing an envelope of plane wavefronts (Musgrave 1970)

$$v_{g,i} = \frac{1}{2\rho v_p} \left[ \frac{p^2}{\alpha^2} \right]_k \left[ (\rho v_p^2 - A) \frac{\partial \alpha^2}{\partial n_i} + \alpha^2 \frac{\partial A}{\partial n_i} \right]_k ; \quad (3.3a)$$

where

$$\alpha_k = \left( \frac{\Gamma_{ik} \Gamma_{jk}}{\Gamma_{ij}} \right)^{1/2} \quad i \neq j \neq k ; \quad (3.3b)$$

and

$$A_k = \Gamma_{kk} . \quad (3.3c)$$

$\Gamma$  is the Kelvin-Christoffel matrix,  $v_p$  is the phase velocity,  $\mathbf{p}$  is the polarization vector and the  $n_i$  are the direction cosines for the phase propagation directions. The group velocity is calculated using equation 3.3a by replacing the  $\mathbf{p}$ ,  $\alpha$  and  $A$  terms with their  $k$  th components and summing the products of the brackets. Note that the expression for  $A_k$  does not involve the summation of the diagonal terms of  $\Gamma$  and the Einstein convention does not apply. This equation is not valid for media of lower symmetries than orthorhombic. In general there is no analytical expression by which the group velocity can be calculated for an arbitrary propagation direction. The forward modelling method by which the group velocity is calculated in the GA is now described. Group velocity vectors are calculated over a regularly spaced grid of phase propagation directions. A search is then performed over this grid to find the propagation direction nearest to the required group direction and interpolation methods applied. This method is clearly more intensive than the corresponding phase velocity calculations. However, symmetries may be exploited for some anisotropic systems. For example, an orthorhombic material, which possesses three orthogonal mirror symmetries, only requires calculations over an octant of propagation directions.

### 3.4 PARAMETRIZATION SCHEMES

The method by which a GA achieves a global search is by the processing of low-order schemata or similarity templates which is summarised by the so called 'Fundamental Theory of Genetic Algorithms' discussed in Chapter 2 (equation 2.1). The formation of these low-order schemata may well depend upon the parametrization scheme employed so that the GA may be critically sensitive to the parameters that are used to define the model vector. To investigate the sensitivity of the GA to the choice of parametrization I use three schemes. The first parametrization scheme is based upon equivalent-media theory whereby an equivalent anisotropic material is constructed by the inclusion of aligned cracks in an isotropic medium. The elastic constants for this type of material are calculated using the second order formulations of Hudson (1980). The second parametrization scheme is based upon the Thomsen parameters which may be used to characterize a material with hexagonal symmetry (Thomsen 1986). The third parametrization scheme is based upon the deviation of the elastic constants from the isotropic case. I now consider these three schemes in more detail. The Thomsen and elastic constants schemes are not restricted to some preconceived physical model as is the case for the Hudson model and so these present a more flexible approach although the elastic constants may be difficult to interpret.

#### *Hudson Model*

The Hudson parameters describe a physical model of aligned penny-shaped cracks which, when inserted into an isotropic medium, define a hexagonally-anisotropic medium with the symmetry axis perpendicular to the crack face. Lower symmetries may be constructed by the addition of further nonparallel crack sets. The Hudson formulations may be written as the sum of the first-order and second-order perturbations to an isotropic medium

$$\mathbf{c} = \mathbf{c}^0 + \mathbf{c}^1 + \mathbf{c}^2 ; \quad (3.4)$$

where  $\mathbf{c}$  are the equivalent anisotropic elastic constants and  $\mathbf{c}^0$  are the elastic constants

for the isotropic background medium.  $c^1$  and  $c^2$  are the first- and second-order perturbations which are defined by the Hudson crack parameters. The exact form of these is given in Hudson, 1980. Lower symmetry systems, simulated by multiple crack sets, can be constructed by summing the first order perturbations of the individual crack sets and calculating the second order perturbations as described by Hudson (1986). A further extension of this scheme allows the introduction of aligned cracks into a background anisotropic medium. In this case, the initial anisotropic system is decomposed into an isotropic part and an anisotropic perturbation which is treated in the same way as the first order Hudson perturbations,  $c^1$ .

### *Thomsen Parameters*

The Thomsen parameters are non-dimensional quantities that can be used to describe a hexagonally anisotropic medium (Thomsen 1986). The three Thomsen parameters,  $\delta$ ,  $\epsilon$  and  $\gamma$ , are given by the following combinations of the elastic constants for an anisotropic material with hexagonal symmetry

$$\begin{aligned}\delta_1 &= \frac{(c_{12}+c_{55})^2-(c_{22}-c_{55})^2}{2c_{11}(c_{11}-c_{55})} \\ \epsilon_1 &= \frac{c_{22}-c_{11}}{2c_{22}} ; \\ \gamma_1 &= \frac{c_{44}-c_{55}}{2c_{55}} ;\end{aligned}\tag{3.5}$$

where the subscript 1 on the Thomsen parameters indicates that the symmetry axis is aligned along the  $x_1$  axis. The angular variation of the velocity variations of the  $qP$ ,  $qSV$  and  $qSH$  can conveniently be written in terms of these parameters. For 'weakly' anisotropic materials the  $qP$  and  $qSV$  velocities are functions of  $\delta$  and  $\epsilon$  only and the  $qSH$  velocity is a function of  $\gamma$  only. The three Thomsen parameters are only valid for anisotropic media with hexagonal symmetry. However, for the inversion problem a parametrization scheme is required to define lower symmetry systems. For



this reason I use a parametrization scheme based upon the algebraic sum of three sets of Thomsen parameters which each individually define hexagonally anisotropic materials with mutually orthogonal symmetry axes to represent an orthorhombic medium

$$c^{orth} = 4c^0 - c(\delta_1, \epsilon_1, \gamma_1) - c(\delta_2, \epsilon_2, \gamma_2) - c(\delta_3, \epsilon_3, \gamma_3) ; \quad (3.6)$$

where  $c^0$  are the isotropic elastic constants and the  $c$  are hexagonally anisotropic materials with the direction of the symmetry axis indicated by the subscripts on the Thomsen parameters. These parameters are only used as a convenient parameter set and do not, as is the case of hexagonal anisotropy, relate to the angular variations of the velocity sheets. However, in the case that one set of Thomsen parameters dominates some meaning may be attached to these values. Values for the Thomsen parameters for commonly occurring anisotropic materials are tabulated by Thomsen (1986) and typically lie between -0.2 and +0.2 for most sedimentary rocks.

#### *Elastic Constants ( $C_{ijkl}$ )*

For isotropic media the elasticity tensor is a function of only two independent stiffnesses  $c_{11}$  and  $c_{44}$

$$\begin{pmatrix} c_{11} & (c_{11}-2c_{44}) & (c_{11}-2c_{44}) & & & \\ & c_{11} & (c_{11}-2c_{44}) & & & \\ & & c_{11} & & & \\ & & & c_{44} & & \\ & & & & c_{44} & \\ & & & & & c_{44} \end{pmatrix}$$

For hexagonal symmetries with the symmetry axis aligned in the  $x$  direction five independent stiffnesses are required;  $c_{11}$ ,  $c_{12}$ ,  $c_{22}$ ,  $c_{44}$  and  $c_{55}$

$$\begin{pmatrix} c_{11} & c_{12} & & & & \\ & c_{22} & (c_{22}-2c_{44}) & & & \\ & & c_{22} & & & \\ & & & c_{44} & & \\ & & & & c_{55} & \\ & & & & & c_{55} \end{pmatrix}$$

In the case of media possessing orthorhombic symmetry nine elastic constants are required;  $c_{11}$ ,  $c_{22}$ ,  $c_{33}$ ,  $c_{23}$ ,  $c_{13}$ ,  $c_{12}$ ,  $c_{44}$ ,  $c_{55}$  and  $c_{66}$

$$\begin{pmatrix} c_{11} & c_{12} & c_{13} & & & \\ & c_{22} & c_{23} & & & \\ & & c_{33} & & & \\ & & & c_{44} & & \\ & & & & c_{55} & \\ & & & & & c_{66} \end{pmatrix}$$

In this parametrization scheme the elastic stiffness tensor is constructed using dimensionless parameters which define a percentage fractional deviation from the isotropic case

$$\Delta c_{ij} = 100 \times \frac{(c_{ij} - c_{ij}^0)}{c_{ij}^0} . \quad (3.7)$$

Thus for the hexagonal and orthorhombic symmetries five and nine parameters

respectively are required. However, for materials with hexagonal symmetry the *qP*-wave velocity sheet is dependent on the four elastic constants  $c_{11}$ ,  $c_{22}$ ,  $c_{55}$  and  $c_{12}$ . In the case that the symmetry axis is aligned in the  $x$  direction then the *qP*-wave velocity variation is independent of the  $c_{44}$  elastic constant.

For the hexagonal inversions the Thomsen  $\gamma$  parameter and the  $\Delta c_{44}$  parameter in the Cijkl scheme are omitted from the parametrization schemes. This is because the *qP*-wave velocities are independent of these parameters. Thus the inclusion of these parameters would be to pad out the model chromosome with null bits, that is, bits with no effect on the models fitness. These extraneous bits would disrupt the formation of the low order schemata and the corresponding convergence of the GA would be inhibited. Thus these parameters are excluded for the hexagonal inversions.

These parametrization schemes do not necessarily define materials which are energetically stable and which satisfy Hearmon's inequality. For the initial random population it is important to ensure that a good sample of the model space is achieved so that if unstable materials are generated at this stage then they are discarded. In later populations it is possible that energetically unrealistic models may be generated by genetic operations. In this case they are assigned a very high misfit value so that the propagation of the model's characteristics into the next generation is unlikely.

#### *Genetic Algorithm Parameters*

The crossover and mutation probabilities controlling the GA search are the same for all the inversions and are set to be  $p_c=0.95$  and  $p_m=0.005$  respectively. Advanced genetic operators of sharing, inversion and Gradient-bit improvement (local search) are also included in the hybrid GA. For the hexagonal inversions the population size was set to  $N_{pop}=40$ . In the case of the orthorhombic inversions a larger population size of  $N_{pop}=60$  individuals was selected. This increase is necessary because of the larger model space defined by the additional parameters which are used to define a

material with orthorhombic symmetry.

### 3.5 INVERSION RESULTS

The inversion results are summarised in Tables 3.1 to 3.6. Tables 3.1 to 3.3 show the best models found by the GA inversion for the Salisbury granite data and Tables 3.4 and 3.6 the results for the Yule marble data. The velocity variations for the model observations are shown in Figures 3.4 to 3.7.

#### *Salisbury Granite*

For all the hexagonal inversions the misfit of the best model found by the GA is approximately 1.0. This indicates that the difference between the predicted *qP*-wave velocities corresponding to the best models and the observations are, on average, within the experimental errors. Of the three parametrization schemes the model found using the Hudson representation has the lowest misfit of  $f(v_0, v_m)=0.974$ . This model corresponds to a near vertical dry crack system of crack density 0.034 and aspect ratio 0.014 striking at  $x97^\circ y$  (symmetry axis at  $x7^\circ y$ ) and dipping  $1^\circ$  from the  $z$  axis towards the  $x y$  quadrant. The theoretically calculated velocity variations corresponding to this model are shown in Figure 3.4(b). The orientation of this crack system is in good agreement with the reported principal micro-crack set found in the quartz crystals. The best model found using the Thomsen parametrization yields a similar model to that obtained for the Hudson scheme. The best model is orientated with the symmetry axis at  $x10^\circ y$  and dipping  $1^\circ$  from the vertical axis towards the  $x y$  quadrant. The independent elastic constants controlling the *qP*-wave velocity variations for this model are similar to the elastic constants corresponding to the best Hudson model. Thus the models derived using the Hudson and Thomsen parametrizations are essentially the same and the small difference in the misfit of the two models is probably due the limitations of resolution imposed by differences in the discretization. The Cijkl parametrization yields a best model of misfit  $f(v_0, v_m)=1.17$  which is similar in most respects to the models for the two other parameter sets. In this case the symmetry axis is aligned at  $x11^\circ y$  and dips  $1^\circ$  from the  $z$  axis

SALISBURY GRANITE			
	Hudson $f(v_0, v_m)$	Thomsen $f(v_0, v_m)$	Cijkl $f(v_0, v_m)$
HEXAGONAL	0.974	1.103	1.170
ORTHORHOMBIC	0.658	1.090	0.882

Table 3.1 - A summary of the best models found by the GA for the inversion of the Salisbury granite data given by the different parametrization schemes.

SALISBURY GRANITE				
	$c_{11}$	$c_{22}$	$c_{55}$	$c_{12}$
Hudson	72.3	88.3	28.1	23.2
Thomsen	74.6	89.5	30.6	16.5
Cijkl	73.7	90.9	36.9	0.4

Table 3.2 - Elastic constants (in GPa) for the best hexagonal models found using the three parametrization schemes. The symmetry axis is aligned in the  $x$  axis direction to allow comparison between the different models.

SALISBURY GRANITE									
	$c_{11}$	$c_{22}$	$c_{33}$	$c_{44}$	$c_{55}$	$c_{66}$	$c_{12}$	$c_{13}$	$c_{23}$
Hudson	91.9	86.0	72.5	26.9	27.6	29.7	29.2	25.6	24.3
Thomsen	93.7	72.0	88.4	38.0	42.2	61.2	-37.3	-3.86	2.2
Cijkl	88.3	83.7	72.5	51.7	48.4	54.2	-9.6	-11.8	-27.2

Table 3.3 - Elastic constants (in GPa) for the best Salisbury granite orthorhombic models found using the three parametrization schemes. In this case the materials are aligned with the three symmetry planes parallel to the  $xyz$  co-ordinate axes for the purposes of comparison between models.

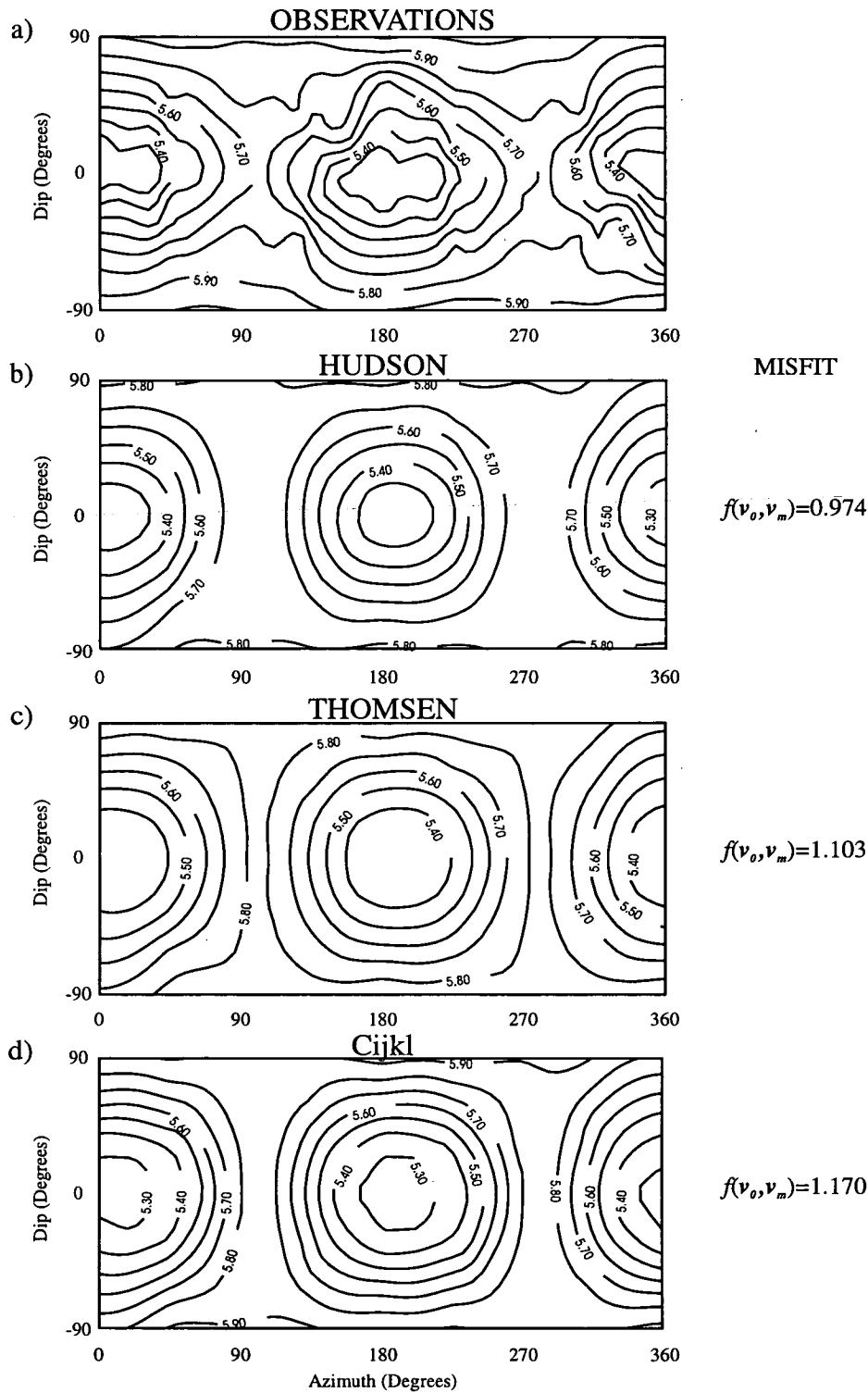


Figure 3.4 - Equal angle projections for an entire hemisphere of propagation directions for the Salisbury granite velocity measurements and b) to d) the velocity variations corresponding to the best models found by the hexagonal inversions for the b) Hudson c) Thomsen and c) Cijkl parametrization schemes

to the  $x$   $y$  quadrant which is in good agreement with the previous two results. The elastic constants for this model also show some similarity to those given by the Thomsen and Hudson schemes with the exception of the  $c_{12}$  constant which is given to be 0.4. It would therefore appear that the inversions using the three different parametrization schemes have converged to essentially the same model. This similarity can be seen on comparison of the theoretically calculated velocity variations for the best models derived using the different parametrization schemes. Therefore, for this particular suite of inversions the choice of parametrization scheme does not appear to be critical to the GA's performance.

The results for the orthorhombic inversions give lower misfit values than the corresponding hexagonal inversions (see Table 3.1 for comparison). This is as expected because of the extra degrees of freedom introduced by the additional parameters necessary to define an orthorhombic medium. The theoretically calculated *qP*-wave velocities for these orthorhombic results are shown in Figure 3.5. As for the hexagonal inversions the lowest misfit is obtained using the Hudson parametrization. The Hudson crack model for this model is defined in terms of only two crack systems with the third set having a negligibly small crack density. The dominant crack set possesses a crack density of 0.04 and is subvertically aligned in the  $yz$  plane and dipping  $2.8^\circ$  from the vertical towards the  $-x$  axis. The secondary crack set with a crack density 0.01 is aligned sub-parallel to the  $xy$  plane and is orthogonal to the dominant crack set. These inversions results are in good agreement with the petrophysical examination of the Salisbury granite specimen which revealed a biplanar crack set. The thin section analysis revealed a principal crack set of well developed microcracks aligned nearly parallel to the  $yz$  plane and an ill defined discontinuous set of cracks orthogonal to the principal set lying nearly parallel to the  $xy$  plane. A slight discrepancy exists between the inverted crack sets and the observed crack systems in that the inversion results suggest that the second weaker crack set is saturated. However, perturbing the best Hudson model by altering the fluid content of the principal crack set does not have a significant effect on the misfit. This suggests that the Hudson crack content parameter is not well resolved for this



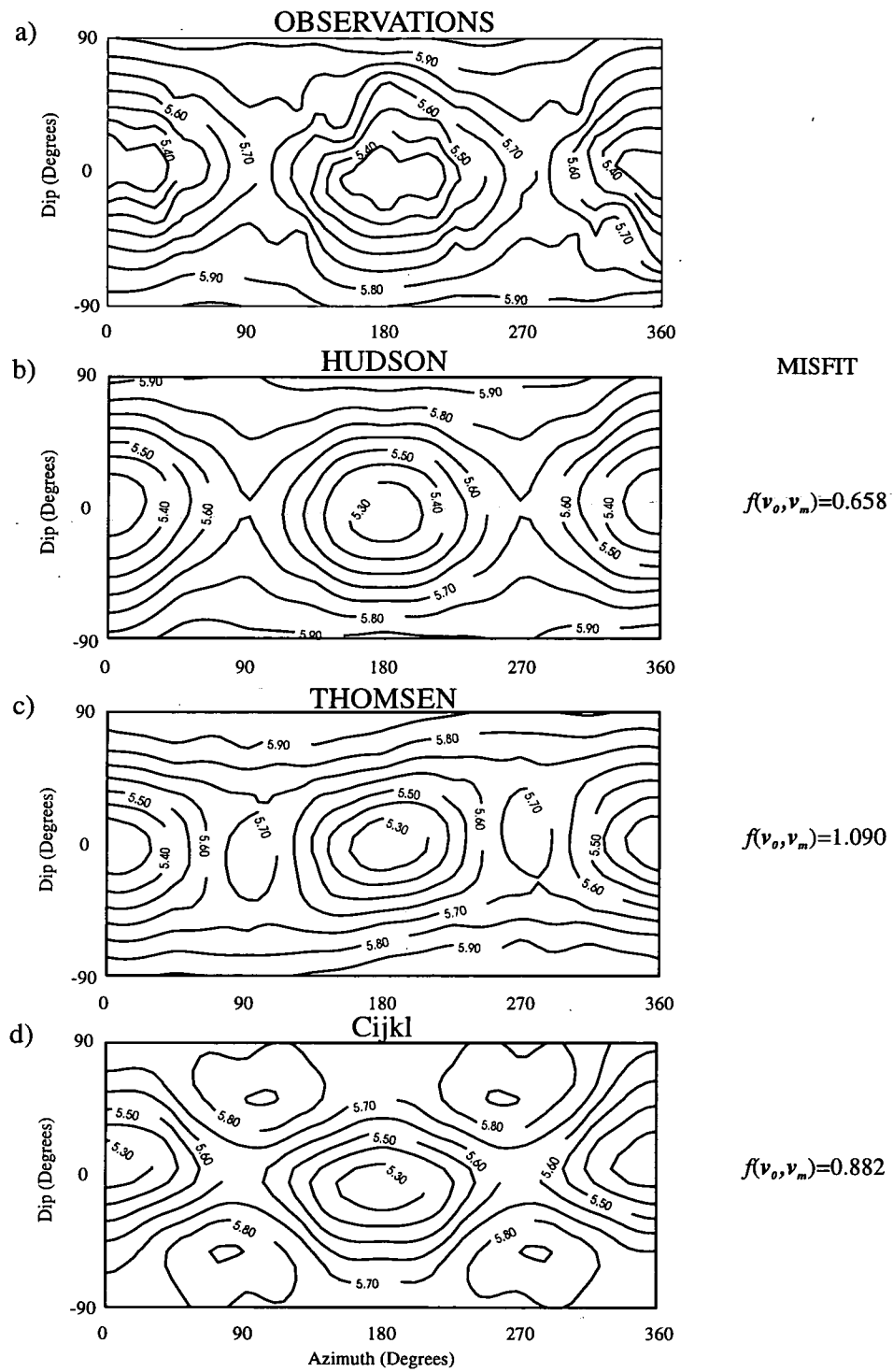


Figure 3.5 - Equal angle projections for an entire hemisphere of propagation directions for the Salisbury granite velocity measurements and b) to d) the velocity variations corresponding to the best models found by the orthorhombic inversions for the b) Hudson c) Thomsen and c) Cijkl parametrization schemes

set of observations. The results for the Thomsen parametrization scheme are difficult to interpret. The best orthorhombic Thomsen model does not represent a significant improvement in the misfit of the hexagonal Thomsen inversion result. Unlike the results for the Hudson parametrization scheme the Thomsen results show significant anisotropy for all three orthogonal Thomsen parameter sets. The set defining the most significant anisotropy is rotated so that the original symmetry direction is at  $x86^\circ y$  dipping by  $11.3^\circ$  from the vertical towards the  $xy$  quadrant. The second most significant Thomsen set is orthogonal to this direction and lies subparallel to the  $xy$  plane. These orientations of the Thomsen parameter sets are close to the biplanar micro fracture sets observed in the Salisbury granite. The third remaining Thomsen parameter set does not coincide with any of the petrophysical results. The Cijkl scheme converges to a best model of 0.8 and is significantly different to the best models found using the two other inversion schemes (Table 3.3). This difference is apparent in both the modelled velocity variations and in the elastic constants of the three solutions (Table 3.3 and Figure 3.3).

The results obtained using the Hudson representation converge to lower misfit values and therefore represent a better match to the observed data. This suggests that for the Salisbury granite inversions the Hudson scheme forms a suitable parameter set for the formation of low order schemata which the GA is able to manipulate efficiently. This may be because the underlying physical cause of the seismic anisotropy, in this particular sample, is due to the presence of a micro crack system. Alternatively, the Hudson parametrization may represent a subset of acceptable models spanning a smaller region of the model space compared with the Thomsen and Cijkl schemes.

#### *Yule Marble*

For the hexagonal suite of inversions all three parametrization schemes find models with misfits of approximately 0.5 (Table 3.4). This indicates that the difference, on average, between the observed *qP*-wave velocity and the corresponding model observations are within half the reported experimental error of 1.3%. Of these three

YULE MARBLE			
	Hudson $f(v_0, v_m)$	Thomsen $f(v_0, v_m)$	Cijkl $f(v_0, v_m)$
HEXAGONAL	0.542	0.502	0.434
ORTHORHOMBIC	0.369	0.937	0.710

Table 3.4 - A summary of the best models found by the GA for the inversion of the Yule marble data using the three different parametrization schemes.

YULE MARBLE				
	$c_{11}$	$c_{22}$	$c_{55}$	$c_{12}$
Hudson	70.6	94.3	23.1	32.4
Thomsen	76.7	103.3	12.4	60.6
Cijkl	74.9	103.1	29.2	27.0

Table 3.5 - Elastic constants (in GPa) for the best Yule marble hexagonal models found using the three parametrization schemes. The symmetry axis is aligned in the  $x$  axis direction to allow comparison between the different models.

YULE MARBLE									
	$c_{11}$	$c_{22}$	$c_{33}$	$c_{44}$	$c_{55}$	$c_{66}$	$c_{12}$	$c_{13}$	$c_{23}$
Hudson	104.3	76.1	100.9	6.36	5.8	6.3	73.4	90.7	72.0
Thomsen	109.8	79.3	103.5	14.2	23.3	7.0	63.3	51.3	55.4
Cijkl	77.6	106.5	101.1	38.2	33.8	40.4	-2.7	14.8	31.5

Table 3.6 - Elastic constants (in GPa) for the best Yule marble orthorhombic models found using the three parametrization schemes. In this case the materials are aligned with the three symmetry planes parallel to the xyz co-ordinate axes for the purposes of comparison between different models.

schemes the best model is found using the Cijkl scheme. A visual comparison of the theoretically calculated velocity variations for the best models obtained using the three schemes (see Figure 3.6) indicates there is little difference between the different models.

The best model obtained using the Hudson parameters corresponds to a saturated crack system of crack density 0.075 with the crack normals oriented at  $x47^\circ y$  and dipping  $3.5^\circ$  from the vertical  $z$  axis towards the  $-x -y$  quadrant. The Thomsen parametrization yields a slightly better model than that given by the Hudson scheme and predicts an identical symmetry axis orientation. The symmetry axis orientation in the case of the best model found using the Cijkl scheme is within a few degrees of the best Hudson and Thomsen models. A comparison of the elastic constants for the best models found using the three schemes is shown in Table 3.5. The elastic constants for the Hudson model show some difference to the results obtained with the other two schemes. This may be due to the inability of the Hudson representation to construct an elastic tensor corresponding to the models obtained using the other representations. The orthorhombic inversions do not converge to lower misfits than the corresponding hexagonal case, with the exception of the Hudson representation (Figure 3.7). This situation is different to that for the Salisbury granite for which the observed velocity variations indicate that symmetry system is essentially orthorhombic. It is likely that in the case of the Yule marble, which essentially possesses hexagonal symmetry, that an orthorhombic model represents an overparametrization of the inversion problem. In these situations the model space is likely to be multi-modal increasing the complexity involved in the inversion problem (Sen and Stoffa 1991). Global schemes are insensitive to such non-linearities, however, the GA shows premature convergence to a sub-optimal solution for the overparametrized orthorhombic inversion. Therefore the GA may not prove to be a suitable global inversion scheme for such overparametrized model spaces.

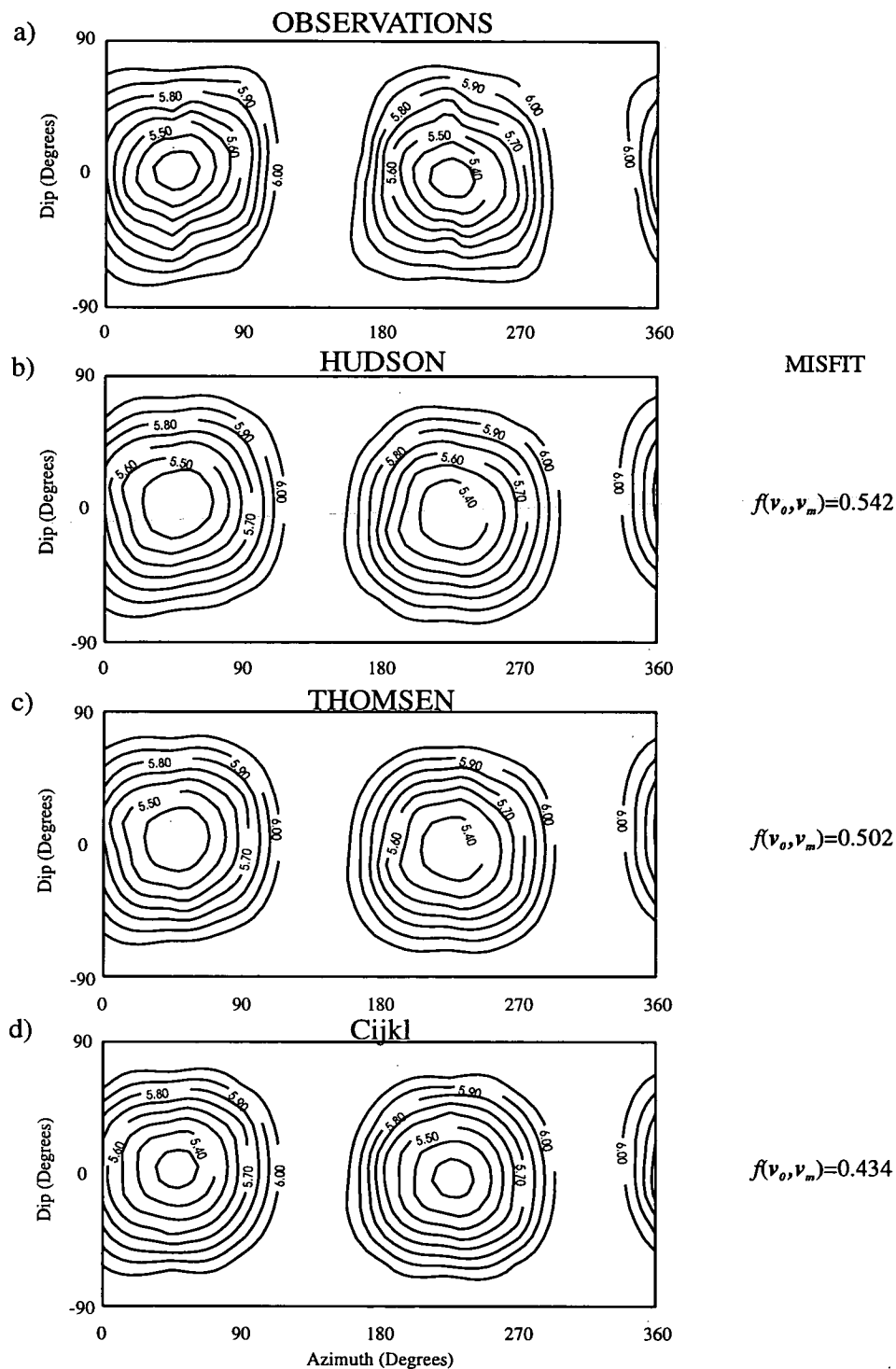


Figure 3.6 - Equal angle projections for an entire hemisphere of propagation directions for the Yule marble velocity measurements and b) to d) the velocity variations corresponding to the best models found by the hexagonal inversions for the b) Hudson c) Thomsen and c) Cijkl parametrization schemes

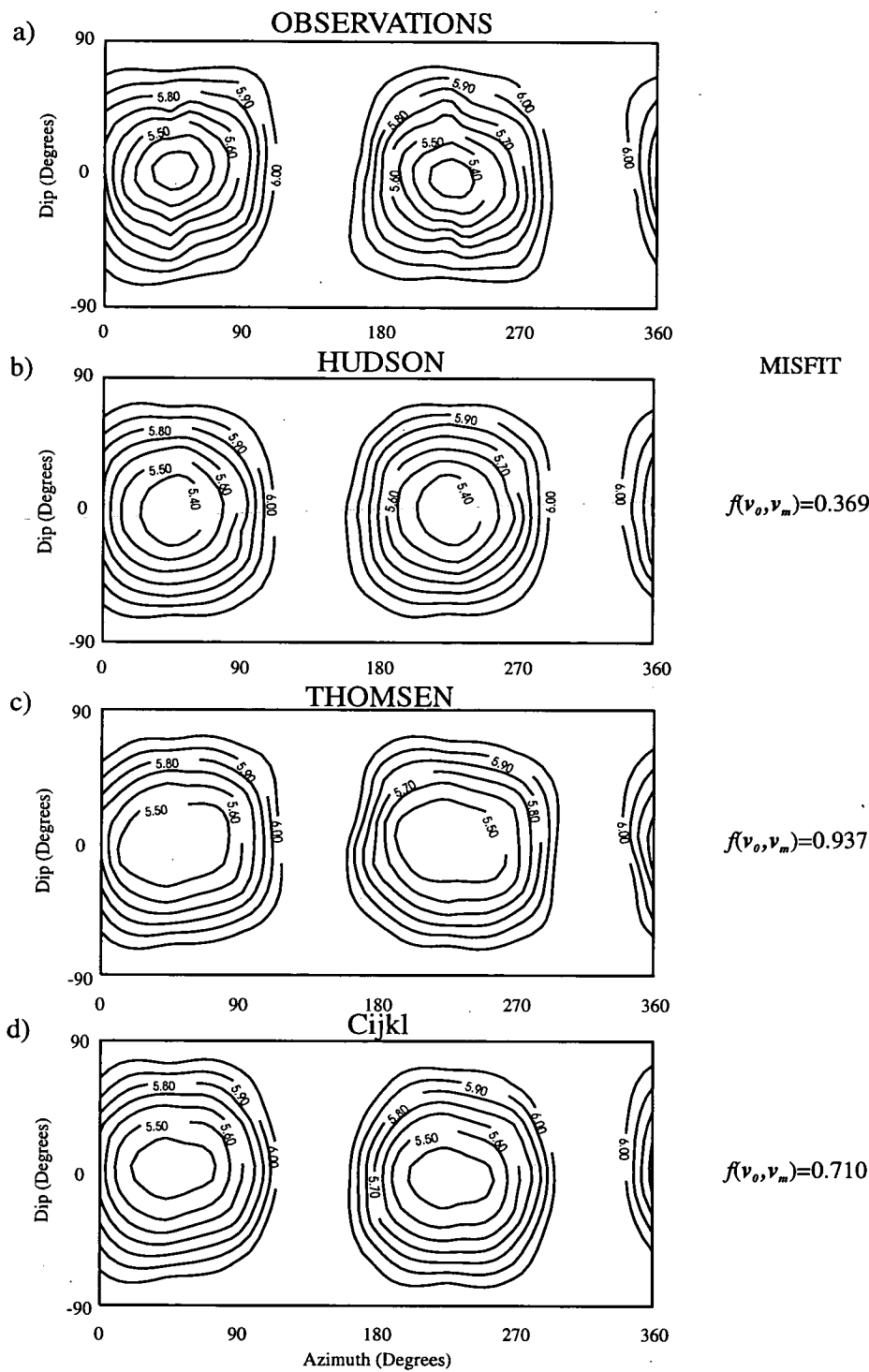


Figure 3.7 - Equal angle projections for an entire hemisphere of propagation directions for the Yule marble velocity measurements and b) to d) the velocity variations corresponding to the best models found by the orthorhombic inversions for the b) Hudson c) Thomsen and c) Cijkl parametrization schemes

### 3.6 DISCUSSION AND CONCLUSIONS

In this chapter I have shown how a hybrid GA can be applied to the problem of inverting *qP*-wave velocity measurements from small scale laboratory experiments. A sensitivity study of the effect of three different parametrization schemes on the GA's performance indicates that, in general, the GA is not critically sensitive to the particular scheme chosen for this specific problem domain. However, some schemes may be more appropriate than others depending on the underlying nature of the anisotropy. This is indicated by the results obtained for the inversion of the *qP*-wave velocities from the Salisbury granite specimen. In this case the seismic anisotropy is thought to be due to microcracks and accordingly the best models are obtained using equivalent-media terms based upon crack systems. These equivalent formulations also have the convenience that they are easily understood whereas other schemes must rely upon some other decomposition to obtain a physical model for the underlying cause of the anisotropy (for example, Hood 1991). This study has also highlighted the inefficiency of the GA search method when applied to an overparametrized problem domain. In these situations the GA tends to converge to sub-optimal solutions and the global nature of these techniques are not apparent. Therefore, in the application of GA's care must be taken to choose a minimal parameter set with which to discretize the problem.



## CHAPTER 4

### AZIMUTHAL VSP INVERSION

#### 4.1 INTRODUCTION AND OVERVIEW

In this chapter I apply the GA described in the previous chapters to the problem of inverting shear-wave splitting estimates from an Azimuthal VSP (AVSP) experiment recorded at the Conoco Borehole Test Facility (CBTF), Oklahoma. I will show that the best model derived from the GA optimisation is in good agreement with independent non-seismic data and also highlights a significant feature associated with shear-wave anisotropy known as a singularity. The results have important implications for the interpretations of shear-wave anisotropy and for the design of shear-wave experiments.

The next section of this chapter reviews the CBTF fracture system and its relation to shear-wave anisotropy (Queen and Rizer 1990). In section 4.3 the processing sequence applied to the shear-wave data from the AVSP is described and the shear-wave splitting results are discussed. In order to invert this shear-wave data I assume that the CBTF's velocity structure is homogeneous. I discuss this approximation in section 4.4 and show that this simplification is appropriate for this AVSP experiment. The inversion method based on this homogeneous halfspace assumption is described in section 4.5. The subsequent section describes the inversion results for models based on a hexagonal symmetry system. From these results a refined model is derived using full-waveform modelling for a realistic velocity model at the CBTF. Section 4.8 describes inversion results for models based upon an orthorhombic symmetry system. Conclusions and a discussion of the more significant points raised in this chapter are the subject of the final section.

## 4.2 REVIEW OF THE CBTF EXPERIMENT

In 1986 a comprehensive shear-wave VSP was conducted at the CBTF in Kay County, Oklahoma in order to test the relation between seismic anisotropy, particularly shear-wave anisotropy, to fracture and crack systems (Crampin 1985). The CBTF is located in north central Oklahoma, an area of relatively simple geology composed of plane layers of shales, limestones and sandstones (Figure 4.1). Geological and geophysical studies have identified the dominant fracture systems in the locality of the CBTF (Table 4.1). The fracture system common to all these studies appears to strike between the NE and ENE directions. The geological simplicity of the test site in conjunction with an abundance of geological, stratigraphic, structural and observed fracture information makes the CBTF a good setting for examining fracture- and crack-related seismic anisotropy (Figures 4.2 and 4.3). Figure 4.2(a) is an example of a borehole televiewer (BHTV) image from well 33-1 at approximately 580 m showing an induced fracture striking approximately N60°E. Figure 4.2(b) is a BHTV image of stress induced borehole breakout from which the maximum horizontal compressive stress direction is measured to be N60°E which is consistent with the regional stress direction (Zoback and Zoback 1980). An aerial photo showing the surface fracture pattern in an exposed limestone quarry pavement approximately 3.5 miles ENE of the CBTF indicates a fracture orientation of approximately N75°E (Figure 4.3).

The AVSP consisted of nine surface shots at locations lying on an arc of radius 290 m centred about well 33-1. Shot point positions were surveyed in 15° intervals from N75°E to N195°E (Figure 4.4). Vibroseis trucks operated using horizontal and vertical vibrators were used as the source of seismic energy. The vibrator trucks were aligned visually along the radial and a surveyed tangential direction to give in-line and cross-line sources respectively. The horizontal vibrator was downswept from 46 Hz to 7 Hz whereas the compressional-wave source was downswept from 96 Hz to 18 Hz. The vibroseis sweep length used was 13s and the recording time was 15s.

Authors	Measurement Type	Fracture system
Hagen (1972)	Aerial Photography	N70°E(systematic) N25°W(nonsystematic)
Gasteiger (1980)	Surface mapping	N75°E to N90°E N5°W to N30°W N30°E(Local feature)
Rizer and Queen (1986)	Surface mapping	N70°E to N85°E (systematic) N10°W to N45°W (non systematic)
Queen and Rizer (1990)	Borehole Televiewer	N55°E to N75°E
	Point Load tests on orientated cores	NE (shale) ENE (limestone)

Table 4.1 - A summary of previous fracture related studies in the vicinity of the CBTF.

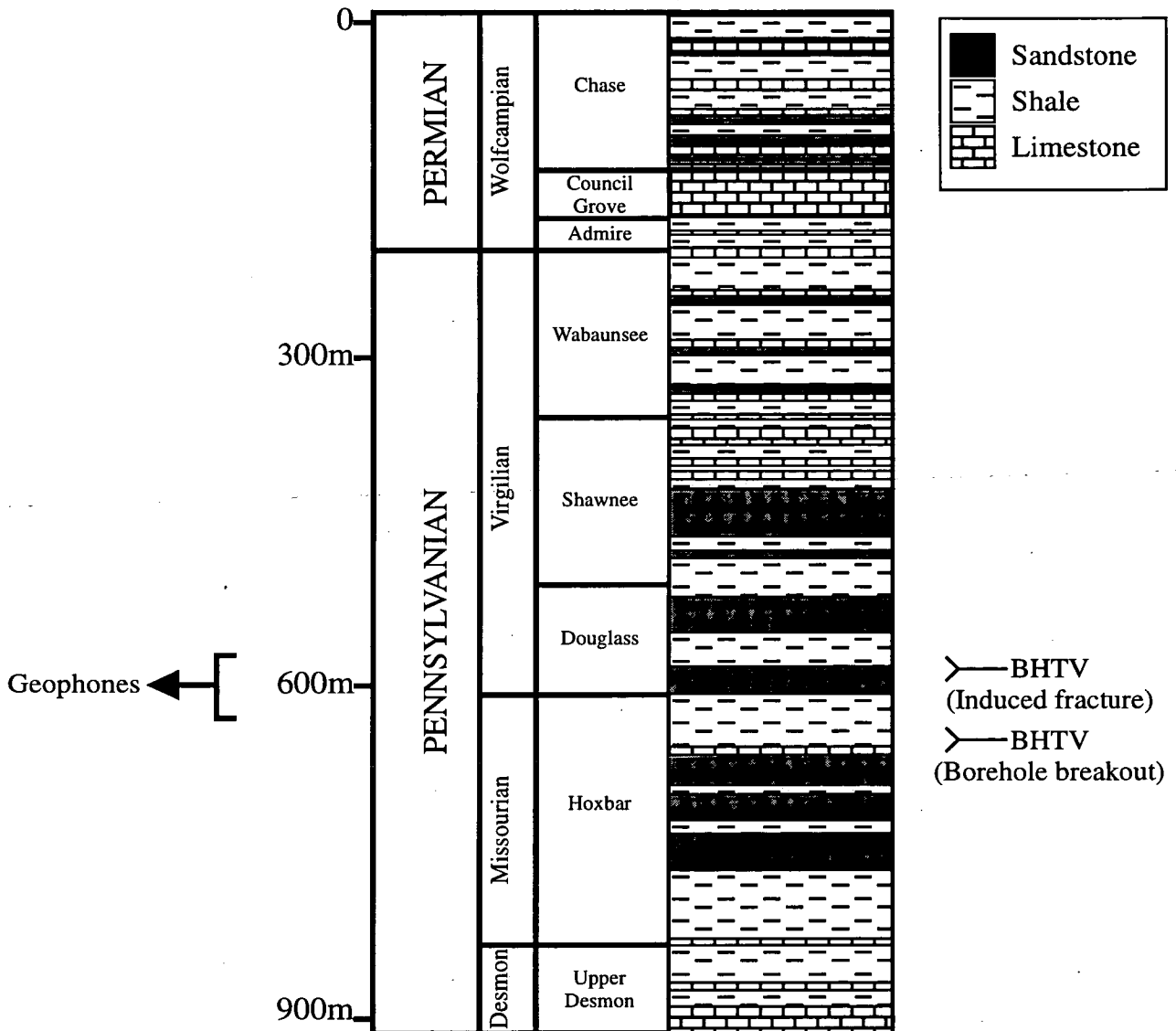


Figure 4.1 -The reported stratigraphy at the Conoco Borehole Test Facility, Kay County, Oklahoma. The five geophone levels used in the azimuthal VSP experiment are located at depths between 580 m and 620 m. Also shown are the two depths for which BHTV images are shown in Figure 4.2 (after Queen and Rizer 1990).

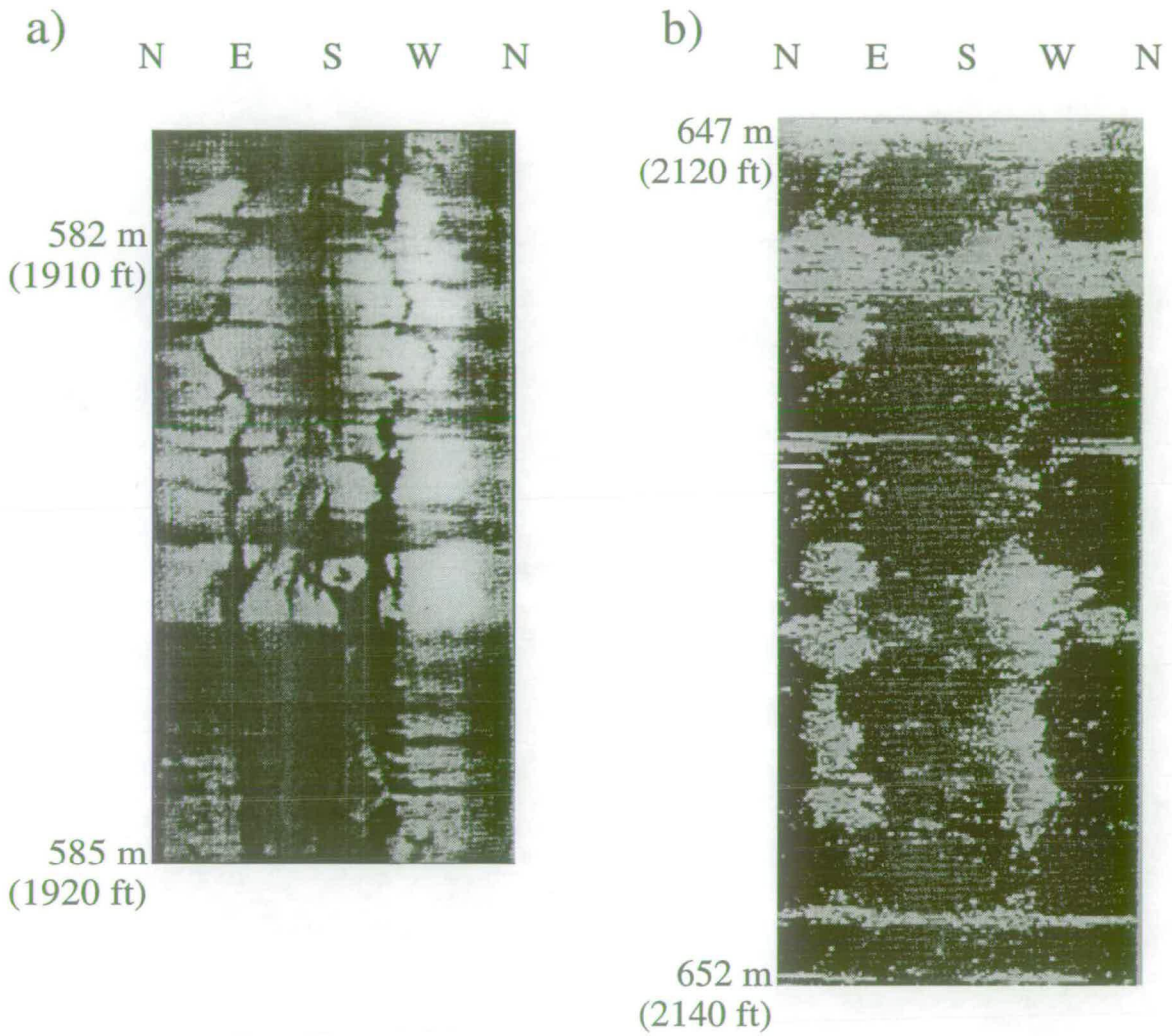
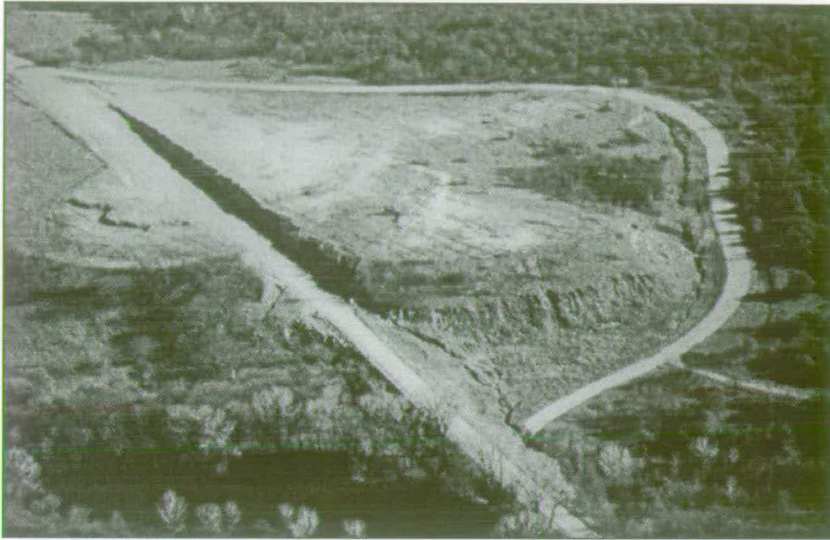


Figure 4.2 - Borehole televiewer images obtained from well 33-1 showing a) an induced fracture striking between N55°E and N65°E and b) stress-induced borehole breakout.

a)



b)

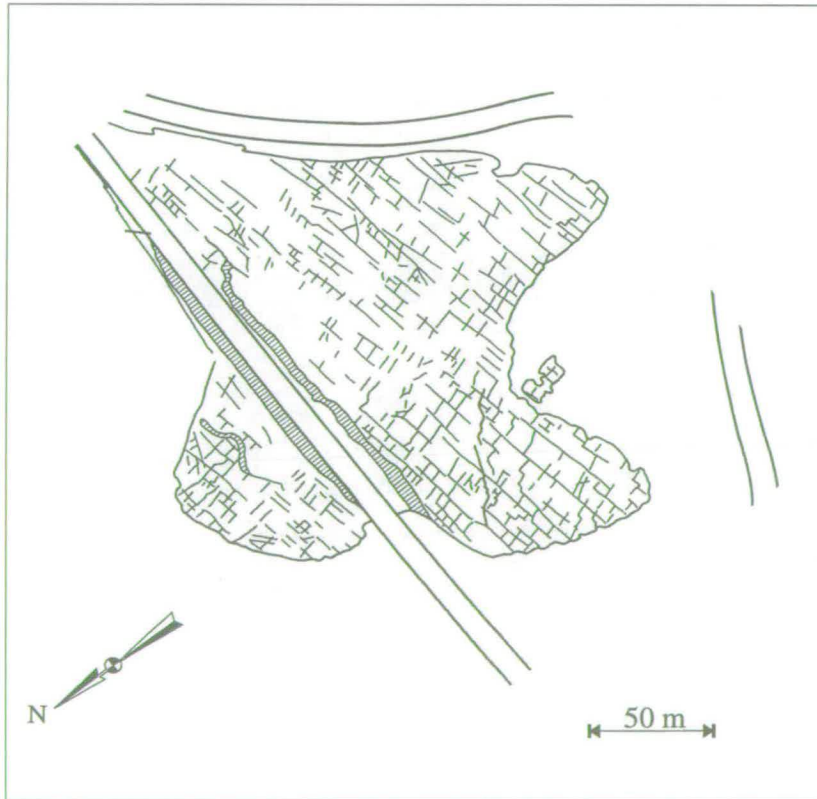


Figure 4.3 - a) An aerial photo showing the surface fracture pattern in an exposed Limestone pavement near to the CBTF. The lower figure b) shows the result of a aerial mapping survey which reveals a systematic set striking N75°E and a non-systematic set striking N165°E.

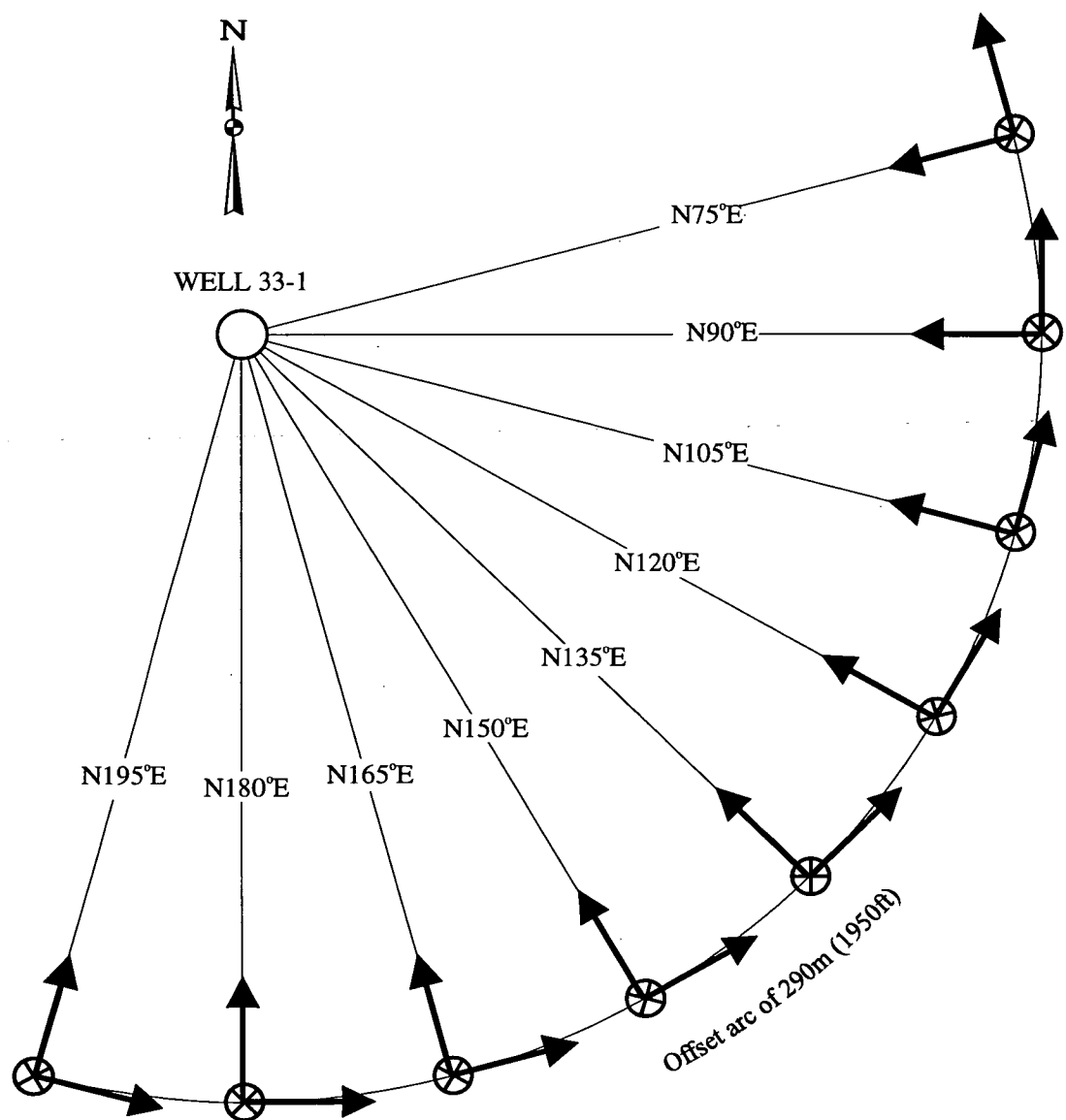


Figure 4.4 -Schematic diagram illustrating a plan view of the acquisition arrangement used for the azimuthal VSP experiment at the Conoco Borehole Test Facility, Oklahoma. Nine source locations were arranged azimuthally about well 33-1 on an arc of offset 290 m. Sources are polarized in in-line, cross-line and vertical directions, these are indicated by the arrows pointing towards the well, tangential to the radial direction and a crossed circle, respectively.

For each source/receiver combination five sweeps were used which were then stacked. Recordings were made using a single-level three-component geophone with a gyroscopic attachment. This tool was locked in position at five depth levels between 580 m and 620 m. A summary of this acquisition arrangement is given in Table 4.2. For each level the geophone package was locked into place and the source moved along the arc. The three source orientations were thus recorded in a common geophone gather for which the geophone is clamped in position giving a constant geophone orientation. This planned source and receiver collection indicates a total of 135 three component recordings. However, due to some operational difficulties some recordings were omitted for the 600 m and 582 m levels when the vibroseis truck became stuck.

#### 4.3 AVSP PROCESSING

Initial processing consisted of cross-correlation, demultiplexing, polarity corrections and stacking of the seismograms. The three-component records are then rotated into in-line and cross-line directions using data from the gyroscopic instrument attached to the receiver package. It has been suggested (Ghose and Takahashi 1991) that the response function of some geophones are azimuthally sensitive so that numerical rotations of the recorded seismograms may introduce errors to the recorded seismograms. This does not seem to be the case for the geophone tool used in the AVSP experiment since although the azimuthal orientation of the tool varied from level to level the seismograms display similar characteristics from level to level. Further evidence for the geophones' azimuthally independent response is reflected by the similarity in the shear-wave splitting estimates with depth on most azimuths. Artificial zero traces are inserted into the seismogram gather file at the locations corresponding to the missing sources so that the gathers can be displayed and processed easily. The processed shear-wave seismograms are shown in Figure 4.5 in a multicomponent display arranged in common receiver gathers. Each panel is arranged azimuthally with the first trace corresponding to the source positioned at



**Sources**

Shear vibrators  $\times 2$

Sweep	46 - 7 Hz
Azimuths	9 azimuths, N75°E to N195°E in 15° intervals
Offsets	290 m

Compressional vibrator

Sweep	96 - 18 Hz
Azimuths	9 azimuths, N75°E to N195°E in 15° intervals
Offset	290 m

**Recording Parameters**

Sweep length	13 s
Record length	15 s
Taper	0.5 s
Sample Interval	2 ms

**Downhole Sonde**      SSC K-Tool, 3-C receiver,  
gyroscopic orientation device

**Depth Locations**      5 levels, 580 m through to 620 m at 10 m intervals

Table 4.2 - Data acquisition parameters for the AVSP.

a)

## 580 m Level

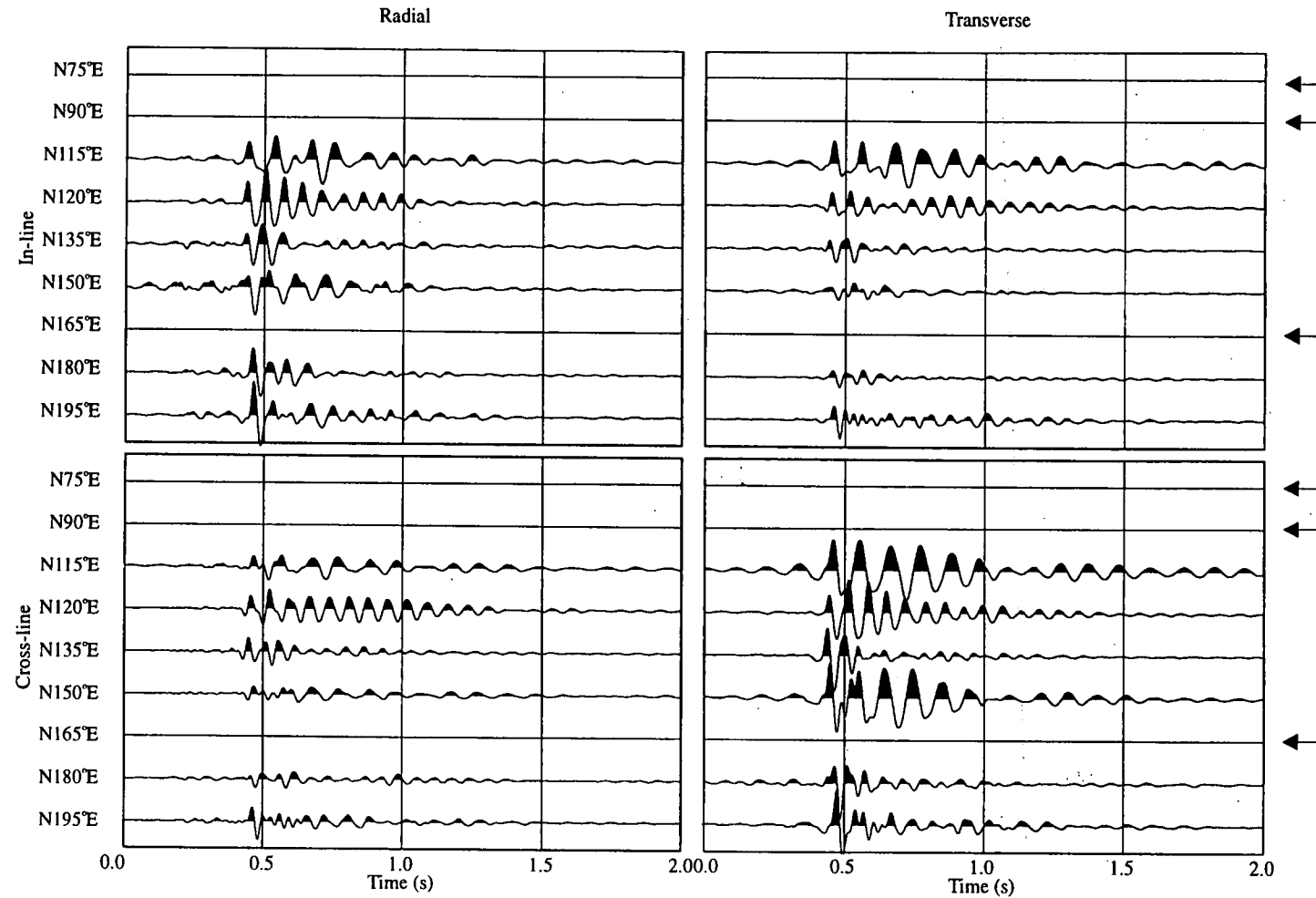


Figure 4.5 - Multicomponent plots showing the shear-wave seismograms recorded at a) the 580 m, b) the 590 m, c) the 600 m, d) the 610 m and e) the 620 m levels for the AVSP experiment at the CBTF. Arrows indicate missing data.

## 590 m Level

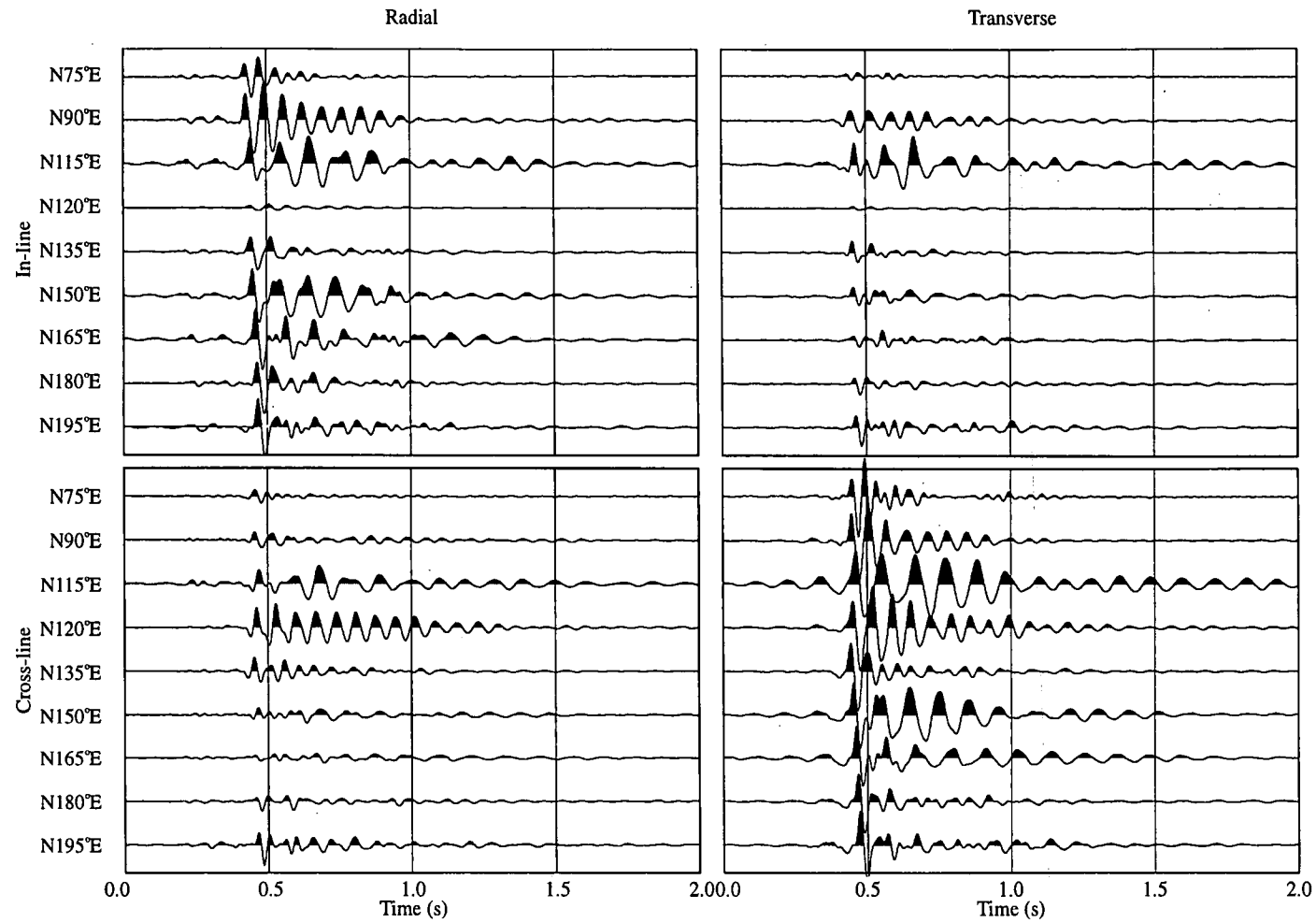


Figure 4.5b

# 600 m Level

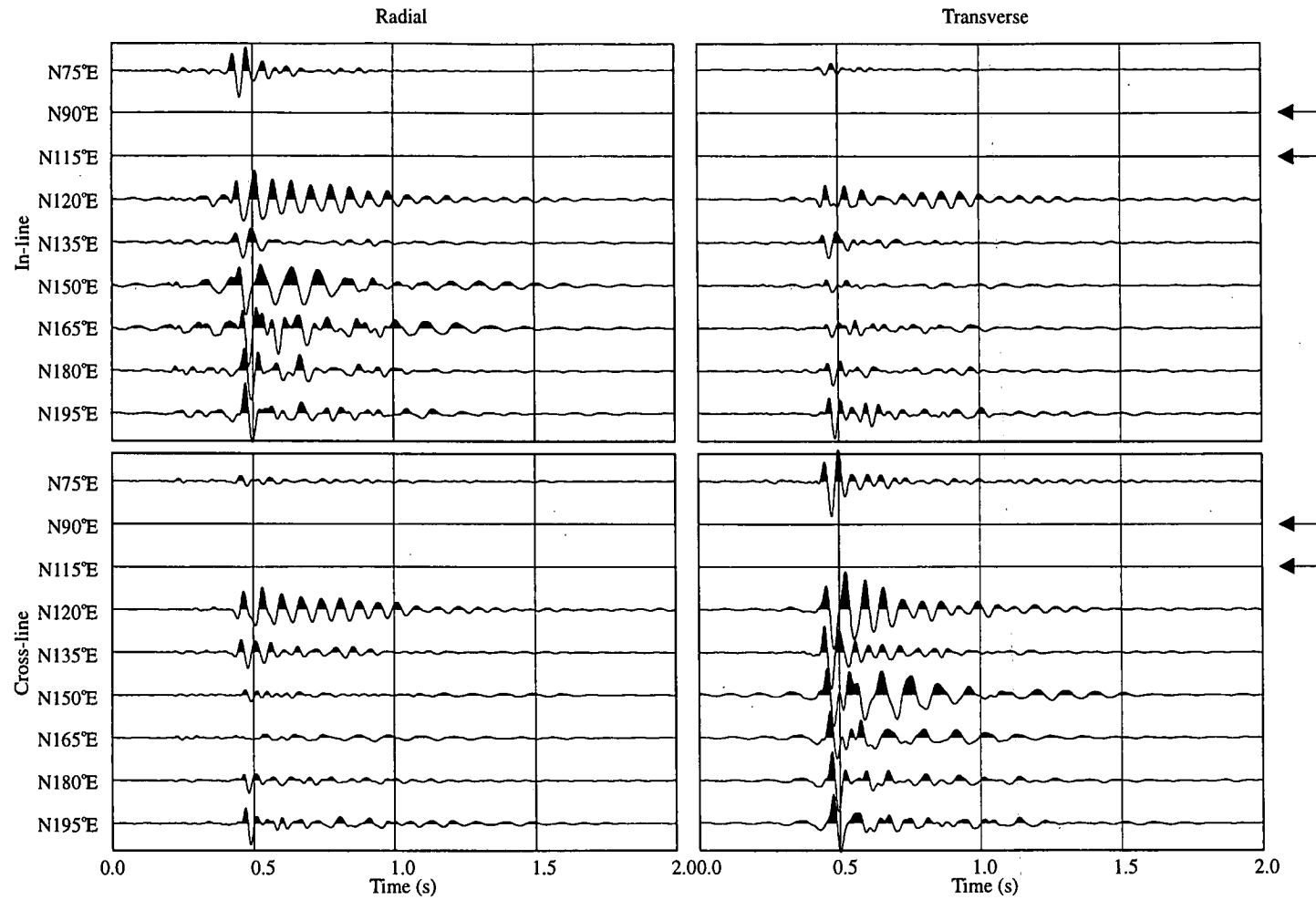


Figure 4.5c

# 610 m Level

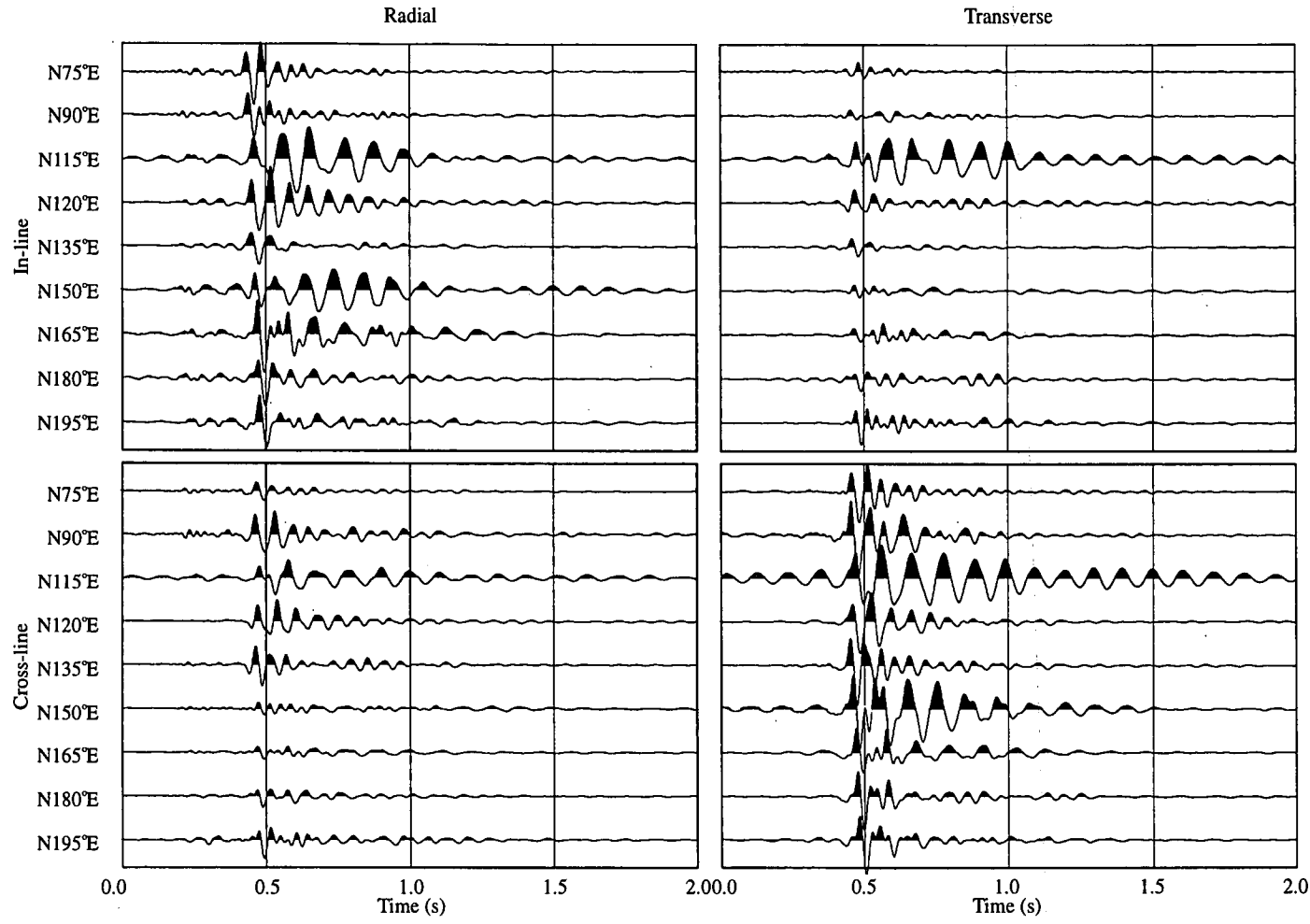


Figure 4.5d

## 620 m Level

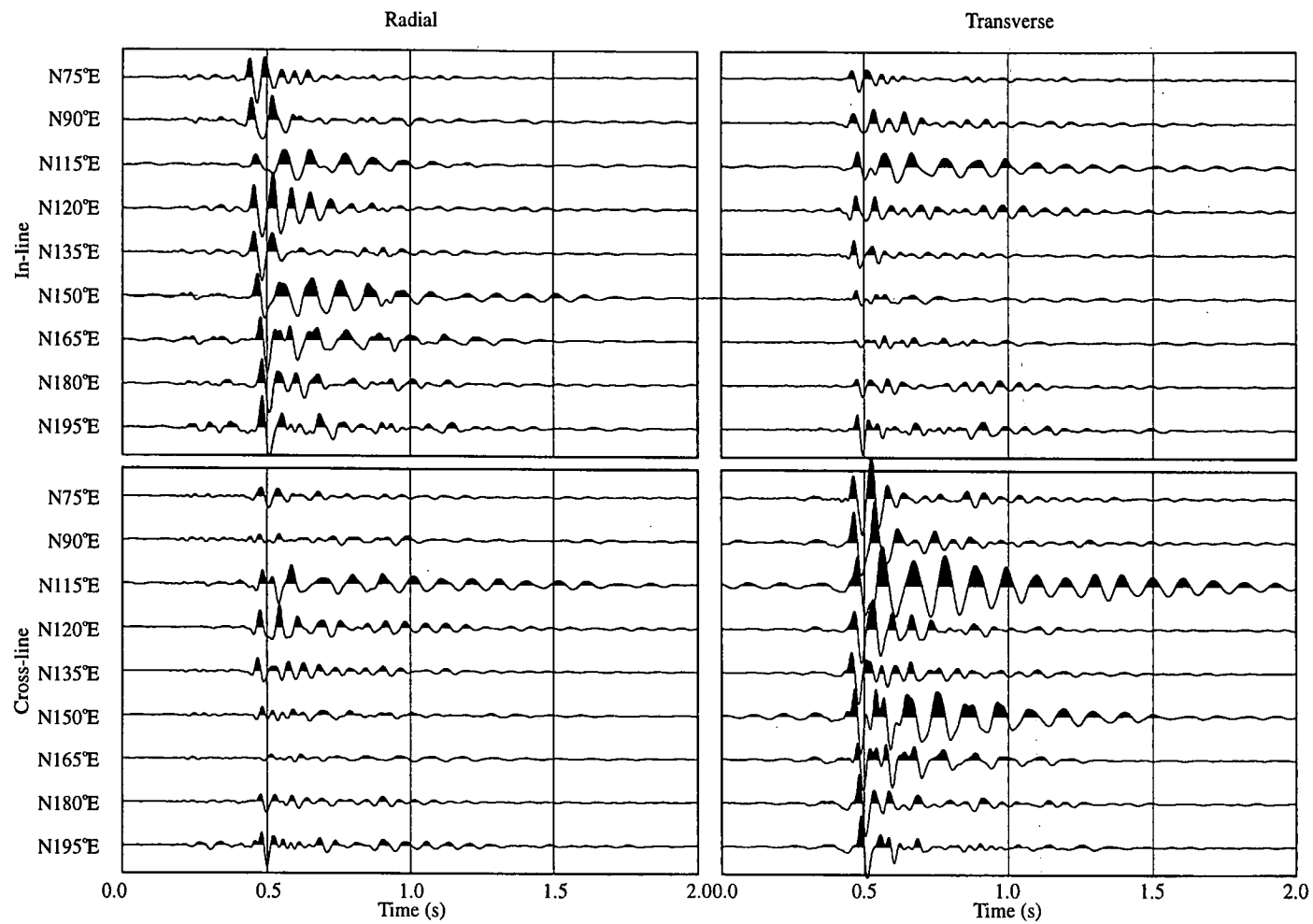
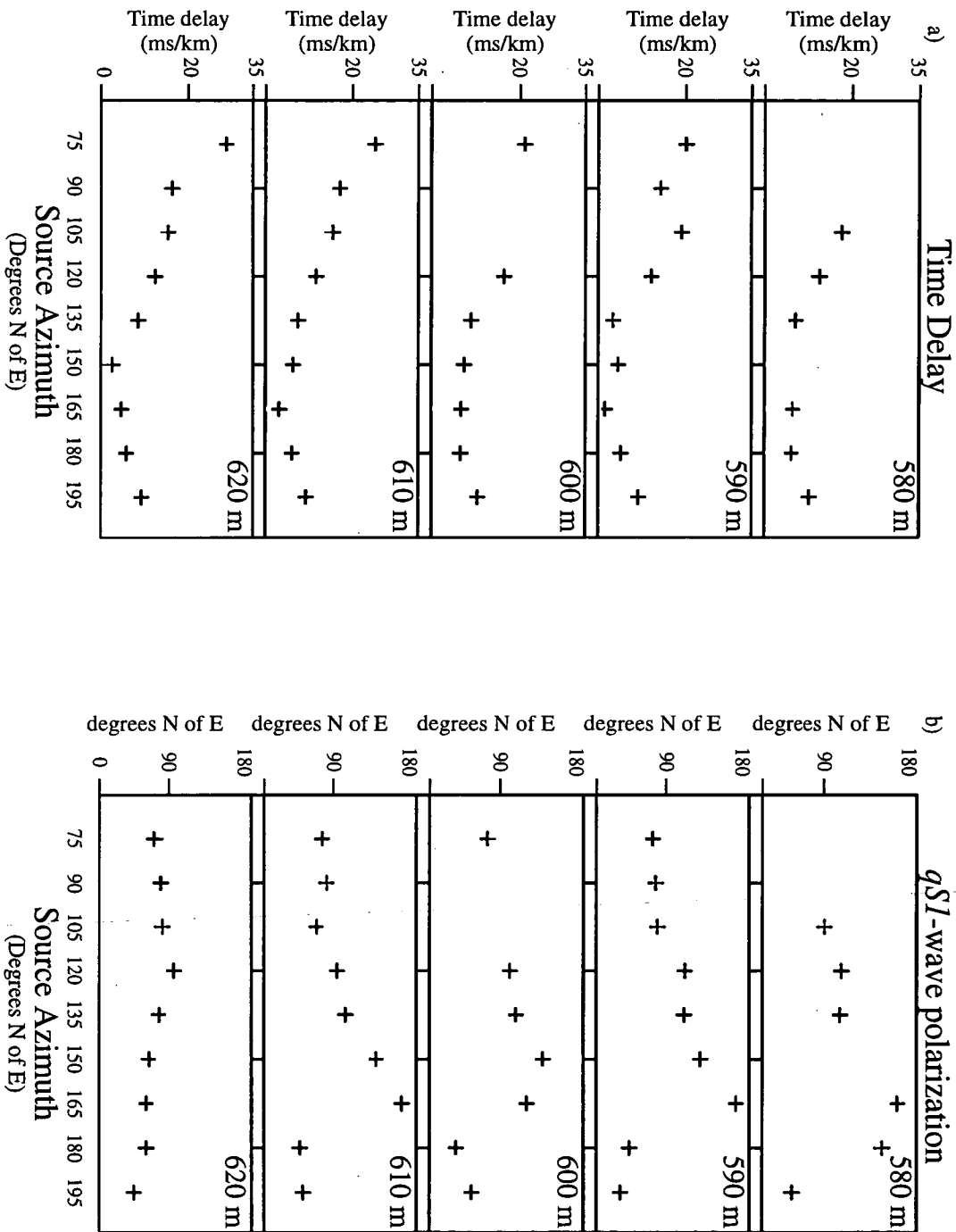


Figure 4.5e

N75°E. It can be seen that the data is of poor quality with an oscillatory wavetrain. Some seismograms display oscillatory recordings over the entire record which is probably due to poor vibrator coupling with the ground (Tatham and McCormack 1991).

Estimates of shear-wave splitting were obtained using an algebraic implementation of the Alford's rotation (Zeng and MacBeth 1993). This technique is more suited to near-zero offset VSPs so that problems may arise in the application of this technique to the non-vertical propagation directions recorded for the AVSP (Queen and Rizer 1990). Unfortunately, a more suitable technique has not yet been developed so that this choice is applied in the absence of any other available techniques. This technique is applied to a 200 ms windowed portion of the direct shear-wave arrival of the horizontal geophone components recorded with the in-line and cross-line sources. My results agree with those published by Queen and Rizer (1990), suggesting a consistent processing sequence although minor differences do exist in the results. This is not unexpected because of the differences in the shear-wave estimation technique. The estimated  $qS1$ -wave polarizations and time delays are shown in Figure 4.6 in an azimuthal sequence. The estimated time delays normalized by the straight raypath distance show a systematic variation with azimuth appearing to decrease from a maximum value of approximately 30 ms/km around the source azimuth N75°E to a minimum of approximately 4 ms/km for the source azimuths N150°E and N165°E. Unfortunately, there does not appear to be any systematic time delay variation with depth. The AVSP experiment was designed to see if a systematic increase in travel time splitting could be observed as the shear waves propagated through a fractured section of Tonkawa sandstone in which the geophones were located. This depth dependent behaviour is not apparent in the observed time delay estimates although the noise level suggested by Queen and Rizer (1990) of 4 ms may obscure any such systematic increase with depth. The estimated shear-wave polarizations are not consistent with a simple vertical crack system which is usually assumed to give a constant  $qS1$ -wave polarization estimate parallel to the crack strike

Figure 4.6 - Estimates of the shear-wave splitting showing a) the time delays and b) the *qSI*-wave polarizations. Figures in the top right of each plot indicate the geophone depth.





for near-vertical incident angles. The  $qSI$ -wave polarizations are plotted in Figure 4.7 on a lower hemisphere equal area projection with the propagation angles correctly defined to be the angle from the source to the receiver. For example, the polarizations plotted at N255°E on the equal area plots correspond to the source located along the azimuth N75°E. For the first four azimuthal shot locations between N75°E and N120°E the shear-wave polarizations appear to be aligned over all the depth levels. Moving clockwise along the arc from the sources located at N75°E to N120°E the  $qSI$ -wave polarizations appear to rotate from N75°E to approximately N100°E. The  $qSI$ -wave polarizations are not aligned over all depth levels for the sources located between N135°E and N180°E. It can be seen that there are abrupt swings in the polarization estimates with depth. The polarizations recorded for the last azimuthal shot position at N195°E show a return to the behaviour displayed for the first four azimuths with the  $qSI$ -wave polarizations aligned over the depth levels at an angle of N50°E. A simple interpretation of the  $qSI$ -wave polarization estimates to be equal to the fracture orientation would imply that this observed seismic anisotropy at the CBTF is due to several vertical fracture sets. Although this may be the case such a solution represents a complicated anisotropy with a low order of symmetry. I will show that the observations can be interpreted in terms of a single non-vertical crack set consistent with surface observations and other studies from the test site (Liu, Crampin and Queen 1991).

#### 4.4 JUSTIFICATION OF HOMOGENEITY ASSUMPTION

These shear-wave splitting observations of time delays and  $qSI$ -wave polarizations are inverted for elastic constants or equivalent media parameters. In order to invert these observations I replace the layered velocity and density CBTF model with a homogeneous anisotropic halfspace. This assumption is justified as follows:

- (i) the depth range of the geophones is very narrow so that the volume of rock sampled by the shear-waves will be confined to a small volume which is essentially

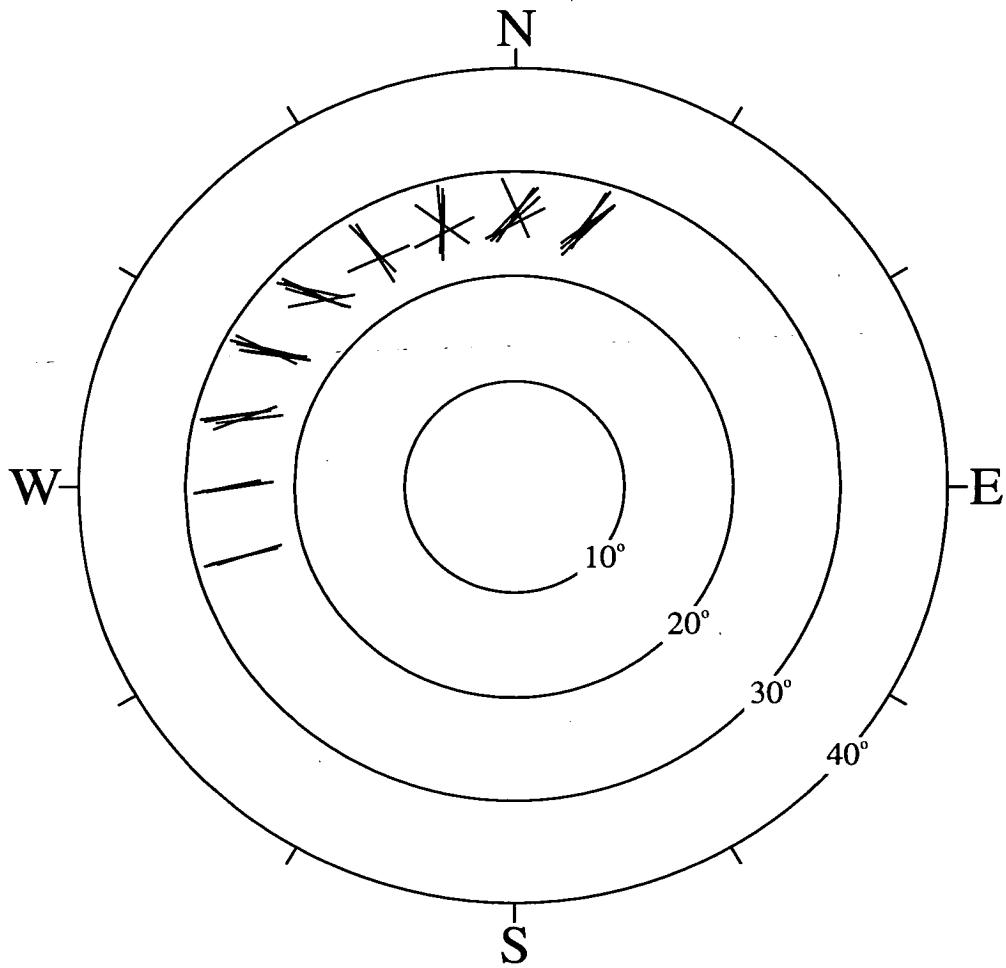


Figure 4.7 - A lower hemisphere equal area plot showing the estimated  $qS1$  polarizations for the azimuthal VSP experiment conducted at the CBTF.

the same for all geophone levels.

(ii) ray tracing through a velocity model obtained from sonic logs shows that there is negligible ray bending (Figure 4.8). In this case the raypaths can be approximated as straight lines connecting the source and receiver positions which is consistent with a homogeneous halfspace approximation.

(iii) information obtained from cores and BHTV images do not indicate any significant changes in fracture orientation with depth (Queen and Rizer 1990). Thus any fracture-related anisotropy is also unlikely to change with depth. However, it should be remembered that such information represents only a sparse sampling of the sub-surface.

(iv) a depth dependent plane layered isotropic structure may be replaced by an equivalent homogenous hexagonally anisotropic media in the case that the seismic wavelength is larger than any fine layering (Postma 1955, Backus 1962, Schoenberg and Muir 1989).

In addition to these arguments an inversion for the more general case of a depth dependent anisotropic structure with different symmetry orientations and/or symmetry classes is too computationally intensive to be realistically attempted with current computational resources. Furthermore, an anisotropic model of different anisotropic orientations and/or symmetry classes may lead to multiple splitting for which reliable estimates of shear-wave splitting are difficult to obtain.

I will test the uniform half-space approximation by computing full waveform seismograms for a horizontally plane layered structure for the CBTF velocity model with various anisotropic systems and orientations. I then apply estimation techniques to these synthetic seismograms to quantify the shear-wave splitting for this layered model. I compare these results with the shear-wave behaviour for a homogeneous

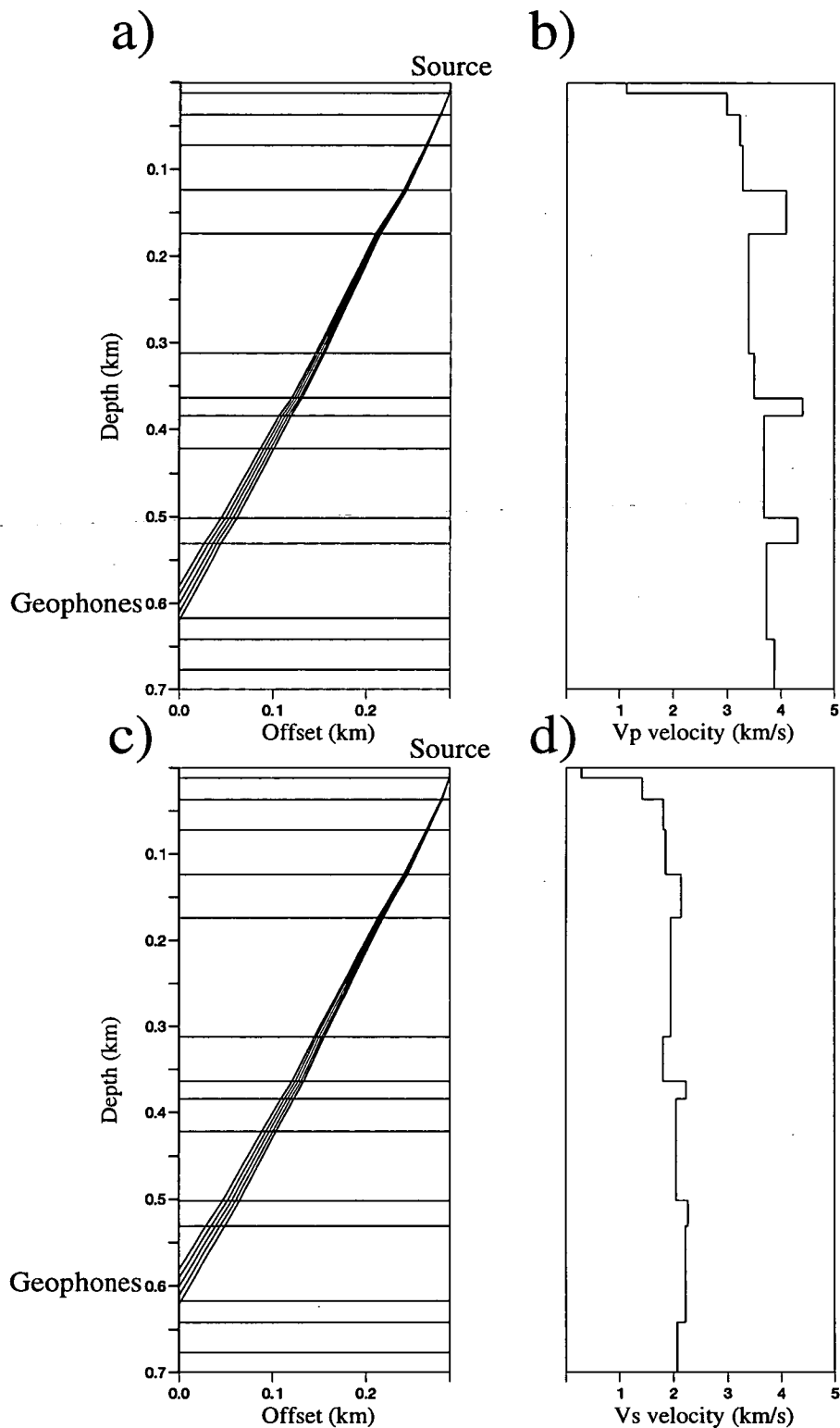


Figure 4.8 - Isotropic ray tracing for blocked velocity models obtained from well log and RVSP data from the CBTF (Queen, J., Conoco Inc., personal communication). Ray diagrams are shown for a) compressional and c) shear waves. Figures b) and d) show the variations of  $P$  and  $S$  velocities with depth.

anisotropic halfspace.

Synthetic seismograms are calculated for nine equi-spaced azimuths between  $N0^\circ E$  and  $N180^\circ E$  using a constant geophone depth of 600 m and five source offsets of 420 m, 350 m, 280 m, 220 m and 160 m (Figure 4.9). These offsets are calculated to give straight line incident angles between the source and receiver of  $35^\circ$ ,  $30^\circ$ ,  $25^\circ$ ,  $20^\circ$  and  $15^\circ$  respectively. This acquisition geometry allows an extensive azimuthal and incident angle sampling of the anisotropic system.

The first model I construct has hexagonal symmetry with a horizontal symmetry axis pointing north. This is achieved using Hudson's second order formulations (Hudson 1980) to calculate the equivalent anisotropic elastic constants for vertical cracks striking east-west. The cracks are modelled as fluid-filled, of crack density 0.04, and aspect ratio 0.001. Estimation results obtained using an algebraic implementation of the Alford's rotation (Zeng and MacBeth 1993) are compared with the shear-wave behaviour for a homogeneous halfspace model (Figures 4.10 and 4.11). The estimated  $qSI$ -wave polarizations for the layered model appear to be very similar to those for the homogeneous halfspace model except for the sources located at  $N67.5^\circ E$  and  $N112.5^\circ E$  at offsets of 420 m. For these directions the time delays are small because the shear-waves are propagating near to the line singularity which may lead to inaccurate  $qSI$ -wave polarization estimates. The systematic variation over both incidence and azimuthal angles is in good agreement for both the  $qSI$ -wave polarizations and time delays.

The second model for which I construct synthetic seismograms is similar to the previous model and possesses the same crack parameters but the cracks are now rotated  $20^\circ$  from the vertical to the north. As for the vertically-cracked model, shear-wave estimation techniques are applied to the seismograms and compared with the theoretical shear-wave behaviour for the homogeneous halfspace model, these results are shown in Figures 4.10(b) and 11(b). The  $qSI$ -wave polarizations for the layered

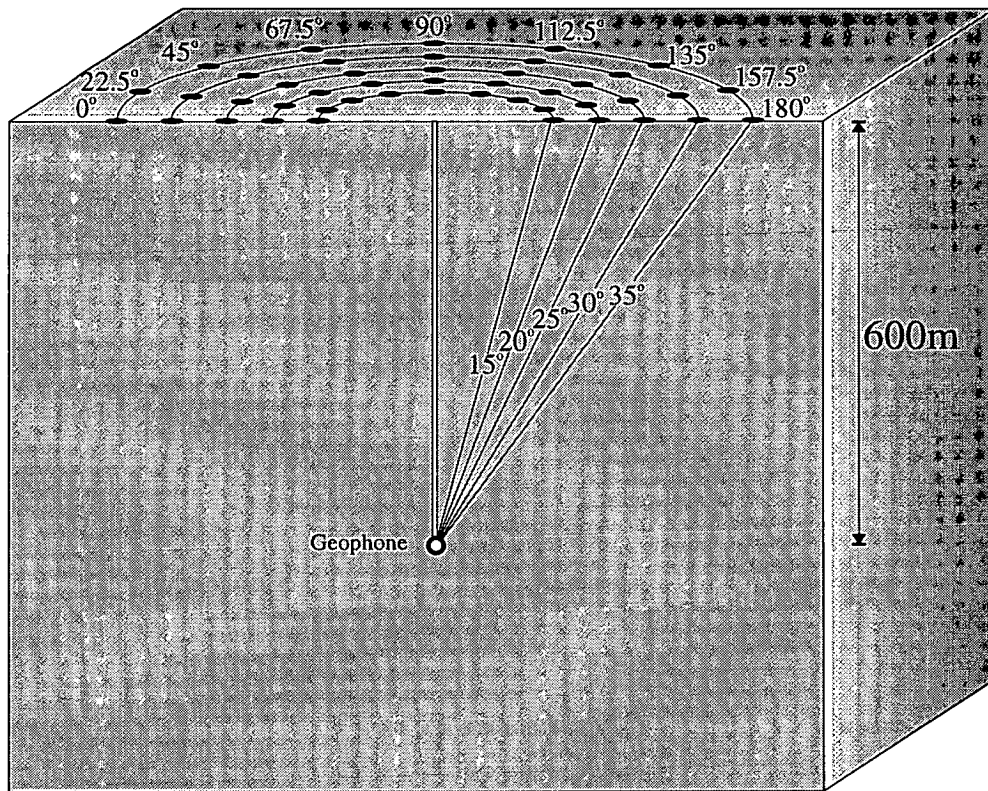


Figure 4.9 - Acquisition geometry used in testing the assumption of replacing a homogeneous anisotropic halfspace with a plane layered anisotropic structure at the CBTF. In-line, cross-line and vertically polarized sources are located along 9 equi-spaced azimuths and 5 offsets (black dots). The receiver (white circle) is at a depth of 600m. This combination of source offset and receiver depth is calculated to give straight line incidence angles of  $15^\circ$ ,  $20^\circ$ ,  $25^\circ$ ,  $30^\circ$  and  $35^\circ$ , as indicated.

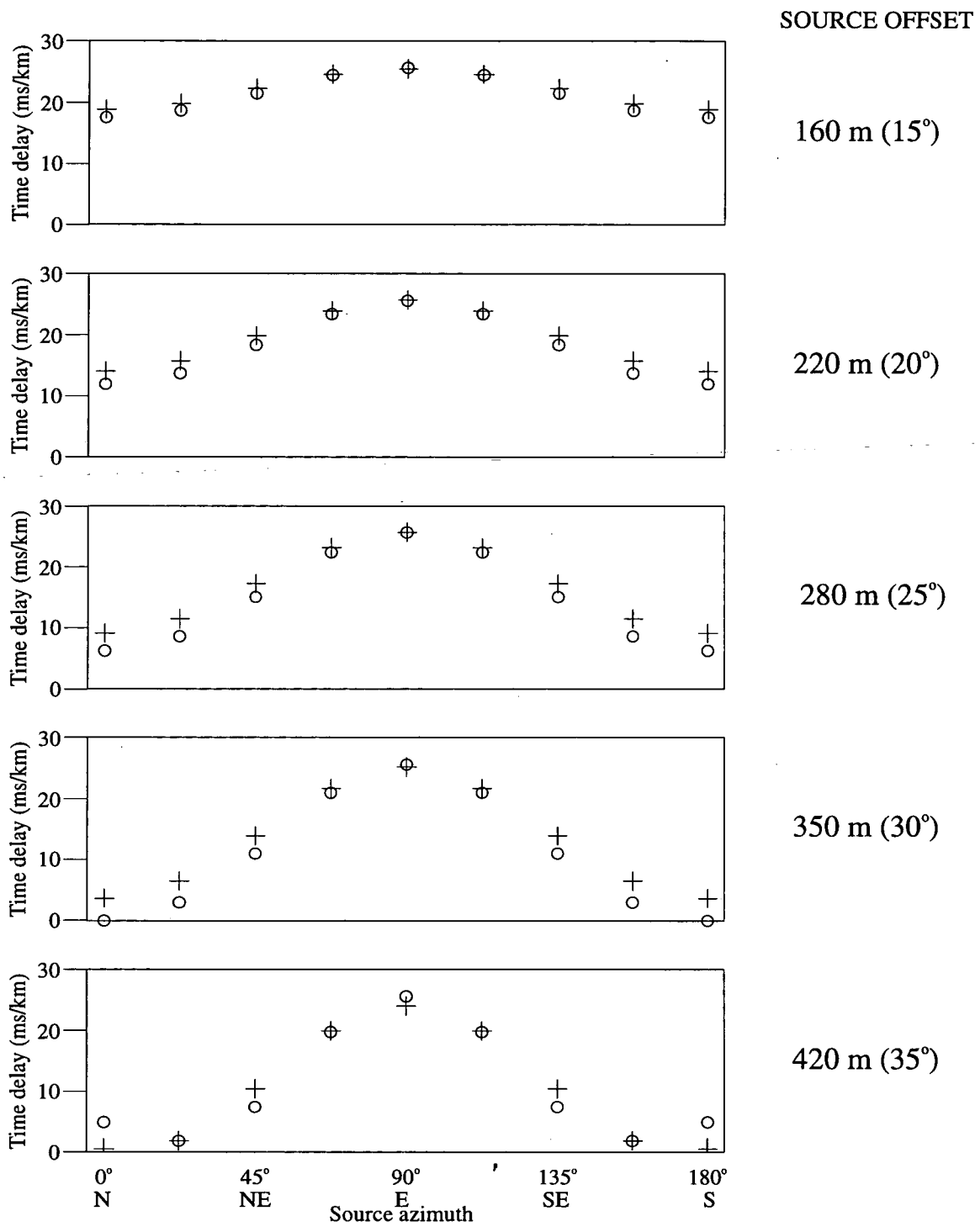


Figure 4.10 - A comparison of normalized time delays calculated for a homogeneous halfspace (cross) and estimated time delays obtained from synthetic seismograms for a one dimensional model (circle) saturated cracks of  $CD=0.04$ ,  $AR=0.001$ , striking east-west and oriented a) vertically and b) dipping  $20^\circ$  from the vertical.

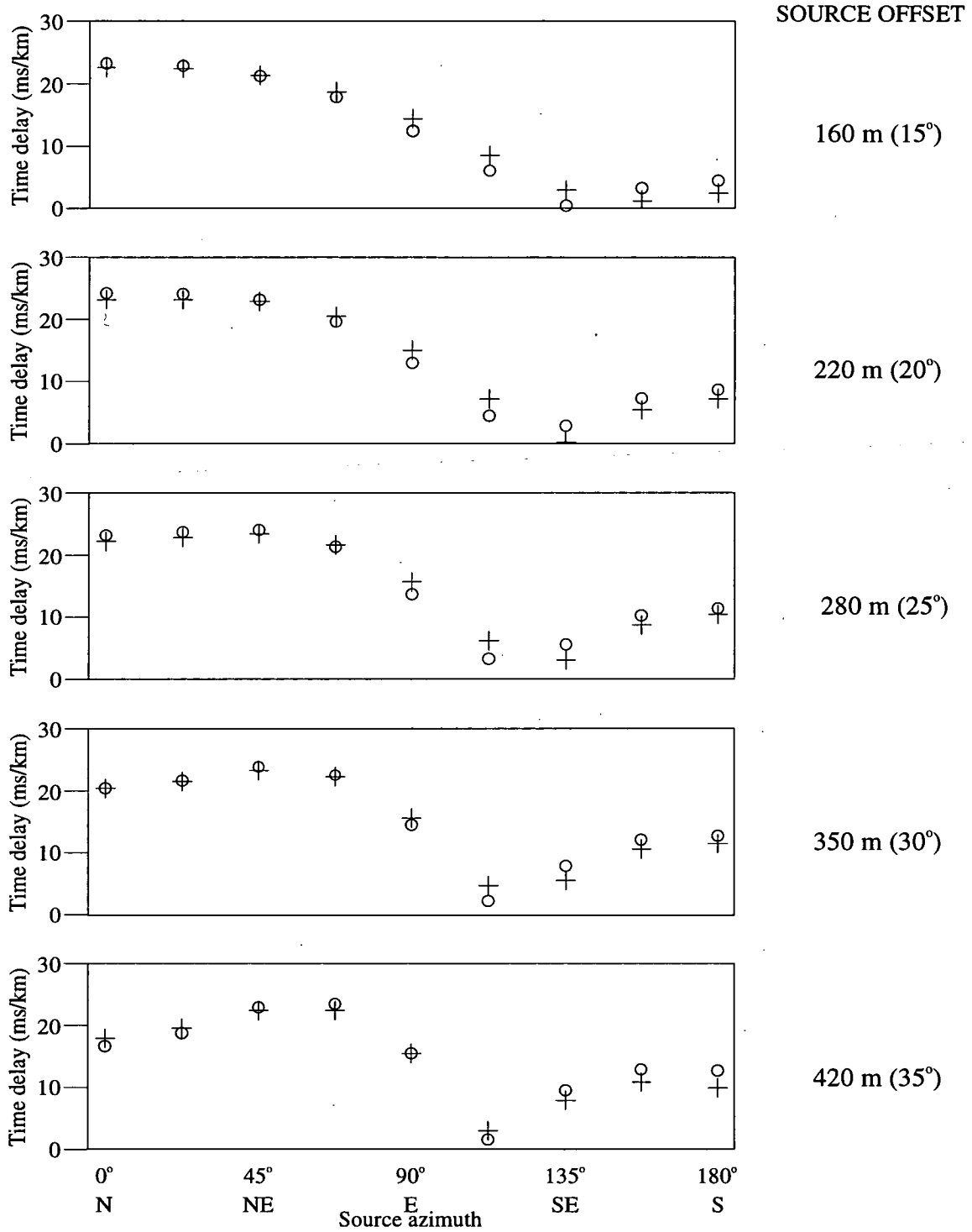


Figure 4.10b



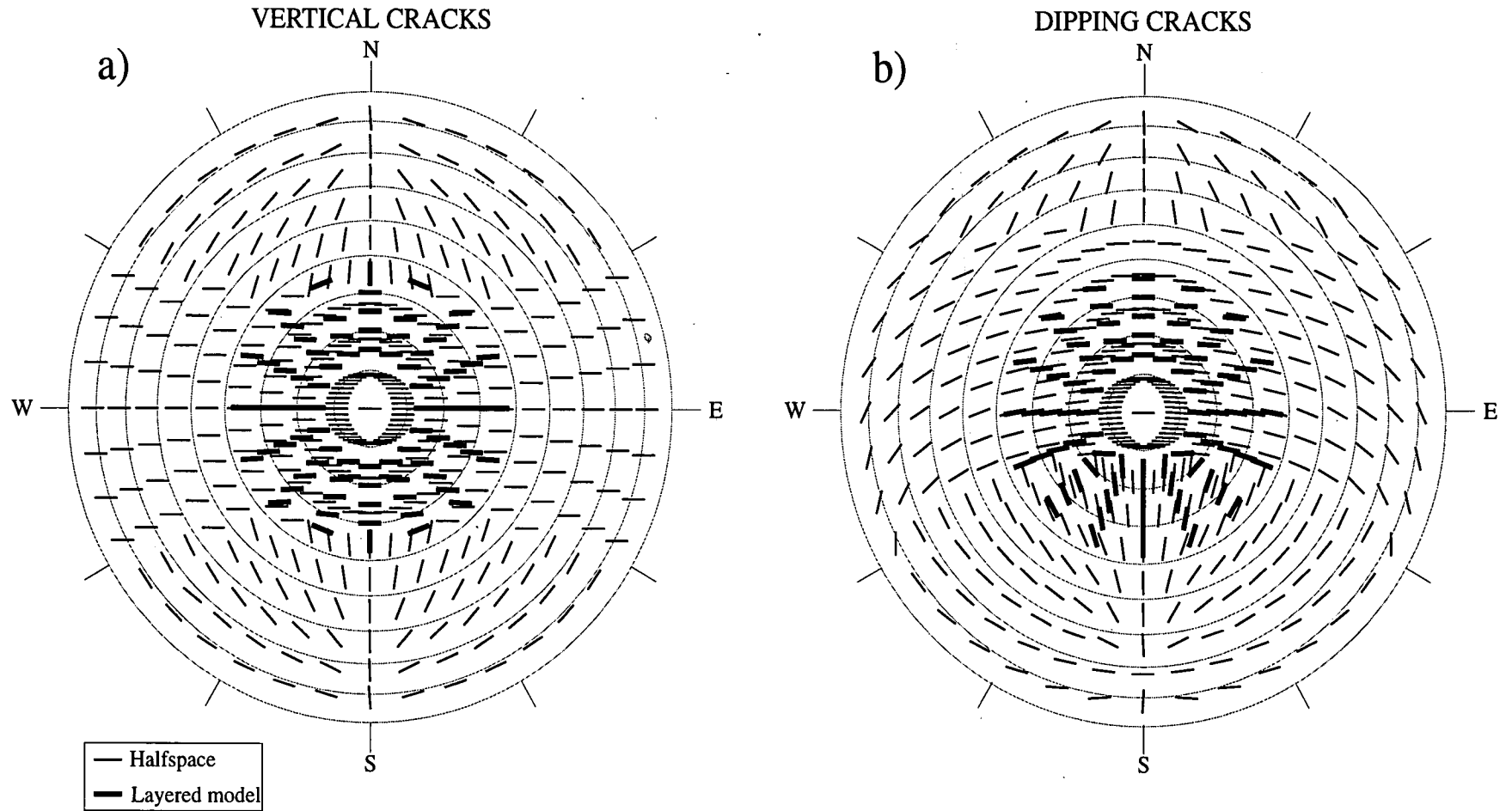


Figure 4.11 - Lower hemisphere equal-area plots showing the  $qS1$ -wave polarizations for a homogeneous halfspace (thin black lines) and estimates from synthetic seismograms for the layered anisotropic model (thick black lines). Figure a) shows the results from the vertical crack model and b) the results from the dipping crack model.

model and homogeneous halfspace model show good agreement for all propagation directions. A comparison of the time delays shows that, as for the vertically cracked model, the systematic variation with incidence and azimuth angle is in good agreement.

Although these two examples do not form a comprehensive study the results are sufficiently encouraging to support the assumption of a homogeneous halfspace that I will make in the AVSP inversion.

#### 4.5 INVERSION PROCEDURE

In view of the assumption made that the depth dependent CBTF model can be replaced by a homogeneous halfspace then the forward modelling requirement is to calculate shear-wave observations for a homogeneous anisotropic material for a given propagation direction. To invert the shear-wave splitting estimates obtained from the AVSP the GA is applied to minimise the difference between the observed shear-splitting estimates and the calculated ray (group) velocity attributes for the models in the GA's population. The misfit function to be minimized by the GA is defined as

$$f(m, \tau^0, p^0) = \frac{1}{2} \left[ \Delta \tau(\tau^0, \tau^m, \delta \tau) + \Delta p(p^0, p^m, \delta p) \right]; \quad (4.1a)$$

where

$$\Delta \tau(\tau^0, \tau^m, \delta \tau) = \frac{1}{40} \sum_{j=1}^5 \sum_{i=1}^9 \frac{(\tau_{ij}^0 - \tau_{ij}^m)^2}{\delta \tau_{ij}^2}; \quad (4.1b)$$

and

$$\Delta p(p^0, p^m, \delta p) = \frac{1}{40} \sum_{j=1}^5 \sum_{i=1}^9 \frac{(p_{ij}^0 - p_{ij}^m)^2}{\delta p_{ij}^2} . \quad (4.1c)$$

$\tau$  and  $p$  are vectors of the time delays and the horizontal projections of the  $qSI$ -wave polarizations.  $m$  is the model parameter vector for which synthetic shear-wave splitting observations are calculated by forward modelling. The subscripts  $i$  and  $j$  are used to identify the azimuth and geophone levels of the observation respectively. The time delay misfit,  $\Delta\tau$ , and  $qSI$ -wave polarization misfit,  $\Delta p$ , are normalized by a factor of 40, rather than 45, because of missing data. The superscripts  $m$  and  $0$  identify the modelled and observed data vectors. The quantities  $\delta\tau$  and  $\delta p$  are error estimates associated with the observed time delays,  $\tau^0$ , and  $qSI$ -wave polarizations,  $p^0$ , respectively. If the observed data vectors  $\tau^0$  and  $p^0$  contain outliers then this choice of misfit function will be unsuitable because the misfit function is based on a least squares criteria implying a Gaussian distribution of errors. Thus any outliers may have an undesirable effect in unduly biasing any solution to match the outlying data.

The time-delay error is estimated to be 4 ms, as suggested by Queen and Rizer (1990). The error associated with the estimated  $qSI$ -wave polarization is dependent upon the time delay and is expected to decrease as the time delay between the split shear waves increases. This uncertainty is reflected in the choice of the error estimates,  $\delta p$ , which are a function of  $\tau^0$  as follows

$$\begin{aligned} \delta p_{ij} &= 15^\circ & \tau_{ij}^0 &> 4 \text{ ms} ; \\ \delta p_{ij} &= 30^\circ & \tau_{ij}^0 &\leq 4 \text{ ms} . \end{aligned}$$

The GA is initially applied to the minimization of equation 4.1 to invert the shear-wave splitting observations from the AVSP for a hexagonal symmetry system. As discussed in Chapter 3 media of this type may be represented in many different ways, the most general of which is in terms of the five independent elastic constants.

However, this choice of parameter set is difficult to interpret without a great deal of experience and it is common for the elastic constants to be condensed or rewritten in terms of other parameters, such as the Thomsen parameters (Thomsen 1986), which may facilitate an interpretation. A choice therefore exists in the parametrization scheme to be used in the GA inversion. Alternative schemes may use equivalent media formulations such as those of Postma (1955) or Hudson (1980) which are based on physical models of seismic anisotropy. These types of parametrizations will be the natural choice in the case that the probable cause of the seismic anisotropy is known. For example, if fine layering is suspected as the source of the measured anisotropy then Postma's formulations may be an appropriate choice. In the case of the seismic anisotropy observed at the CBTF other independent information (Table 4.1) indicates that the underlying cause of the seismic anisotropy is due to aligned fractures. This implies that an appropriate choice of the parametrization scheme for the seismic anisotropy observed at CBTF is an equivalent media formulation based on a fracture system. There are many different equivalent media formulations which attempt to model fracture/crack related seismic anisotropy (for example Schoenberg and Douma 1988, Thomsen 1991, Nishizawa 1982). For this suite of inversions I will use the Hudson crack model (1980). These formulations have been extensively used and have been shown to model realistically some aspects of wave propagation in cracked media (Rathore *et al.* 1992). However, as discussed in Chapter 3, it should be remembered that the Hudson representation may prove to be restrictive and may constrain solutions according to the assumptions involved with the physical model. In view of the GA's possible sensitivity to the parametrization schemes I will also use the elastic and Thomsen schemes described in Chapter 3. The Hudson, Thomsen and Cijkl parametrization schemes are discretized for the GA search as described in Tables 4.3, 4.4 and 4.5. The GA control parameters for all three inversions are given in Table 4.6.

Hudson Parametrization Scheme				
Parameter		$P^L$	$P^U$	$N_{int}$
Crack Density	$CD$	0.0001	0.1271	128
Aspect Ratio	$AR$	0.0001	0.1271	128
Content	$CT$	0(dry)	1(sat)	2
Alpha (Degrees)	$\alpha$	-180.0	0.0	128
Beta (Degrees)	$\beta$	-45.0	45.0	128

Table 4.3 -The discretization scheme for the Hudson parametrization of model space.  $P^L$  and  $P^U$  represent the lower and upper discretization parameter bounds which are divided into  $N_{int}$  intervals. The Hudson cracks are initially aligned in the  $x_2x_3$  plane and are then rotated by the angles  $\beta$  and  $\alpha$  about the  $x_2$  and  $x_3$  axis respectively.

Cijkl Parametrization Scheme			
Parameter	$P^L$	$P^U$	$N_{int}$
$\Delta C_{1111}$ ( $\Delta C_{11}$ )	-30.0	+30.0	128
$\Delta C_{2222}$ ( $\Delta C_{22}$ )	-30.0	+30.0	128
$\Delta C_{2323}$ ( $\Delta C_{44}$ )	-30.0	+30.0	128
$\Delta C_{1313}$ ( $\Delta C_{55}$ )	-30.0	+30.0	128
$\Delta C_{1133}$ ( $\Delta C_{13}$ )	-30.0	+30.0	128
Alpha $\alpha$ (Degrees)	-180.0	0.0	128
Beta $\beta$ (Degrees)	-45.0	45.0	128

Table 4.4 -The discretization scheme for the elastic constant parametrization of model space. The  $\Delta C_{ijkl}$  refer to the % deviations of the elastic constants from the isotropic material,  $\Delta C_{ijkl} = [ C^{HEX}_{ijkl} - C^{ISO}_{ijkl} ] / C^{ISO}_{ijkl} \times 100$ . The  $\Delta C_{ij}$  in brackets give the alternative condensed 2 index Voigt notation of the elastic tensor. The symmetry axis is initially aligned along the  $x_1$  axis and is then rotated in the same way as described for the Hudson model.

Thomsen Parametrization Scheme			
Parameter	$P^L$	$P^U$	$N_{int}$
Delta $\delta_1$	-0.2201	+0.2201	128
Gamma $\gamma_1$	-0.2201	+0.2201	128
Epsilon $\epsilon_1$	-0.2201	+0.2201	128
Alpha $\alpha$ (Degrees)	-180.0	0.0	128
Beta $\beta$ (Degrees)	-45.0	45.0	128

Table 4.5 -The discretization scheme for the Thomsen parametrization of model space. The  $\delta_1$ ,  $\gamma_1$  and  $\epsilon_1$  refer to the Thomsen parameters for a hexagonally anisotropic medium with the symmetry axis initially aligned along the  $x_1$  axis (Thomsen 1986). The material is then rotated in the same way as described for the Hudson scheme.

GA Parameter		
Population size	$N_{pop}$	40
Number of Generations	$N_{gen}$	80
Crossover probability	$p_c$	1.000
Mutation Probability	$p_m$	0.050
Inversion		Enabled
G-bit Search		Enabled
Elitism		Enabled
Sharing		Enabled

Table 4.6 - The search parameters and operators used in the GA for the hexagonal symmetry inversion problem.

#### 4.6 INVERSION RESULTS: HEXAGONAL SYMMETRY

The best solutions and the associated misfits obtained from the GA inversion are shown in Table 4.7 in terms of the actual parameters used in the inversion. Table 4.8 presents these results in a common format of elastic parameters with the symmetry axis aligned in the  $x_1$  direction allowing a comparison between the different models. For all three inversions the GA converged to models with similar misfit values, with the Thomsen parameter inversion converging to the lowest overall value. If the misfit function is viewed in terms of the sum of the time delay,  $\Delta\tau$ , and  $qS1$ -wave polarization misfits,  $\Delta p$ , it can be seen that although the time delays appear to be adequately modelled,  $\Delta\tau \sim 1.0$ , there is still a considerable difference between the model and observed  $qS1$ -wave polarizations for the best fitting model. Although these values are not particularly low, the match between the model observations and the observed shear wave behaviour compares well with other studies (for example Yardley 1994, Liu, Crampin and Queen 1991) although few experiments have attempted to match such an extensive azimuthal coverage of propagation directions. The synthetic  $qS1$ -wave polarizations corresponding to the best solutions from the three inversion schemes are shown in Figure 4.12 for a hemisphere of propagation directions with the field observations superimposed on the plots.

##### *Hudson model*

The best Hudson model found by the GA suggests that the observed estimates of shear-wave splitting correspond to a sub-vertical saturated crack system striking at N73°E and dipping 9° to the south east from the vertical. This orientation is in good agreement with the direction of the systematic fracture set observed in the limestone formations (Table 4.1). Perhaps the most significant result is the suggestion that the fracture orientation is sub-vertical. Non-seismic observations from the CBTF support this model and the orientation of the systematic fracture system is reported as dipping approximately 17° to the south east (Queen, J., Conoco Inc, personal communication). Liu, Crampin and Queen (1991) also interpret shear-wave splitting observations,



	Parameters						$\Delta\tau$	$\Delta p$	$f(m,\tau^o,p^o)$	
Hudson	$CD$ 0.0551	$AR$ 0.0721	$CT$ 1(sat)			$\alpha$ -17°	$\beta$ -9°	0.97	2.32	1.64
Cijkl	$\Delta C_{11}$ 5.901	$\Delta C_{22}$ -17.244	$\Delta C_{44}$ -1.181	$\Delta C_{55}$ 0.709	$\Delta C_{13}$ -2.598	$\alpha$ -160°	$\beta$ -31°	1.086	2.39	1.74
Thomsen	$\delta$ 0.113	$\gamma$ -0.033	$\epsilon$ 0.050			$\alpha$ -154°	$\beta$ -41°	0.45	2.48	1.47

Table 4.7 - Results from GA inversion for the three different parametrization schemes with associated misfit values.

	Elastic Constants							$\Delta\tau$	$\Delta p$	$f(m, \tau^o, p^o)$
	$C_{11}$	$C_{22}$	$C_{44}$	$C_{55}$	$C_{13}$	$\alpha$	$\beta$			
Hudson	16.318	17.580	4.500	4.000	8.159	-17°	-9°	0.97	2.32	1.64
Cijkl	19.063	14.896	4.447	4.532	8.766	-160°	-31°	1.086	2.39	1.74
Thomsen	18.000	19.809	4.204	4.500	10.895	-154°	-41°	0.45	2.48	1.47

Table 4.8 - GA inversion results presented in a common format of elastic constants (in GPa) for a hexagonally anisotropic material with the axis of symmetry aligned along the  $x_1$  direction.

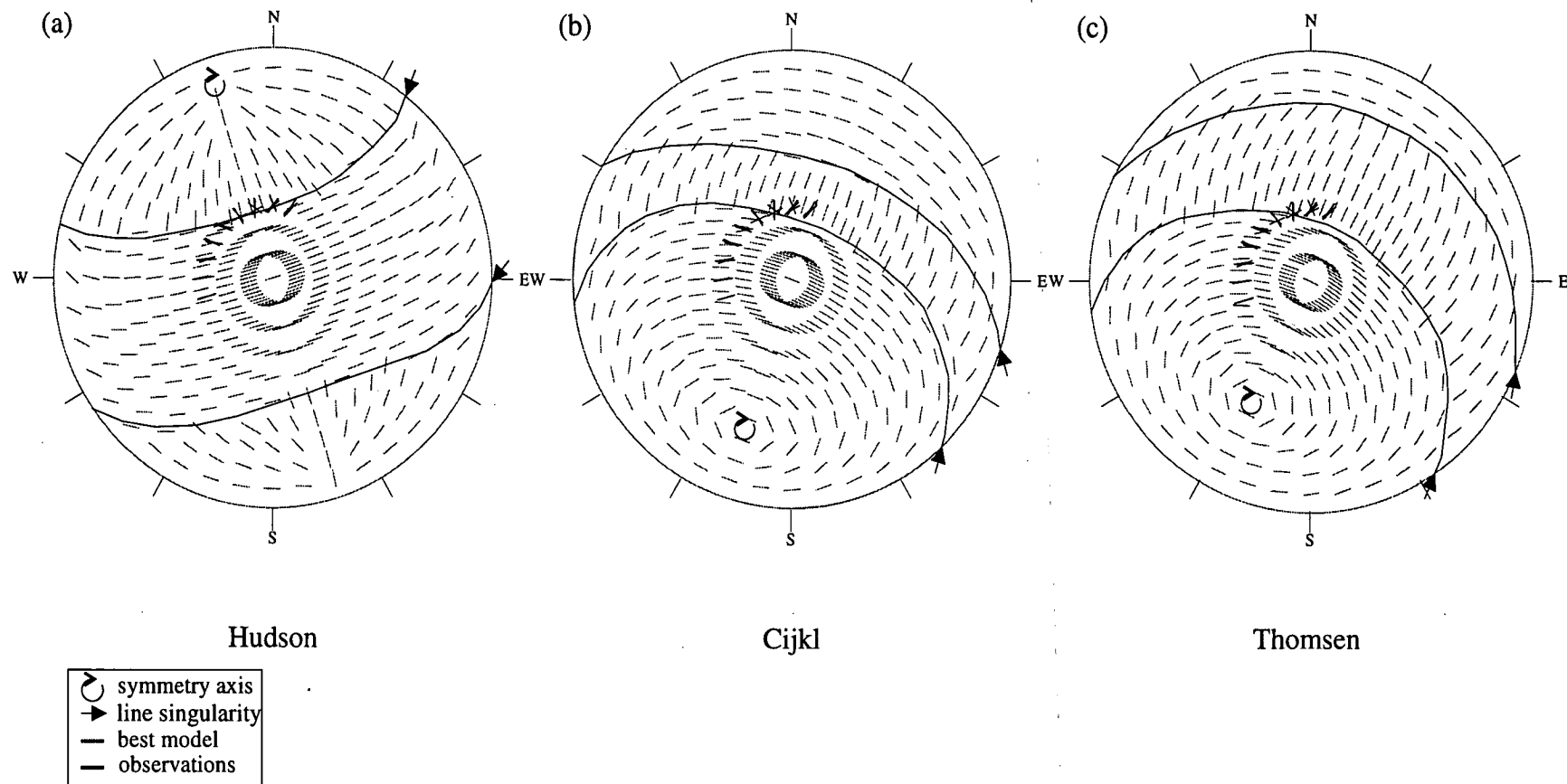


Figure 4.12 - Lower hemisphere equal-area plots showing the  $qS1$ -wave polarizations for downgoing propagation directions for the best models found by the GA using a) the Hudson, b) the Cijkl and c) Thomsen representations. Superimposed on these plots are the estimated  $qS1$ -wave polarizations from the AVSP experiment.

determined from reverse VSP and crosswell surveys at the CBTF, in terms of a sub-vertical crack-system. It would therefore seem plausible that the observed shear-wave anisotropy at the CBTF is consistent with a dipping fracture system.

Another interesting point to emphasise is that the shear-wave observations predicted by the best Hudson model correspond to propagation directions crossing a feature known as a line singularity. Line singularities exist for hexagonal symmetry systems where the two shear-wave velocity sheets intersect each other. For these directions the two shear wave sheets swap over so that there is an abrupt change in the  $qS1$ -wave polarization. In addition to this the time delays approach a minimum as the two shear waves become degenerate at the intersection of the shear-wave sheets. This behaviour can clearly be illustrated using lower hemisphere equal area plots showing the  $qS1$ -wave polarizations and cross-sections through the velocity sheets (Figure 4.13). The equal-area plot comparing the observed and the modelled  $qS1$ -wave polarizations show that the rapid changes in the  $qS1$ -wave polarization estimates are reproduced by the Hudson model as features of propagation near a line singularity (Figure 4.12). Furthermore, the modelled time delays approach a minimum for the source located at N150°E. This behaviour is in good agreement with the observed time delay estimates and is modelled as a feature of propagation near to a line singularity. Observations of shear-wave singularities have been previously reported (Douma *et al.* 1990, Bush 1990) but this is, I believe, the first study in which a quantitative approach has been adopted. This AVSP experiment is also unique in that, unlike other surveys, an unusually extensive azimuthal sample was used in the data acquisition. This reduces the ambiguity in the interpretation of the shear-wave splitting observations.

#### *Thomsen and Cijkl models*

The inversion results for the Thomsen and Cijkl parametrization schemes produce similar models in that the shear-wave behaviour is characterized by the elastic constant  $c_{44} < c_{55}$  (Table 4.8). For hexagonally anisotropic materials with the

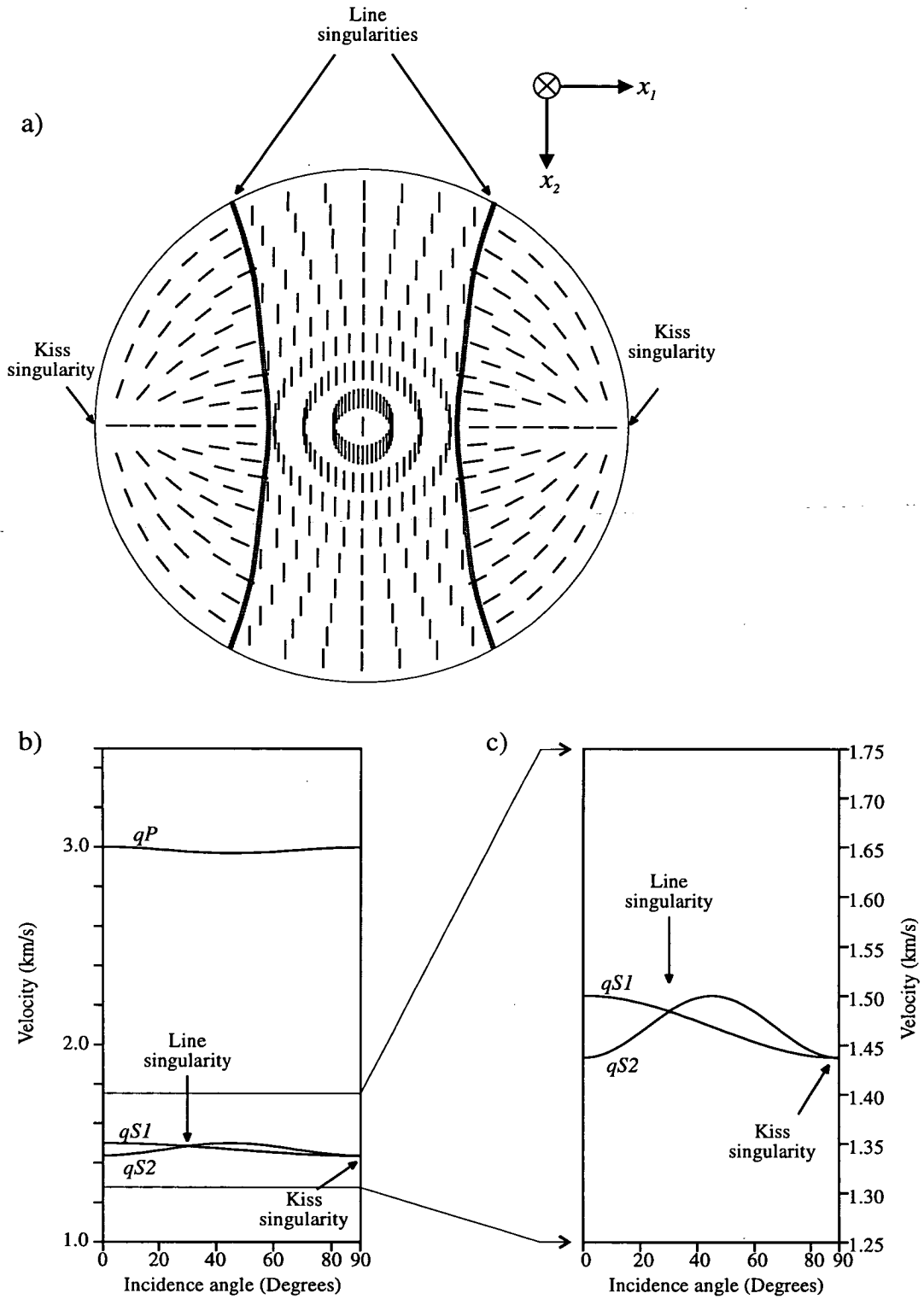


Figure 4.13 Behaviour of a hexagonally anisotropic material, a) shows a lower hemisphere equal-area plot showing the faster  $qS1$ -wave polarizations with the singularities identified. b) and c) show the velocity variation with incident angle through the line singularity for the plane of symmetry  $x_2=0$ .

symmetry axis aligned in the  $x_1$  direction the inequality of  $c_{44} < c_{55}$  implies that the fast shear-wave arrival for near-vertical directions sub-parallel to the  $x_3$  direction will be aligned in the plane containing the symmetry axis, as shown in Figure 4.14. This behaviour is particularly intriguing since if equivalent media of this type can be constructed from realistic fracture systems then the commonly used interpretation of the fast shear-wave polarization being parallel to the fracture strike will be wholly in error. Given the importance of such an implication I will now investigate whether such systems can be constructed for crack systems. Assuming that the Hudson model accurately reproduces shear-wave behaviour for a crack system we may relate the inequality of  $c_{44} < c_{55}$  to the crack parameters. The second-order formulations of Hudson can be written as

$$c = c^0 + c^1 + c^2 ; \quad (4.2)$$

where  $c$  are the equivalent anisotropic constants,  $c^0$  are the isotropic elastic constants of the background medium and  $c^1$  and  $c^2$  are the first- and second- order Hudson perturbations describing the crack inclusions (Hudson 1980). The first and second order perturbations for the elastic constants of  $c_{44}$  and  $c_{55}$  are

$$c_{55}^1 = -\epsilon \mu u_{33} ; \quad (4.3a)$$

$$c_{55}^2 = \frac{\epsilon^2}{15} \mu \frac{(3\lambda + 8\mu)}{(\lambda + 2\mu)} u_{33}^2 ; \quad (4.3b)$$

$$c_{44}^1 = c_{44}^2 = 0 . \quad (4.3c)$$

$\epsilon$  is the crack density,  $\lambda$  and  $\mu$  are the Lamé constants of the isotropic uncracked solid. The term  $u_{33}$  is defined by boundary conditions across the cracks, which for dry and fluid filled inclusions gives the result  $u_{33} = 16(\lambda + 2\mu) / 3(3\lambda + 4\mu)$ . Inserting these quantities into equation 4.2 the inequality,  $c_{44} < c_{55}$  can be reduced to

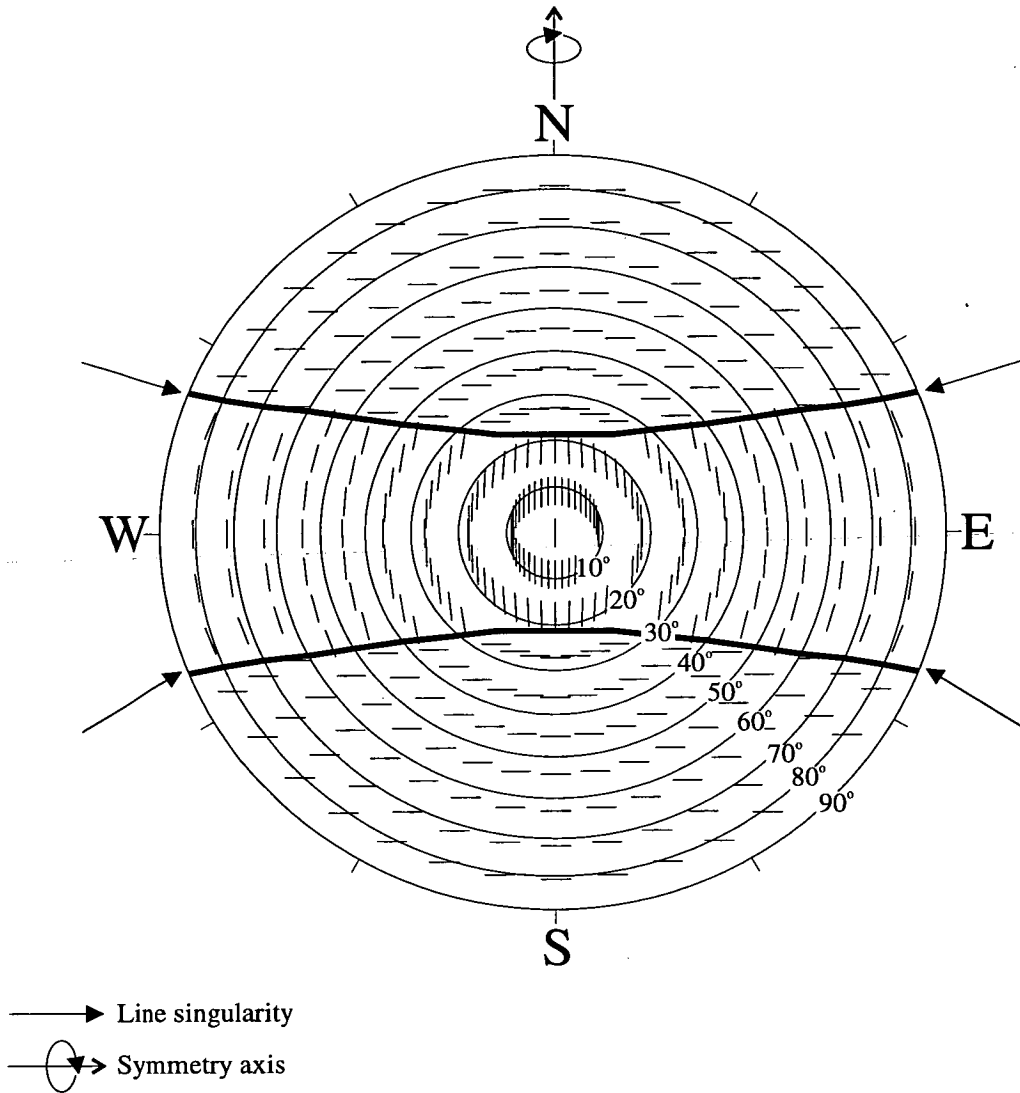


Figure 4.14 - A lower hemisphere equal-area plot showing the  $qSI$ -wave polarizations for a hexagonal symmetry system with the symmetry axis aligned north-south. For this material the elastic constants satisfy the inequality  $c_{44} < c_{55}$ . This defines a material for which the  $qSI$ -wave polarizations within the region bounded by the line singularity, indicated by the thick black line, are polarized in the plane containing the symmetry axis.

$$\eta > \frac{90 + 32\epsilon}{135 - 48\epsilon}; \quad (4.4)$$

where  $\eta$  is the square of the  $v_p$  to  $v_s$  ratio. This inequality is not satisfied for realistic values of  $\epsilon$  and  $\eta$ . Therefore the Hudson model is unable to reproduce the type of shear-wave behaviour exhibited by the best Thomsen and Cijkl models. Further confirmation of this result may be obtained using the Schoenberg-Muir decomposition (Schoenberg and Douma 1988). This technique allows the anisotropic elastic tensor to be decomposed into a combination of a fracture and a 'background' compliance. This method constructs a diagonal 3×3 fracture compliance matrix,  $Z$ , which for fractures aligned parallel to the  $x_2x_3$  plane is given by (Hood 1991)

$$z_3 = \frac{1}{c_{55}} - \frac{1}{c_{44}};$$

$$z_2 = \frac{1}{c_{66}} - \frac{2c_{13}}{c_{11}c_{23} - c_{12}c_{13}};$$

$$z_N = \frac{c_{23} - c_{13}}{c_{11}c_{23} - c_{12}c_{13}}.$$

The  $z_3$  term will be negative in the case that  $c_{44} < c_{55}$ . This violates the definition of the fracture compliance matrix,  $Z$ , to be positive definite so that materials of this type are unlikely to exist as a result of fracture induced anisotropy. Thus the inversion results given by the Thomsen and Cijkl parametrizations appear to be inconsistent with crack induced seismic anisotropy. An alternative interpretation for these results must be sought. Possible sources of the seismic anisotropy include fine layering or intrinsic anisotropy. Fine layering is unlikely to be a reasonable interpretation for the Thomsen and Cijkl inversion results. This is because the geology at the test site is essentially plane and uniform so that the non-vertical symmetry axis required by the

inversion results cannot be accounted for. Nonetheless I consider if equivalent media can be constructed due to fine layering that satisfy the inequality  $c_{44} < c_{55}$ . I use the fine layering formulations of Postma (1955) for which a hexagonally anisotropic medium can be constructed from the isotropic Lamé constants and thicknesses of two alternating layers. The relevant formulations, assuming the symmetry axis to be aligned along the  $x_1$  axis (for consistency), are

$$c_{44} = \frac{\mu_1 d_1 + \mu_2 d_2}{d_1 + d_2} \quad (4.5b)$$

$$c_{55} = \frac{(d_1 + d_2) \mu_1 \mu_2}{d_1 \mu_2 + d_2 \mu_1} ; \quad (4.5b)$$

where the subscripts identify the layers,  $d$  is the individual layer thickness. Substituting these into the inequality gives the following result

$$(\mu_1 - \mu_2)^2 < 0 . \quad (4.6)$$

Thus a fine layering medium cannot, according to Postma's equations, account for the model derived by the Thomsen and Cijkl inversion results. I now finally consider 'intrinsic' anisotropy as an interpretation of these results. Thomsen (1986) tabulates an extensive list of intrinsically anisotropic materials. Only four of the materials in this list satisfy the inequality  $c_{44} < c_{55}$ . These are two sandstone samples, a mudshale sample and quartz. Although the geology at the CBTF does partially consist of sandstones and mudshales a thin section analysis of core samples reveals that there is no preferential orientation of grain boundaries or long axes (Queen and Rizer 1990). It therefore appears that the best models obtained using the Thomsen and Cijkl parametrizations must be regarded as unlikely explanations for the observed shear-wave splitting from the AVSP experiment. In contrast the agreement between other independent information regarding the fracture orientations and the inversion result based on the Hudson scheme suggests that these results be considered in



greater detail.

### *Non-uniqueness*

Non-uniqueness is an important concept which needs to be addressed if any confidence is to be placed in inversion results. GA's are particularly useful in terms of addressing issues of non-uniqueness because of their global nature and their sampling bias towards the significant portions of the model space. The models sampled by the GA using the Hudson representation are shown in Figure 4.15 as a distance-misfit scatter plot (as described in Chapter 2) with the 'better' models plotted towards the top of the plot. As might be expected the sampled models do not define a single well resolved peak but several groups of solutions, labelled a to f in Figure 4.15(b), which rise above a background model space hypervolume for which  $f(m, \tau^0, p^0) > 2$ . The average model parameters and the lowest model misfit for each of the groups is given in Table 4.9. The solutions falling within group a correspond to models surrounding the best Hudson model found by the GA. Groups b and c comprise a single model with similar parameters, predicting a highly fractured dry crack system striking at N65°E and dipping approximately 30° from the vertical to the south east. Groups d and e also appear to be closely related to each other containing models describing a saturated crack system striking within the range N79°E to N89°E and dipping 8° to the south east from the vertical. The solutions within group f are dissimilar to those within the other groups in that it predicts a crack system striking at N285°E. It may be that this group represents a sub-optimal solution about the best models complimentary solution at N255°E which is to be expected because of mirror symmetry about the vertical plane. All of the solution groups, except f, predicted a crack dip of between 8° and 30° in the south east quadrant measured from vertical and a crack strike lying between N75°E and N90°E. The most significant discrepancy in the solution groups is between groups b and c, predicting dry cracks of high crack density and group a predicting a saturated crack model of moderate crack density. From other studies it is unusual to find crack densities as high as 0.10 except in the near surface and it has been suggested that

	Group a	Group b	Group c	Group d	Group e	Group f
$\langle CD \rangle$	0.054	0.119	0.127	0.053	0.0457	0.037
$\langle AR \rangle$	0.070	0.034	0.050	0.062	0.0413	0.059
$\langle CT \rangle$	1(sat)	0(dry)	0(dry)	1(sat)	1(sat)	1(sat)
$\langle \alpha \rangle$	-17°	-26°	-25°	-11°	-1°	-165°
$\langle \beta \rangle$	-8°	-30°	-25°	-9°	-8°	13°
$f_{min}(m, \tau^u, p^u)$	1.642	1.937	1.924	1.997	2.035	2.011

Table 4.9 - Mean parameter values and lowest group model misfit for the solutions identified in the distance-misfit scatter plots shown in Figure 4.15. These groups are for the Hudson parametrization of the model space.

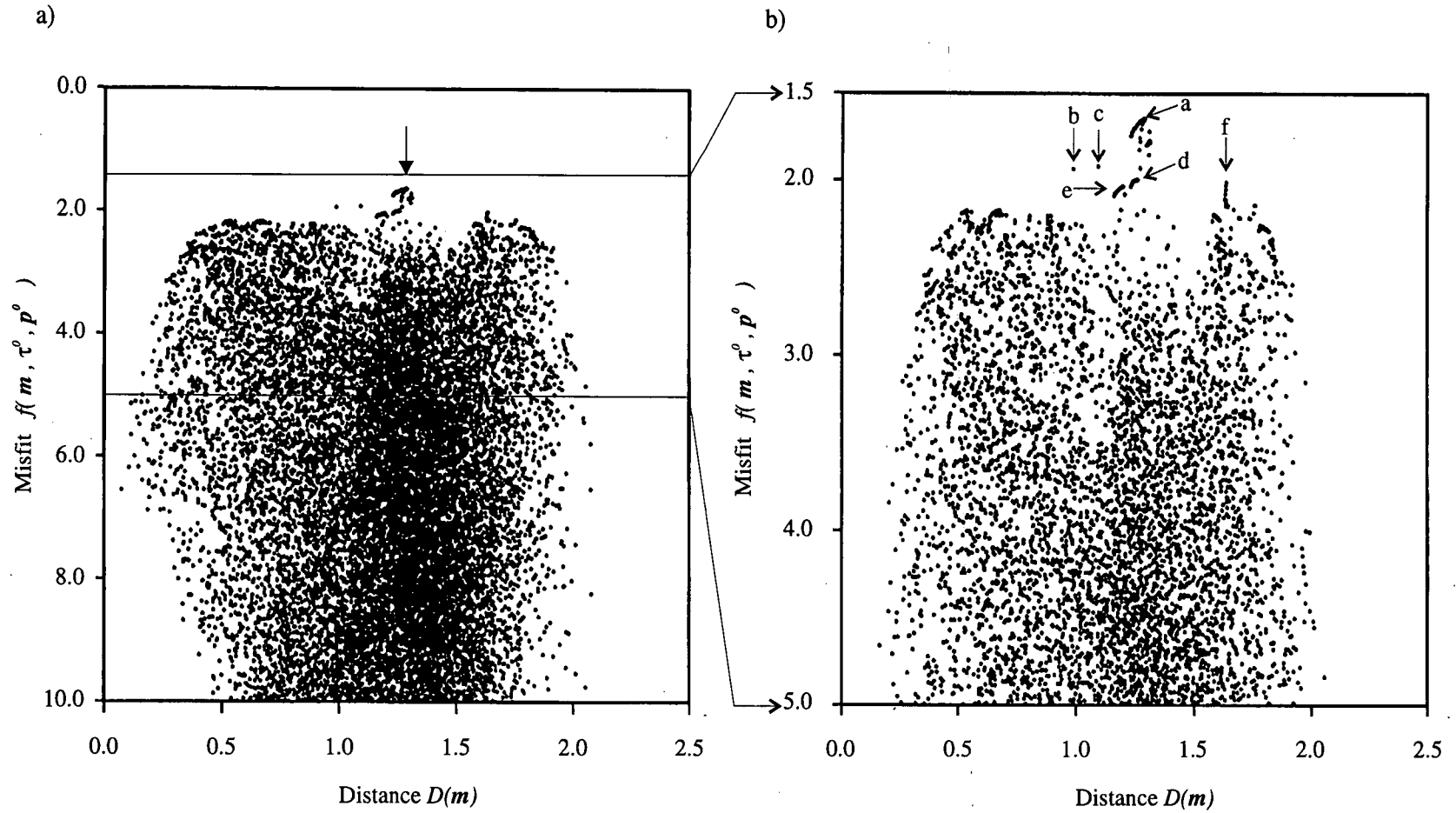


Figure 4.15 - Distance-misfit plots for the inversion of shear-wave observations from the AVSP experiment at the CBTF using the Hudson parameter representation, showing a) sampled models within the misfit range of 0 to 10 with the best solution found by the GA indicated by the arrow and b) models sampled within the misfit range  $f(m, \tau^o, p^o) = 1.5$  to 5.0 with different solution groups labelled from a to f (see text for explanation).

crack densities of 0.04 represent a critical bound for intact rocks (Crampin 1994). On the basis of these observations and the lower misfit presented by the models within group a, I select the best Hudson crack model given in Table 4.7 as the most probable interpretation for the observed shear-wave splitting observations.

#### 4.7 FULL-WAVEFORM MODELLING

To verify the results derived from the GA inversion for the dipping crack model I construct full-waveform synthetics using the ANISEIS package (Taylor 1990) which is based upon the reflectivity method (Kennett 1983). The most important difference between the full-waveform and forward modelling used in the GA is that a realistic depth varying structure is used. The model that I use is based upon an isotropic velocity and density model derived from shallow RVSP data and well logs from the neighbouring well 33-5. The anisotropic model is constructed using the equivalent media formulations of Hudson (1980) to simulate a hexagonally anisotropic media derived by the insertion of cracks with parameters based upon the solution derived from the GA. The resulting synthetic seismograms are analyzed using the same shear-wave estimation techniques applied to the field data.

A comparison of the shear-wave estimation results from the synthetic and field data are presented in Figures 4.16 and 4.17. To model accurately the time delay variations it necessary to increase the  $CD$  to 0.12 for the upper 130 m of the model and reduce it to 0.065 below this. This high  $CD$  value for the near surface is in agreement with other studies from the CBTF (Liu, Crampin and Queen 1991). The fracture orientation for the final refined model strikes at  $N74^{\circ}E$  and is rotated  $17^{\circ}$  from the vertical to the south east. This fracture orientation is in very good agreement with the reported fracture orientation observed in the shallow limestone formations at the site which is reported to be  $N75^{\circ}E$  and rotated approximately  $20^{\circ}$  to the south east from the vertical (Queen, J., Conoco Inc, personal communication). The modelling of the  $qSI$ -wave polarizations is extremely sensitive to the orientation of the fractures

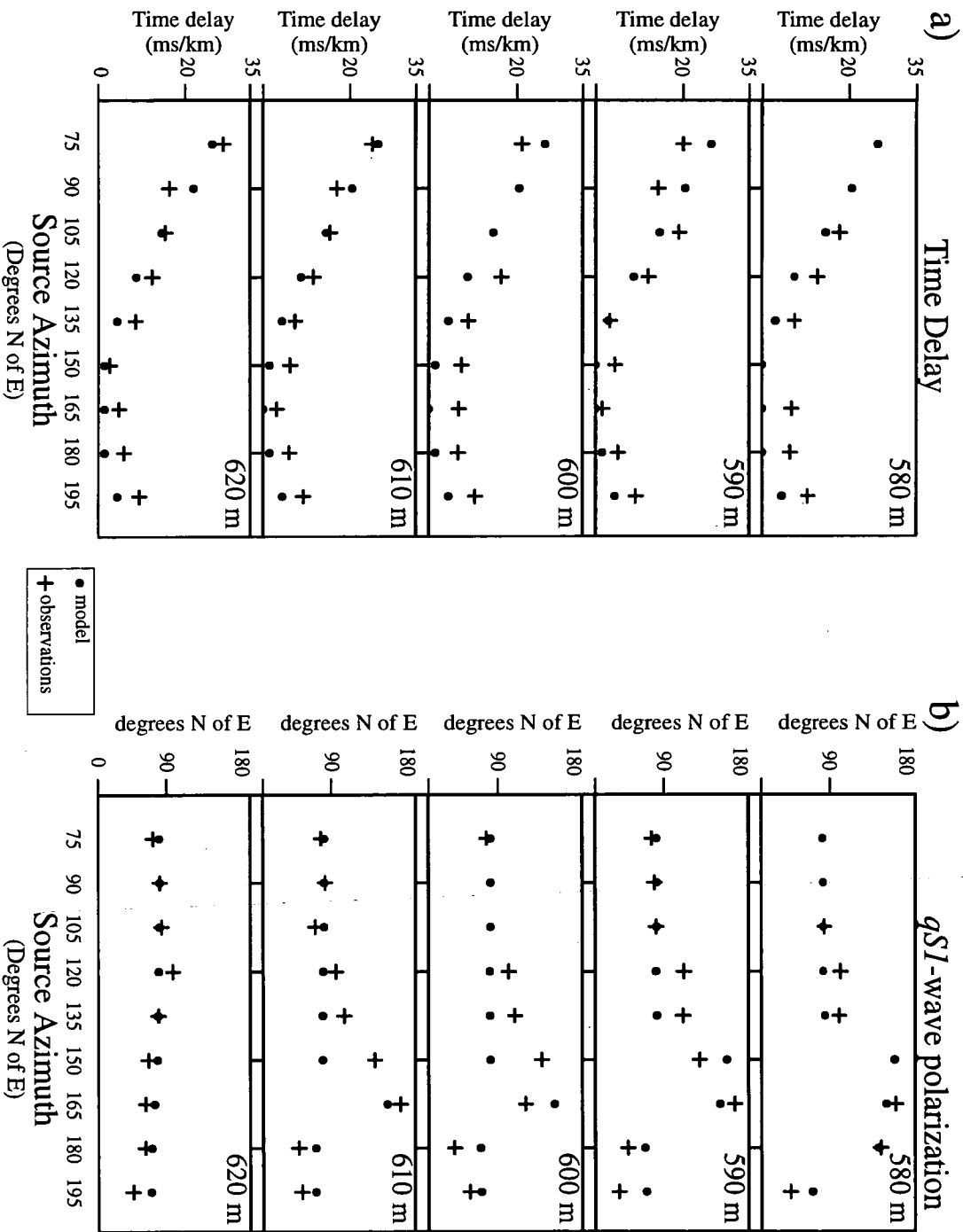


Figure 4.16 - Comparison of a) the estimated time delays and b) estimated *qSI*-wave polarizations for the field data from the AVSP and the full waveform synthetic modelling results for the dipping Hudson crack model.

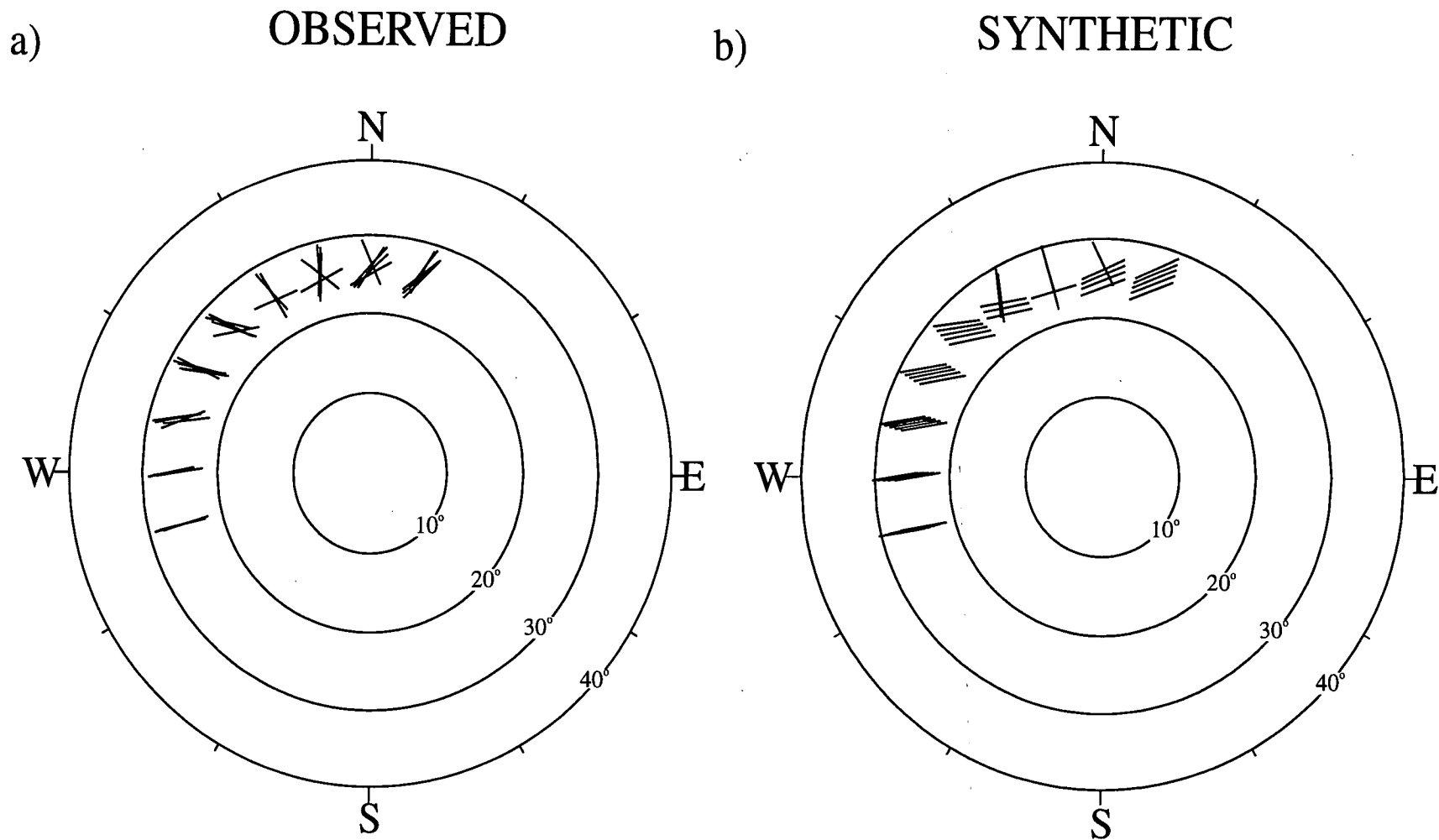


Figure 4.17 - Lower hemisphere equal-area plots showing the estimated  $qS1$ -wave polarizations for a) the field data and b) the synthetic full waveform modelling results for the dipping crack model.

and rotational increments of  $0.25^\circ$  about the final model are necessary to achieve a final satisfactory match. This is because the model observations correspond to features of a line singularity whereupon there is an rapid change in the  $qSI$ -wave polarizations with propagation direction. The velocity structure introduces a small but noticeable effect in the synthetic shear-wave polarizations whereby they are slightly rotated towards radial direction. This effect is due to the layering within the model and is significant since this improves the match between the observed and synthetic  $qSI$ -wave polarizations. Thus this model is, in effect, a weakly monoclinic equivalent media due to the combination of the dipping fractures and horizontal layering.

#### 4.8 INVERSION RESULTS: ORTHORHOMBIC SYMMETRY

To complete this case study I now consider the possibility of the lower symmetry class of orthorhombic materials as a possible explanation for the observed shear-wave splitting behaviour. As for the hexagonal inversion I use three parametrizations which are

- 1) Thomsen/Hudson scheme defined for vertical Hudson cracks inserted into a hexagonal material with a vertical symmetry axis defined by Thomsen parameters
- 2) the sum of three sets of Thomsen parameters each individually defining hexagonal symmetries with mutually orthogonal symmetry axis as ,

$$c^{orth} = 4 c^0 - c(\delta_1, \gamma_1, \epsilon_1) - c(\delta_2, \gamma_2, \epsilon_2) - c(\delta_3, \gamma_3, \epsilon_3) ;$$

where  $c^{orth}$  defines the elastic constants for an orthorhombic medium and  $c^0$  indicates the isotropic material. Elastic constants for media possessing hexagonal symmetry with the symmetry axis aligned in the  $x_i$  direction are defined by the elastic constants  $c(\delta_i, \gamma_i, \epsilon_i)$ .

3) the deviation of the nine elastic parameters defining an orthorhombic medium from the isotropic values (as described in equation 3.7)

As for the hexagonal inversions the GA is applied in the minimization of equation 4.1 using the different parametrization schemes given in Tables 4.10, 4.11 and 4.12. The best orthorhombic models found by the GA are shown in Table 4.13. These solutions are of a lower misfit than those obtained for the hexagonal inversions. This is not unexpected because of the extra degrees of freedom introduced by the additional parameters required to define an orthorhombic material. The inversion schemes using the Thomsen/Hudson combination and Thomsen parameters converge to solutions with similar misfits of approximately 0.75. The Cijkl inversion result produces a model with a misfit of 1.176 although some experimentation in the GA parameters is required to achieve satisfactory convergence. The best model misfit is 0.71 and is found using the Thomsen/Hudson parametrization scheme.

The best model derived from the Thomsen/Hudson parametrization predicts a near vertical saturated crack system striking N72°E with a crack density of 0.03 and aspect ratio of 0.06. The hexagonal system defined by the Thomsen parametrization, into which the Hudson cracks are embedded, is essentially a weak TIV material. This TIV model can be interpreted in terms of an equivalent media composed of fine layering since Postma's inequality, which is conveniently expressed as  $\epsilon > \delta$ , is satisfied (Thomsen 1986). The  $qSI$ -wave polarizations for this model exhibit polarization swings around the source azimuths of N150°E and N165°E (Figure 4.18). In the orthorhombic case these swings are associated with a point singularity where the two shear-wave velocity sheets touch over a small range of propagation directions. For these directions there is a rapid change in polarization directions and time delays approach zero. This result offers an alternative interpretation to that given by the dipping Hudson crack model predicted by the hexagonal inversion scheme. Shear-wave estimates from synthetic modelling studies based upon the



Thomsen/Hudson Parametrization Scheme				
Parameter		$P^L$	$P^U$	$N_{int}$
Crack Density	$CD$	0.0001	0.1271	128
Aspect Ratio	$AR$	0.0001	0.1271	128
Content	$CT$	0	1	2
Delta	$\delta_3$	-0.2201	+0.2201	128
Gamma	$\gamma_3$	-0.2201	+0.2201	128
Epsilon	$\epsilon_3$	-0.2201	+0.2201	128
Alpha	$\alpha$	-180.0	0.0	128
(Degrees)				
Beta	$\beta$	-45.0	45.0	128
(Degrees)				

Table 4.10 -The discretization scheme for the Thomsen/Hudson parametrization of model space.  $\alpha$  and  $\beta$  are rotations of the orthorhombic material about the  $x_3$  and  $x_2$  axes respectively. Hudson's second order formulations are used to simulate an equivalently hexagonally anisotropic material. This parametrization defines a total of  $2^{50}$  ( $1.1 \times 10^{15}$ ) models.

Cijkl Parametrization Scheme			
Parameter	$P^L$	$P^U$	$N_{int}$
$\Delta C_{1111}$ ( $\Delta C_{11}$ )	-30.0	+30.0	128
$\Delta C_{2222}$ ( $\Delta C_{22}$ )	-30.0	+30.0	128
$\Delta C_{2323}$ ( $\Delta C_{44}$ )	-30.0	+30.0	128
$\Delta C_{1313}$ ( $\Delta C_{55}$ )	-30.0	+30.0	128
$\Delta C_{1133}$ ( $\Delta C_{13}$ )	-30.0	+30.0	128
$\Delta C_{3333}$ ( $\Delta C_{33}$ )	-30.0	+30.0	128
$\Delta C_{1212}$ ( $\Delta C_{66}$ )	-30.0	+30.0	128
$\Delta C_{1122}$ ( $\Delta C_{12}$ )	-30.0	+30.0	128
$\Delta C_{2233}$ ( $\Delta C_{23}$ )	-30.0	+30.0	128
Alpha $\alpha$ (Degrees)	-180.0	0.0	128
Beta $\beta$ (Degrees)	-45.0	45.0	128

Table 4.11 -The discretization scheme for the elastic constant parametrization of model space. The  $\Delta C_{ijkl}$  refer to the % deviations of the elastic constants from the isotropic material,  $\Delta C_{ijkl} = [ C^{orth}_{ijkl} - C^{ISO}_{ijkl} ] / C^{ISO}_{ijkl} \times 100$ . The  $\Delta C_{ij}$  in brackets give the alternative condensed 2 index Voigt notation of the elastic tensor. This defines a model space of  $2^{77}$  ( $1.5 \times 10^{23}$ ) models.

Thomsen Parametrization Scheme			
Parameter	$P^L$	$P^U$	$N_{int}$
Delta <sub>1</sub> $\delta_1$	-0.2201	+0.2201	128
Gamma <sub>1</sub> $\gamma_1$	-0.2201	+0.2201	128
Epsilon <sub>1</sub> $\epsilon_1$	-0.2201	+0.2201	128
Delta <sub>2</sub> $\delta_2$	-0.2201	+0.2201	128
Gamma <sub>2</sub> $\gamma_2$	-0.2201	+0.2201	128
Epsilon <sub>2</sub> $\epsilon_2$	-0.2201	+0.2201	128
Delta <sub>3</sub> $\delta_3$	-0.2201	+0.2201	128
Gamma <sub>3</sub> $\gamma_3$	-0.2201	+0.2201	128
Epsilon <sub>3</sub> $\epsilon_3$	-0.2201	+0.2201	128
Alpha $\alpha$	-180.0	0.0	128
Beta $\beta$	-32.0	31.0	128

Table 4.12 -The discretization applied to the orthorhombic Thomsen parametrization scheme. This parametrization defines a total of  $2^{70}$  ( $1.2 \times 10^{21}$ ) models.

	Parameters										$\Delta\tau$	$\Delta p$	$f(m, \tau^o, p^o)$
Thomsen/ Hudson	$CD$ 0.03	$AR$ 0.06	$CT$ sat	$\delta_3$ -.05	$\gamma_3$ .03	$\epsilon_3$ -.01				$\alpha$ -18°	$\beta$ 1°	.46 .96	0.71
Cijkl	$\Delta C_{11}$ 6.85	$\Delta C_{33}$ 1.18	$\Delta C_{44}$ 1.18	$\Delta C_{55}$ 0.71	$\Delta C_{13}$ 9.69	$\Delta C_{22}$ -14.4	$\Delta C_{66}$ 10.63	$\Delta C_{12}$ -7.32	$\Delta C_{23}$ -4.02	$\alpha$ -9°	$\beta$ 8°	.42 1.9	1.2
'Thomsen'	$\delta_1$ .11	$\gamma_1$ -.07	$\epsilon_1$ .10	$\delta_2$ -.11	$\gamma_2$ -.01	$\epsilon_2$ -.20	$\delta_3$ .05	$\gamma_3$ .01	$\epsilon_3$ .05	$\alpha$ -20°	$\beta$ -29°	.47 1.1	0.77

Table 4.13 - Results from GA inversion for the three different parametrization schemes with associated misfit values for the orthorhombic inversions.

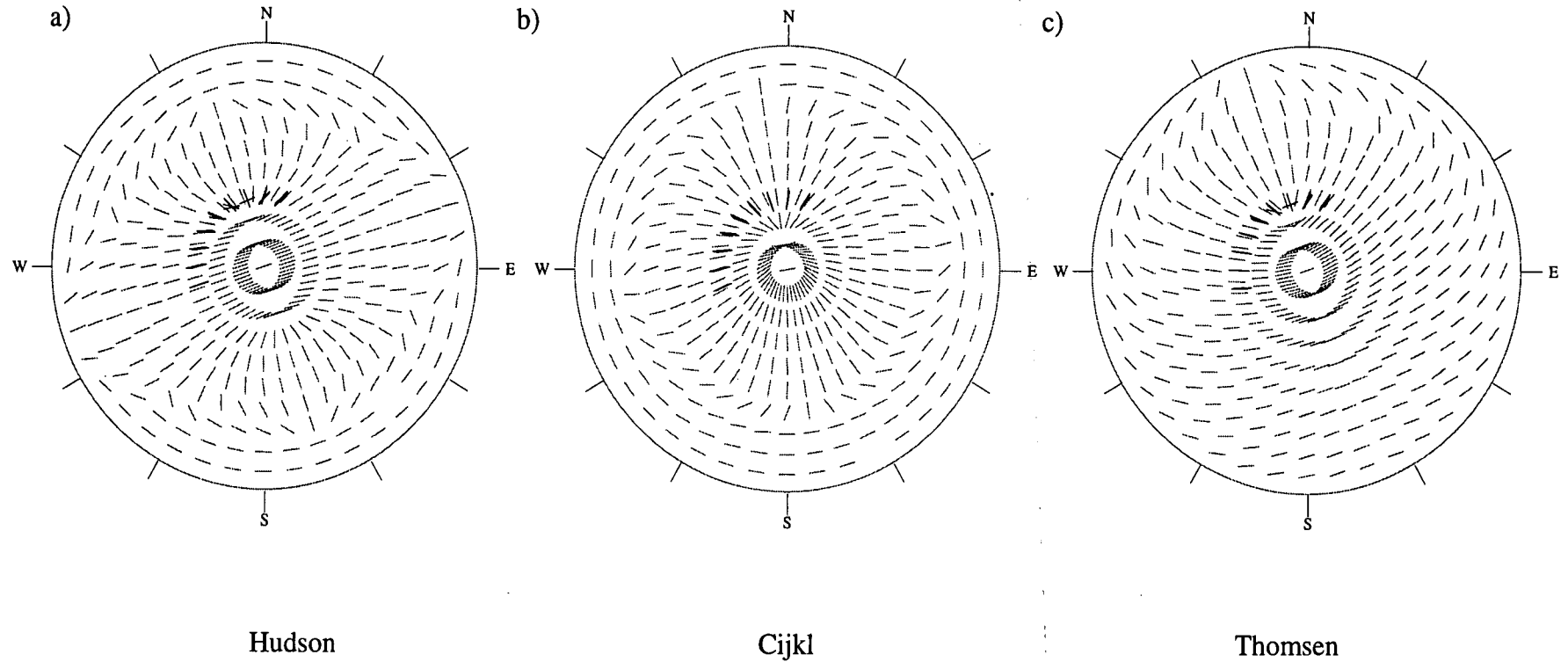


Figure 4.18 - Equal-area plots showing the  $qSI$ -wave polarizations over a hemisphere of propagation directions for the optimal models derived from the GA inversion using the a) Hudson/Thomsen b) Cijkl and c) Thomsen parameter sets. Superimposed on these equal area plots are the model observations shown in black (not the field observations).

Thomsen/Hudson result are shown in Figures 4.19 and 4.20. To achieve a satisfactory match between the estimation results from the synthetic seismograms and the field observations the crack density is increased to 0.04 and the Thomsen  $\epsilon$  parameter is decreased to  $\epsilon=-0.05$ . Thus the final model uses a saturated vertical crack system striking N72°E embedded into a weakly elliptically anisotropic TIV medium defined by the Thomsen parameters  $\delta=-0.05$   $\epsilon=-0.05$  and  $\gamma=0.03$ . This model is unable to reproduce the polarization variations observed on the source azimuths N150°E and N180°E. However, the abrupt changes in shear-wave polarizations for the source azimuth N165°E and the minima in time delay observations are reproduced in this synthetic model as a feature of a point singularity.

The Thomsen parametrization is difficult to interpret although if the  $\epsilon_1$ ,  $\gamma_1$  and  $\delta_1$  are associated with a crack system the best model once again suggests a dipping crack system striking N71°E and rotated 30° from the vertical to the south east. However, there are no reports of fabrics aligned in the two complimentary orthogonal directions required by the inversion results. The relatively poor performance of the GA for the Cijkl parametrization scheme is reflected in the large misfit value and suggests that the best model may not represent an optimal solution. In view of this I do not consider these results further. Of the three inversion schemes the most realistic model is given by the Thomsen/Hudson parametrization scheme.

#### 4.9 CONCLUSIONS AND DISCUSSION

In this chapter I have applied an inversion process based upon a GA to shear-wave splitting observations recorded from an AVSP. The inversion results predict a dipping fracture system which is used as a starting point for full-waveform modelling of the field data. The fracture orientation of the final refined model is in very good agreement with observations from the test site. This study suggests that the fracture dip may be resolved if an appropriate geometry is used. However, the results of an orthorhombic inversion suggest an alternative interpretation based upon a combination

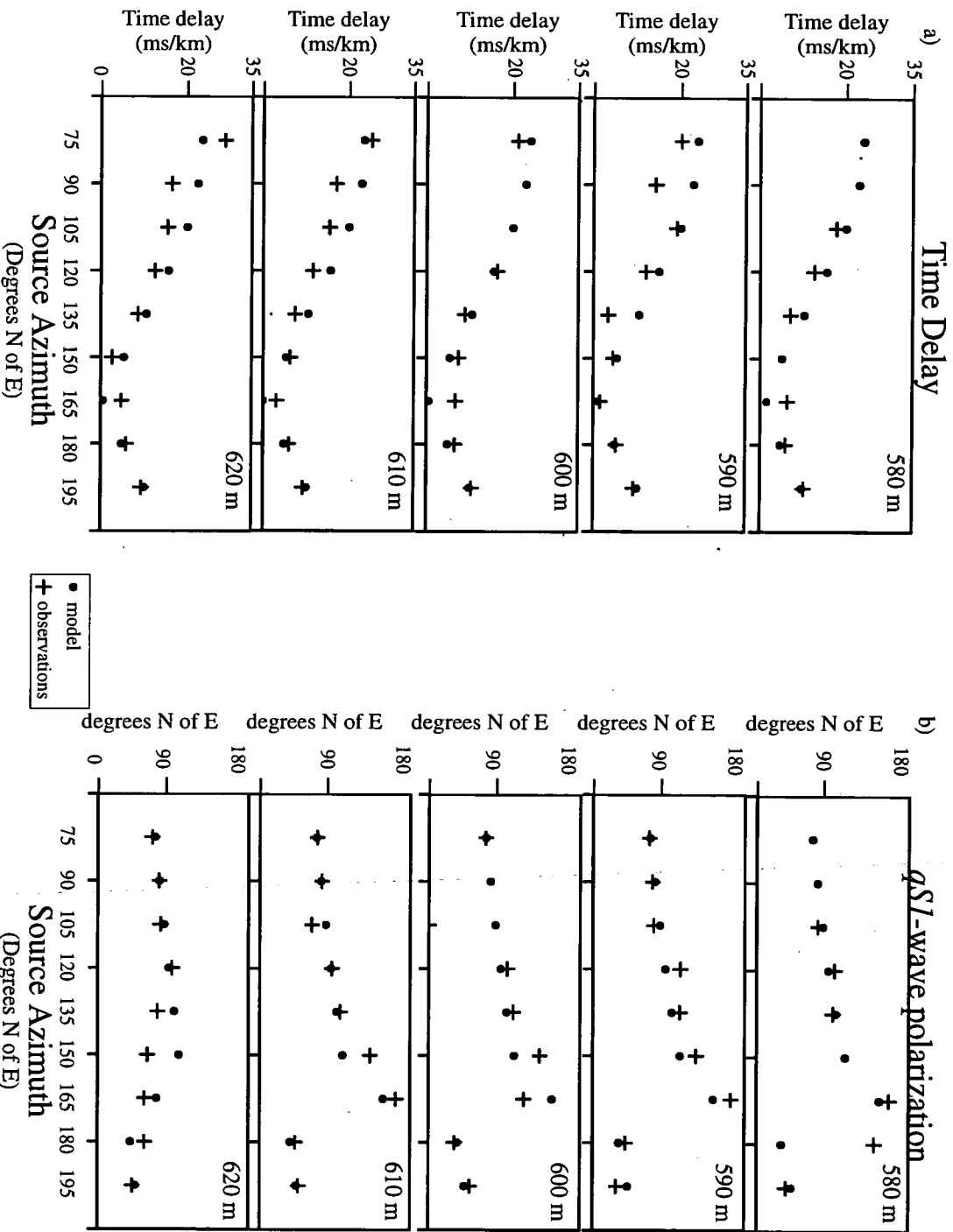
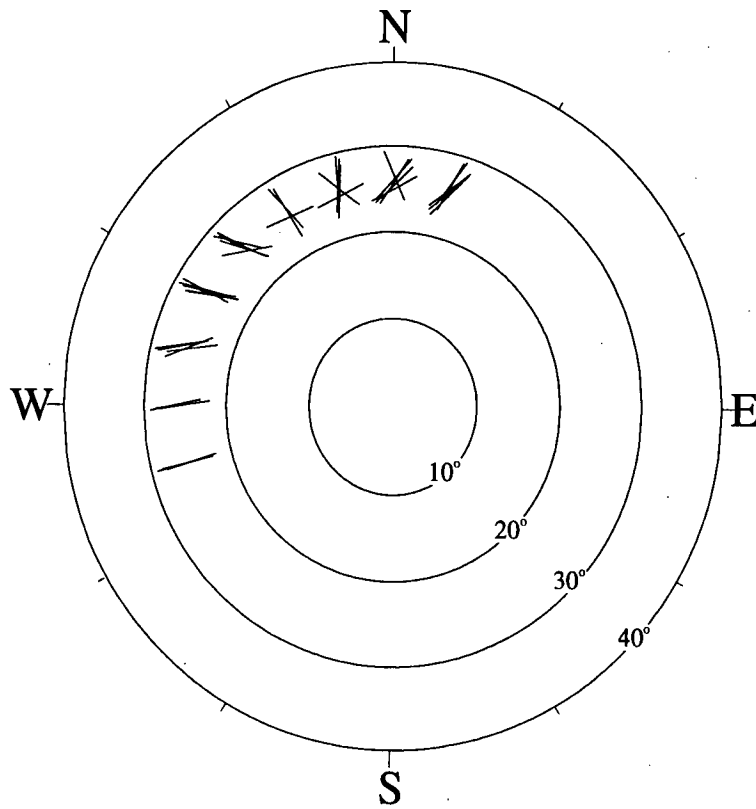


Figure 4.19 - Comparison of shear-wave estimates of a) the time delays and b) the  $qS1$ -wave polarizations for the AVSP field data and the full waveform synthetic for the Thomsen/Hudson orthorhombic model.

a)

## OBSERVATIONS



b)

## SYNTHETICS

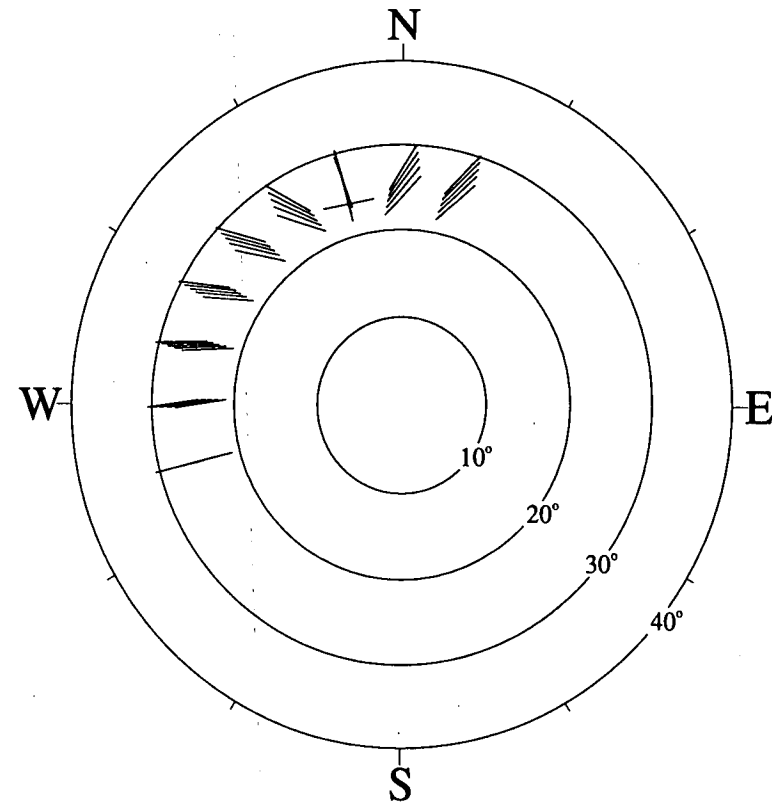


Figure 4.20 - Lower hemisphere equal-area plots showing the estimated  $qSI$ -wave polarizations for a) the field data and b) the synthetic results for the Thomsen/Hudson orthorhombic model.



of fine layering and vertical fracturing. Given the limited angular coverage used in the experiment it is difficult to resolve this ambiguity. A possible offset VSP configuration to clarify this non-uniqueness using two sources located along diametrically opposite azimuths about the well and shooting to common geophone levels may prove suitable (Figure 4.21). In the case that the fracture system is vertical the recorded shear-wave splitting response will be identical for the two source azimuths (in the absence of any lateral variations). However, for non-vertical fracture sets there will be an asymmetric response in the shear-wave splitting estimates, providing the source azimuths are not coincident with the fracture strike. Although the maximum asymmetry will be exhibited at azimuths perpendicular to the fracture strike this choice will be unsuitable for two reasons. Firstly these azimuths are planes of symmetry for which there is a decoupling of the velocity sheets so that the response is determined by a subset of the elastic constants. Thus the information content along these directions decreases thereby limiting any interpretation of the symmetry class of the system. Secondly, it is common practice to record shear-wave surveys with sources aligned along the in-line and cross-line directions which results in pure  $SH$  and  $SV$  energy in a symmetry plane. This implies that there will be no off-diagonal energy in the multicomponent survey and estimation techniques may prove to be unreliable in these cases (MacBeth *et al.* 1993). In the next chapter I will show how two near-offset VSPs which nearly satisfy most of these acquisition requirements can be used to resolve the ambiguity relating to the fracture dip.

This study has also identified a singularity which is indicated in the field data by abrupt changes in the  $qSI$ -wave polarization direction and a systematic decrease in time delays. This behaviour can be reproduced in forward modelling and heavily constrains the fracture orientation of the best solution. This result reinforces the conclusions of Bush (1990) who suggested that the observation of singular behaviour may help to constrain any interpretation of the shear-wave anisotropy.

The GA has proven to be an effective tool for the shear-wave splitting inversion

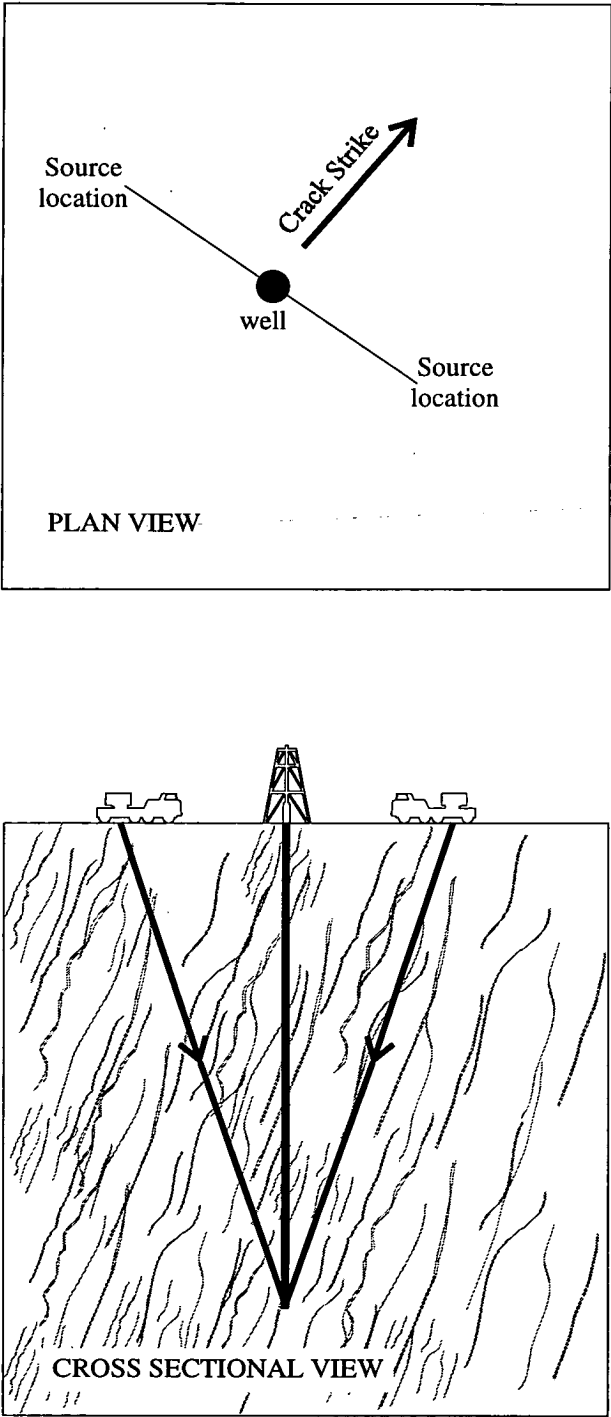


Figure 4.21 - A schematic diagram showing an opposite azimuth VSP survey which may be used to detect fracture dip

problem. The application of the GA highlighted a previously unconsidered solution of non-vertical fracturing which was found to be consistent with field observations and previous studies. This agreement was confirmed after the inversion had been applied. Application of the GA prior to full-waveform modelling also allowed a significant saving in time. This is readily demonstrated by comparing the forward modelling computational requirements of the GA and the full-waveform reflectivity method used to find the final refined model. The full waveform modelling required approximately 4 hours per model whereas the GA search requires 2 hours during which approximately 4000 models are sampled. Although refinement is necessary to achieve a satisfactory match with the field data the best model found by the GA is sufficiently close to justify the approximations applied in the GA's forward modelling.

The GA is sensitive to the choice of parametrization scheme. This is probably because the underlying GA search process relies upon the processing of low order schemata, the so called 'building block hypothesis'. Thus parametrizations which construct a more favourable arrangement of the schemata will show superior convergent behaviour. This implies that care must be taken in application of GA since they cannot be treated as 'black box' optimization routines.

## CHAPTER 5

### NEAR-OFFSET VSP INVERSION

#### 5.1 INTRODUCTION

In the previous chapters I have shown how a GA may be applied to the inversion of seismic data for anisotropic parameters. However, the usefulness of these inversions have been limited by the approximations involved with the forward modelling. Specifically, the assumption of a homogeneous anisotropic material is not generally useful and a more flexible approach is required allowing a spatial variation in the anisotropic parameters. To attempt inversions of this kind requires sophisticated forward modelling methods which, in general, are too computationally expensive to be included into a Monte Carlo type inversion scheme. In this Chapter I design an efficient forward modelling approach based on a ray tracing algorithm which is fast enough to be included into a GA. The ray tracing GA inversion is applied to two VSP experiments from the Conoco Borehole Test Facility (CBTF). The inversion results support the interpretation of a dipping fracture model which is suggested from the inversion of data obtained from the Azimuthal VSP (AVSP) experiment described in the previous chapter. I now consider forward modelling methods which may be applied to the more general case of spatially varying anisotropic structures and in the context of their suitability for inclusion to the GA based inversion.

#### 5.2 FORWARD MODELLING TECHNIQUES

Wave propagation in anisotropic media is considerably more complicated than for the isotropic case. Perhaps the most fundamental complication arises from the existence of three distinct body waves propagating with different velocities and polarizations. These form an orthogonally polarized set which is not generally coincident with the dynamic axes and, except for symmetry directions, cannot be described in terms of

$P$ ,  $SH$  and  $SV$  wavetypes. This implies that each body wave impinging on an interface from an isotropic to an anisotropic medium may excite three transmitted body waves. Thus there is a possibility of nine conversions compared with five for the isotropic case.

Another important distinction between wave propagation in isotropic and anisotropic media arises from the deviation between the group and phase velocities. In general, the energy that is recorded in field experiments is associated with the group velocity as the source is represented as a point source. Another significant difference between the isotropic and anisotropic case is that out-of-plane deviations of seismic energy may be expected even when the incident wave propagates in a plane orthogonal to the interface. This phenomenon arises because of the necessary conservation of tangential components of slowness which for an anisotropic media are a function of the propagation direction. For these reasons wave propagation in anisotropic media is not a trivial matter and all forward modelling methods to a greater or lesser extent use approximations. I now review some of these forward modelling methods and their associated approximations and assumptions.

#### *Propagator matrix and reflectivity method*

The propagator matrix method uses matrices which connect stress-displacement vectors across welded interfaces within a stacked layer model. Problems arise with this technique due to a loss of precision because of exponential terms in the propagator matrices. The reflectivity method is essentially a refinement of the propagator matrix technique avoiding the uncontrolled growth of these exponential terms (Kennett 1983). This is achieved by a factorization separating the wave field into up- and down-going parts. A similar approach to the propagator matrix method is then used to construct the reflectivity response for a sequence of layers. Although the propagator matrix and reflectivity methods may be used to compute full-wave synthetic seismograms, approximations are often made to avoid the large cost involved with a comprehensive summation over frequency and slowness. For

example, summations over azimuthal slowness may be restricted to a few planes and an interpolative scheme applied for intermediate values. Furthermore, it is important to emphasise the restriction imposed by the plane layered stack model which is implicit to the formulation of both the propagator matrix and reflectivity techniques.

### *Finite difference*

These schemes solve a representation of the elastic wave equation in which the partial differentials are rewritten as finite differences. The model is represented in terms of homogeneous elements. The finite difference equation is applied to the discretized model subject to some initial boundary conditions. The model response is then extrapolated in time by iteratively solving the finite difference equation. This type of scheme is particularly suited to a massively-parallel computational architecture so that each model element can be assigned to a single processor. Although finite difference schemes can be applied to realistic earth models some errors exist in the calculation of the phase and group velocities (Igel, Mora and Riollet 1993).

### *Ray tracing*

This is a high-frequency approximation which effectively follows the advance of a plane wavefront through a structure by application of Snell's Law. This statement is true for wave propagation in both isotropic and anisotropic media although Snell's Law needs some reformulation for the anisotropic case (Helbig 1994). Ray tracing in continuous anisotropic media essentially requires the integration of six coupled differential equations (Červený 1972). These may be solved in a variety of ways for example, using Runge Kutta (Li, Leary and Aki 1990) or finite difference methods (Pereya, Lee and Keller 1980). Although ray tracing schemes are fast, efficient and may be applied to complex heterogeneous three dimensional structures, considerable errors may be introduced for singular regions (Gajewski and Pšenčík 1990). It should also be remembered that ray tracing implicitly assumes plane wavefronts so that the calculations are for the phase rather than the group velocities.

GAs typically sample several thousands of models during a search so that any forward modelling scheme requiring any more than a couple of seconds becomes prohibitively expensive in computational time. This implies that most of the forward modelling techniques discussed previously must be discounted for inclusion in the inversion scheme. Of these methods, the ray tracing method presents the most attractive option in terms of flexibility and computational expense. However, further concessions are still required if such a scheme is to be included in the GA inversion.

### 5.3 RAY TRACING

The ray-tracing method is a very general technique which may be applied to complicated three dimensional heterogeneous anisotropic models. There will clearly be a tradeoff between the computational speed and the model complexity. It is therefore possible to decrease significantly the computational time by increasing the model simplicity. For this reason I approximate the models to be a one dimensional stack of plane layers. A further increase in speed can be achieved if out-of-sagittal plane deviations are neglected. This reduces the ray tracing method to a root searching problem as a function of one variable. This second approximation will be valid in the case of weak anisotropy or in the case that the propagation plane is a plane of symmetry.

The concept that underlies ray tracing in both isotropic and anisotropic media is the conservation of the tangential components of slowness at an interface, as described by Snell's Law. In the case of a horizontally plane-layered model this implies that the horizontal components  $p_x$  and  $p_y$  are the quantities conserved at the interfaces. In the isotropic case the vertical component of slowness is simply given by  $p_z = (1/v_{iso} - p_x^2 - p_y^2)^{1/2}$ . However, for the anisotropic case the velocity is a function of the propagation direction which complicates matters considerably. In the case of triclinic symmetry the vertical components of slowness,  $p_z$ , can be derived by the solution of a sextic equation. However, the use of this equation is to be avoided because of the

numerical imprecision associated with roundoff errors (Fryer and Frazer 1987) and the complexity of the coefficients. A considerable simplification is achieved if the medium possesses a monoclinic or a higher symmetry with a horizontal plane of symmetry. In this case the slowness equation may be written in terms of a cubic, the three roots of which are simply the squares of the vertical slowness,  $p_z$ ,

$$a_3 P_z^3 + a_2 P_z^2 + a_1 P_z + a_0 = 0 ; \quad (5.1)$$

where  $P_z = p_z^2$  and the coefficients  $a_0$ ,  $a_1$ ,  $a_2$  and  $a_3$  are functions of the horizontal slowness components and the elastic constants. It is also possible to rewrite this equation in terms of the horizontal slowness,  $p_h$ , defined as  $p_x = p_h \cos(\theta)$  and  $p_y = p_h \sin(\theta)$ , so that

$$b_3 P_h^3 + b_2 P_h^2 + b_1 P_h + b_0 = 0 ; \quad (5.2)$$

where  $P_h = p_h^2$  and the cubic coefficients  $b_3$ ,  $b_2$ ,  $b_1$  and  $b_0$  are functions of the vertical slowness and the elastic constants. Equations 5.1 and 5.2 suggest that a further factorization is possible and I rewrite the equations in terms of a matrix operation which benefits computational efficiency

$$\mathbf{Q} \mathbf{A} \mathbf{P} = 0 ;$$

where  $\mathbf{Q}$  is the row vector of the vertical slownesses  $(P_z^3 \ P_z^2 \ P_z^1 \ 1)$ ,  $\mathbf{P}$  is the column vector of horizontal slownesses  $(P_h^3 \ P_h^2 \ P_h^1 \ P_h \ 1)^T$  and  $\mathbf{A}$  is a lower diagonal  $3 \times 3$  matrix which is a function of the elastic constants only (for a complete description of  $\mathbf{A}$  and its derivation see Appendix A.)

An alternative approach that I also use to solve the slowness equation is to initially construct a table of slowness curves before implementing the ray tracing algorithm. Intermediate values of slowness can be derived by the application of interpolation methods. This approach has the advantage that a horizontal plane of symmetry need not be assumed, as is the case with the analytical slowness equations,



but it should be noted that out of plane deviations are still neglected and a loss of precision may be involved with the interpolation approach. Horizontal and vertical slowness are calculated for a range of incidence angles between vertical and horizontal directions in the sagittal plane by solution of the Kelvin-Christoffel equation. Care must be taken in the choice of incidence angles used in the interpolation scheme since the derivatives of the slowness curve will be sensitive to the horizontal slowness sampling interval. For example, if the slowness curve is sampled with equi-spaced angles then the errors in the derivatives will increase for horizontal propagation directions. A more appropriate scheme is to calculate the incremental change in the incidence angle so that the horizontal slowness is sampled at approximately equal intervals. Thus starting at vertical incidence with a velocity given as  $v_0$  the angular increment,  $d\theta$ , will be given as

$$d\theta \approx \frac{p_h(\theta=90^\circ)}{N-1} \frac{v_0}{\cos(\theta)};$$

where  $N$  is the number of horizontal slowness intervals. I find that satisfactory results are obtained using a cubic-spline interpolation routine with the slowness curves calculated at 16 angles.

These two approaches, the analytical or interpolative, are employed in the ray tracing algorithm to calculate the vertical slowness component of a transmitted wave for a given horizontal slowness. The horizontal and vertical slownesses define the propagation direction within the layer. In this way the ray may be traced through a stack of layers for a trial value of horizontal slowness. The ray is terminated after it has travelled a horizontal distance corresponding to the source-geophone distance. The ray tracing algorithm therefore searches over the horizontal slowness parameter for a ray which connects the source and geophone. This is achieved using a shooting method whereby an initial course scan is performed over the horizontal slowness to bracket the solution. The horizontal slowness for the connecting ray is then refined using standard numerical procedures (Press *et al.* 1992).

Care must be taken when applying Snell's Law at each interface to ensure that there is continuity between the incident and transmitted shear waves. This implies that the body waves must be separated according to the polarization of the wavetype. For materials with hexagonal symmetry this can be achieved as one of the shear waves is entirely independent of the two other wavetypes (Musgrave 1970) so that it is possible to distinguish the two shear-waves by application of the equality,

$$\rho v^2 - c_{44}m^2 - c_{66}n^2 = 0 ;$$

$$m^2 = 1 - n^2 ;$$

where the symmetry axis is aligned along the  $x_1$  direction,  $n$  is the direction cosine in the  $x_1$  direction and  $v$  is the velocity of the shear-wave.

#### 5.4 VERIFICATION OF RAY TRACING METHOD

To test my ray tracing algorithm  $qP$ ,  $qS1$  and  $qS2$  travel times and  $qS1$ -wave polarizations are calculated and compared with results derived from synthetic seismograms constructed using the full-waveform reflectivity method. The test structure is based upon a model which has previously been used in the evaluation of numerical modelling packages (Thomsen 1989). The Anisotropic Modelling Collaboration (AMC) model is a plane horizontally layered structure with the anisotropy based upon vertical cracks striking along the  $x_2$  direction for all the layers. The elastic constants vary as a function of depth simulating changes in  $v_p$ ,  $v_s$ , density and crack density (Table 5.1). The AMC model was used to compare synthetic modelling results from different anisotropic forward modelling packages. The transmission survey is based upon a VSP experiment using 30 geophone levels with an inter-geophone spacing of 100 m with the shallowest geophone at 100 m. The source is offset 500 m from the wellhead along an azimuth  $45^\circ$  to the crack strike. This VSP geometry is shown in Figure 5.1.

Elastic Constants (GPa)					Density (g/cm <sup>3</sup> )	Thickness (m)	Comments
$c_{11}$	$c_{22}$	$c_{44}$	$c_{55}$	$c_{13}$			
36.33	36.33	11.36	11.36	13.62	2.151	500	Isotropic
36.84	39.93	12.41	11.89	13.58	2.232	500	$CD=0.02$
41.55	41.55	12.93	12.93	15.68	2.314	500	Isotropic
33.98	41.59	16.54	12.00	12.49	2.395	500	$CD=0.10$
43.56	47.19	14.66	14.05	16.39	2.477	100	Anisotropic gradient
43.95	47.65	14.80	14.18	16.57	2.477	100	
44.37	48.10	14.94	14.31	16.74	2.477	100	
44.79	48.55	15.08	14.45	16.92	2.477	100	
45.20	49.00	15.22	14.58	17.10	2.477	100	
45.62	49.45	15.36	14.71	17.27	2.477	500	$CD=0.02$

Table 5.1 - Elastic constants, densities and thicknesses of the constituent layers for the AMC model.

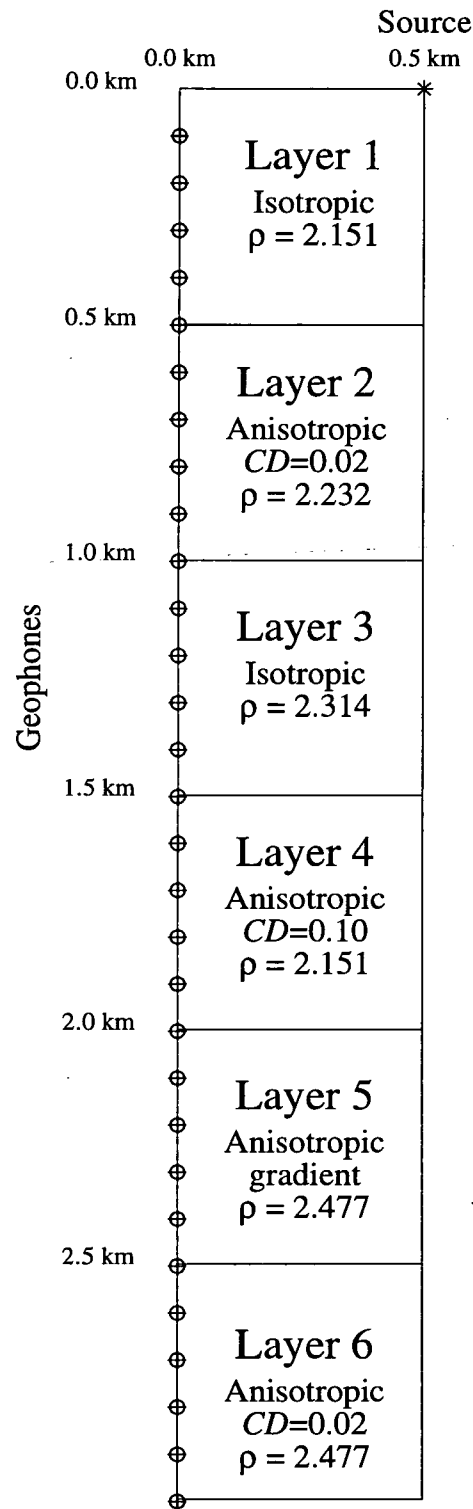


Figure 5.1 - A schematic illustration showing the AMC model and offset VSP acquisition geometry used to test the ray tracing algorithm. The asterisk denotes the source location and the crossed circles the geophone locations.

Full-waveform synthetic seismograms are constructed for the AMC model using the reflectivity method (Taylor 1990) and are shown in Figures 5.2 and 5.3. Overlain on these seismograms plots are lines corresponding to the predicted arrival times of the  $qP$ ,  $qS1$  and  $qS2$  wave modes calculated using the ray tracing algorithm. I used an antisymmetric pulse centred about the time  $t_0$  defined by the function

$$f(t) = \sin[\omega(t-t_0)] e^{-\frac{\omega|t-t_0|}{d}} ;$$

where  $\omega$  is the angular frequency and  $d$  is a damping factor. The parameters used are  $\omega=40\pi$  rad s<sup>-1</sup> (20 Hz) and  $d=3$ .

The radial components of the seismograms recorded with in-line and vertical forces are shown in Figure 5.3 allowing a more detailed examination of the arrivals. The first set of seismograms shown in Figure 5.3(a) is chosen since the shear-wave energy is dominant for this combination of source polarization and geophone component. The lines representing the two shear-wave arrivals noticeably diverge after the 14 geophone level (1.4 km) indicating shear-wave splitting. The two shear-waves continue to separate and the final trace indicates significant splitting approximately equal to one period of the source wavelet. Figure 5.3(b) shows the radial component recorded with the vertical source so that the  $qP$  arrivals now dominate the seismograms. There is good agreement between the results obtained using the reflectivity and ray tracing results for all the  $qP$  and  $qS1$  and  $qS2$  arrivals. Further confidence may be placed in the ray tracing algorithm when time delays and  $qS1$ -wave polarizations are compared for the two methods. Shear-wave estimation techniques are applied to the full waveform synthetic seismograms to extract the shear-wave splitting parameters, the results are shown in Figure 5.4. Overlain in this figure are the predicted shear-wave splitting results calculated from the ray tracing modelling. Time delay and  $qS1$ -wave polarization estimates obtained from the two methods show good agreement below the 10 th geophone level (1.0 km). The results above this level are not in agreement and require further explanation. The shear-

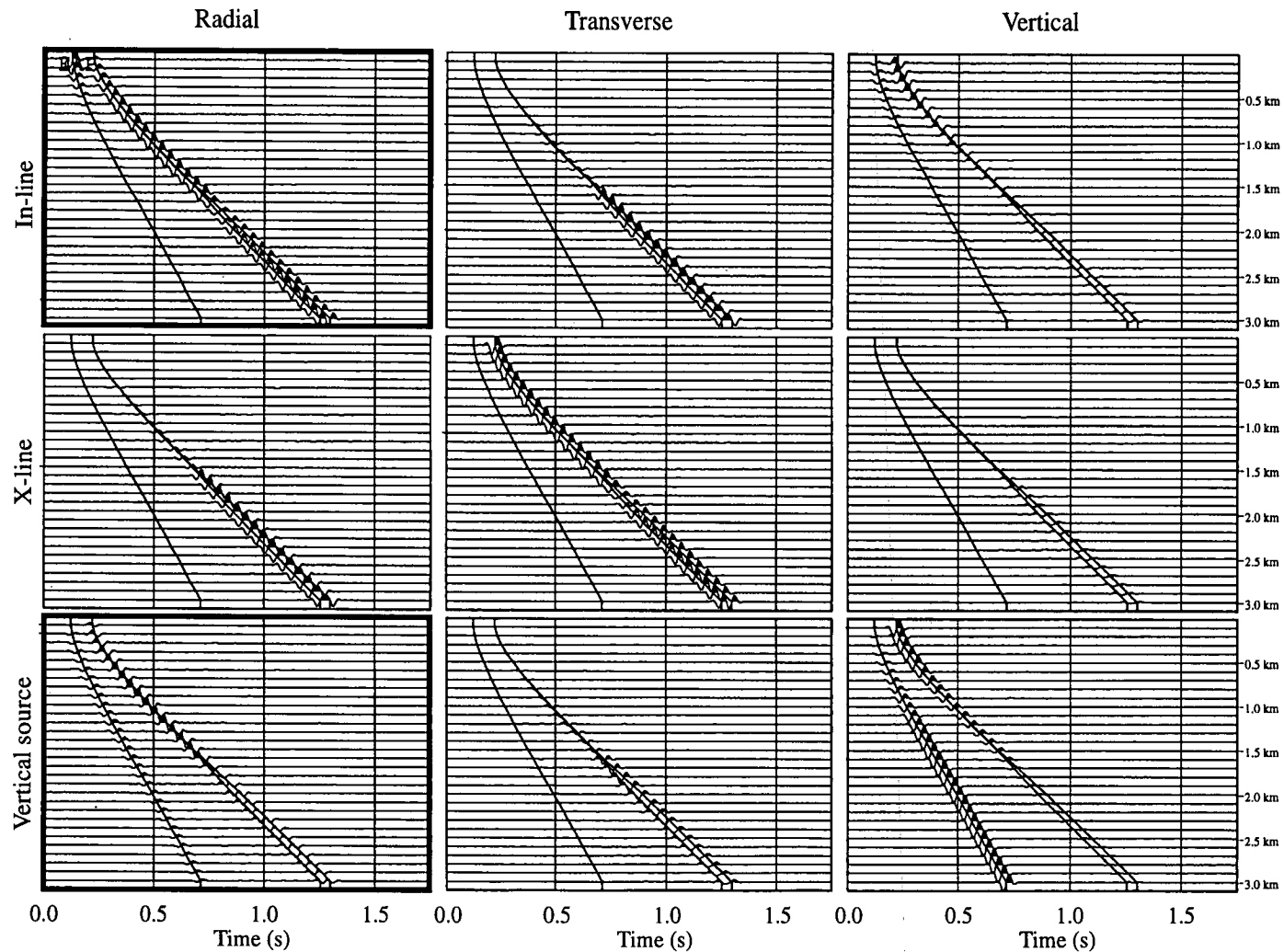


Figure 5.2 - Multicomponent display of synthetic seismograms for the AMC model generated by the reflectivity method overlain with curves corresponding to the  $qP$ ,  $qS1$  and  $qS2$  arrival times calculated using the ray tracing algorithm described in the text. Plots outlined in thick black are shown in detail in Figure 5.3.

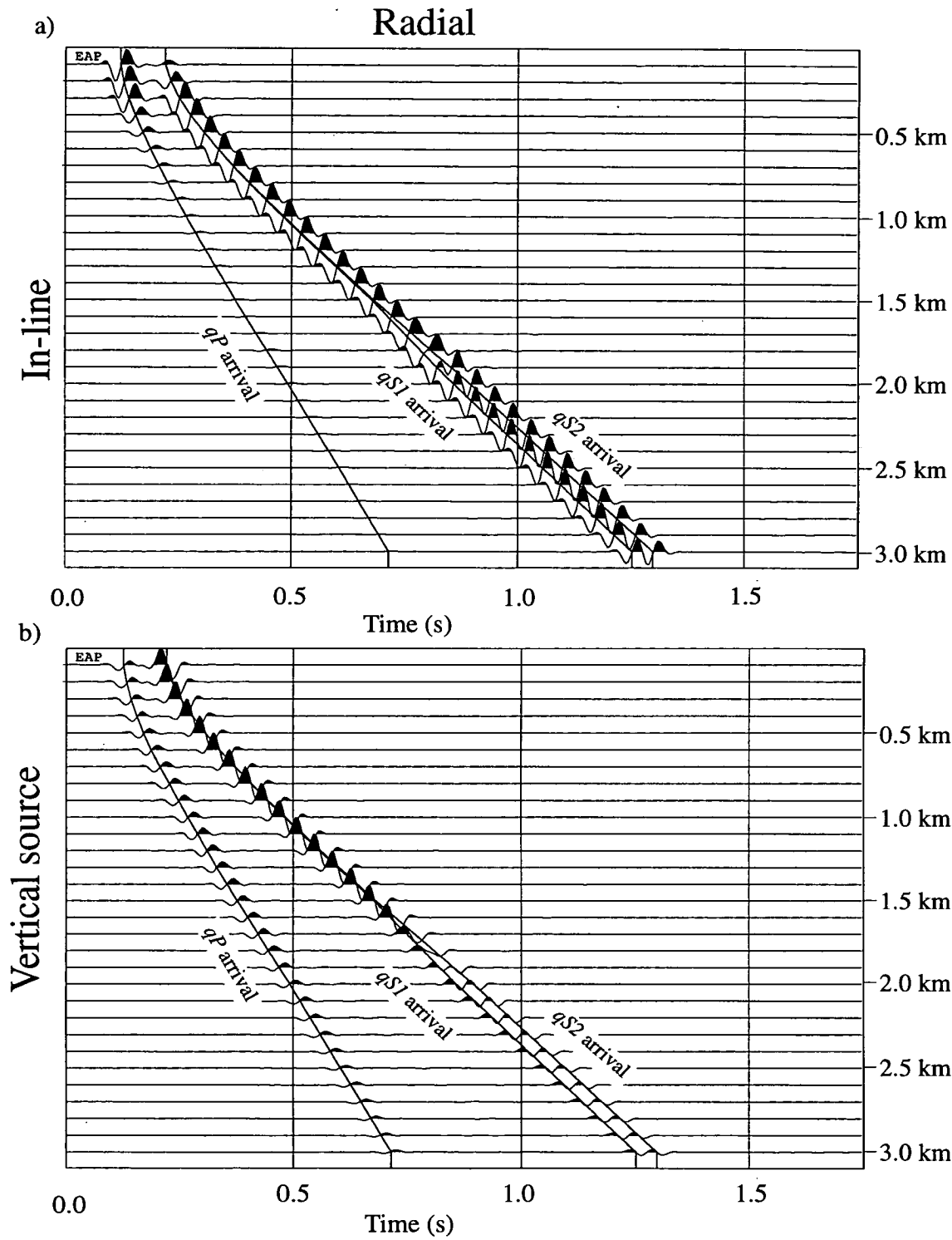


Figure 5.3 - Synthetic seismograms calculated using the reflectivity method for the radial geophone component overlain with arrival time curves calculated by the ray-tracing algorithm described in the text for a) the in-line horizontal source and b) the vertical source.

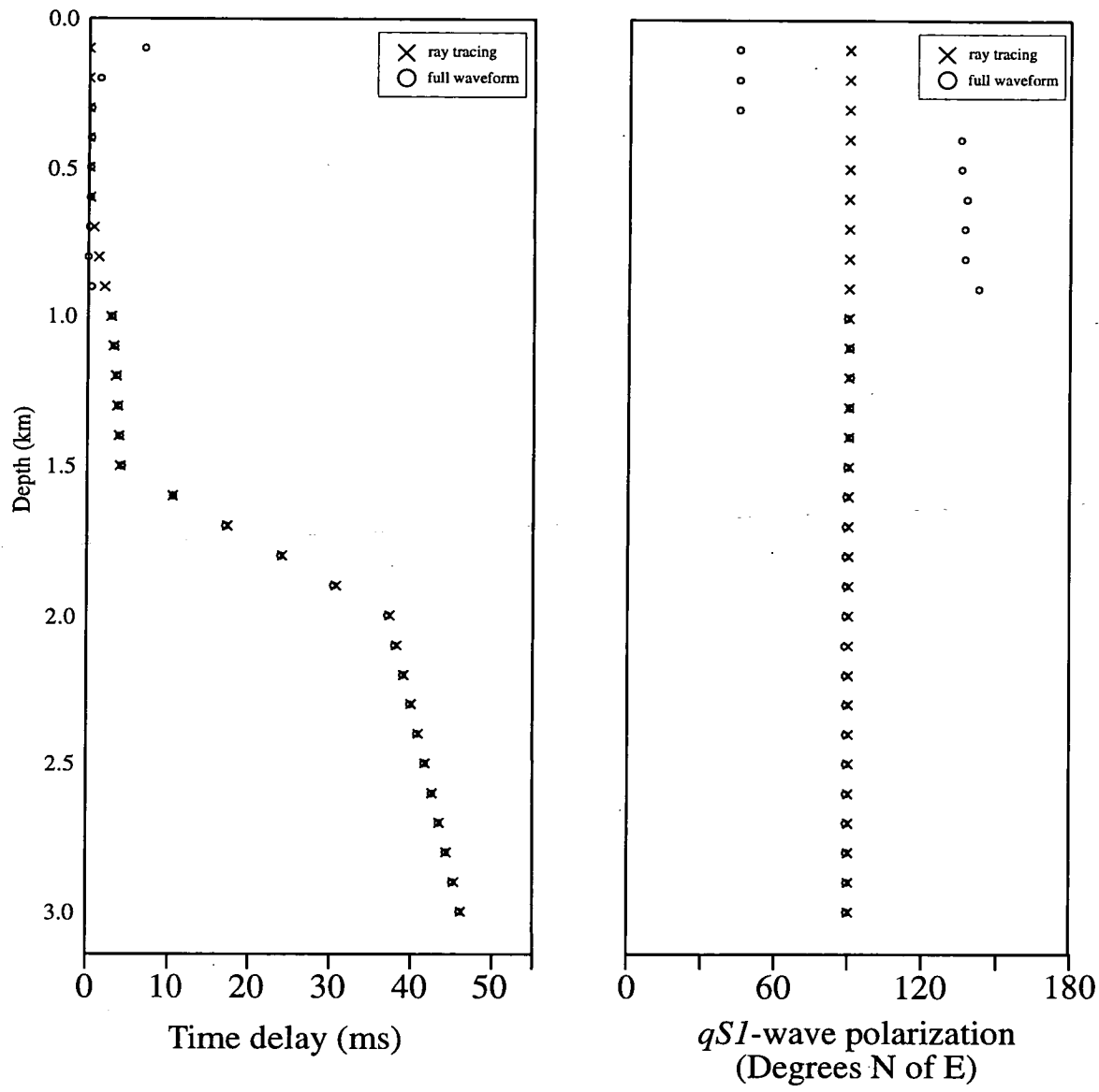


Figure 5.4 - A comparison of shear-wave splitting parameters for the AMC model derived from the full-waveform synthetic seismograms (circles) and the ray tracing algorithm (crosses).



wave estimation results from the full waveform synthetics for the first five levels are incorrect since time delays are predicted even though the shear-waves are propagating through an isotropic layer. This inaccuracy may arise because of inhomogeneous surface waves contaminating the shear-wave arrivals. Alternatively, the inaccuracy may be due to source imbalancing for these near horizontal raypaths at these shallow levels. For these depths the in-line source essentially generates *P*-wave energy (Figure 5.3). The poor agreement in the shear-wave splitting estimates between the 6<sup>th</sup> (600 m) and 9<sup>th</sup> (900 m) geophone levels correspond to small time delays for which shear-wave estimation techniques are inaccurate. In conclusion, the ray tracing results show good agreement with those obtained using the full waveform synthetics indicating that my ray tracing method is accurate.

## 5.5 APPLICATION TO FIELD DATA

The ray tracing algorithm is incorporated into the GA which I then apply to inverting shear-wave splitting observations from two near-offset VSP experiments. The near-offset VSP experiments were shot about two different wells within 1 km of each other at the CBTF. Although the acquisition geometries are essentially the same, the azimuth along which the sources were located are approximately diametrically opposite. Shear-wave estimation techniques are applied to the two datasets and the resulting polarization and time delay estimates are inverted.

The inversion procedure I will adopt is similar to that used for the AVSP inversion described in Chapter 4, with the important difference that the ray tracing algorithm allows the modelling of a depth dependent anisotropic structure. The velocity structure at the CBTF is split into eighteen isotropic layers based upon lithological, well log and VSP data. A model vector is used to describe a perturbation which is applied to this initial isotropic model to construct an anisotropic model for which shear-wave splitting parameters are calculated using the ray tracing method. The geology of the test site is previously described in Chapter 4 (section 4.2).

## 5.6 NEAR-OFFSET VSP ACQUISITION GEOMETRIES

I will identify the two near-offset VSPs as the 33-1 VSP and the Peel VSP, referring to the two wells about which the experiments were shot. The Peel well is located approximately 740 m to the south east of well 33-1 (Figure 5.5). The acquisition geometries for these two experiments are similar in terms of the incidence angles sampled but the azimuthal propagation directions sampled correspond to almost diametrically opposite raypaths. The importance of information obtained along such opposite azimuths will become apparent and will be discussed in relation to vertical and non-vertical crack systems. A summary of the acquisition geometries and the source and receiver parameters is given in Tables 5.2 and 5.3. Plan views of both VSP acquisition geometries are shown in Figure 5.6.

### *33-1 VSP*

A vibroseis source truck was located 36 m (120 ft) along the azimuth N279°E relative to the well 33-1. The vibroseis source was operated in in-line, cross-line and vertical directions. Seismograms were recorded at 50 levels between depths of 152 m (500 ft) and 887 m (2910 ft) using a constant geophone spacing of 15 m (50 ft). The horizontally-polarized vibroseis source was downswept through a frequency range of 51 to 6 Hz whereas the vertically-polarized vibrator was downswept through a range of 102-12 Hz.

### *Peel VSP*

In this experiment the vibroseis source trucks were sited 65 m (210 ft) from the well Peel along the azimuth N122°E. In-line and cross-line shear-wave sources and a vertical *P*-wave source were used to excite seismic energy which was recorded at 44 equi-spaced depth levels between 306 m (1003 ft) and 951 m (3120 ft). The horizontally polarized vibrators were downswept from 60 Hz to 7 Hz. The vertically polarized vibrator was downswept from 150 Hz to 7 Hz.

**Sources**Shear vibrators  $\times 2$ 

Sweep	51 - 6 Hz
Azimuth	279°
Offsets	36 m, 30 m

Compressional vibrator

Sweep	102 - 12 Hz
Azimuth	279°
Offset	39 m

**Recording Parameters**

Sweep length	30 s
Record length	32 s
Taper	0.5 s
Sample Interval	2 ms

**Downhole Sonde** DESCO 3-C receiver**Depth Locations** 50 levels, 152 m through to 887 m at 15 m intervals

Table 5.2 - Data acquisition parameters for the 33-1 VSP.

**Sources**

Shear vibrators × 2

Sweep	60 - 7 Hz
Azimuth	122°
Offsets	65 m

Compressional vibrator

Sweep	150 - 7 Hz
Azimuth	123°
Offset	71 m

**Recording Parameters**

Sweep length	14 s
Record Length	15 s
Taper	0.2 s
Sample Interval	1 ms

**Downhole Sonde** GSC-20D 3-C receiver

**Depth Locations** 44 levels, 306 m through to 951 m at 15 m intervals

Table 5.3 - Data acquisition parameters for the Peel VSP.

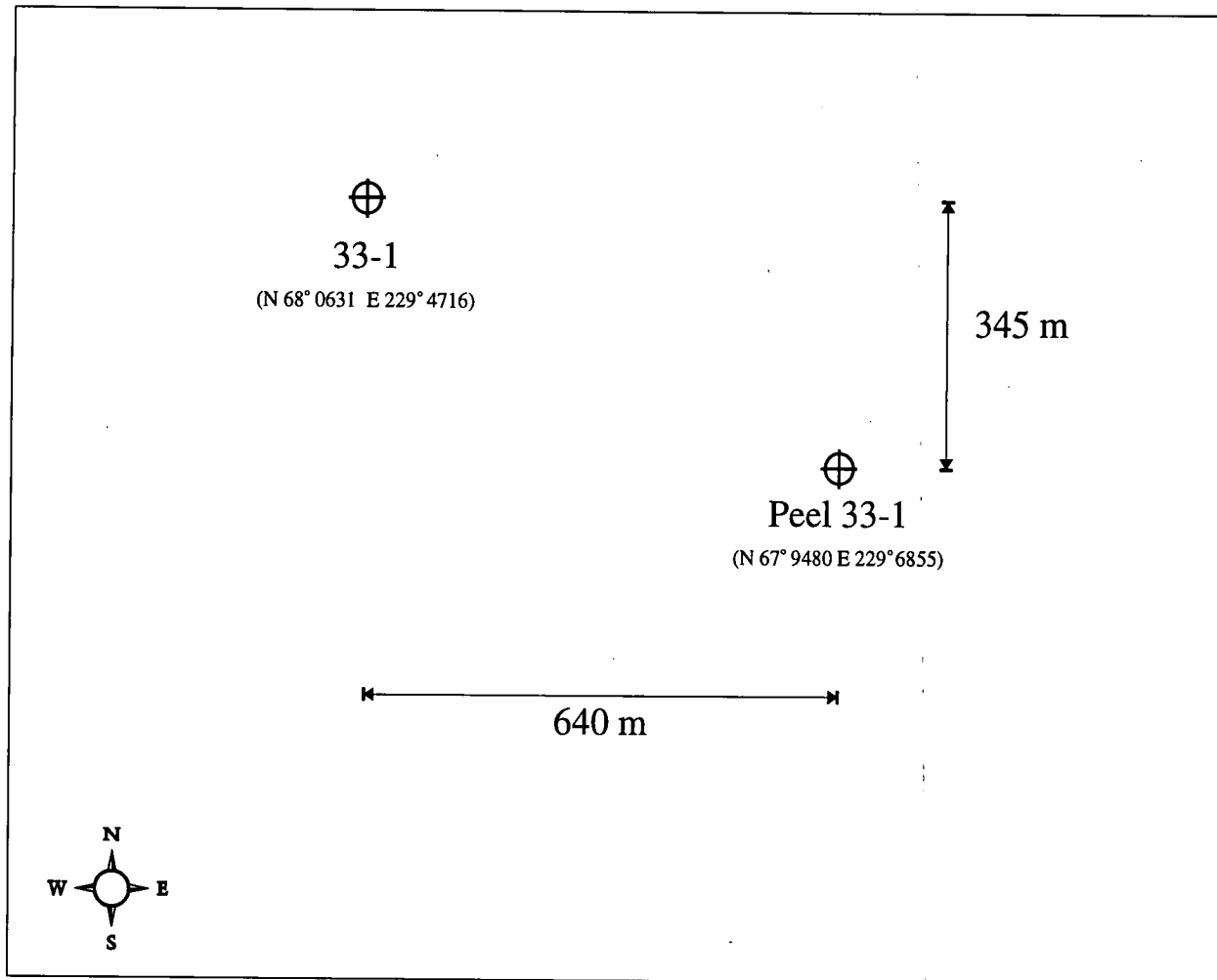


Figure 5.5 - Plan view of the Conoco Borehole Test Facility, Kay County, Oklahoma showing the relative location of the 33-1 and Peel wells. Grid references are USGS state plane co-ordinates.

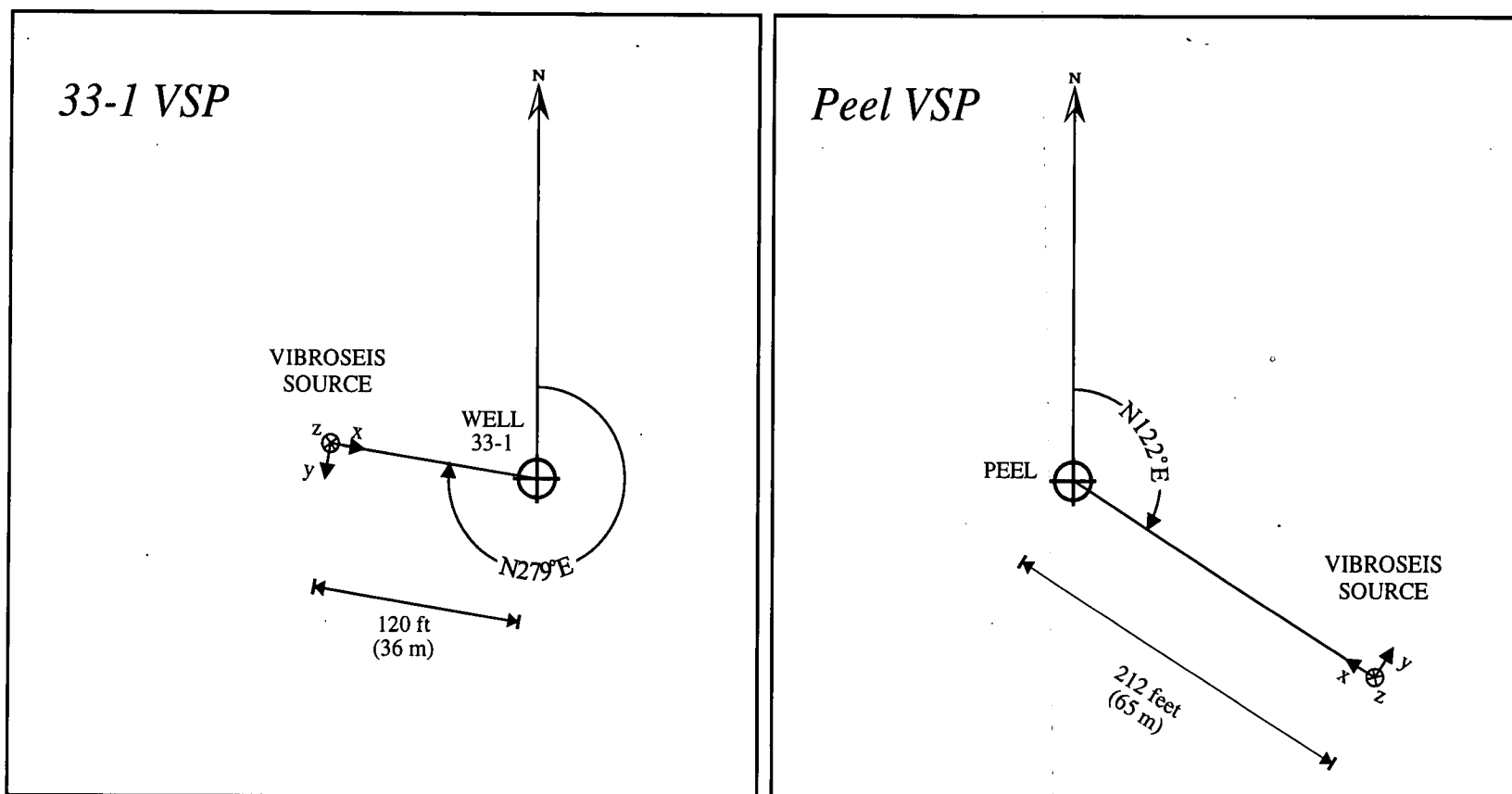


Figure 5.6 - Plan views showing the surface location of the vibroseis sources relative to the wells for the near-offset VSPs.

## 5.7 PROCESSING SEQUENCE APPLIED TO SHEAR-WAVE DATA

I apply a common processing sequence to both VSP datasets for the purposes of consistency. The data processing steps that I use are,

1. horizontal geophone rotation into the in-line and cross-line directions. This is necessary to correct for downhole tool spin.
2. f-k filtering, to separate the up- and down-going shear wavefields.
3. near-surface correction, to remove any possible inconsistencies due to variations in the near-surface layers.

After each of the processing steps above a visual check is made of the processed seismograms and shear-wave estimation techniques are applied. The purpose of this is to verify that these processing steps do not distort the shear-wavefield. The details and results of these processing steps are now described in more detail with reference to the 33-1 and Peel VSP surveys.

### 33-1 VSP

Gyro data are not available for these records and so geophone orientations are determined using offset *P*-wave data recorded from vibroseis sources located 213 m (700 ft) and 457 m (1500 ft) along the azimuth N155°E (MacBeth *et al.*, 1995). This method is expected to be valid because of the structural simplicity known to exist at the test site. The rotated seismograms from the experiment are shown in Figure 5.7 in a multicomponent 3×3 layout with rows corresponding to sources and columns corresponding to geophone components. At this initial stage of processing it can be seen that the seismograms are of high quality and the presence of off-diagonal energy is suggestive of shear-wave splitting. The shear-wave data are now filtered using a quadrilateral f-k reject filter designed to separate the up- and down-going wavefields

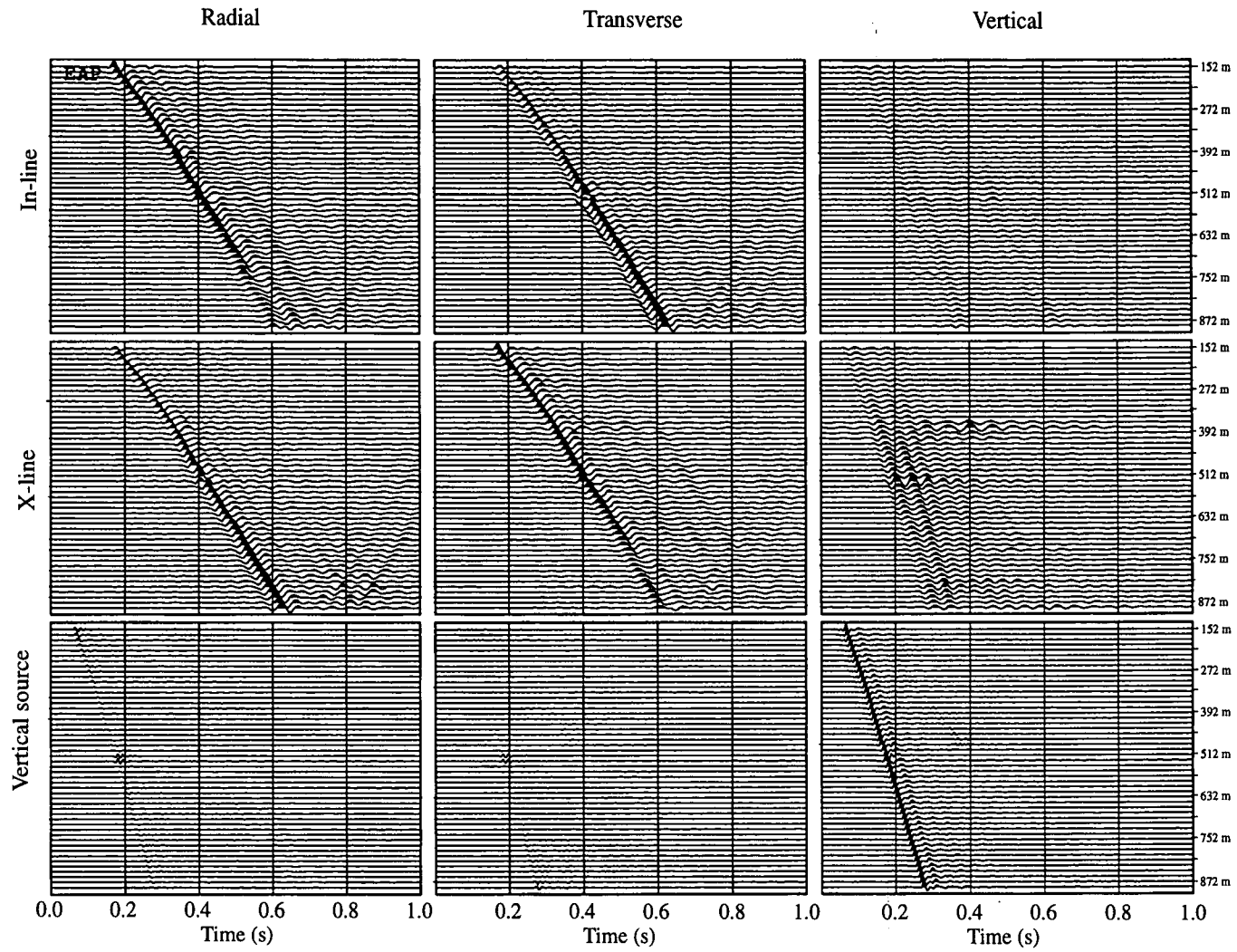


Figure 5.7 - A nine component plot showing the seismograms recorded from the 33-1 VSP. Seismograms have been rotated in the horizontal plane to align the geophone components with the in-line and x-line directions using *P*-wave energy on radial components.



(Figures 5.8 and 5.9). Several reflected events can be observed, the presence of which would bias the shear-wave splitting estimation. However, it should be remembered that f-k filtering can introduce considerable smoothing over the depth levels. This 'smearing' is minimised by the use of a quadrilateral reject filter in preference to the use of a f-k fan pass filter. A near-surface correction operator, based on a deconvolution model (MacBeth *et al.* 1995), is now constructed from the multicomponent data matrix between geophone levels 12 and 13 corresponding to the depths 317 m and 332 m. These levels are chosen to coincide with the shallowest depth level at which a near-surface correction could be applied to the Peel VSP data. The resulting seismograms after near-surface correction are shown in Figure 5.10.

The shear-wave splitting is quantified in terms of the fast shear-wave polarization and the time delay between the split shear-waves by the use of an analytical implementation of the Alford rotation (Zeng and MacBeth 1993). The estimation results for the 33-1 VSP data after each of the processing steps are shown in Figure 5.11. The f-k filtering essentially smooths the variation with depth of the  $qSI$ -wave polarizations and the time delay estimates. The  $qSI$ -wave polarization estimates show little change after application of f-k filtering and near-surface correction and indicate a constant shear-wave polarization of approximately N50°E. The time delay estimates after near-surface correction are shifted by approximately 5 ms so that, as expected, there is negligible splitting at the depth at which the correction is applied. The rate of time delay increase with depth is not continuous and significant discontinuities can be identified at the four depth levels 422 m, 617 m, 677 m and 767 m, as indicated on Figure 5.11. The zone between the near-surface correction reference level and the first discontinuity at 422 m reveals a moderate increase in the time delay of approximately 12 ms/km. The second anisotropic zone lying between 422 m and 617 m corresponds to a time delay gradient of 33 ms/km. The third zone is apparently isotropic as there is no appreciable change in the time delay estimates over this depth range. Between 677 m and 767 m there is a significant increase in the time delay gradient to 97 ms/km. Below this depth range the time delay

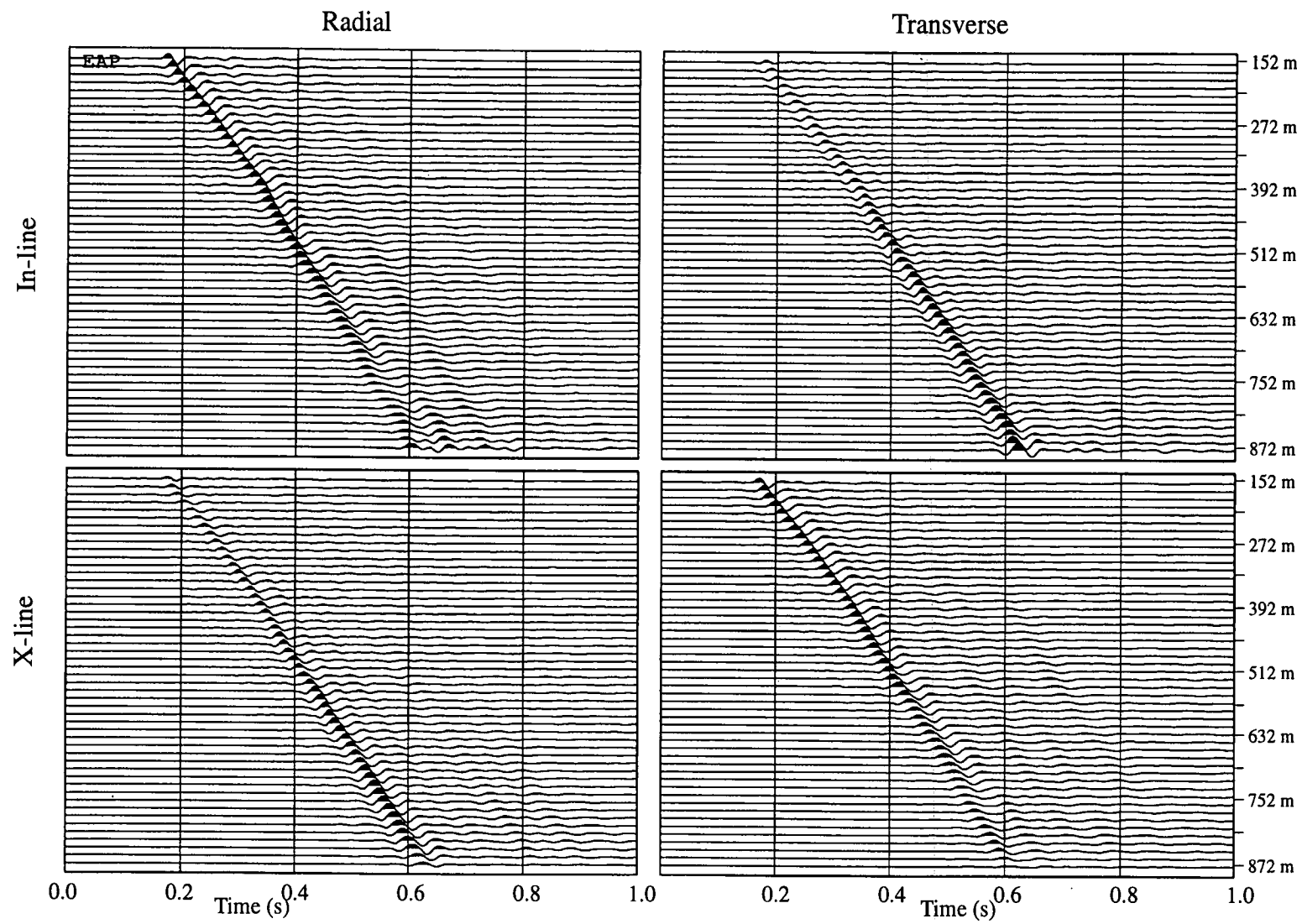


Figure 5.8 - Multicomponent plot showing the downgoing wavefield for the 33-1 VSP after f-k filtering.

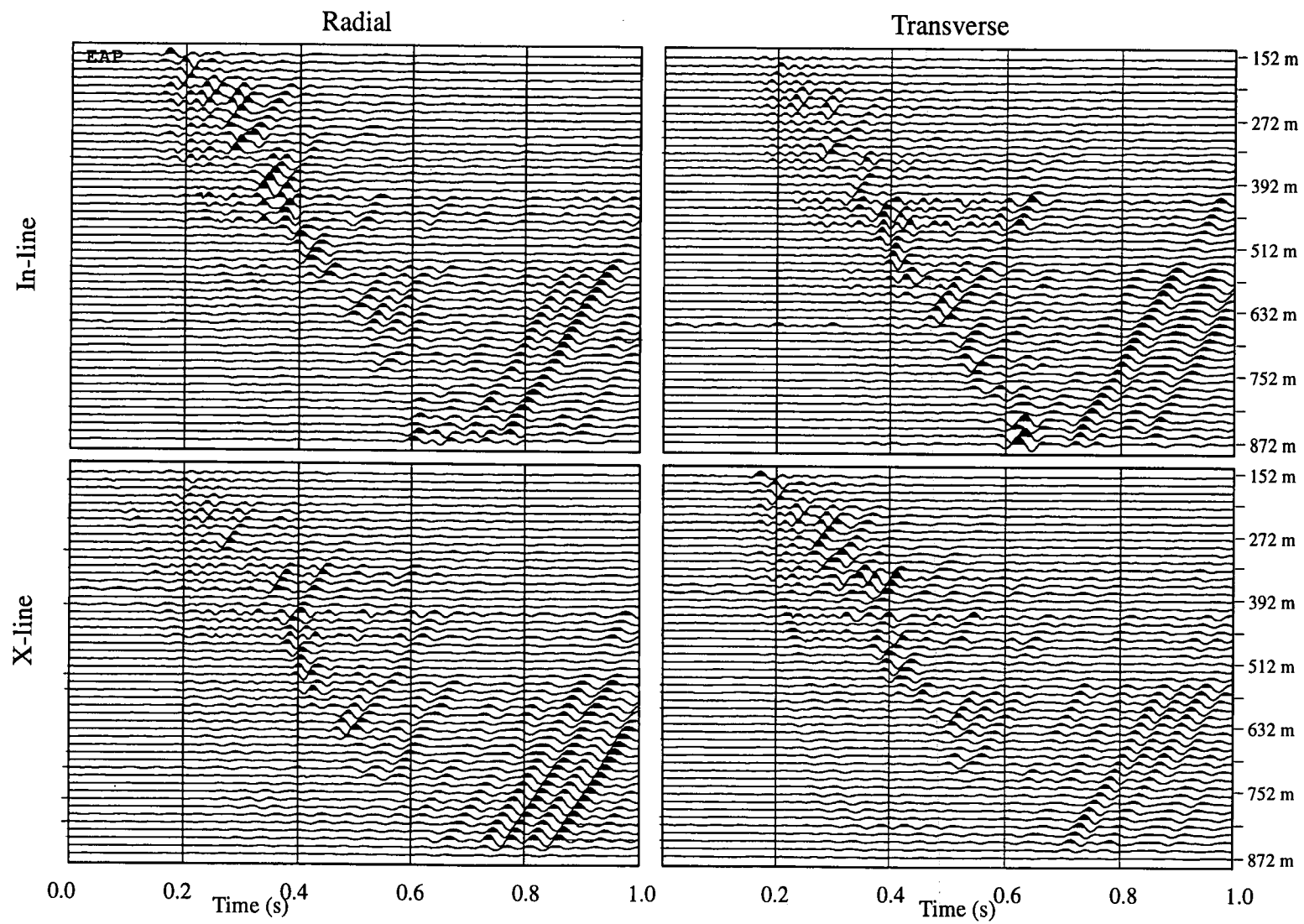


Figure 5.9 - Multicomponent plot showing the upgoing wavefield for the 33-1 VSP after f-k filtering.

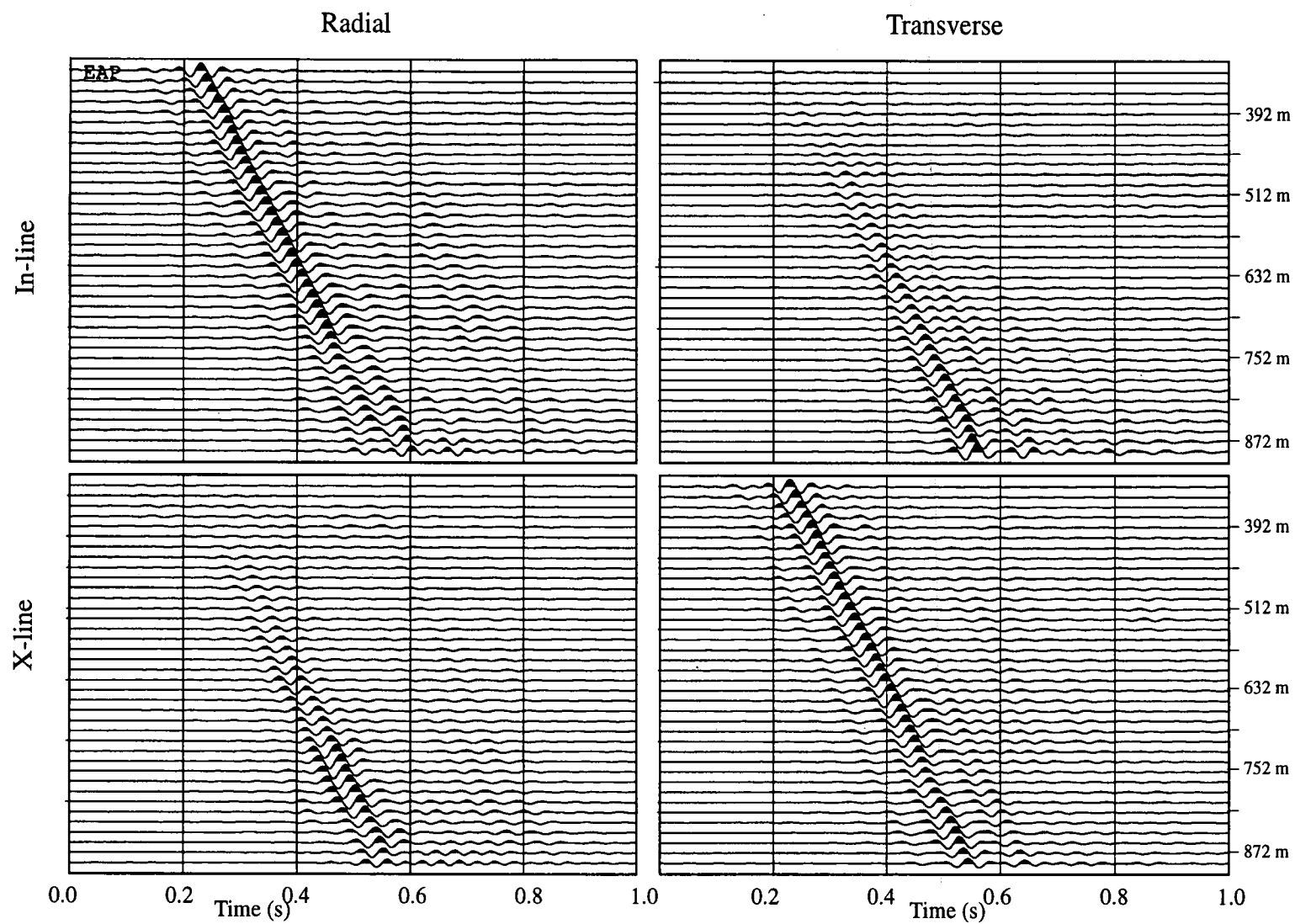


Figure 5.10 - Multicomponent plot showing the downgoing wavefield for the 33-1 VSP after f-k filtering and near surface

### 33-1 VSP

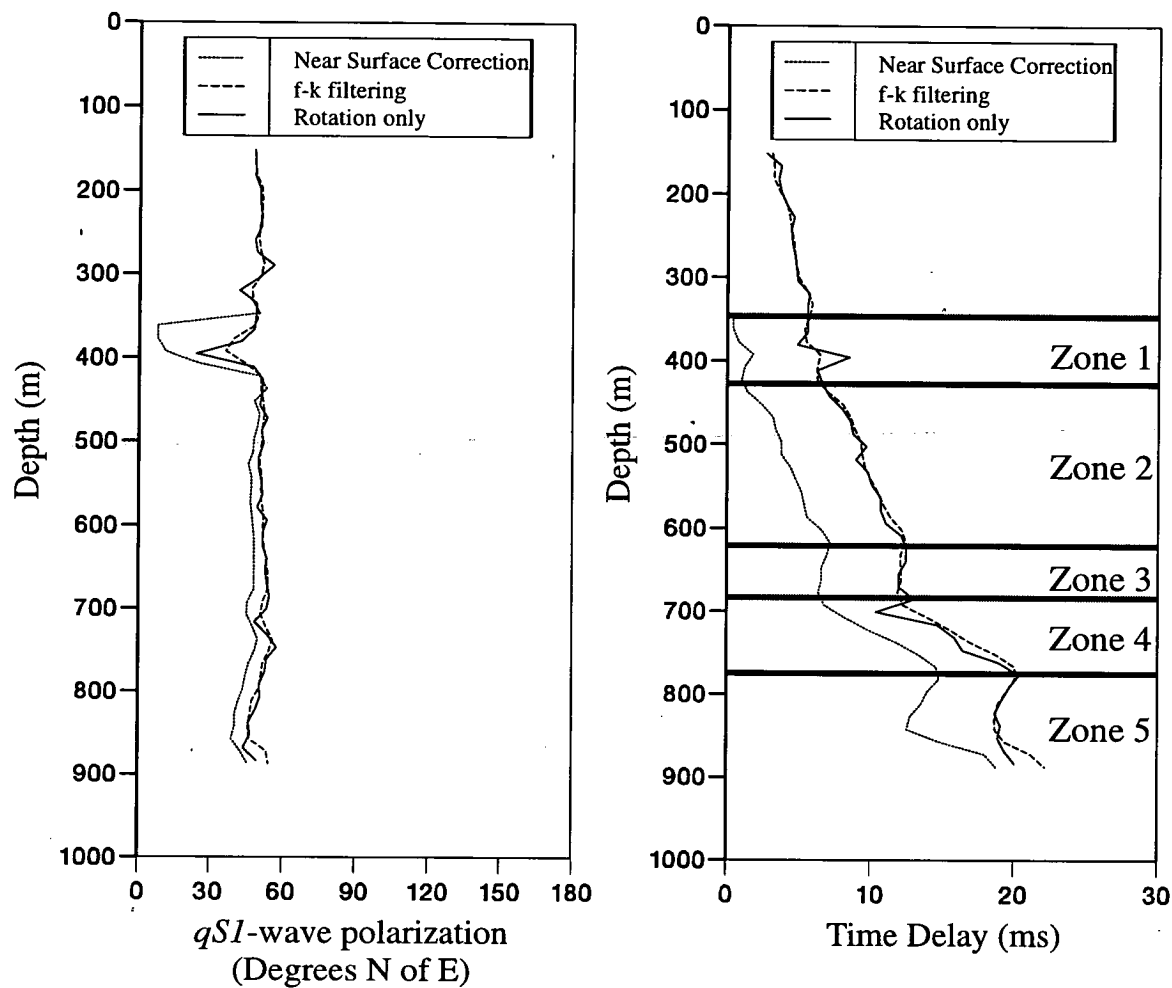


Figure 5.11 - A comparison of shear-wave estimation results for the 33-1 VSP after various processing steps.

estimates decrease to a minima of 12 ms at 827 m and then increases to 19 ms for the deepest recording at 887 m.

### *Peel VSP*

Gyrodata are also unavailable for these seismograms and so tool rotation is compensated for by the rotation of the horizontal geophone components to maximise the *P*-wave energy on the geophones  $x_1$  component (Cox, V., Conoco Inc, personal communication). The multicomponent representation of the seismic data after rotation is shown in Figure 5.12. Although the seismograms are generally of high quality, inconsistent traces can be identified at the levels 1 and 23. Before application of the *f-k* filter these levels must be processed to avoid 'smearing' these bad traces over adjacent depth levels. This is achieved by the deletion of the level 1 records and the replacement of the level 23 records by interpolation between adjacent levels. The shear wavefields are separated into the up- and down-going components by the application of a quadrilateral *f-k* reject filter (Figures 5.13 and 5.14). Near-surface correction is now applied to this *f-k* filtered data at the third geophone level at 336 m. This depth is chosen to coincide with that used for the near-surface correction applied to the 33-1 VSP. The resulting seismograms are shown in Figure 5.15. Results from the application of shear-wave estimation techniques are shown in Figure 5.16. As for the 33-1 VSP the result of *f-k* filtering is a smoothing of both the time delay and *qSI*-wave polarization estimates. However, unlike the results for the 33-1 VSP, the near-surface correction has a considerable effect in clarifying the estimation results. Before near-surface correction the estimated *qSI*-wave polarizations decrease steadily with depth from N90°E at shallow levels to N60°E. After the correction this rotation becomes less apparent and the *qSI*-wave polarizations are shifted towards N55°E. Before the near-surface correction there is no clear time delay variation with depth as observed for the 33-1 VSP estimation results. Nonetheless, discontinuities can be observed at similar depths to those identified in the 33-1 VSP results. However, after the near-surface correction the time delay gradients can be measured with more confidence. The first anisotropic

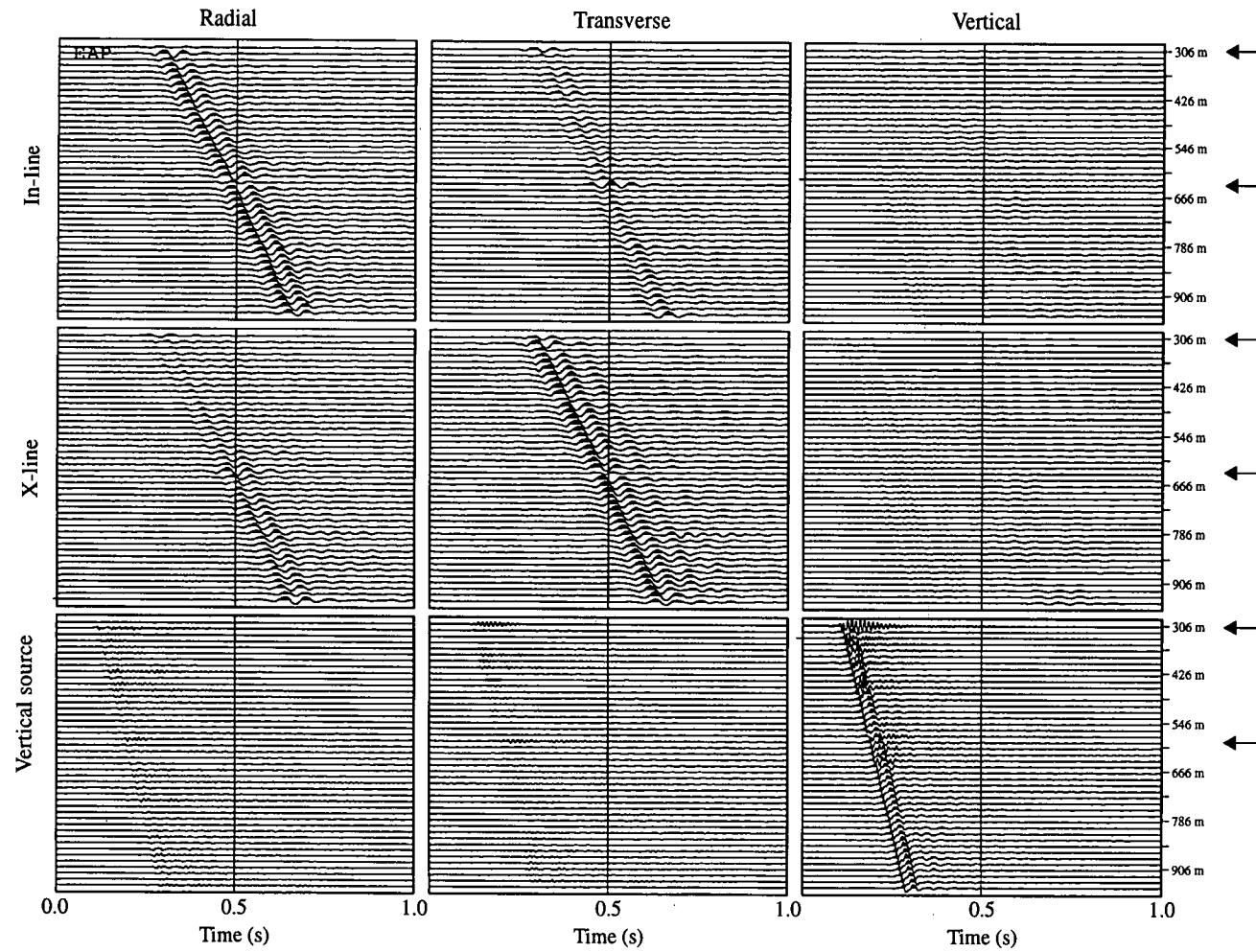


Figure 5.12 - A nine component plot showing the seismograms recorded from the Peel VSP. Seismograms have been rotated in the horizontal plane to align the geophone components with the in-line and x-line directions using *P*-wave energy on radial

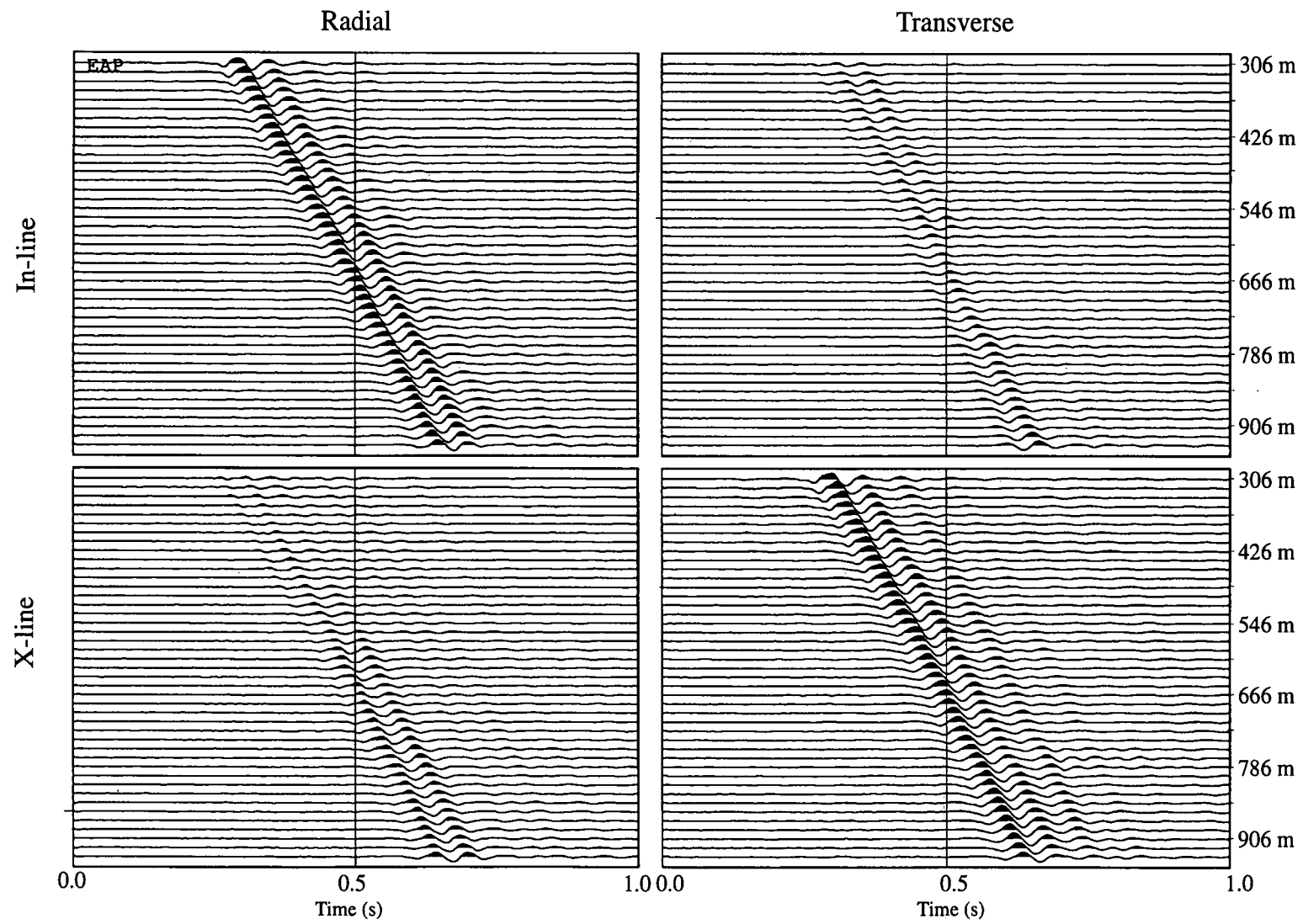


Figure 5.13 - Multicomponent plot showing the downgoing wavefield for the Peel VSP after f-k filtering.



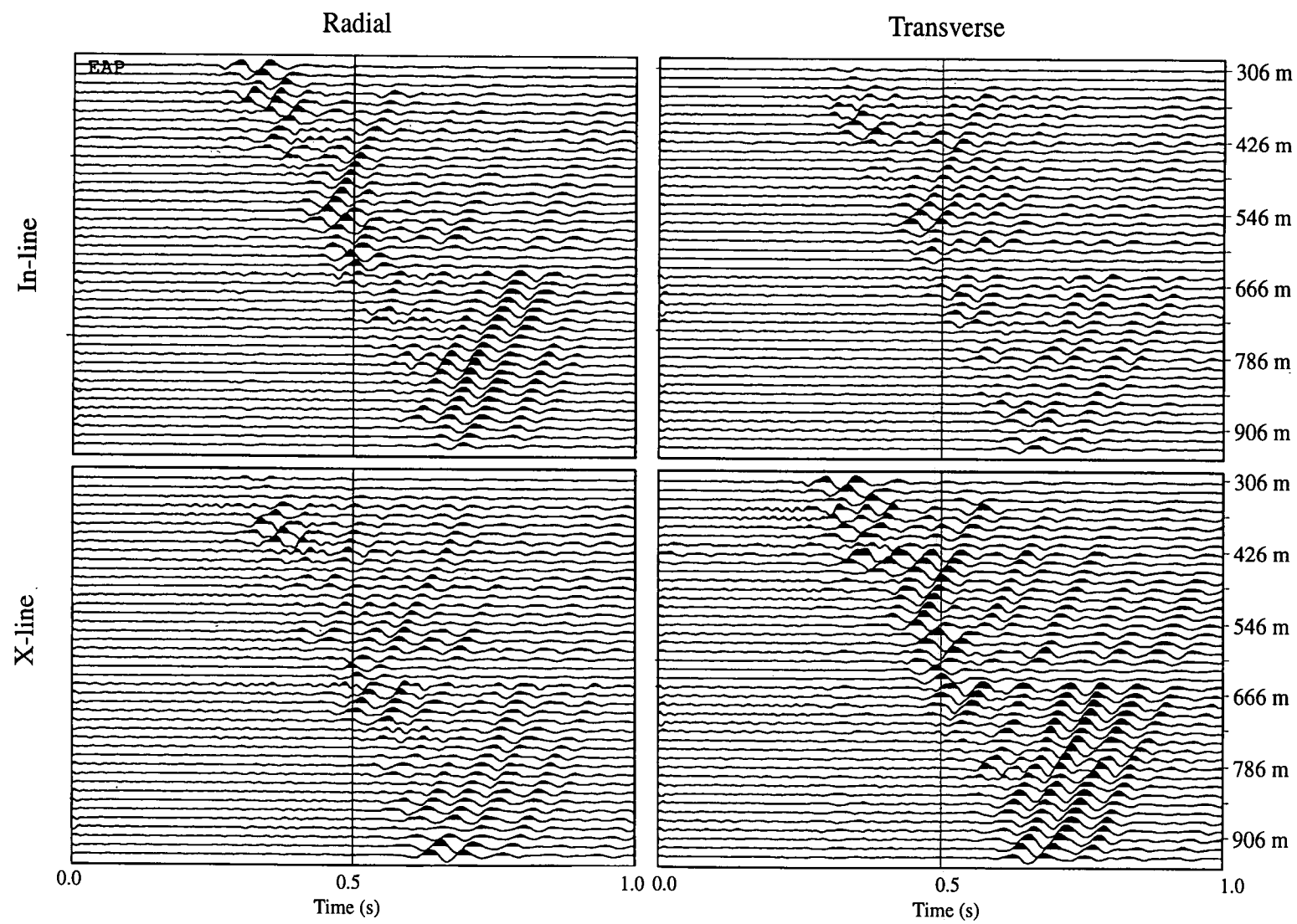


Figure 5.14 - Multicomponent plot showing the up-going wavefield for the Peel VSP after f-k filtering.

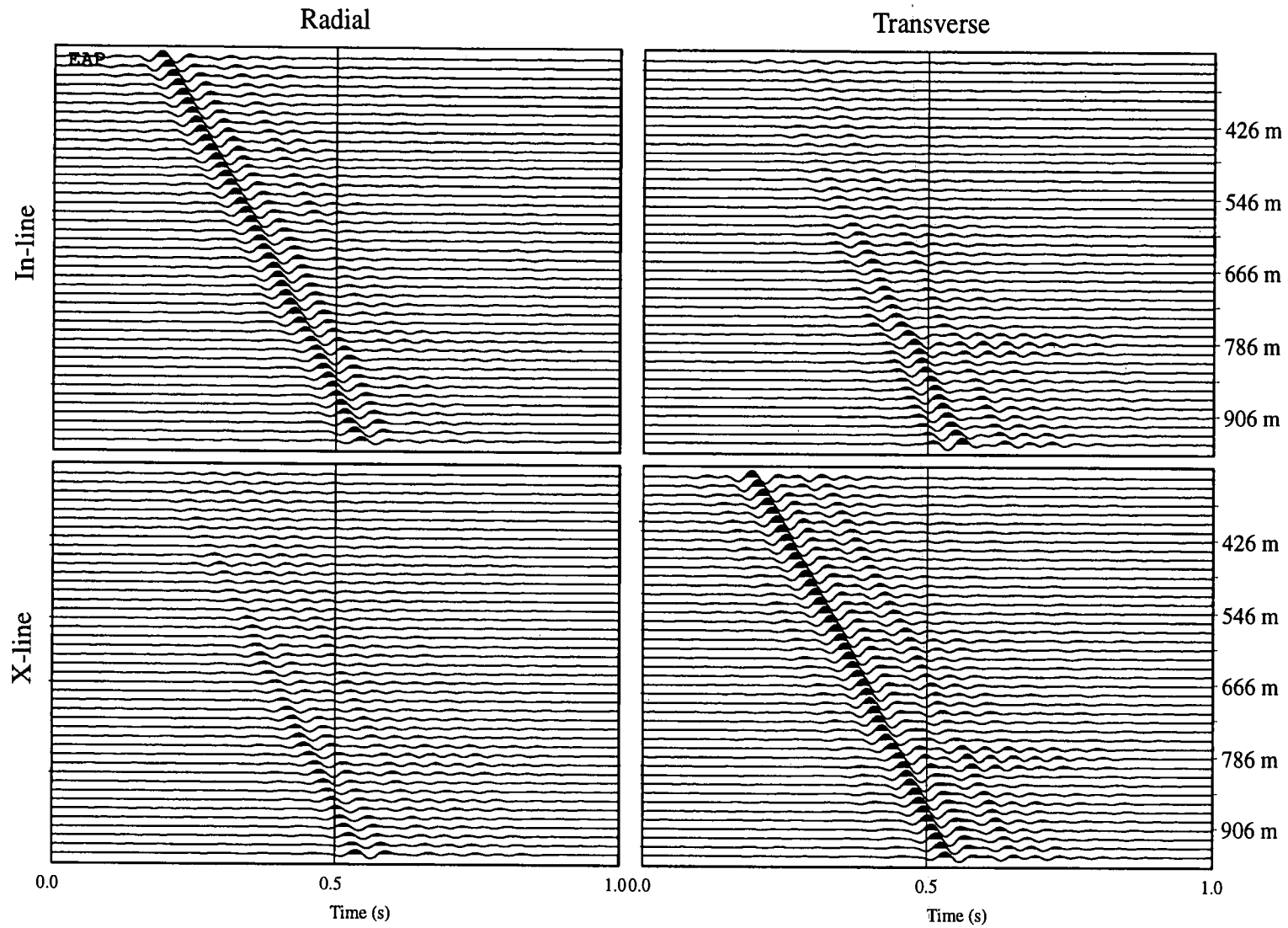


Figure 5.15 - Multicomponent plot of the Peel VSP data after f-k filtering and near-surface correction.

# Peel VSP

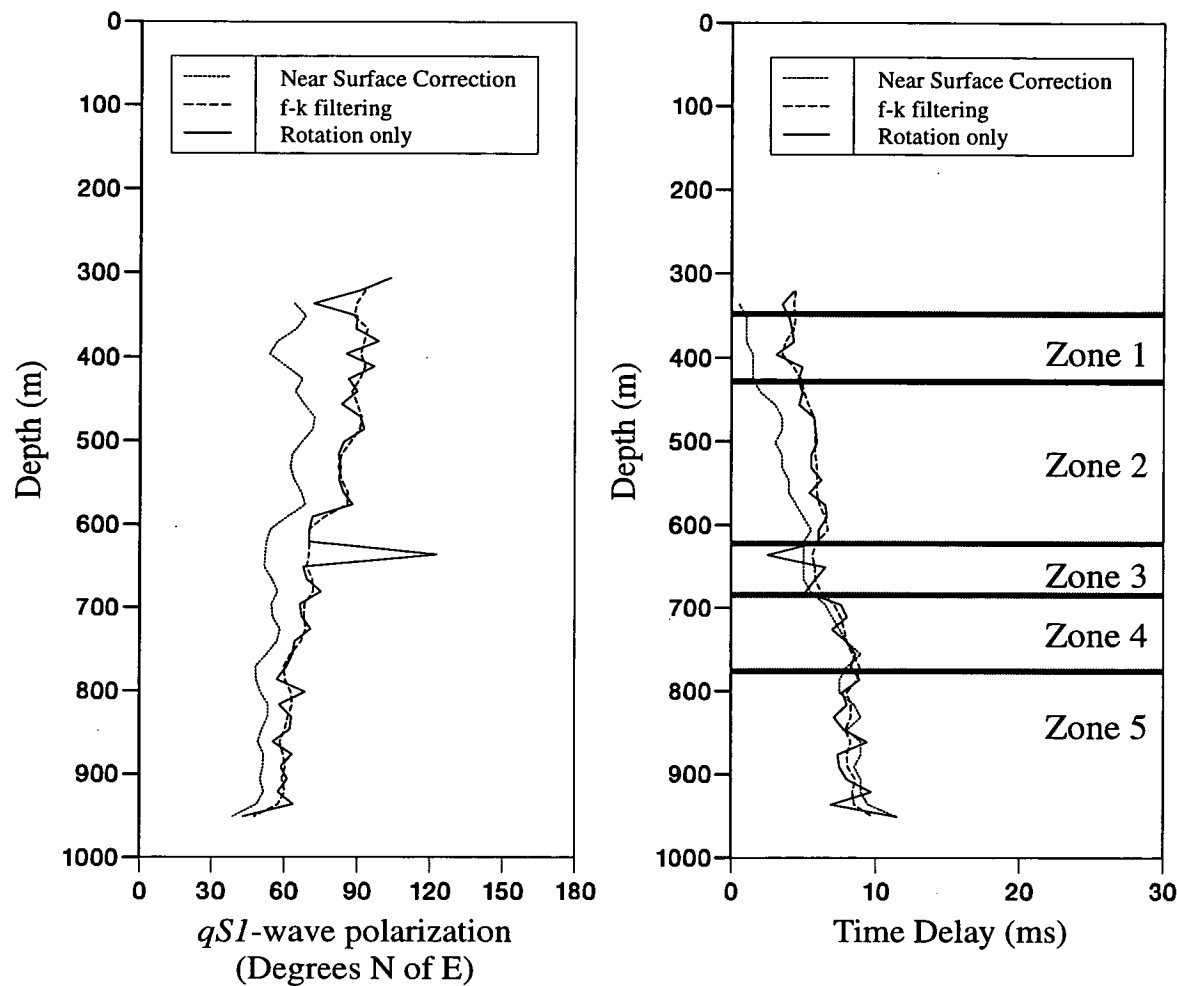


Figure 5.16 - A comparison of shear-wave estimation results for the Peel VSP after various processing steps.

zone, between the reference level at which the near-surface correction is applied and 422 m depth, corresponds to a time delay gradient of 11 ms/km. This increases to approximately 20 ms/km in the second zone which extends to a depth of 617 m. No significant change in the time delays are observed between 617 m to 677 m so that this zone is likely to be isotropic. A time delay gradient of 42 ms/km is observed between 677 m and 766 m. Below this depth there is no clear trend in the time delays and this zone appears isotropic.

A comparison of the estimation results from the two VSPs reveal a similar time delay variation with discontinuities in the time delay gradients occurring at similar depths (Figures 5.11 and 5.16). There are also similarities in the relative time delay gradients in the five anisotropic regions with the results obtained from the 33-1 VSP. In particular, shear-wave splitting is pronounced in the second and fourth zones with the intermediate zone being isotropic. However, the overall degree of splitting for the Peel VSP is significantly smaller than that observed for the 33-1 VSP. An obvious explanation is offered in terms of lateral variability since the two wells are 740 m apart. Although this is a plausible explanation the similarity in the variations of the time delay estimates with depth suggest that there may be some correspondence between the observed anisotropy in the two wells. Furthermore the two VSPs are shot in a relatively simple geological setting so that lateral changes are unlikely, although this possibility cannot be ruled out. The inversion results that I obtain will show that such lateral changes need not be invoked to explain these shear-wave splitting observations.

## **5.8 STRATIGRAPHIC CORRELATION WITH SHEAR-WAVE BIREFRINGENCE**

Before proceeding to the main subject of this chapter I will note a correlation between the measured shear-wave anisotropy and the stratigraphy. The results I have obtained for the shear-wave birefringence observed from both near-offset VSP

experiments show a clear correlation with the reported approximate stratigraphy at the CBTF. This is shown in Figure 5.17 in which a stratigraphic depth section of the geology at the test site is plotted on the same depth scale as the splitting estimates. The large time delay gradients observed over the two depth ranges 422 - 617 m and 677-767 m correspond to sandstone formations. Sandstones are more likely to support open fractures than rocks such as shales or carbonates. This is due to the large grain size of sandstones which leads to rough fracture surfaces. These are more resistant to closure than the smooth fracture surfaces observed in shales or carbonates (Ehlig-Economides, Ebbs and Meehan 1990). This correlation suggests that the shear-wave birefringence is sensitive to the presence of open fractures in the sandstones. This conclusion is supported by borehole televiewer and core data which indicate that the highly anisotropic zone between 677 m and 767 m corresponds to intense natural fracturing (Queen *et al.* 1992). This depth interval has also been observed to correspond to known fluid loss in all of the deep wells at the test-site which is attributed to large open fractures within this zone (Queen *et al.* 1992). Further confidence in this interpretation is gained from permeability and porosity logs obtained recently from the test site (Figure 5.17c-d). These show that the highly permeable and highly porous regions tend to coincide with the sandstone intervals and that within these regions shear-wave splitting is more pronounced. Furthermore it is also possible to identify a highly permeable/highly porous sub-zone within zone 3 which corresponds to a Tonkawa sandstone section between 580 m and 620 m. This formation was the target of the AVSP experiment discussed in Chapter 4. One of the objectives of the AVSP was to investigate the ability of shear-wave birefringence to resolve thin fracture zones by the observation of a systematic increase in travel time splitting. For the AVSP experiment such a behaviour could not be detected because of the choice of offset which appears to have detected a shear-wave singularity. However, for these near-offset VSPs such an increase can be observed within this zone indicating that such thin zones of fracturing may be resolved if appropriate geometries are employed. An alternative explanation for the observed anisotropy in these sandstone formations may be due to preferential grain

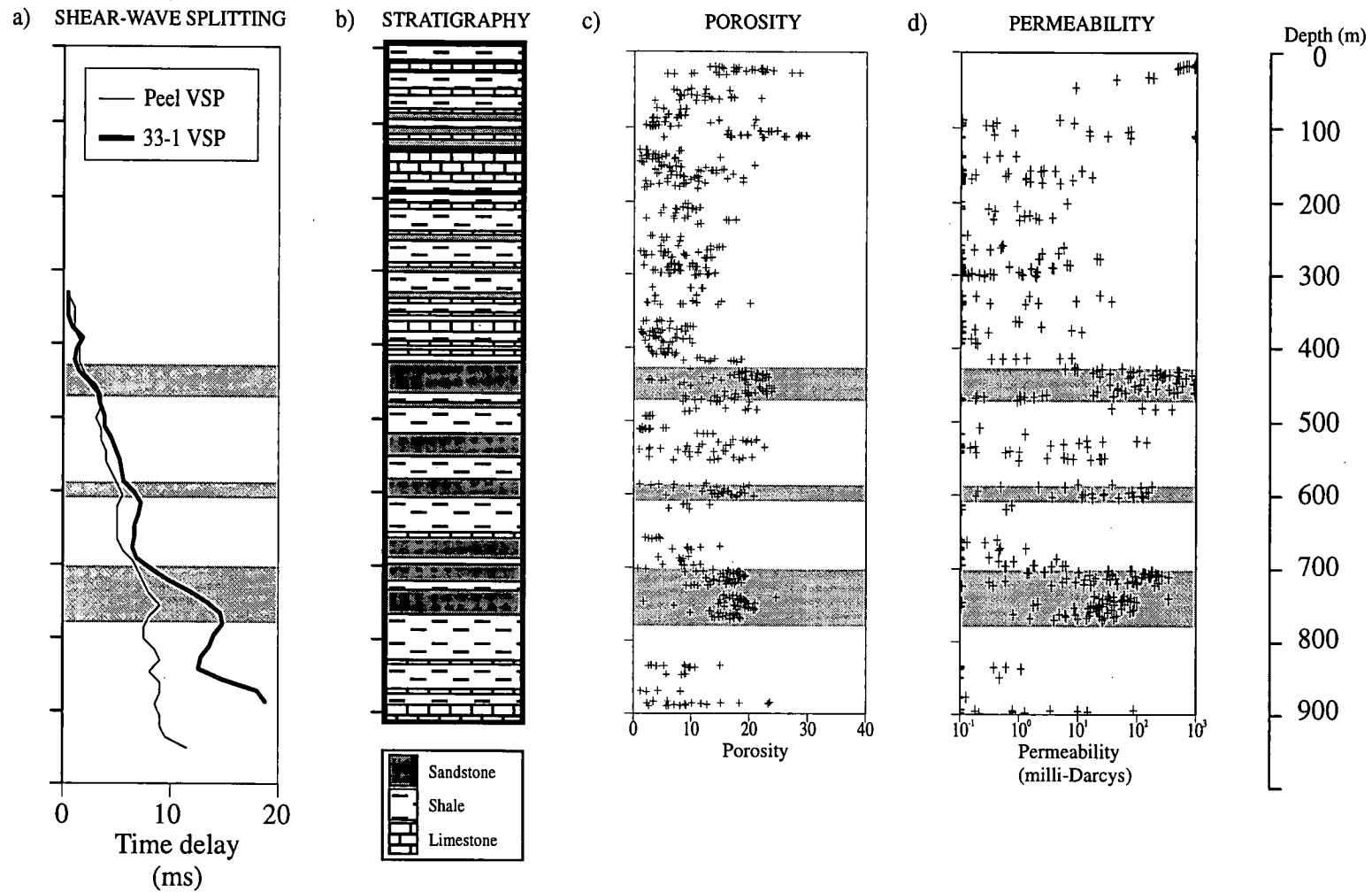


Figure 5.17 - A comparison of a) the estimation results (after application of  $f$ - $k$  filtering and near-surface correction) from the 33-1 and Peel VSP data sets with b) the stratigraphy, c) the porosity and d) the permeability reported at the Conoco Borehole Test Facility (after Queen and Rizer 1990, W. Rizer, Conoco Inc., personal communication). The shaded regions correspond to highly permeable and highly porous zones of sandstone for which shear-wave birefringence is pronounced.

alignment due to depositional conditions leading to equivalent anisotropic behaviour (Helbig 1994). However, the coincidence of the  $qS1$ -wave polarizations with the maximum compressive stress direction (Zoback and Zoback 1980) suggests that the observed seismic anisotropy is not related to such depositional fabrics. Furthermore, thin section analysis of core samples from the test site do not indicate any depositional fabrics (Queen and Rizer 1990).

## 5.9 INVERSION PROCEDURE

The misfit function to be minimized by the GA is defined in a similar way to the goal function used in the AVSP inversion described in Chapter 4. In this case the objective function is defined to be

$$f(m, \tau^0, p^0) = \frac{1}{2} \left[ \Delta \tau(\tau^0, \tau^m, \delta \tau) + \Delta p(p^0, p^m, \delta p) \right]; \quad (5.3a)$$

where

$$\Delta \tau(\tau^0, \tau^m, \delta \tau) = \frac{1}{N} \sum_{j=1}^N \left( \frac{\tau_j^0 - \tau_j^m}{\delta \tau_j} \right)^2; \quad (5.3b)$$

and

$$\Delta p(p^0, p^m, \delta p) = \frac{1}{N} \sum_{j=1}^N \left( \frac{p_j^0 - p_j^m}{\delta p_j} \right)^2. \quad (5.3c)$$

$\tau$  and  $p$  vectors of the time delays and the  $qS1$ -wave polarizations respectively.  $m$

is the model parameter vector describing the anisotropic perturbation to be added to the isotropic layered model for which shear-wave splitting observations are calculated by the ray tracing algorithm. The subscript  $j$  identifies the observation number and  $N$  is the total number of observations from both VSPs. The superscripts identify quantities relating to the model, superscript  $m$ , and the observed, superscript 0, vectors.  $\delta\tau$  and  $\delta p$  are error estimates associated with the observed time delays,  $\tau^0$ , and  $qSI$ -wave polarizations,  $p^0$ , respectively. The shear-wave splitting estimates are assigned estimated errors of  $10^\circ$  for the  $qSI$ -wave polarizations and 2 ms for the time delays.  $qSI$ -wave polarization estimates associated with time delays less than 2 ms are assigned an estimated error of  $20^\circ$ . This reflects the uncertainty of the  $qSI$ -wave polarization estimates associated with small time delays for which estimation techniques are inaccurate. This choice of objective function implies that the errors follow a Gaussian distribution.

The predicted shear-wave splitting observations,  $\tau^m$  and  $p^m$ , are calculated for a layered anisotropic model based on a perturbation defined by the model vector,  $m$ . The model for the CBTF uses eighteen layers (Table 5.4) whose velocities, densities and thicknesses are derived from an initial fifty-five layer model measured from logging information and, for shallow depths, reverse VSP surveys (Queen, J., Conoco Inc, personal communication). This eighteen layer model is shown in Figure 5.18 in comparison with the initial velocity model composed of fifty-five layers. This reduction is achieved by selecting depth levels at which significant changes are judged to occur in either the compressional or the shear-wave velocities. The effective velocities and density in each of these regions is then calculated using a thickness-weighted velocity average based upon the initial velocity and density models. An alternative approach is to use a thickness-weighted average of the elastic constants from which average velocities may be calculated. This layering reduction is necessary to increase the computational speed of the ray tracing routines. This blocked model is then split into five different anisotropic zones corresponding to the observed changes in the shear-wave splitting estimates from the two VSP



$V_p$ (km/s)	$V_s$ (km/s)	$\rho$ (g/cm <sup>3</sup> )	Thickness (m)	Zone
1.12	0.29	2.00	12	iso
2.98	1.42	2.37	25	iso
3.23	1.82	2.37	35	iso
3.28	1.86	2.25	52	iso
4.10	2.15	2.49	50	iso
3.39	1.95	2.49	138	iso
3.50	1.81	2.47	52	1
4.40	2.24	2.56	20	1
3.68	2.05	2.48	38	1
3.68	2.05	2.48	80	2
4.31	2.28	2.16	29	2
3.73	2.23	2.51	86	2
3.73	2.23	2.51	25	3
3.88	2.07	2.54	35	3
3.88	2.07	2.54	90	4
3.88	2.07	2.54	47	5
4.19	2.22	2.64	40	5
4.93	2.59	2.64	(Halfspace)	5

Table 5.4 - Isotropic velocity model used in the full waveform and ray tracing forward modelling. This eighteen layer model is based upon velocity and density logs and RVSP experiments conducted at the CBTF (Queen, J., Conoco Inc, personal communication).

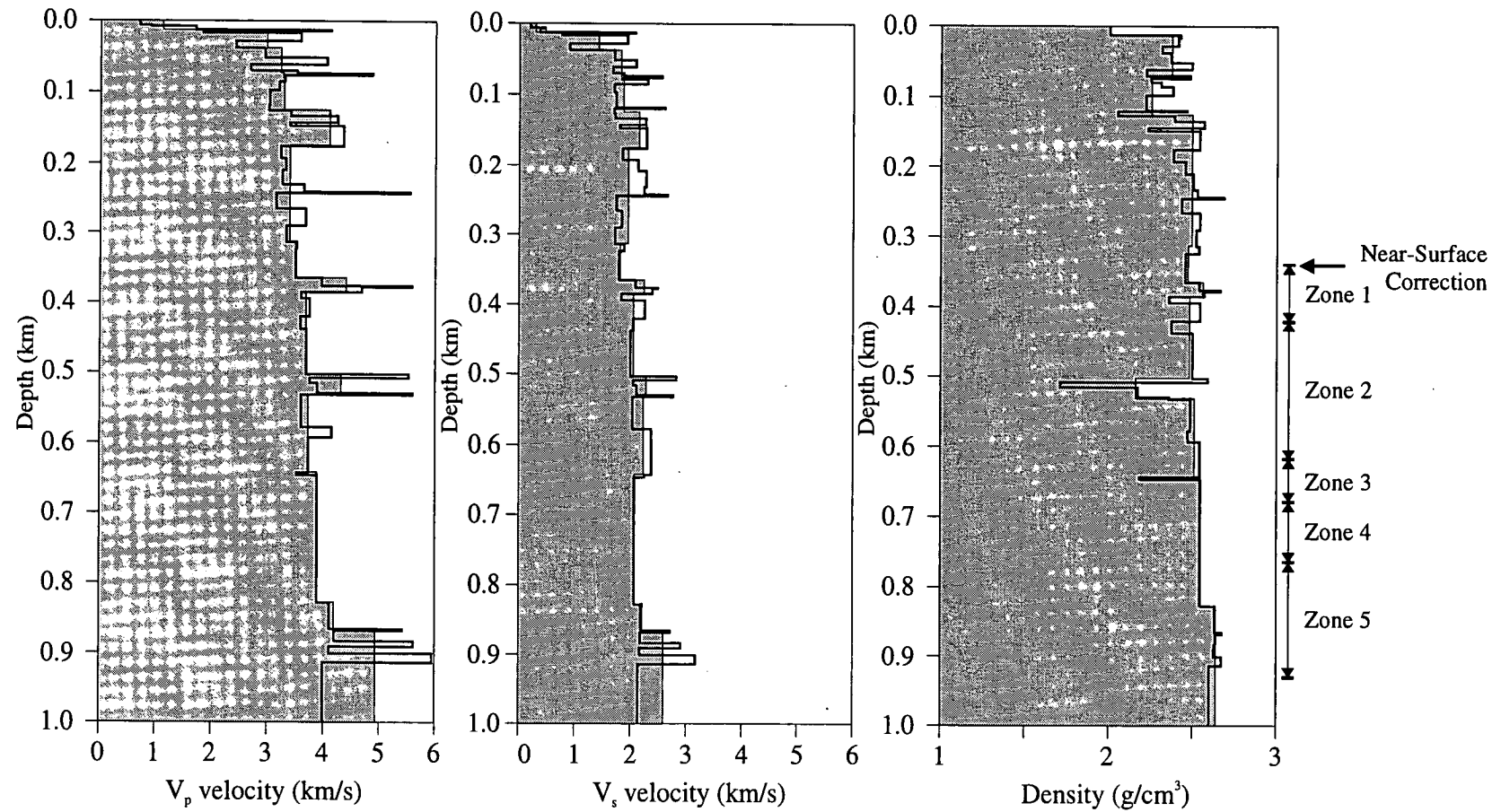


Figure 5.18 - This figure shows the velocity and density models used in this inversion study. The initial 55 layered model, shown in continuous black, is reduced to the 18 layered model shown as the grey shaded area. Also shown are the anisotropic zones identified from shear-wave estimation results.

surveys. The imposition of a common symmetry axis for each of these regions is applied to avoid any problems associated with multiply split shear waves. Furthermore, inversions are only attempted for hexagonal symmetry systems due to limitations within the ray tracing scheme.

Several inversions are applied to the shear-wave splitting estimates using different parametrizations for the model space. The parametrization schemes that are adopted for these inversions essentially follow the same procedures described in Chapters 3 and 4. These are equivalent media formulations based upon Hudson's crack formulations, Thomsen parameters and a deviation from the isotropic tensor based upon the elastic constants. However, in the case of the Hudson scheme a logarithmic function is used to represent the aspect ratio since seismic data from near-offset VSP's are relatively insensitive to this parameter (MacBeth 1991). The GA control parameters for the three different inversions are given in Table 5.5.

## 5.10 INVERSION RESULTS

The model parameters for the best solutions found by the GA using the Hudson, Thomsen and Cijkl representations are shown in Tables 5.6, 5.7 and 5.8 respectively. All the best model misfits are less than 1.0 indicating that, on average, all the model observations are within the estimated error bounds. The best model obtained using the Thomsen parametrization possesses a misfit of  $f(\mathbf{m}, \boldsymbol{\tau}^0, \mathbf{p}^0) = 0.420$ . This value is significantly larger than the misfits for the best models obtained using the Hudson and Cijkl schemes for which the misfit values are 0.265 and 0.207 respectively. The reason for the Thomsen model's large misfit lies in the poor modelling of the  $qS1$ -wave polarizations for the Peel VSP (Figure 5.19). The predicted  $qS1$ -wave polarizations for the Peel VSP show an abrupt change in direction from N140°E to N50°E at a depth of 480 m. This behaviour is due to the sampling of shear-wave line singularity in the model observations. The inferred fracture orientation for the best Thomsen model is N50°E dipping 11° to the north west. This dip direction is

GA Parameter		Hudson	Thomsen	Cijkl
Population size	$N_{pop}$	60	80	100
Number of Generations	$N_{gen}$	60	80	100
Crossover probability	$p_c$	0.950	0.950	0.950
Mutation Probability	$p_m$	0.010	0.010	0.010
Sharing		✓	✓	✓
Inversion		✓	✓	✓
G-bit improvement		✓	✓	✓

Table 5.5 - Parameters used in the GA inversion scheme for the three parametrizations.

	HUDSON		
	<i>CD</i>	<i>AR</i>	<i>CT</i>
ZONE 1	0.079	$10^{-2}$	sat
ZONE 2	0.022	$10^{-4}$	dry
ZONE 3	0.025	$10^{-2}$	dry
ZONE 4	0.097	$10^{-3}$	dry
ZONE 5	0.405	$10^{-4}$	dry
Crack Strike (Degrees N of E)	50°		
Crack Dip (Degrees)	18° to south east		
Misfit $f(m, \tau^o, p^o)$	0.265		

Table 5.6 - The best solution found using the GA for the Hudson scheme.

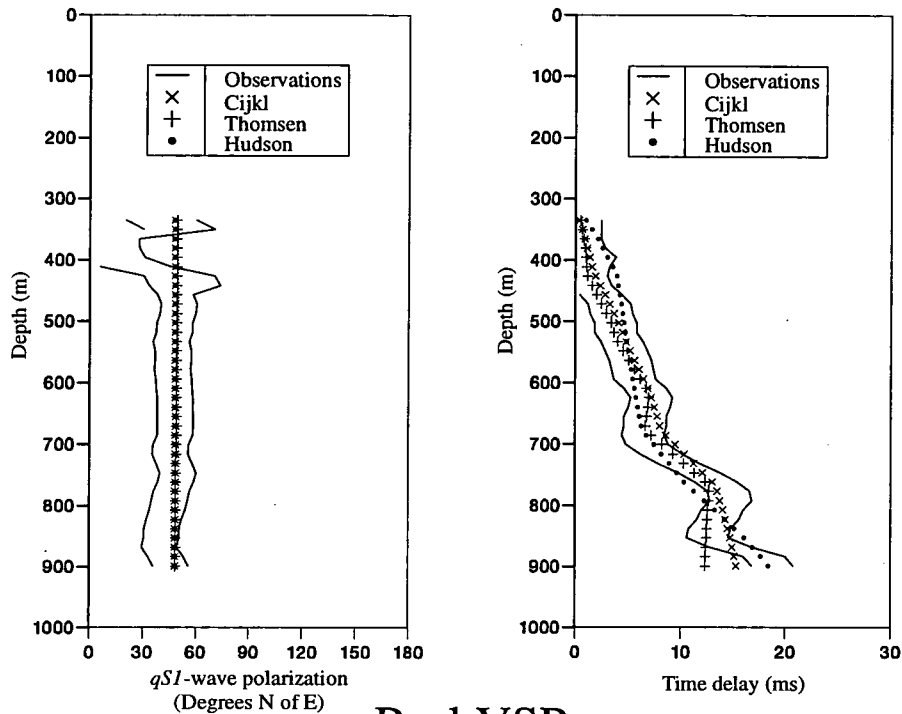
	THOMSEN		
	$\delta$	$\gamma$	$\epsilon$
ZONE 1	-0.019	-0.057	-0.185
ZONE 2	-0.376	0.121	0.223
ZONE 3	0.032	-0.006	0.083
ZONE 4	-0.261	0.057	-0.034
ZONE 5	0.376	-0.019	0.248
Inferred Crack Strike (Degrees N of E)	50°		
Inferred Crack Dip (Degrees)	11° to north west		
Misfit $f(m, \tau^o, p^o)$	0.420		

Table 5.7 - The best solution found using the GA for the Thomsen scheme.

	Cijkl				
	$\Delta c_{11}$	$\Delta c_{22}$	$\Delta c_{44}$	$\Delta c_{55}$	$\Delta c_{13}$
ZONE 1	7.14	-26.19	0.79	-3.97	-13.49
ZONE 2	-7.14	18.25	23.02	3.97	-42.06
ZONE 3	-3.97	45.24	-15.08	-29.37	5.56
ZONE 4	13.49	32.54	-3.97	-30.95	50.00
ZONE 5	50.00	-26.19	42.06	26.19	-38.89
Inferred Crack Strike (Degrees N of E)	50°				
Inferred Crack Dip (Degrees)	16° to south east				
Misfit $f(\mathbf{m}, \tau^o, \mathbf{p}^o)$	0.207				

Table 5.8 - The best solution found using the GA for the Cijkl scheme.

## 33-1 VSP



## Peel VSP

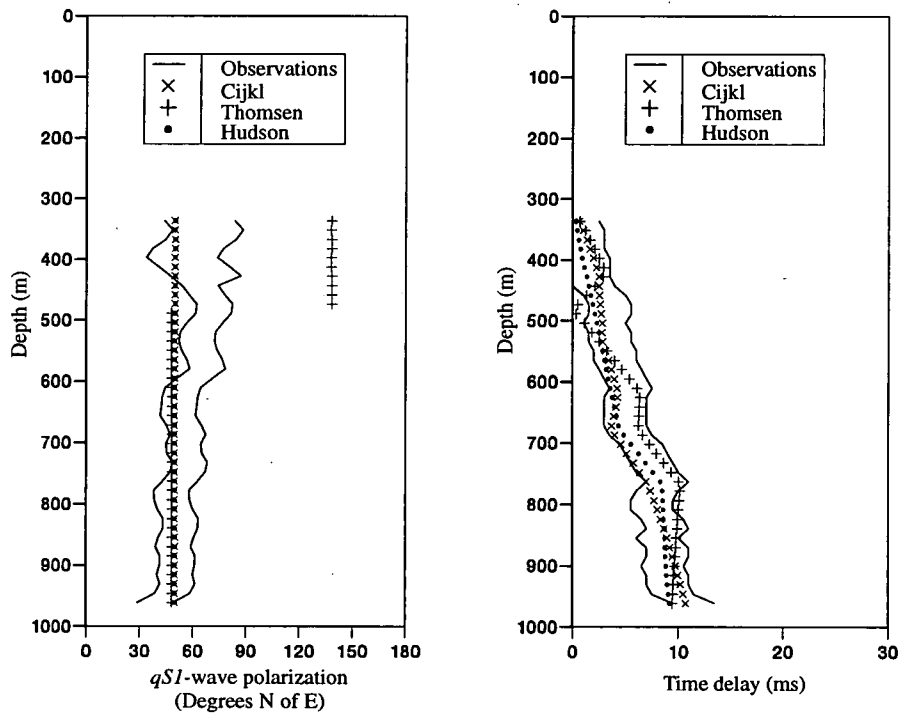


Figure 5.19 - A comparison of the observed shear-wave splitting estimates with those predicted for the best models obtained using the three parametrization schemes. The solid lines show the upper and lower bounds on the observations defined by the error estimates.

not in agreement with surface observations (Queen, personal communication), inversion results obtained using the Hudson and Cijkl schemes, inversion results from an AVSP (reported in Chapter 4) and other studies from the CBTF (Liu, Crampin and Queen 1991). For these reasons the best model obtained using the Thomsen scheme represents an unlikely solution and will not be considered in any depth.

The best models obtained using the Hudson and Cijkl representations predict the fracture orientation to be striking N50°E and dipping between 16° to 18° to the south east respectively. For both these models the predicted *qSI*-wave polarizations remain constant as a function of depth and are orientated parallel to the fracture strike. This behaviour appears to model most of the observed *qSI*-wave polarizations at depths below 600 m for the Peel and 400 m for the 33-1 VSP. For the 33-1 VSP the oscillation in the polarizations above 400 m could not be modelled. This feature appears to be related to the poor resolution of *qSI*-wave polarizations for which the associated time delay is small.

Although the crack orientation parameters for the best Hudson and Cijkl models are similar the other model parameters define different anisotropic parameters for the constituent layers. This is shown in Table 5.9 in which Thomsen parameters are calculated for the best models obtained using the Cijkl and Hudson parametrizations. It can clearly be seen that the models found using these two schemes do not represent the same solution.

In the case of the Peel VSP the rotation in *qSI*-wave polarizations observed with depth is not reproduced. Unlike the estimates from the 33-1 VSP this behaviour is not introduced after the near-surface correction although this processing step reduces this effect. The inability of the model observations to reproduce this behaviour could lie in the failure of the optimization method to converge to a better solution or in the assumptions employed in the forward modelling scheme. It is possible that the GA fails to converge to a lower misfit value since there is no proof that such methods are



zone	layer	Hudson				Cijkl			
		$\epsilon$	$\gamma$	$\delta$	% anis	$\epsilon$	$\gamma$	$\delta$	% anis
1	7	0.02	0.09	-0.06	8.2	-0.16	0.02	-0.13	2.4
	8	0.03	0.09	-0.05	8.1	-0.16	0.02	-0.13	2.4
	9	0.02	0.10	-0.07	8.4	-0.16	0.02	-0.13	2.4
2	10	0.06	0.02	0.06	2.4	0.14	0.09	-0.06	8.1
	11	0.06	0.02	0.06	2.3	0.14	0.09	-0.06	8.1
	12	0.06	0.03	0.06	2.5	0.14	0.09	-0.06	8.1
3	13	0.07	0.03	0.07	2.9	0.26	0.10	-0.14	8.8
	14	0.07	0.03	0.07	2.7	0.26	0.10	-0.14	8.8
4	15	0.28	0.12	0.24	10.0	0.08	0.20	-0.08	15.2
5	16	-0.23	0.53	-0.34	30.2	-0.25	0.06	-0.27	5.8
	17	-0.24	0.53	-0.34	30.2	-0.25	0.06	-0.27	5.8
	18	-0.24	0.53	-0.34	30.3	-0.25	0.06	-0.27	5.8

Table 5.9 - A comparison of the layer parameters for the best models obtained using the Hudson and Cijkl schemes in terms of Thomsen parameters and the % anisotropy defined as  $(V_{qS1} - V_{qS2})/V_{qS1}$  for propagation directions perpendicular to the symmetry axis.

able to find the global minima (Goldberg 1989). The alternative explanation of restrictive assumptions which do not allow a realistic representation of the problem is now addressed. Essentially there are three main assumptions used in the forward modelling. These are the approximation of the geology at the test site to be a one dimensional stack of plane layers, the use of a ray tracing method and the representation of the seismic anisotropy to be transversely isotropic medium with an arbitrary orientation of the symmetry axis which is constant with depth. This first assumption is judged to be valid through the consideration of geological data from the CBTF. The second assumption of the ray tracing method appears justified through the comparison tests presented earlier. The remaining assumption of transverse isotropy may be inappropriate since horizontal fine layering and sub-vertical fracturing, both of which are likely to be present at the test site, lead to equivalent media of the monoclinic symmetry class. For near-vertical propagation directions the observed anisotropy will be dominated by the near-vertical fractures. On moving away from the vertical direction the fine layering anisotropy becomes increasingly dominant and for some systems this leads to the  $qSI$ -wave shear-wave to be polarized in the radial direction. This combination of sub-vertical fracturing and fine layering anisotropy can be used to explain the measured  $qSI$ -wave behaviour observed for both VSPs. For the 33-1 VSP the source is located along the azimuth N279°E. This implies that shear-wave energy is propagating closer to the supposed fracture system striking at N50°E and dipping 18° to the south east. This compares with the Peel VSP source which is located approximately downdip along the azimuth N122°E. Thus the  $qSI$ -wave polarizations observed from the 33-1 VSP will be dominated by the fracturing anisotropy whereas the  $qSI$ -wave polarizations for the Peel VSP will be more sensitive to the fine layering anisotropy. Equal area plots for the situations described are shown in Figure 5.20. This effect may also account for the inconsistency in crack strikes inferred from the AVSP inversion results and the inversion results for the near-offset VSPs. For the AVSP the inverted crack strike is N75°E whereas the near-offset inversions suggest a crack strike of N50°E. The AVSP sampled a narrow range of incidence angles at approximately 25° which

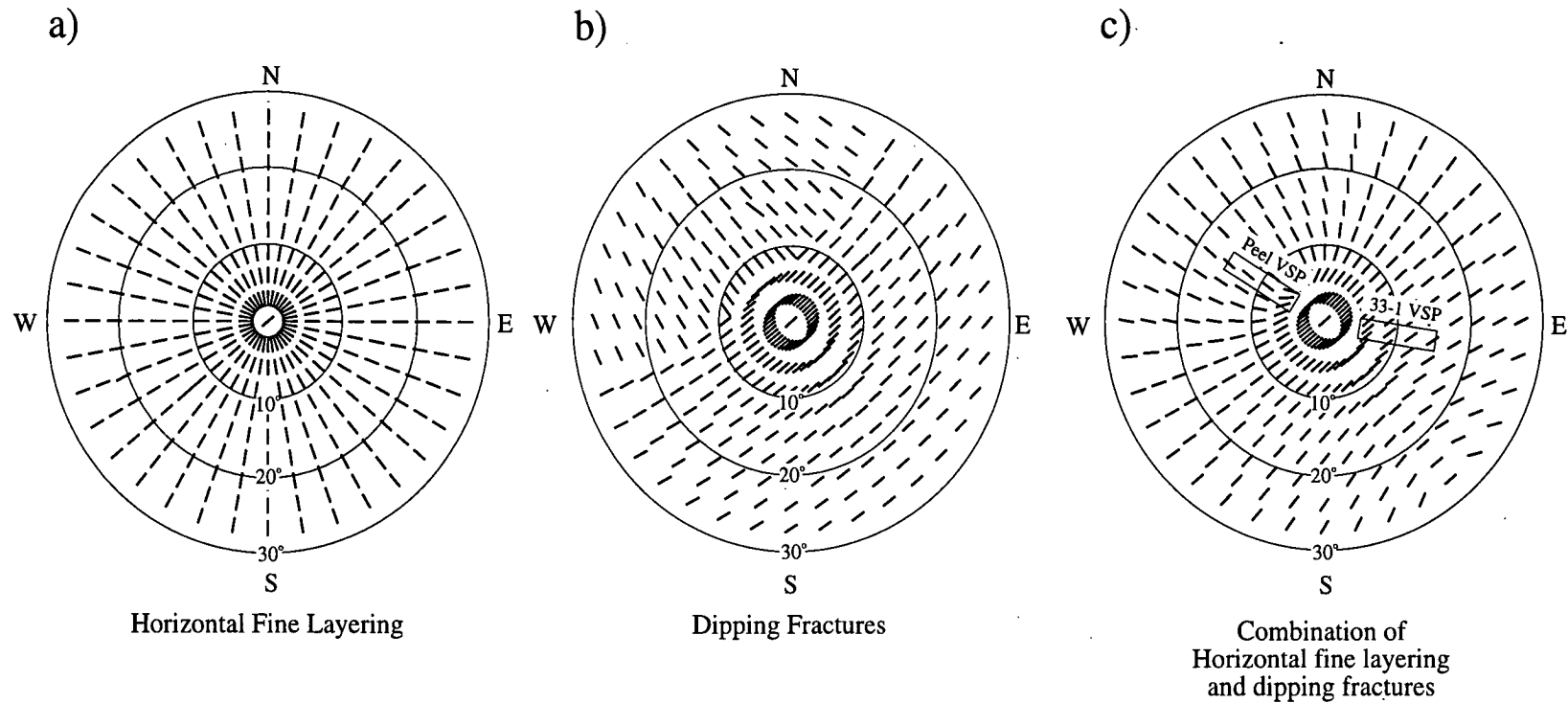


Figure 5.20 - Lower hemisphere equal area plots showing  $qSl$  polarizations between incidence angles of  $0^\circ$  and  $30^\circ$  for a) a TIV medium constructed for horizontal fine layering b) a TI medium constructed from Hudson cracks dipping  $24^\circ$  to the south east and striking  $N50^\circ E$  and c) a monoclinic medium constructed by combining the horizontal fine layering and the dipping crack system. Marked on this figure are the two angular apertures corresponding to the Peel and 33-1 VSPs. For the 33-1 VSP the  $qSl$  polarizations are aligned with the crack strike whereas the polarizations measured using an aperture corresponding to that used for the Peel VSP show a rotation towards the radial direction with increasing incidence.

compares with incidence angles of approximately  $11^\circ$  for the shallowest recording in the near-offset VSPs. Thus the AVSP results will be more sensitive to the fine layering. This may account for the inability of the dipping hexagonal or orthorhombic models to fully explain the observed radial  $qS1$ -wave polarizations on some azimuths. Unfortunately a forward modelling scheme able to produce accurate results for monoclinic symmetry systems could not be efficiently implemented within the GA.

The majority of the predicted time delays fall within the estimated error bounds for both the Hudson and Cijkl models (Figure 5.19). The poorest agreement below 800 m for the 33-1 VSP. In this region the observed time delays decrease between 800 m and 850 m and increase below this depth. For this depth range the raypaths are essentially vertical with the straight line incidence angles ranging between  $2.58^\circ$  and  $2.43^\circ$ . Since the incidence angle is essentially the same over this interval it is unlikely that this variation is due to anisotropic propagation effects. Decreases in time delay can be explained in terms of multiple splitting which may be caused by a change in the symmetry system or its orientation. Such a change can be introduced through a variation in the fracture orientation with depth. However, the implemented ray tracing scheme assumes there is no such change and this effect cannot be modelled with the present inversion scheme. It should be emphasized that this assumption is necessary to construct an efficient forward modelling scheme and is not a limitation of either ray tracing or the GA optimization scheme.

#### *Non-uniqueness*

The more significant models sampled by the GA for which  $f(\mathbf{m}, \tau^o, \mathbf{p}^o) < 1.0$  are shown in distance-misfit scatter plots (Figure 5.21). These clearly show that the problem is non-unique. For the Hudson, Cijkl and Thomsen schemes there are, respectively, 233, 176 and 254 different models within this window of acceptable solutions (defined by  $f(\mathbf{m}, \tau^o, \mathbf{p}^o) < 1.0$ ). For both the Cijkl and Thomsen inversion results linear features can be identified in the scatter plots along which the sampled models are

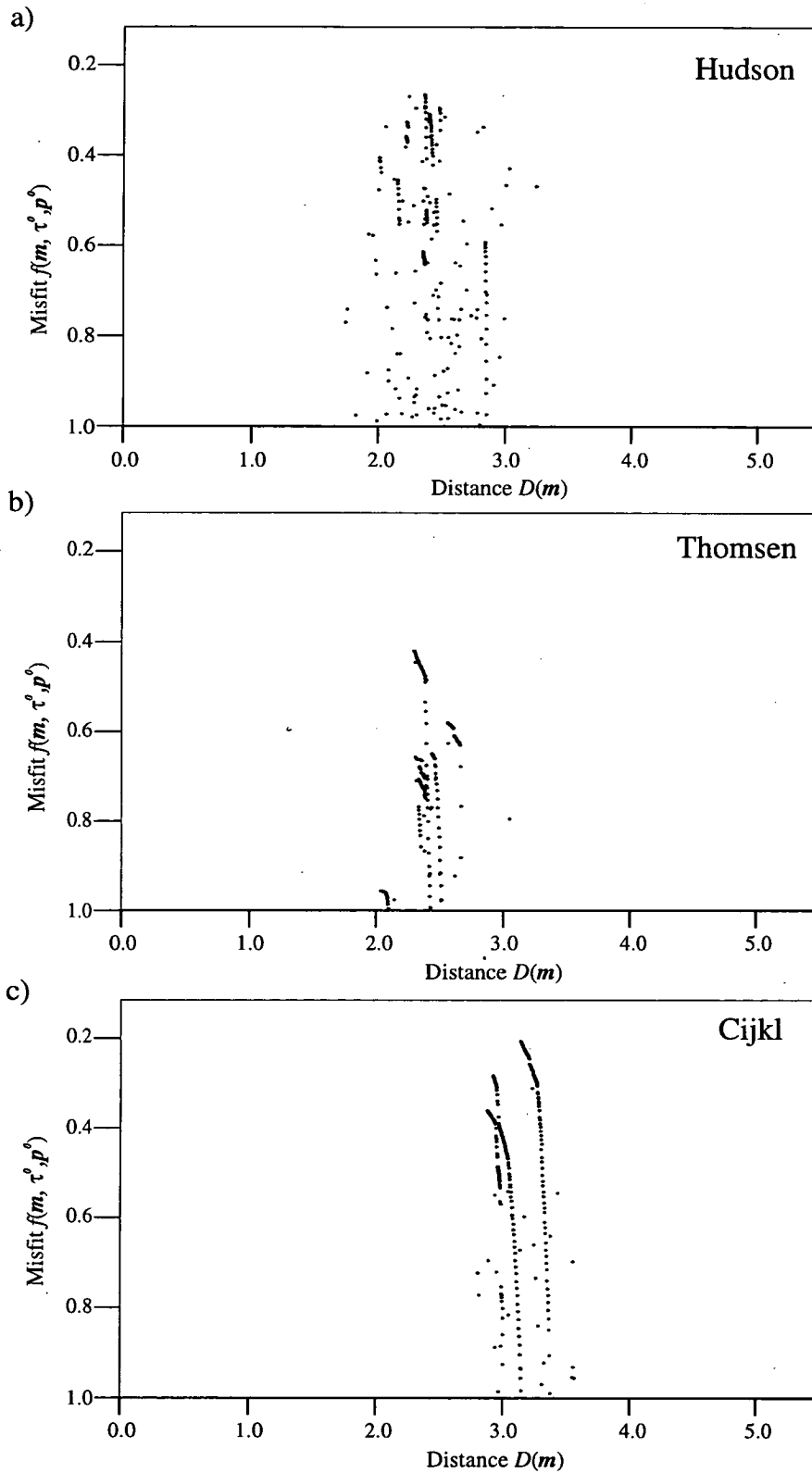


Figure 5.21 - Distance-misfit plots showing models sampled by the GA for a) the Hudson, b) the Thomsen and c) the Cijkl parametrization schemes.

aligned. These are characteristic of the local search mechanism, Gradient-bit improvement, for which a small stepwise improvement is applied to the best model in each generation. Inspection of Figure 5.21 indicates that it is this local search mechanism that dominates the convergence for the Cijkl and Thomsen schemes. Conversely, these features are mostly absent from the Hudson results so that it would appear that most of the convergence for this representation is due to the GA search mechanism. Further evidence supporting this interpretation can be obtained using a graph binning technique, such as that used by Sen and Stoffa (1992). For these plots a likelihood function is introduced which is used to weight the solution parameters. The misfit function given in equation 5.3 is based upon the minimization of a least squares quantity implying that a suitable form for the likelihood function,  $L$ , is (Tarantola 1987)

$$L(f) = e^{-\frac{1}{2}f}; \quad (5.4)$$

where  $f$  is the misfit function defined in equation 5.3. I apply this graph binning procedure to solutions within the window of acceptable solutions and normalize the resulting bins. The solution bins for the Hudson models show that the parameters are sampled across a wide parameter range compared with the results obtained using the Thomsen and Cijkl schemes (Figure 5.22). The discrete nature of the solution bins for the Thomsen and Cijkl models is due, as suggested by the distance misfit plots, to the dominance of the local search mechanism for which many similar models are generated about the best model.

The non-uniqueness associated with the orientation of anisotropy is shown using a scatter plot for which each dot represents a model sampled by the GA and is shaded according to that model's misfit value (Figure 5.23). The scatter plot for the Hudson results clearly show a cluster of models about the best solution ranging between crack strikes of N35°E and N65°E and crack dips between 10° and 40° to the south east. The distribution of solutions for the Cijkl and Thomsen results show a similar

## HUDSON

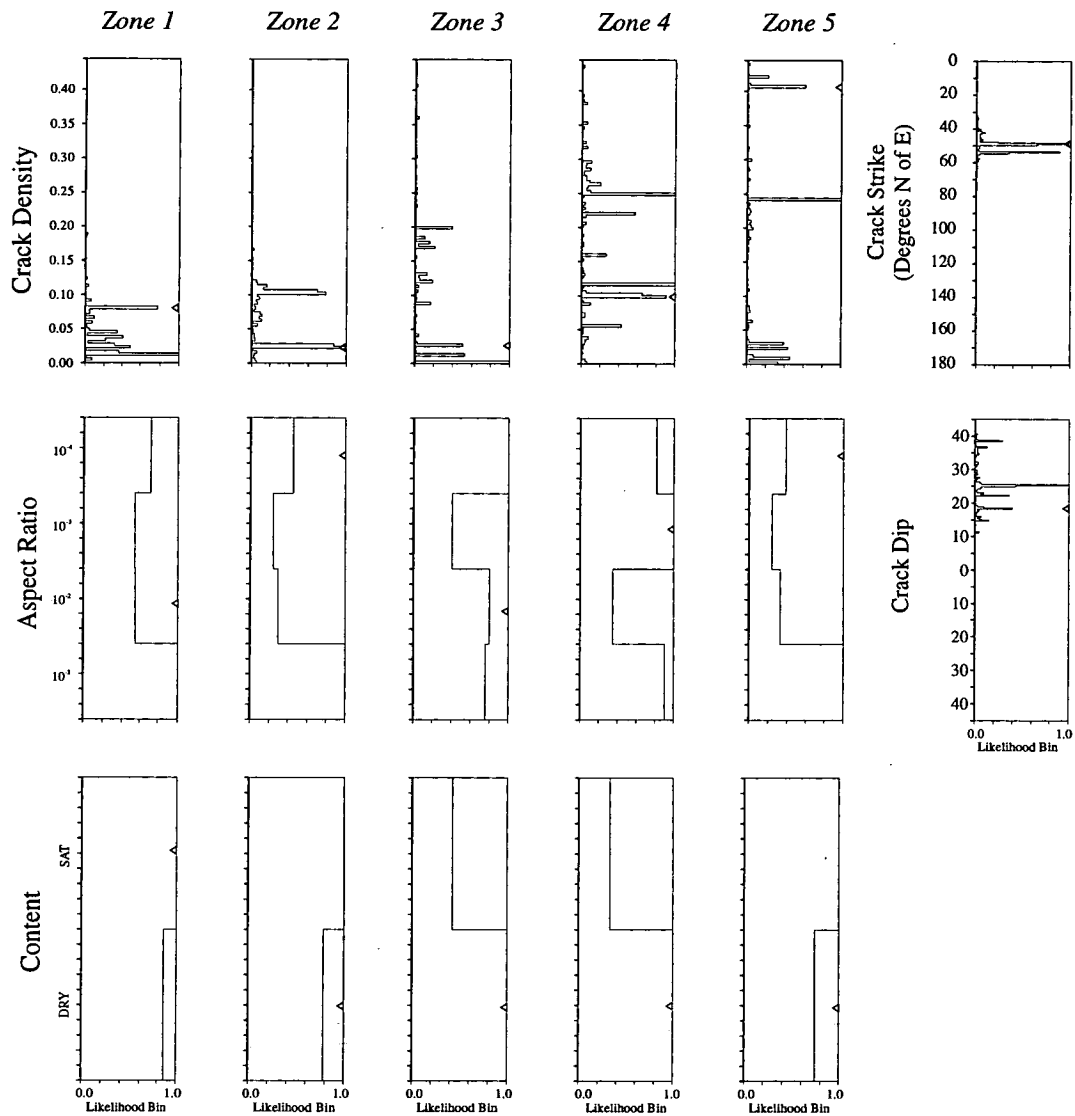


Figure 5.22 - Binned likelihood functions for models within the domain of acceptable solutions defined by  $f(m, \tau^0, p^0) < 1.0$  using a) Hudson b) Thomsen and c) Cijkl parametrizations. Each parameter bin is normalized so that the maximum value in the bin is 1.0. The small triangles indicate the best solution found using the GA.

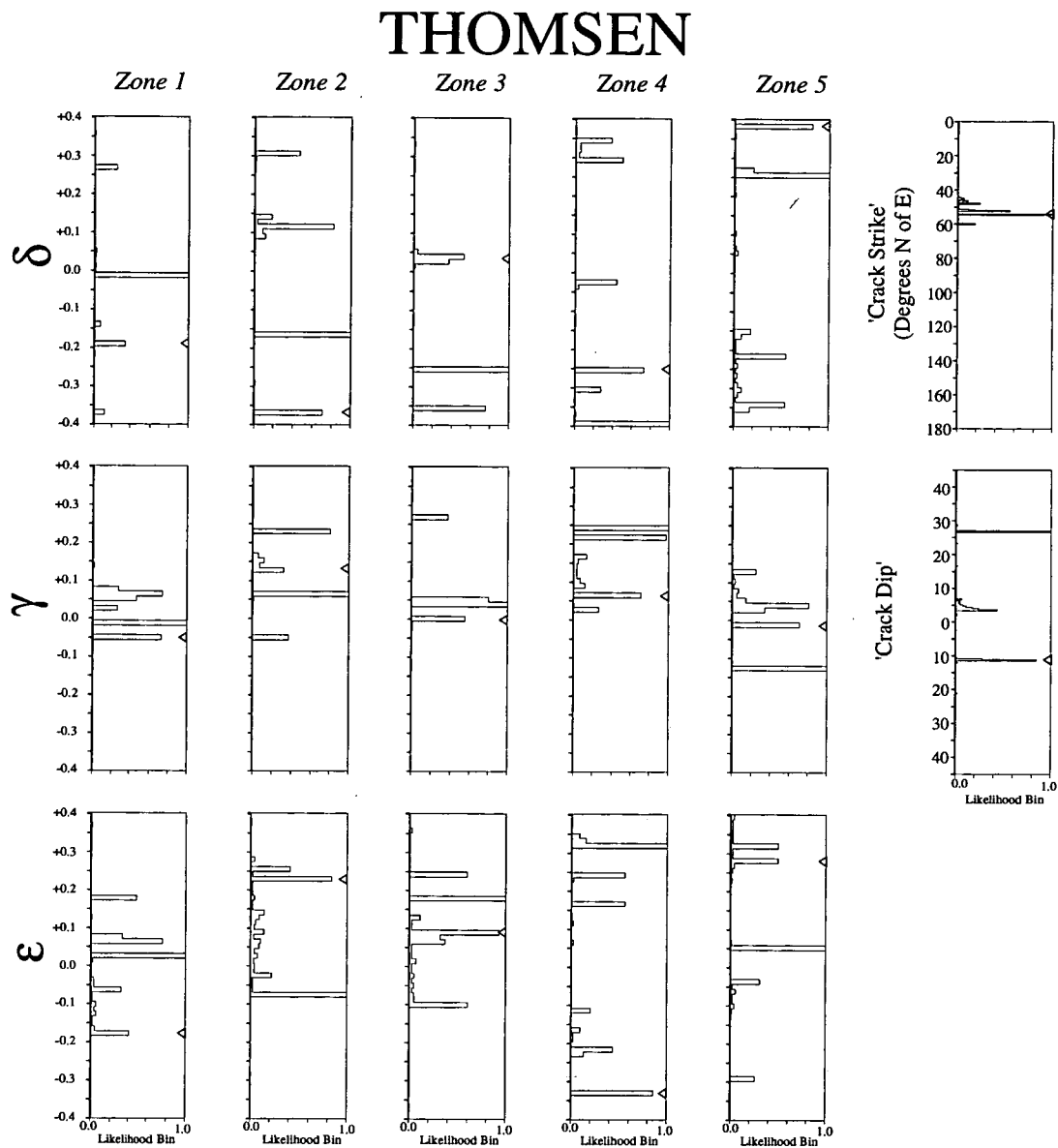


Figure 5.22(b)



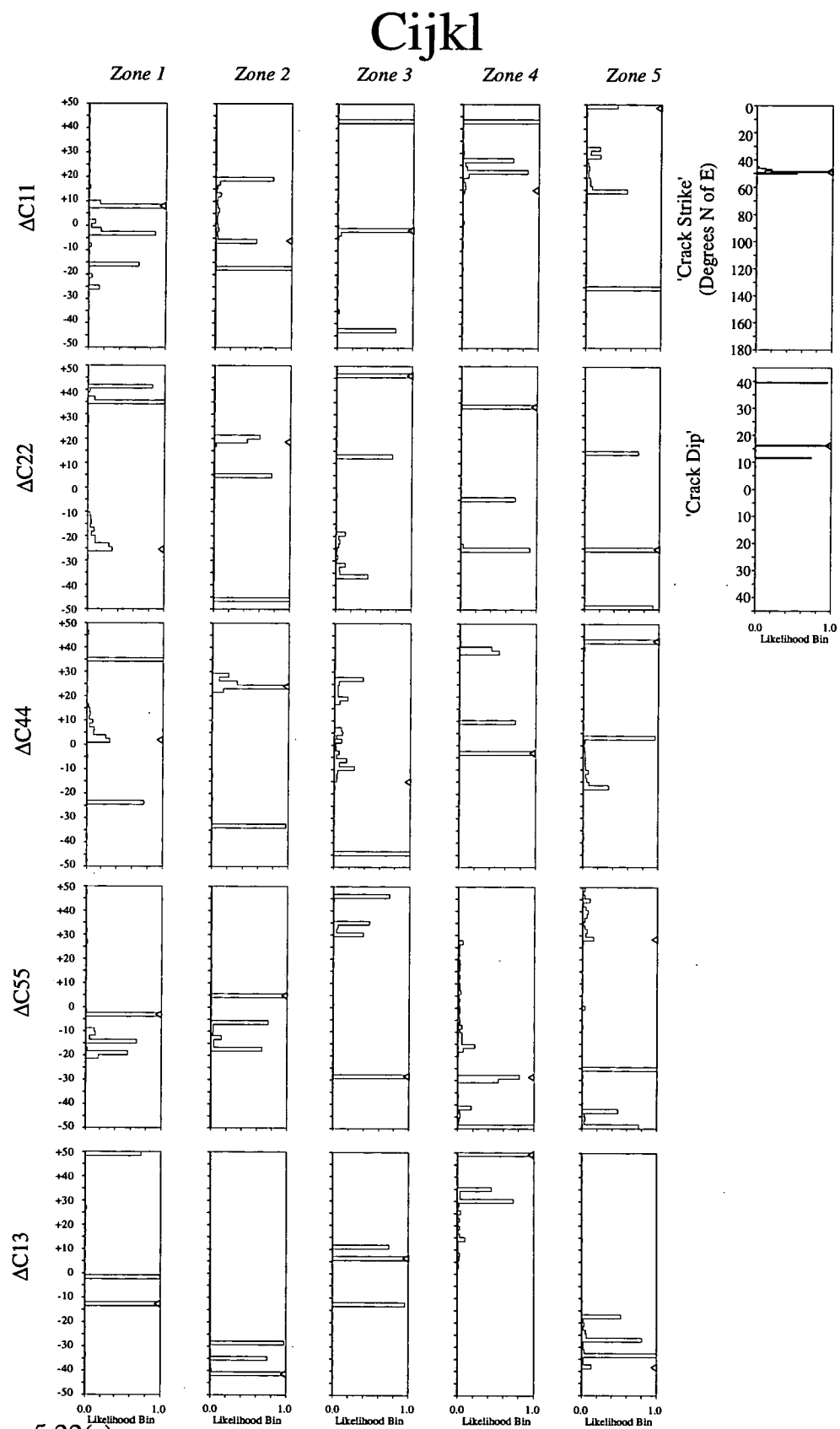


Figure 5.22(c)

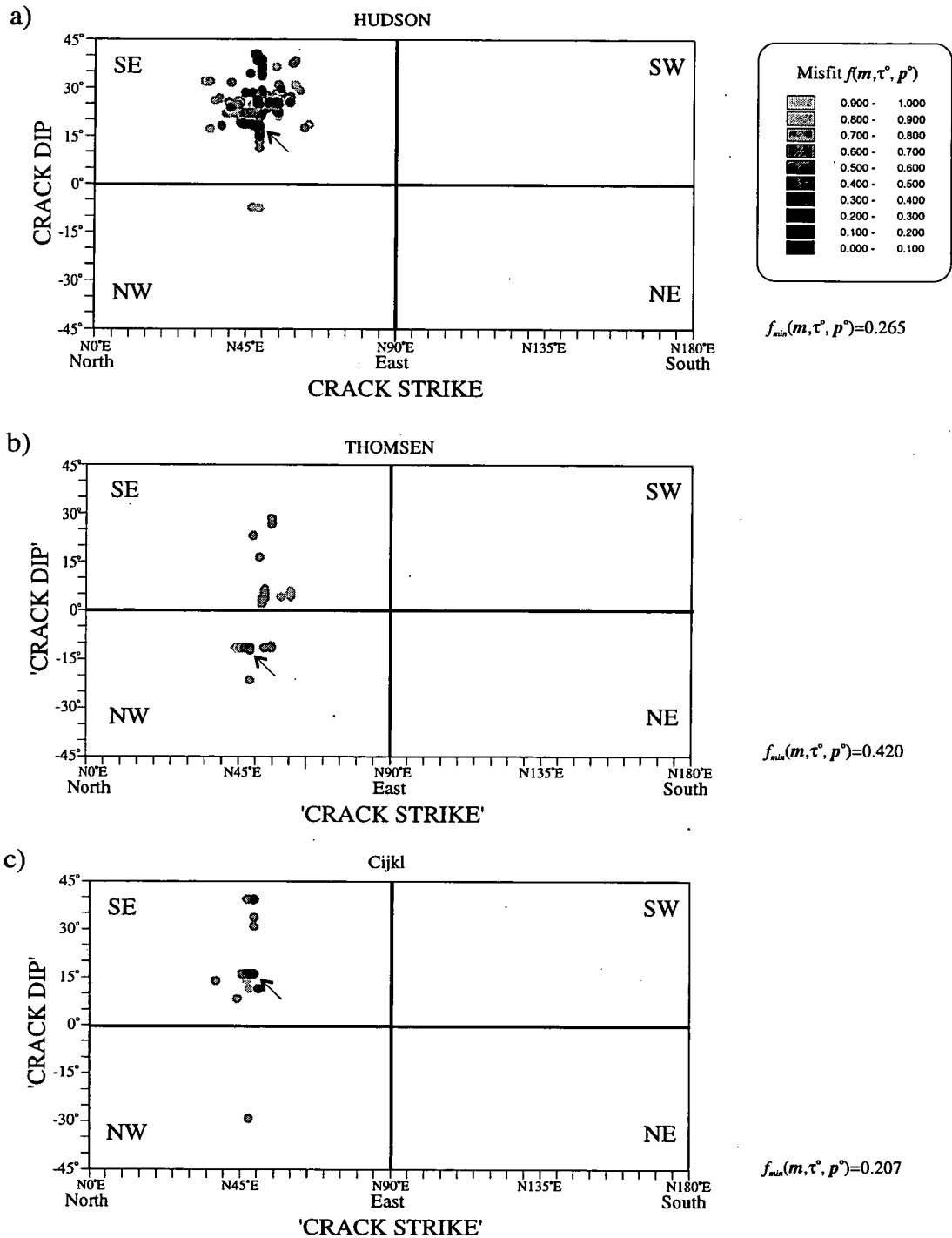


Figure 5.23 - Scatter plot of crack strike versus crack dip for the models sampled using the GA for a) the Hudson, b) the Thomsen and c) the Cijkl representations. The dots representing the sampled models are coloured according to the solution misfitness. The direction of dip is indicated in the corner of each quadrant. The arrows indicate the best solution in each plot.

distribution although the sampling is more sparse. Again, this is due to convergence through the application of the local search procedure. The fracture dips for the better models are concentrated about values of approximately  $20^\circ$  to the south east. This clustering is controlled by the time delay observations which for the 33-1 VSP are considerably larger than those observed for the Peel VSP. The reason for this can be clearly explained using Figure 5.24 in which velocity sheets and lower hemisphere equal area plots of time delays are shown for equivalent anisotropic media constructed from vertical fractures and sub-vertical fractures. Referring to the cross sections of both the velocity sheets and the time delay plots in the plane perpendicular to the crack strike, it can be seen that the seismic anisotropy for the dipping fractures is no longer symmetrical in the vertical plane. If we now consider two near offset VSPs with sources located along diametrically opposite azimuths, which is approximately the case for the Peel and 33-1 VSPs, then the observed shear-wave birefringence will be the same for vertical fracture anisotropy. However, for the sub-vertical fracture system the shear-wave birefringence is greater for the VSP transmitting shear-waves along the fracture plane than for the VSP located on the opposite azimuth, provided that the source azimuth is not coincident with the fracture strike. I propose that this technique of opposite azimuth VSP surveys may be of use in the detection and measurement of sub-vertical fracture systems.

It appears that the Hudson parametrization, although not producing the best overall model, represents a better scheme for inclusion to the GA since the more significant parts of the model space are sampled more extensively. However, such an interpretation is difficult to make because the different discretization ranges cannot readily be compared for the different parametrizations. It may be that the higher sampling density achieved using the Hudson scheme is because this scheme already represents a sub-set of acceptable solutions. Alternatively, it is possible that the suitability of the Hudson scheme lies in the formation of the low order schemata which are essential to the GA's performance.

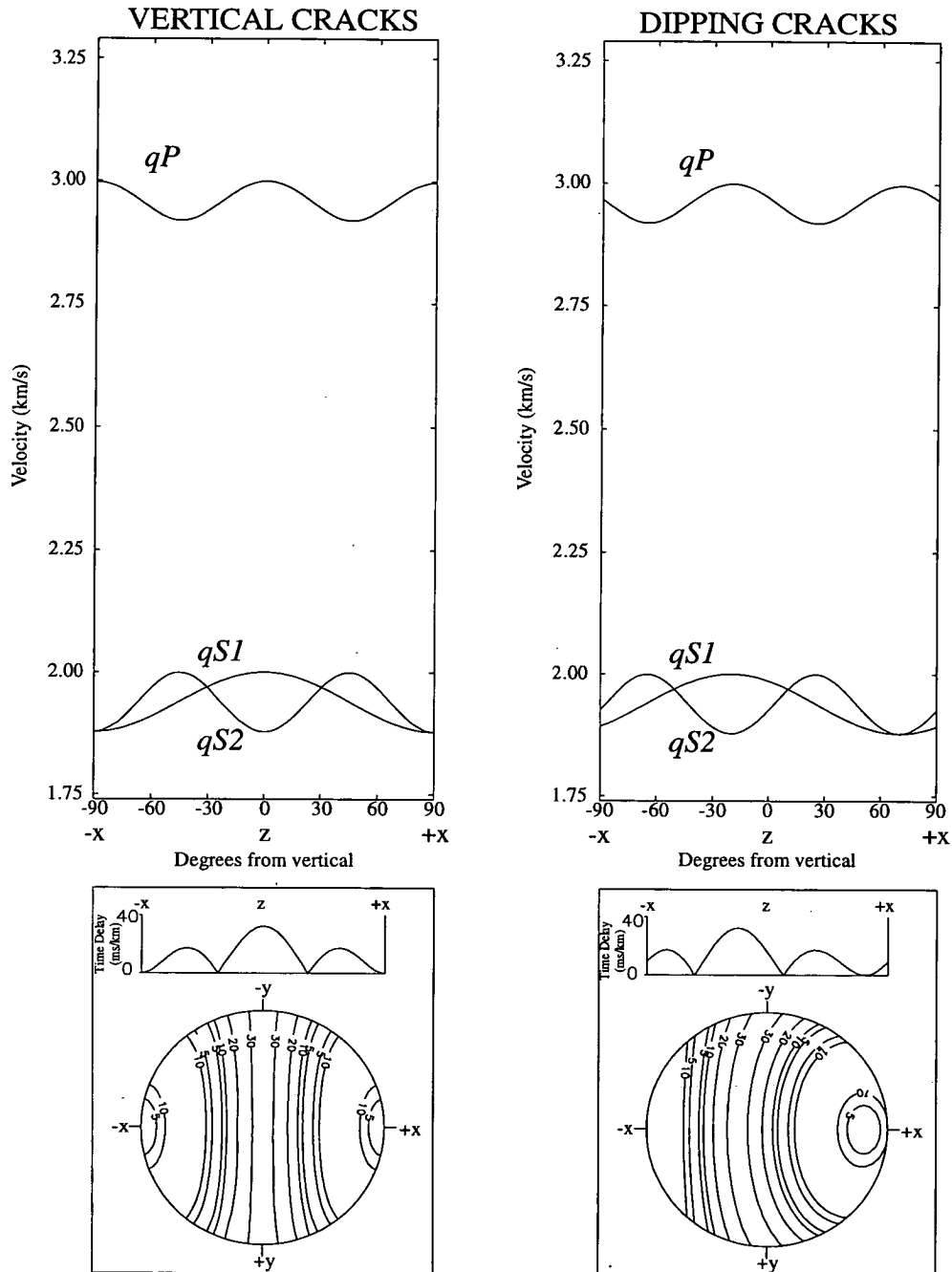


Figure 5.24 - A comparison of anisotropic behaviour for materials constructed from vertical (left) and sub-vertical fractures (right). The isotropic properties are  $V_p=3.0$  km/s,  $V_s=2.0$  km/s and  $\rho=2.0$  g/cm<sup>3</sup> with embedded Hudson type saturated cracks of  $CD=0.05$  and  $AR=0.001$ . The sub-vertical cracks are rotated 20° from the the vertical. The lower plots show the time delay variations over a lower hemisphere of propagation directions.

### Resolution

I calculate the model parameter resolution by computing cross sections through the model space of misfit values about the best solution. I achieve this by sweeping through one component of the model vector whilst keeping all other components equal to the best model parameters. The resolution for each parameter is calculated using a measure of dispersion,  $\sigma$ , given by

$$\sigma(m_i) = \left[ \sum_{m_i^L}^{m_i^U} (m_{i,best} - m_i)^2 L(f) \right]^{1/2} ;$$

where  $L$  is the likelihood function defined in equation 5.4 and  $m_i$  is the  $i$  th component of the model vector  $\mathbf{m}$ .  $m_{i,best}$  is the  $i$  th component for the best model.  $m_i^U$  and  $m_i^L$  are the upper and lower discretization bounds for the  $i$  th parameter. The quantity  $\sigma^2(m_i)$  is equivalent to  $i$  th diagonal element of the covariance matrix (Tarantola 1987).

The results of this analysis are given in Tables 5.10, 5.11 and 5.12 and in cross section plots of the likelihood function for each component of the model vector (Figure 5.25). For the Hudson and Cijkl results the dispersion is calculated to be less than  $10^\circ$  for both the crack strike and the crack dip. The crack dip cross section plots for the Hudson and Cijkl reveal a bimodal function with two narrow peaks located at approximately opposite dips with the most significant peak located at about  $20^\circ$  to the south east (Figure 5.25). The secondary maxima are located outside the window of acceptable solutions as indicated by the shaded region in the cross section plots. If this secondary solution is omitted from the dispersion calculation then the fracture dip resolution reduces to less than  $1^\circ$ . To identify the source of this secondary solution I construct cross section plots for the separate time delay and  $qSI$ -wave polarization misfit terms in equation 5.3 (Figure 5.26). Plots are shown only for the Hudson results since the crack orientation cross sections obtained for the Cijkl scheme shows the same behaviour. The crack dip cross section reveals that the

	HUDSON		
	$\sigma(CD)$	$\sigma(AR)$	$\sigma(CT)$
ZONE 1	0.039	1.3	0.8
ZONE 2	0.039	2.0	0.9
ZONE 3	0.19	2.0	0.9
ZONE 4	0.16	2.0	0.9
ZONE 5	0.19	2.0	0.7
$\sigma(\text{Crack Strike})$	8.0°		
$\sigma(\text{Crack Dip})$	9.3°		

Table 5.10 - Resolution estimates for the Hudson parametrization results. Note that the AR parameter is based on a logarithmic function.

	THOMSEN		
	$\sigma(\delta)$	$\sigma(\gamma)$	$\sigma(\epsilon)$
ZONE 1	0.25	0.01	0.20
ZONE 2	0.38	0.02	0.23
ZONE 3	0.45	0.11	0.34
ZONE 4	0.01	0.02	0.37
ZONE 5	0.80	0.07	0.29
$\sigma(\text{Inferred Crack Strike})$	8.1°		
$\sigma(\text{Inferred Crack Dip})$	13.5°		

Table 5.11 - Resolution estimates for the Thomsen parametrization results.

	Cijkl				
	$\sigma(\Delta c_{11})$	$\sigma(\Delta c_{22})$	$\sigma(\Delta c_{44})$	$\sigma(\Delta c_{55})$	$\sigma(\Delta c_{13})$
ZONE 1	20.30	19.39	5.92	12.33	15.97
ZONE 2	20.83	19.97	5.71	8.13	30.55
ZONE 3	30.65	41.10	20.47	28.49	33.46
ZONE 4	25.84	20.66	16.43	21.60	50.00
ZONE 5	50.00	36.51	17.92	28.93	37.45
$\sigma(\text{Inferred Crack Strike})$	8.4°				
$\sigma(\text{Inferred Crack Dip})$	8.8°				

Table 5.12 - Resolution estimates for the Cijkl parametrization results.

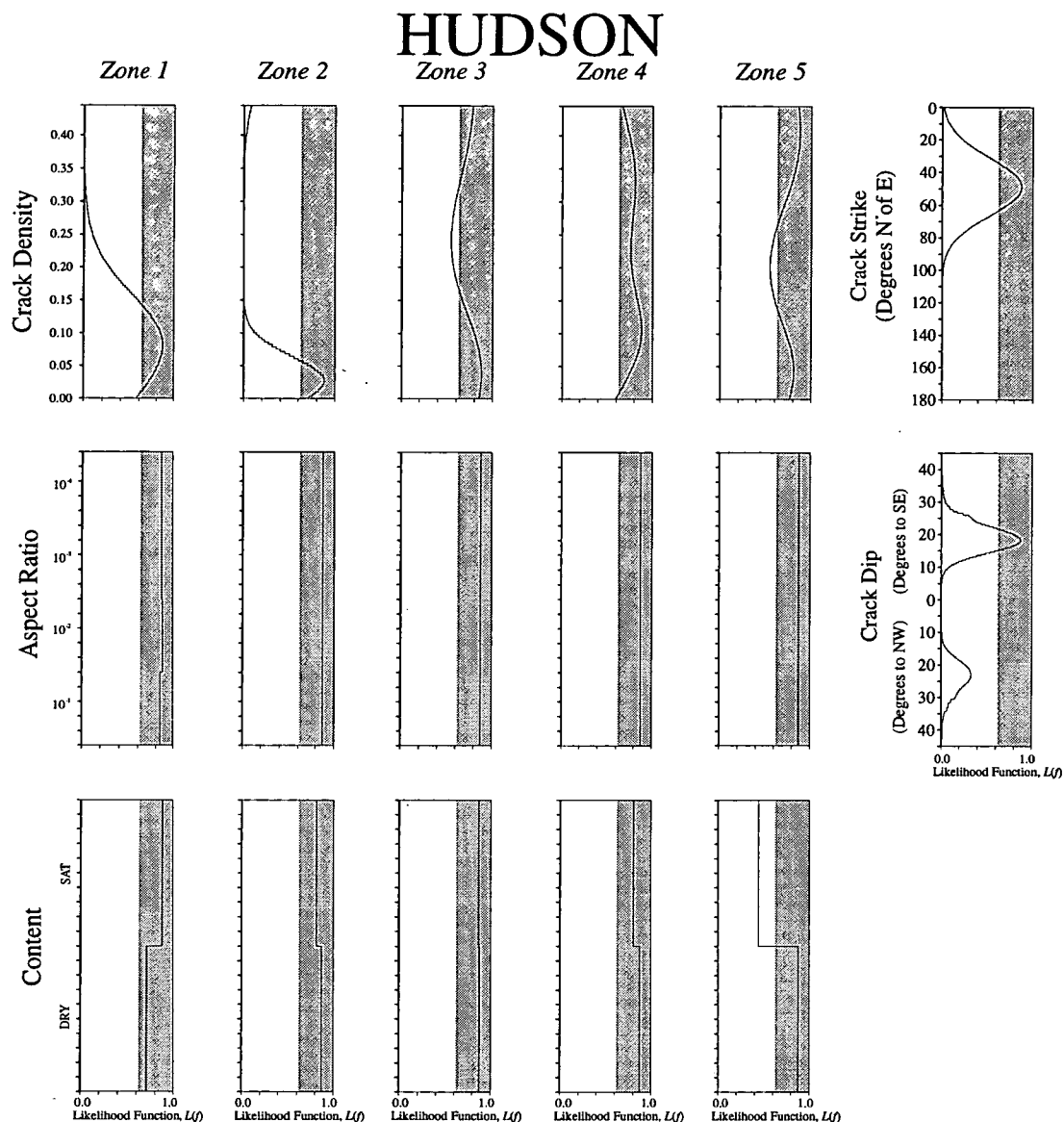


Figure 5.25 - Likelihood cross sections plots about the best model found by the GA using a) the Hudson b) the Thomsen and c) the Cijkl parametrization schemes. The shaded regions indicate the range of acceptable solutions satisfying the condition  $f(m, \tau^0 p^0) < 1.0$ .



# THOMSEN

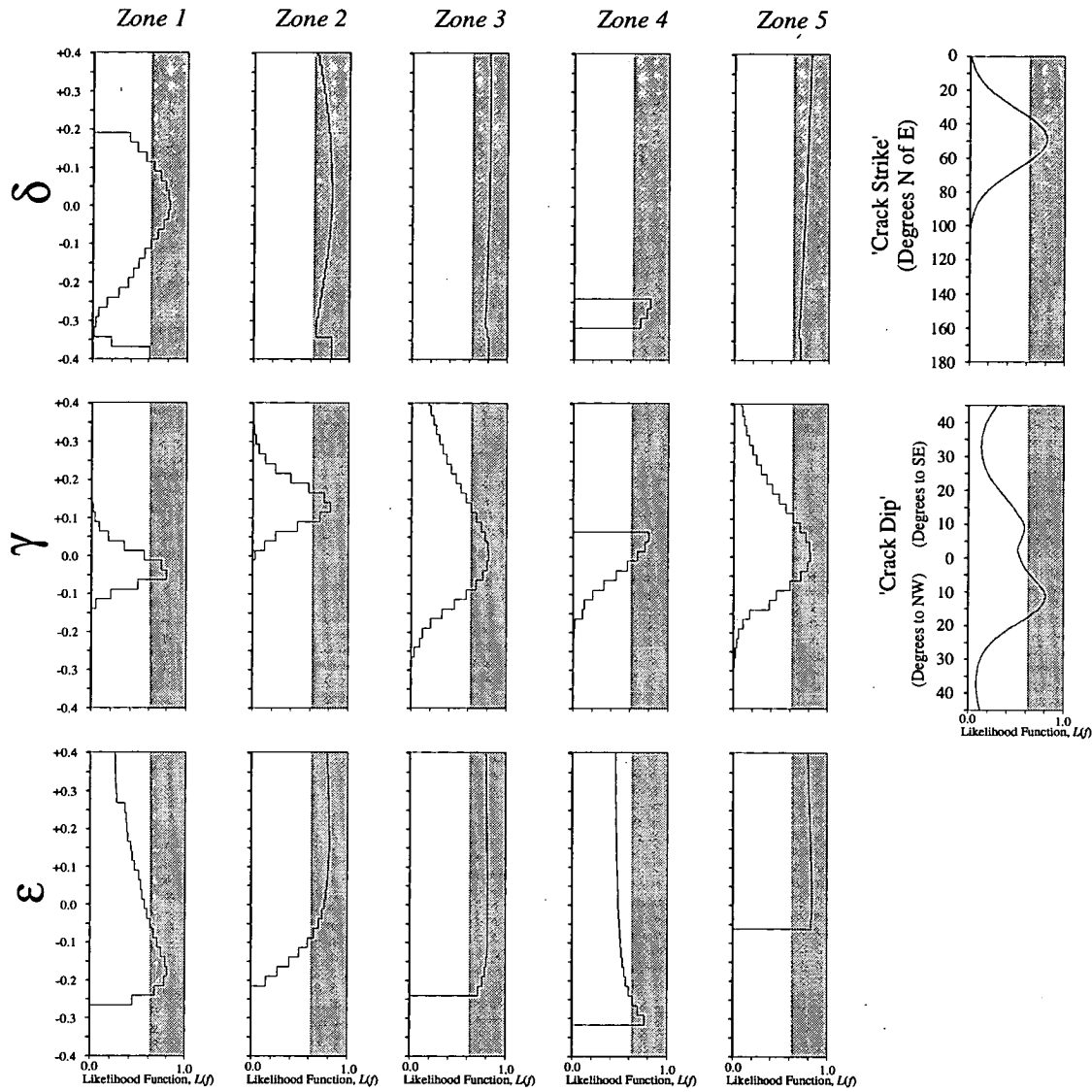


Figure 5.25(b)

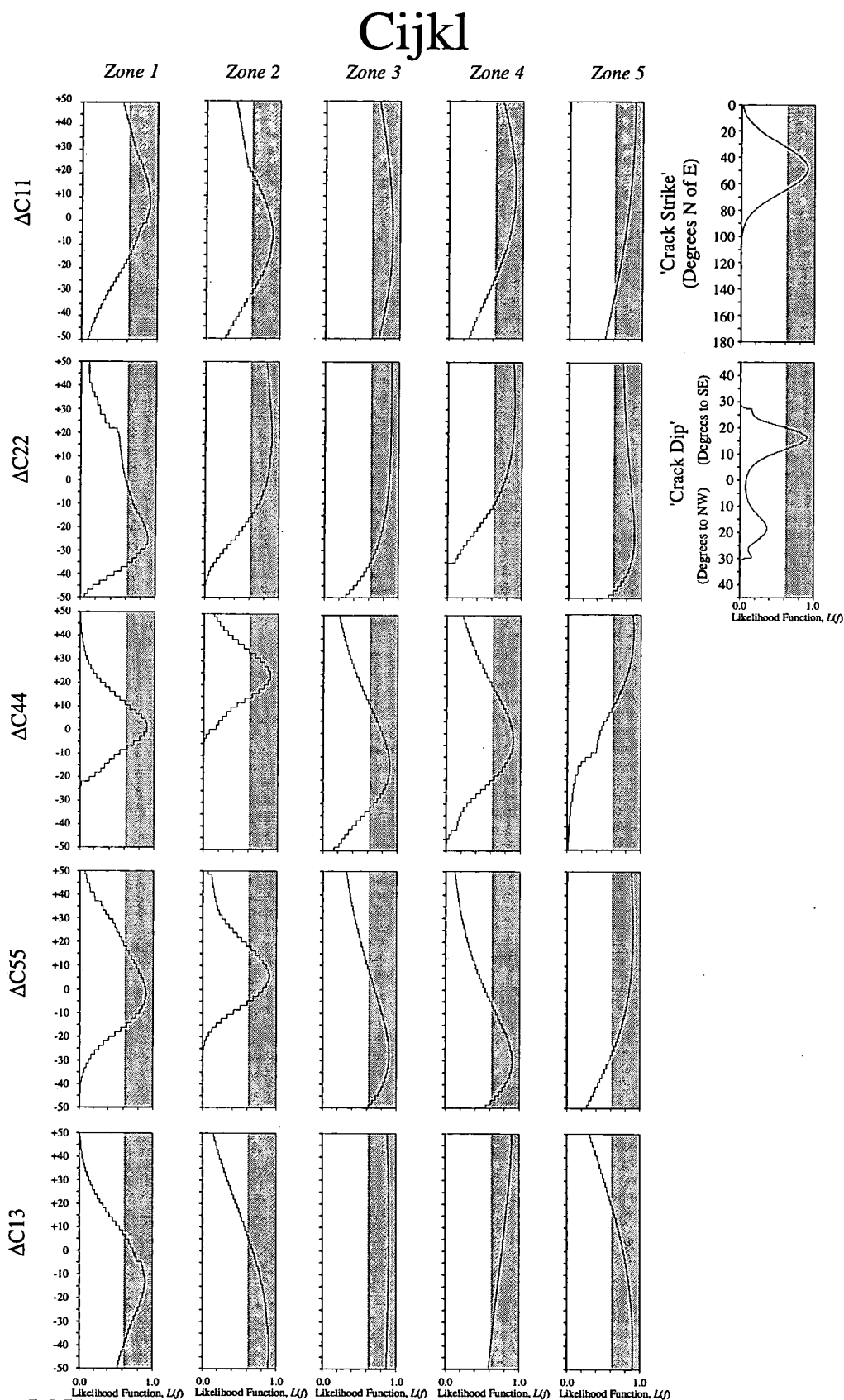


Figure 5.25(c)

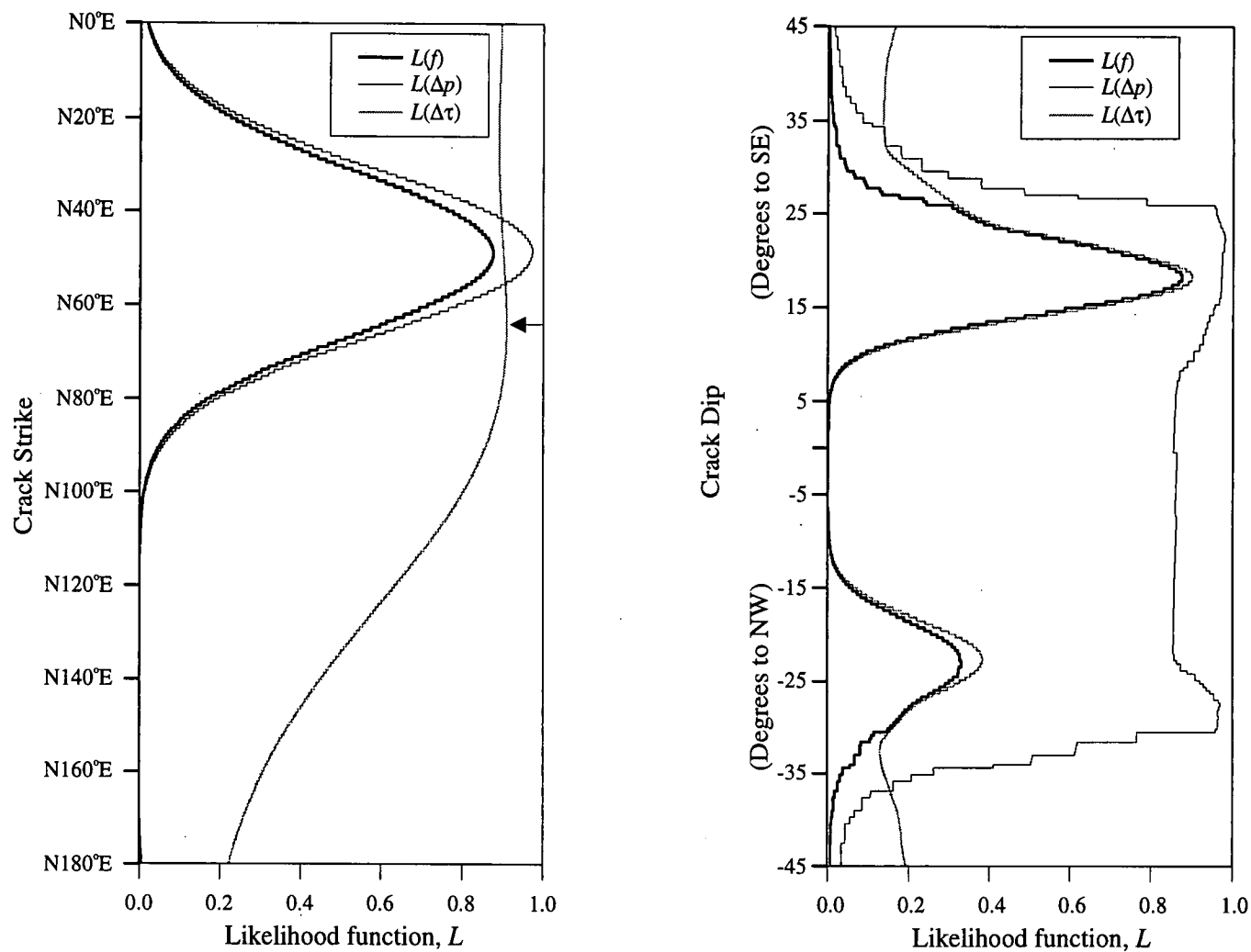


Figure 5.26 - Cross-sections through model space about best Hudson model found by the GA. The curves correspond to the likelihood functions for the misfit function and the separate time delay and  $qS1$ -wave polarization misfit terms. The arrow indicates the maxima occurring for cracks striking at N65°E in the time delay likelihood function

contribution from the  $qSI$ -wave polarization misfit is essentially constant between dips of  $\pm 25^\circ$ . Beyond this range the likelihood function rapidly decreases to zero. This cutoff is due to the rapid changes in the predicted  $qSI$ -wave observations which occur for these large values of dip as the line singularity is sampled. The time delay likelihood function is bimodal with well defined peaks at dips of  $18^\circ$  to the south east and  $24^\circ$  to the north west. The peak located at  $18^\circ$  to the south east corresponds to the best model found by the GA using the Hudson scheme. Thus it appears that the crack dip is essentially determined by the time delay misfit term. This compares with the crack strike which is determined by the  $qSI$ -wave polarization misfit term (Figure 5.26). A possible explanation for this bi-modality is a lateral variation in the anisotropy between the two wells leading to data which is inconsistent with a single model. To test this supposition I construct an ideal data set using a ray tracing method corresponding to the two near-offset VSP geometries for the best Hudson model. Crack orientation cross sections are now calculated for this noise free and consistent dataset to see if the secondary maxima is eliminated (Figure 5.27). The cross sections show an almost identical form to that obtained with the observed dataset. This demonstrates that lateral variations are not responsible for the bi-modality in the cross sections. Instead it appears that it is the acquisition geometries for these two near-offset VSPs which leads to this behaviour.

The Hudson parameters of aspect ratio and crack content are not well resolved. This low resolution is probably related to the limited sampling of incidence angles by the near-offset VSPs. The resolution for the crack density is better than that obtained for the aspect ratio parameters and crack content but is still poor. An improvement in the crack density resolution could be achieved through an improvement in the accuracy of the time delay measurements. This implies that the resolution of crack density is coupled to the time delay resolution. Unfortunately, the error estimate of 2 ms is thought to be a realistic estimate which further processing will not reduce.

The cross section plots for the Cijkl scheme generally reveal a broad unimodal

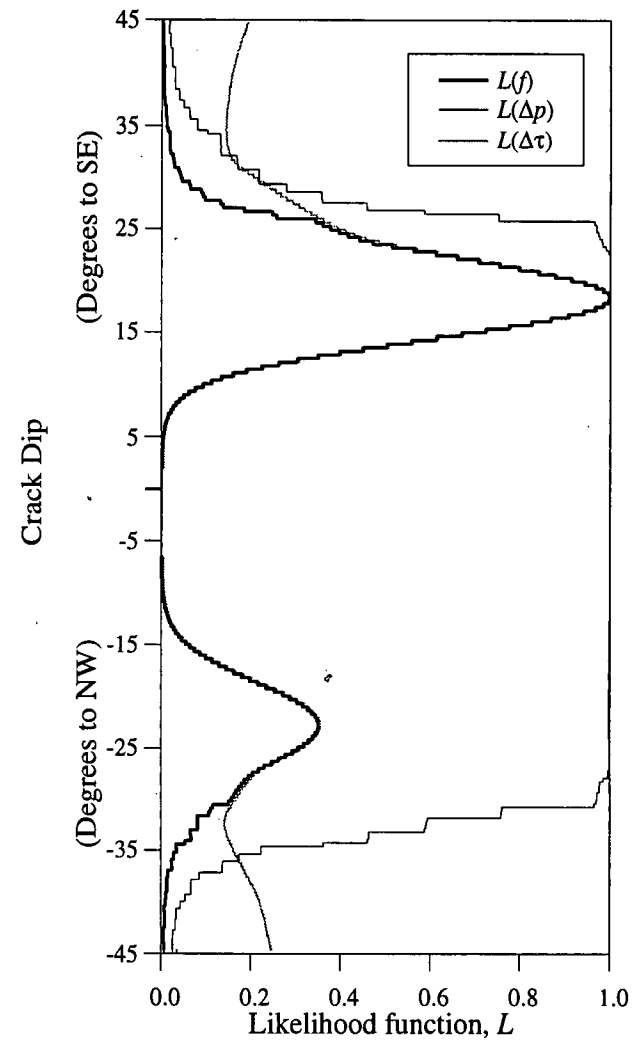
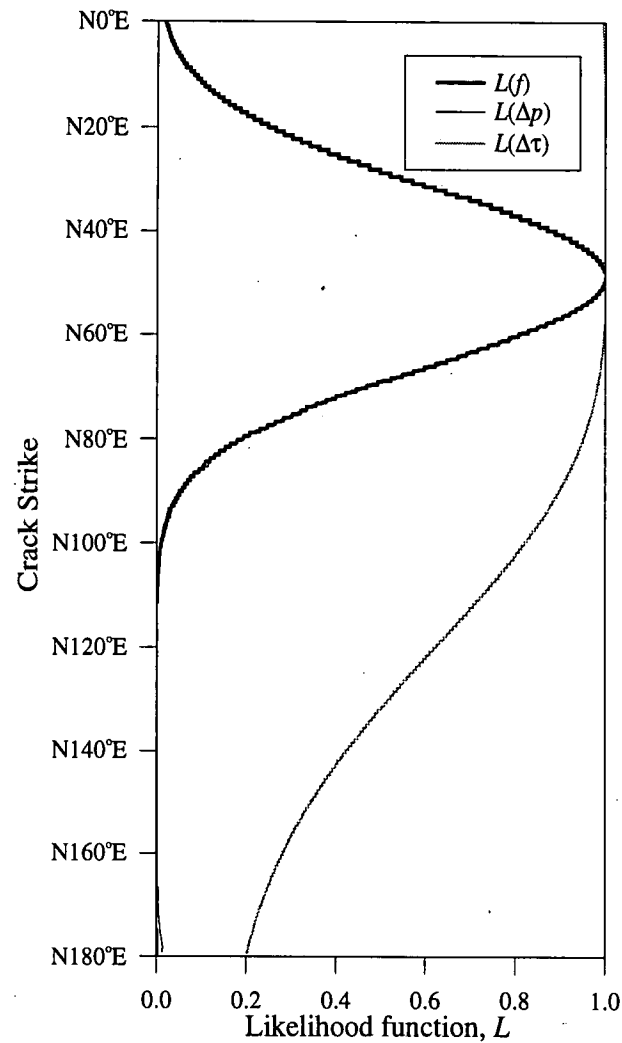


Figure 5.27 - Likelihood cross-sections for theoretical shear-wave splitting estimates generated for the best Hudson model and the 33-1 and Peel VSP geometries.

function for the elastic constant components (Figure 5.25). The  $\Delta C_{44}$  and  $\Delta C_{55}$  parameters appear to be resolved better than the other parameters. This is because these parameters dominate the degree of shear-wave birefringence for near-vertical propagation directions in equivalent media constructed from near-vertical fracture systems. This effect is also shown in the resolution of the Thomsen  $\gamma$  parameter which is well resolved in comparison with the  $\delta$  and  $\epsilon$  parameters. The resolution for the  $\Delta C_{44}$  and  $\Delta C_{55}$  parameters is approximately 10% for the first two anisotropic zones but decreases to approximately 25% for the remaining three zones. A similar resolution variation is also observed with the Hudson  $CD$  and the Thomsen  $\gamma$  parameters in that the resolution decreases for the lower three zones. The reason for the relatively good resolution of these first two anisotropic zones is due to greater number of observations within these zones. This suggests that an objective function using a normalization factor proportional to the number of observations within each zone may be more suitable for this inversion problem.

### 5.11 COMPARISON OF AVSP AND NEAR-OFFSET VSP INVERSION RESULTS

These inversion results for the near-offset VSPs support one of the conclusions reached in the previous Chapter that the observed anisotropy at the Conoco Borehole Test Facility is likely to be due to a sub-vertical fracture set dipping approximately  $18^\circ$  to the south east. However, there is some discrepancy between the inverted crack strike obtained for the azimuthal and near-offset VSP datasets. Inversion results from the AVSP data suggest that the crack strike is  $N75^\circ E$  whereas  $N50^\circ E$  is predicted from the near-offset VSP data. Consideration of core data and surface mapping cannot adequately resolve this discrepancy since there is evidence for both fracture orientations. Non-seismic data obtained for the limestone formations indicate the fracture strike to be between  $N65^\circ E$  and  $N80^\circ E$  (see Figure 5.28). This compares with fracture orientations of between  $N45^\circ E$  and  $N70^\circ E$  indicated by borehole televiewer images and induced fractures in a shale sample. From the shear-wave

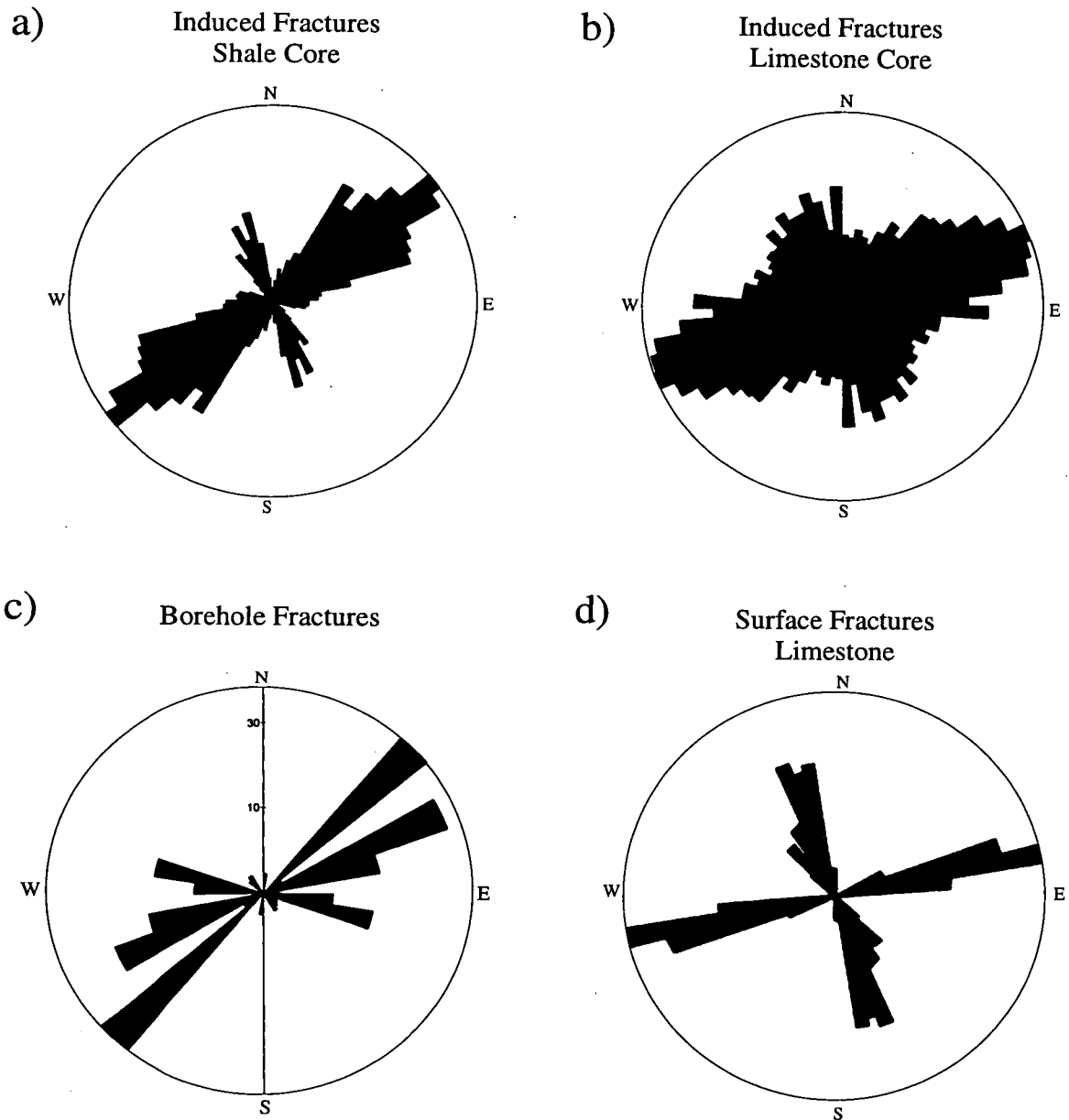


Figure 5.28 - Rose plots showing a) the normalized cumulative fracture length versus direction for induced fractures in a shale core from a depth of 734m, b) the normalized cumulative fracture length versus direction for induced fractures in a limestone sample, c) cumulative length (metres) versus strike direction for fractures observed in borehole televiwer images and d) surface fracture pattern observed in the limestone pavement at Vaps Pass (after Queen and Rizer 1990).

birefringence analysis I have identified that the most significant anisotropic regions are related to the sandstone and not the limestone formations. Thus the data obtained from the limestone and shale analyses may not be appropriate for resolving the discrepancy in the inversion results. Although the data obtained from borehole televiewer images does indicate the dominant fracture orientation to be N45°E there is also a significant number of fractures orientated at N65°E. It should also be emphasized that these geological results represent only a sparse sampling of the fracture system so that these analyses may be inadequate.

An interesting feature relating to this discrepancy can be observed in the cross-section likelihood plots for the crack strike (Figure 5.26). It can be seen that the likelihood maxima for the time delay and  $qS1$ -wave polarization misfit contributions are not coincident. The  $qS1$ -wave polarization misfit term suggests a crack strike of N50°E whilst the time delay misfit term predicts a crack strike of N65°E. Since it is the  $qS1$ -wave polarization misfit term that dominates the overall misfit function, the crack strike for the resulting best model will essentially be determined by the  $qS1$ -wave polarization estimates. However, the  $qS1$ -wave polarization measurements are not, in general, as robust as the measurements of time delays (Zeng and MacBeth 1993). Thus the inversion results for the crack strike may be unduly biased by incorrect  $qS1$ -wave polarization estimates. A possible source for erroneous  $qS1$ -wave polarization estimates lies in the rotation applied to correct for downhole tool rotation for both near-offset VSPs. In both cases gyrodata was not available, unlike the AVSP experiment, so that the rotation applied was based upon the assumption that  $P$ -wave energy is coincident with the propagation direction. Although, in most cases this is thought to be a valid assumption (Crampin, Stephen and McGonigle 1982) the combination of dipping fractures embedded in a finely layered media resulting in a monoclinic system may violate this assumption.



## 5.12 CONCLUSION

Although the discrepancy between the AVSP and near-offset VSP inversion results cannot be resolved using independent data I have suggested that an equivalent anisotropic system constructed from a combination of horizontal fine layering and a sub-vertical fracture system striking approximately N50°E system can explain most of the observed shear-wave birefringence. This system represents a likely solution to this problem however an inversion scheme for monoclinic systems could not be efficiently implemented with current computational resources. Nonetheless, the inversion scheme based upon a simple model of sub-vertical fracturing appears to have been successful since most of the observations are adequately modelled and the final model is consistent with most of the existing information relating to the fracture system.

A significant correlation is observed to exist between the lithology at the Conoco Borehole Test Facility and the shear-wave birefringence. Specifically, the degree of birefringence is considerably higher in the sandstone formations than for the shale or limestone formations suggesting that the sandstone formations may be intensely fractured. Sandstone formations, such as the Spraeberry Field, Texas, are of importance to the petroleum industry since they may often be the location of hydrocarbon reservoirs (Aguilera 1980). For these reservoirs the formation permeability anisotropy is of essential importance to production. Therefore, shear-wave birefringence studies may prove to be useful for the characterization of sandstone reservoirs. I have also shown that the fracture dip can be obtained from measurements of shear-wave anisotropy if appropriate acquisition geometries, such as an opposite azimuth VSP, are employed. This information may be of practical importance if directional drilling is to be employed since productivity flow rates are maximised for wells which perpendicularly intersect the fractures (Mueller 1992). The fracture system's dip is also important with respect to the reservoir's structural behaviour since this controls the water cut behaviour of producing wells (Brown, A.

Petrocorp, personal communication). Furthermore, this information may help in designing the optimum drilling trajectory to ensure a mechanically stable borehole (Zhou *et al.* 1994).

## **CHAPTER 6**

### **SUMMARY AND CONCLUSIONS**

#### **6.1 INTRODUCTION**

The primary purpose of this thesis has been to develop non-linear anisotropic inversion techniques for the processing of seismic data. This has been achieved by the implementation of a global optimization technique known as a Genetic Algorithm (GA). The techniques have been verified on experimental data and have been shown to be consistent with independent data relating to the anisotropy. These results show that shear-wave anisotropy can be successfully used to characterize a fracture system in a simple geological setting. The results also emphasize the importance of appropriate acquisition geometries if fracture properties are to be adequately, and correctly, resolved. The main conclusions of this thesis may be broadly classified into the three topic areas which I will now discuss.

#### **6.2 GENETIC ALGORITHMS**

The GA that I have used in this thesis included several so-called 'advanced operators'. In some circumstances these operators have enhanced the search characteristics of the GA although the generality of this result is unclear. However, in general the simple three operator GA of reproduction, crossover and mutation appears to form an effective and efficient search strategy. Perhaps the most important aspect of this thesis is to stress the simplifications that I have needed to implement in the forward modelling scheme which is used in the evaluation of the objective function. These simplifications are necessary if the inversions are to be conducted within realistic time scales. As computer technology evolves and more efficient forward modelling methods are developed more realistic problems may be tackled with Monte Carlo

type schemes, such as Simulated Annealing (SA) or GAs. It is also likely that more effective global search strategies will be developed, such as the Very Fast Simulated Reannealing method which is claimed to be an order of magnitude faster than both GAs and SA (Ingber and Rosen 1992, Stoffa *et al.* 1994). Another important point to stress is that, unlike SA, the underlying convergent behaviour of GAs is not well understood and considerable doubt has been placed upon the importance of schemata processing (Fogel and Stayton 1994). Nonetheless, the GA has been used successfully in anisotropic inversion schemes to produce results which are consistent with existing information.

### **6.3 FRACTURE CHARACTERIZATION AT THE CONOCO BOREHOLE TEST FACILITY**

The GA inversion technique has been used to invert observations of shear-wave anisotropy recorded from several experiments conducted at the Conoco Borehole Test Facility (CBTF), Oklahoma. The inversion of shear-wave splitting estimates have been shown to be in agreement with geological information regarding fracture observations at the site. This correlation suggests that the observed anisotropy is due to aligned fractures. If this argument is followed it is then possible to conclude that the sandstone formations at the CBTF, through which the shear-wave birefringence is most pronounced, are heavily fractured. Furthermore, the inversion results presented in Chapters 4 and 5 suggest that the observed anisotropy is due to a sub-vertical fracture system dipping about 20° to the south east. This result suggests that orientation of fractures from the vertical may be resolved if appropriate acquisition geometries are used. This may be of significant use in the design of horizontal drilling technology in fractured reservoirs. In these situations the productivity is a function of the angle of intersection between the fractures and the well, with maximum fracture intersection occurring for wells deviated in a direction perpendicular to the plane of fracturing. Shear-wave anisotropy could be applied to determine the fracture dip using the concept of an opposite azimuth survey, as

discussed in Chapters 4 and 5. This need for carefully planned acquisition shear-wave surveys is further supported by the detection of a shear-wave singularity reported in Chapter 4. The identification of this feature significantly constrains the domain of acceptable solutions although improved resolution of the fracture orientation could have been obtained using a better choice of azimuths.

GA inversion techniques have also been applied to inverting shear-wave observations generated from natural events recorded at the Cajon Pass scientific borehole (Liu 1995) and also from a comprehensive controlled source shear-wave experiment to characterize an *in-situ* granite rock mass (Holmes 1995). In both cases the GA inversion method is claimed to be successful in that a significantly better match is obtained using the GA compared with other qualitative methods. In the case of the controlled source experiment the inversion results indicate that a line singularity is detected in the experiment.

#### 6.4 SHEAR-WAVE ANISOTROPY

In this thesis I have successfully related observations of shear-wave anisotropy to the fracture system at the CBTF. However, it should be emphasized that the CBTF represents a good setting for these types of experiments but in general geology and fracture systems tend to be far more complicated. This is especially true for hydrocarbon reservoirs which are almost always associated with some complex geometry relating to structural or stratigraphic traps. In these situations the simple models which I have used to analyse the shear-wave splitting, including estimation techniques, will no longer be appropriate. Related to this is the assumption of fracture alignment at the CBTF over all depths which is justified through the use of geological information. However, if the fracture orientation does change with depth this will lead to multiple shear-wave splitting for which no general estimation technique has yet been developed. In this thesis shear-wave splitting has been quantified in terms of only two parameters, that is, the time delay between the fast

and slow split shear waves and the polarization direction of the fast shear-wave in the horizontal plane. A further quantification of the shear-wave field which may yield important information is the measurement of the vertical shear-wave polarizations. For example, in the case that the observed anisotropy is transversely isotropic then the measurement of the  $qSP$  polarization in the vertical plane will yield information relating to the vertical orientation of the symmetry axis (Liu, Crampin and Queen 1991). Further parametrization of the shear-wave field is possible and desirable since the inclusion of such information will constrain the inversion problem thereby reducing the considerable non-uniqueness associated with this problem. Thus it is likely that more research will be devoted to the processing and interpretation of shear-wave anisotropy.

## 6.5 SUGGESTIONS FOR FUTURE WORK

This thesis has identified several avenues for further research. Of these I believe that the most promising is the proposed use of the Opposite Azimuth VSP described in Chapters 4 and 5 for the measurement of fracture dip. In the first instance this experiment should be conducted at the CBTF to resolve the ambiguity between dipping fractures and lateral variations. Further confirmation of this interpretation should also be sought from alternative methods such as formation microscanners. These tools have produced very clear images of fractures which are of a much higher resolution than those obtained using borehole televiwers (Lefevre *et al.* 1993). The subsequent development of the inversion methods presented in this thesis are likely to be closely coupled to the evolution of computer science and its associated technology. Current supercomputers may well allow more realistic models of seismic anisotropy to be efficiently modelled and incorporated into a global optimization scheme, such as a GA.

At present the necessary interpretation, processing and modelling tools are still being developed. However, it is likely that research into seismic anisotropy will continue

and may well contribute to the characterization of fracture systems in the future.

## APPENDIX A

### DERIVATION OF SLOWNESS EQUATIONS FOR MONOCLINIC MEDIA

For a monoclinic medium the elastic tensor can be written in terms of thirteen non-zero elastic constants and in the case that the symmetry plane lies in the  $x_3=0$  plane then the elastic tensor may be written as (Musgrave 1970)

$$\begin{pmatrix} c_{11} & c_{12} & c_{13} & 0 & 0 & c_{16} \\ c_{12} & c_{22} & c_{23} & 0 & 0 & c_{26} \\ c_{13} & c_{23} & c_{33} & 0 & 0 & c_{36} \\ 0 & 0 & 0 & c_{44} & c_{45} & 0 \\ 0 & 0 & 0 & c_{45} & c_{55} & 0 \\ c_{16} & c_{26} & c_{36} & 0 & 0 & c_{66} \end{pmatrix} \quad (\text{A-1})$$

From these elastic constants the Kelvin-Christoffel matrix can be constructed. This defines a slowness surface which may be obtained in two ways. The first method is to construct the Kelvin-Christoffel matrix equation in terms of direction cosines and solve this by application of Eigen analysis techniques. Alternatively the Kelvin-Christoffel matrix may be expanded to give the characteristic equation which is a sixth order polynomial for triclinic symmetry. Adopting this second approach the characteristic equation for monoclinic symmetry systems is,

$$\begin{vmatrix} \alpha - \rho & \delta & \eta \\ \delta & \beta - \rho & \zeta \\ \eta & \zeta & \gamma - \rho \end{vmatrix} = 0 \quad (\text{A-2})$$



where the coefficients are (Fryer and Frazer 1987)

$$\alpha = c_{11}p_x^2 + c_{66}p_y^2 + c_{55}p_z^2 + 2c_{16}p_xp_y + 2c_{15}p_xp_z + 2c_{56}p_y p_z ; \quad (\text{A3})$$

$$\beta = c_{66}p_x^2 + c_{22}p_y^2 + c_{44}p_z^2 + 2c_{26}p_xp_y + 2c_{46}p_xp_z + 2c_{24}p_y p_z ;$$

$$\gamma = c_{55}p_x^2 + c_{44}p_y^2 + c_{33}p_z^2 + 2c_{45}p_xp_y + 2c_{35}p_xp_z + 2c_{34}p_y p_z ;$$

$$\delta = c_{16}p_x^2 + c_{26}p_y^2 + c_{45}p_z^2 + (c_{12} + c_{66})p_xp_y ;$$

$$\eta = [(c_{13} + c_{55})p_x + (c_{45} + c_{36})p_y]p_z ;$$

$$\zeta = [(c_{36} + c_{45})p_x + (c_{44} + c_{23})p_y]p_z ;$$

I rewrite these coefficients into a more compact notation in terms of the vertical slowness as,

$$\begin{aligned} \alpha &= \alpha_1 + \alpha_2 p_z^2 \\ \beta &= \beta_1 + \beta_2 p_z^2 \\ \gamma &= \gamma_1 + \gamma_2 p_z^2 \\ \delta &= \delta_1 + \delta_2 p_z^2 \\ \eta &= \eta_1 p_z \\ \zeta &= \eta_1 p_z \end{aligned} \quad (\text{A-4})$$

Expanding the characteristic equation and collecting vertical slowness terms together yields the cubic in terms of the vertical slowness squared,

$$a_3 (p_z^2)^3 + a_2 (p_z^2)^2 + a_1 p_z^2 + a_0 = 0 \quad (\text{A-5})$$

These coefficients are,

$$\begin{aligned}
 a_3 &= \alpha_2 \beta_2 \gamma_2 - \delta_2^2 \gamma_2 \\
 a_2 &= \alpha_2 \beta_2 \gamma_1 + \alpha_1 \beta_2 \gamma_2 + \\
 &\alpha_2 \beta_1 \gamma_2 - \alpha_2 \beta_2 \rho - \alpha_2 \gamma_2 \rho - \\
 &\gamma_2 \beta_2 \rho - \alpha_2 \zeta_1^2 - \delta_2^2 \gamma_1 - \\
 &2\delta_1 \delta_2 \gamma_2 + \delta_2^2 \rho + 2\delta_2 \eta_1 \zeta_1 - \\
 &\eta_1^2 \beta_2 \\
 a_1 &= \alpha_1 \beta_2 \gamma_1 + \alpha_2 \beta_1 \gamma_1 + \alpha_1 \beta_1 \gamma_2 - \\
 &\alpha_1 \beta_2 \rho - \alpha_2 \beta_1 \rho - \alpha_1 \gamma_2 \rho - \\
 &\alpha_2 \gamma_1 \rho + \alpha_2 \rho^2 - \gamma_1 \beta_2 \rho - \\
 &\gamma_2 \beta_1 \rho + \beta_2 \rho^2 + \gamma_2 \rho^2 - \\
 &\alpha_1 \zeta_1^2 + \zeta_1^2 \rho - 2\delta_1 \delta_2 \gamma_1 - \\
 &\delta_1^2 \gamma_2 + 2\delta_1 \delta_2 \rho + 2\delta_1 \eta_1 \zeta_1 - \\
 &\eta_1^2 \beta_1 + \eta_1^2 \rho \\
 a_0 &= \alpha_1 \beta_1 \gamma_1 - \alpha_1 \beta_1 \rho - \alpha_1 \gamma_1 \rho + \\
 &\alpha_1 \rho^2 - \gamma_1 \beta_1 \rho + \beta_1 \rho^2 + \\
 &\gamma_1 \rho^2 - \delta_1^2 \gamma_1 + \delta_1^2 \rho - \rho^3
 \end{aligned} \tag{A-6}$$

It is also interesting to note that if the two horizontal components are rewritten as  $p_x = p_h \cos(\theta)$  and  $p_y = p_h \sin(\theta)$  so that equation (A-4) may be written as,

$$\begin{aligned}
 \alpha &= \alpha_1' + \alpha_2' p_h^2 \\
 \beta &= \beta_1' + \beta_2' p_h^2 \\
 \gamma &= \gamma_1' + \gamma_2' p_h^2 \\
 \delta &= \delta_1' + \delta_2' p_h^2 \\
 \eta &= \eta_1' p_h \\
 \eta &= \eta_1' p_h
 \end{aligned} \tag{A-7}$$

then the cubic coefficients for the cubic equation in terms of the horizontal slowness,

$$a_3' (p_h^2)^3 + a_2' (p_h^2)^2 + a_1' p_h^2 + a_0' = 0 \tag{A-8}$$

have exactly the same form as that given in equation (A-6) with all the terms replaced by their primed counterparts.

These two forms of the cubic may be combined together so that the characteristic equation can be written in terms of the matrix equation,

$$\mathbf{QAP} = 0 \tag{A-9}$$

where  $\mathbf{Q}$  is the row matrix of vertical slowness terms only,  $\mathbf{Q} = (p_z^6 \ p_z^4 \ p_z^2 \ 1)$  and  $\mathbf{P}$  is the column matrix of horizontal slownesses,  $\mathbf{P}^T = (p_h^6 \ p_h^4 \ p_h^2 \ p_h \ 1)$ .  $\mathbf{A}$  is a lower diagonal 4x4 matrix with the elements

$$\begin{aligned}
a_{14} &= \alpha_2 \beta_2 \gamma_2 - \delta_2^2 \gamma_2 \\
a_{23} &= \alpha_2 \beta_2 \gamma_1' + \alpha_1' \beta_2 \gamma_2 + \alpha_2 \beta_1' \gamma_2 - \alpha_2 \zeta_1^2 - \delta_2^2 \gamma_1' - 2\delta_1' \delta_2 \gamma_2 + 2\delta_2 \eta_1 \zeta_1 - \eta_1^2 \beta_2 \\
a_{24} &= (-\alpha_2 \beta_2 - \alpha_2 \gamma_2 - \gamma_2 \beta_2 + \delta_2^2) \rho \\
a_{32} &= \alpha_1' \beta_2 \gamma_1' + \alpha_2 \beta_1' \gamma_1' + \alpha_1' \beta_1' \gamma_2 - \alpha_1' \zeta_1^2 - 2\delta_1' \delta_2 \gamma_1' - \delta_1'^2 \gamma_2 + 2\delta_1' \eta_1 \zeta_1 - \eta_1^2 \beta_1' \\
a_{33} &= (-\alpha_1' \beta_2 - \alpha_2 \beta_1' - \alpha_1' \gamma_2 - \alpha_2 \gamma_1' - \gamma_1' \beta_2 - \gamma_2 \beta_1' + \zeta_1^2 + 2\delta_1' \delta_2 + \eta_1^2) \rho \\
a_{34} &= (\alpha_2 + \beta_2 + \gamma_2) \rho^2 \\
a_{41} &= \alpha_1' \beta_1' \gamma_1' - \delta_1'^2 \gamma_1' \\
a_{42} &= (-\alpha_1' \beta_1' - \alpha_1' \gamma_1' - \gamma_1' \beta_1' + \delta_1'^2) \rho \\
a_{43} &= (\alpha_1' + \beta_1' + \gamma_1') \rho^2 \\
a_{44} &= -\rho^3
\end{aligned} \tag{A-10}$$

This form has advantages over the cubic forms given in equations (A-5) and (A-8) as the matrix  $A$  is a function of the elastic constants and densities only. The separation of the horizontal and vertical slownesses also implies that ray tracing may simply be applied to two dimensional models constructed from homogeneous cells with either vertical or horizontal interfaces.

## REFERENCES

- AGUILERA, R. 1980. Naturally fractured reservoirs. PennWell Publishing Company, Tulsa, Oklahoma.
- ALFORD, R.M. 1986. Shear data in the presence of azimuthal anisotropy. 56th SEG meeting, Houston. 476-479.
- ARTS, R.J., RASOLOFOSAON, P.N.J., ZINSZNER, B.E. 1991. Complete inversion of the anisotropic elastic tensor in rocks: Experiment versus theory. 61st SEG meeting, Houston. Expanded Abstracts. 1538-1541.
- BACKUS, J. E. 1962. Long-wave elastic anisotropy produced by horizontal layering. *Journal of Geophysical Research*. 67 4427-4440.
- BASU, A., FRAZER, L.N. 1990. Rapid determination of the critical temperature in simulated annealing inversion. *Science* 249 1409-1412.
- BATES, C.R., LYNN, H.B., LAYMAN, M. 1995. Natural fracture characterization using P-wave reflection and multicomponent VSP. 57th EAEG meeting, Glasgow. Expanded Abstracts.
- BERG, E. 1991 Convergent Genetic Algorithm for Inversion. 61st SEG meeting, Houston. Expanded Abstracts. 948-950.
- BRODOV, L.U., TIKHONOV, A.A., CHESNOKOV, E.M., TERTYCHNYI, V.V., ZATSEPIN, S.V. 1991. Estimating physical parameters of cracked-porous oil reservoirs by inverting shear-wave splitting. *Geophysical Journal International* 107(3) 329-432.
- BUSH, I. 1990. Modelling shear-wave anisotropy in the Paris Basin. Ph.D. Thesis. University of Edinburgh.
- CAMPDEN, D. A. 1990. Analysis of multicomponent VSP data for shear-wave anisotropy. Ph. D. Thesis. University of Edinburgh.
- ČERVENÝ, V. 1972. Seismic rays and ray intensities in inhomogeneous anisotropic media. *Geophysical Journal of the Royal astronomical Society* 29 1-13.
- CLIENT, Ch., BRODOV, L., TIKHONOV, A., MARIN, D., MICHON, D. 1991. Anisotropy survey for reservoir definition. *Geophysical Journal International* 107(3) 417-427.
- COOKE-YARBOROUGH, P. 1994. Analysis of fractures yields improved gas

- production from Zechstein carbonates, Hewett Field, UKCS. *First Break* 12 (5) 243-252.
- CRAMPIN, S. 1981. A review of wave motion in anisotropic and cracked elastic-media. *Wave Motion* 3 343-391.
- CRAMPIN, S. 1994. The fracture criticality of crustal rocks. *Geophysical Journal International* 118 428-438.
- CRAMPIN, S. 1985. Evaluation of anisotropy by shear-wave splitting. *Geophysics* 50(1) 142-152.
- CRAMPIN, S., STEPHEN, R.A., MCGONIGLE, R. 1982. The polarization of *P*-waves in anisotropic media. *Geophysical Journal of the Royal astronomical Society* 68 477-485.
- DAVIS, L. 1991. *Handbook of genetic algorithms*. Van Nostrand Reinhold, New York.
- DELLINGER, J., VERNIK, L. 1994. Do traveltimes in pulse-transmission experiments yield anisotropic group or phase velocities? *Geophysics* 59 (11) 1774-1779.
- DOUMA, J., HELBIG, K., SCHOKKING, F., TEMPELS, J. 1990. Shear-wave splitting in shallow clays observed in a multi-offset and walk-around VSP. *Geologie en Mijnbouw* 69 417-428.
- EHLIG-ECONOMIDES, C., EBBS, D., MEEHAN, D.N. 1990. Factoring anisotropy into well design. *Oilfield Review* (October) 24-33.
- FOGEL, D.B., STAYTON, L.C. 1994. On the effectiveness of crossover in simulated evolutionary optimization. *BioSystems* 32 171-182.
- FRYER, J.F., FRAZER, L.N. 1987. Seismic waves in stratified anisotropic media - II. Elastodynamic eigensolutions for some anisotropic systems. *Geophysical Journal of the Royal astronomical Society* 91 73-101.
- GAJEWSKI, D., PŠENČIK, I. 1990. Vertical seismic profile synthetics by dynamic ray tracing in laterally varying layered anisotropic structures. *Journal of Geophysical Research* 95 11301-11315.
- GALLAGHER, K., SAMBRIDGE, M., DRIJKONINGEN, G. 1991. Genetic Algorithms: An evolution from Monte Carlo methods for strongly non-linear geophysical optimization problems. *Geophysical Research Letters* Vol 18 (12) 2177-2180.

- GAL'PERIN, E.I. 1974. Vertical Seismic Processing. Society of Exploration Geophysicists, Tulsa.
- GHOSE, R., TAKAHASHI, T. 1991. Multiazimuthal seismic reception in a borehole: Implications on field delineation of seismic anisotropy. 61st SEG meeting, Houston. Expanded Abstracts. 34-37.
- GOLDBERG, D.E. 1989. Genetic Algorithms in Search, Optimization, and Machine Learning. Addison-wesley, Reading, Mass.
- HEARMON, R.F.S. 1961. Introduction to applied anisotropic elasticity. Oxford University Press.
- HELBIG, K. 1994. Foundations of anisotropy for exploration seismics. Seismic Exploration 22, Elsevier Science.
- HOLLAND, J.H. 1975. Adaptation in natural and artificial systems. Ann Arbor: The University of Michigan Press.
- HOLMES, G.M. 1995. Anisotropy in Granite and the Effects of Tunnel Excavation in a Controlled Source Shear-Wave Experiment. Ph. D. Thesis. University of Edinburgh.
- HOOD, J.A. 1991 A simple method for decomposing fracture-induced anisotropy. Geophysics. 56 (8) 1275-1279.
- HUDSON, J.A. 1980. Overall properties of a cracked solid. Mathematical Proceedings of the Cambridge Philosophical Society. 88 371-384.
- HUDSON, J.A. 1986. A higher order approximation to the wave propagation constants for a cracked solid. Geophysical Journal of the Royal astronomical Society 87 265-274.
- IGEL, H., MORA, P., RIOLLET, B. 1993. Anisotropic wave propagation through finite difference grids. Canadian Journal of Exploration Geophysics 29(1) 59-77.
- INGBER, L., ROSEN, B. 1992. Genetic algorithms and very fast simulated reannealing: A comparison. Mathematical Computer Modelling 16(11) 87-100.
- JIN, S., MADARIAGA, R. 1993. Background velocity inversion with a genetic algorithm. Geophysical Research Letters Vol 20 (2) 93-96.
- KANASEWICH, E.R. 1981. Time series analysis in geophysics. University of

Alberta Press, Edmonton.

- KENNETT, B.L.N. 1983. Seismic wave propagation in stratified media. Cambridge University Press.
- LEFEUVRE, F., TURPENING, R., CARAVANA, C., BORN, A., NICOLETIS, L. 1993. Vertical open fractures and shear-wave velocities derived from VSPs, full waveform acoustic logs, and televiewer data. *Geophysics* 58(6) 818-834.
- LI, X. 1992. Shear-wave splitting in reflection surveys: Theory, methods and case studies. Ph. D. Thesis. University of Edinburgh.
- LI, Y.G., LEARY, P.C., AKI, K. 1990. Ray series modelling of seismic wave travel times and amplitudes in three-dimensional heterogeneous anisotropic crystalline rock: Borehole vertical seismic profiling seismograms from the Mojave Desert, California. *Journal of Geophysical Research* 95 (B7) 11255-11239.
- LIU, E., CRAMPIN, S., BOOTH, D. 1989. Shear-wave splitting in cross-hole surveys: Synthetic modelling. *Geophysics* 54 57-65.
- LIU, E., CRAMPIN, S., QUEEN, J.H., 1991. Fracture detection using crosshole surveys and reverse vertical seismic profiles at the Conoco Borehole Test Facility, Oklahoma. *Geophysical Journal International* 107 (3) 449-463.
- LIU, Y. 1995. Shear-wave anisotropy and the interpretation of temporal change in time delays. Ph. D. Thesis. University of Edinburgh.
- MACBETH, C. 1991. Inversion for subsurface anisotropy using estimates of shear-wave splitting. *Geophysical Journal International* 107 (3) 585-595.
- MACBETH, C. 1995. How can anisotropy be used for reservoir characterization? *First Break* 13 (1) 31-37.
- MACBETH, C., WILD, P., CRAMPIN, S., BRODOV, L. 1993. Optimal acquisition geometry for determining seismic anisotropy. *Canadian Journal of Exploration Geophysics*. 29(1) 132-139.
- MACBETH, C., ZENG, X., LI, X.-Y., QUEEN, J. H. 1995. Multi-component near-surface correction for land VSP data. *Geophysical Journal International* 121 301-315.
- MUELLER, M., 1992. Using shear waves to predict lateral variability in vertical fracture intensity. *The Leading Edge*. 11(2) 29-35.
- MUSGRAVE, M., J., P. 1970. Crystal acoustics. Holden-Day, San Francisco,



California.

- NISHIZAWA, O., 1982. Seismic velocity in a medium containing oriented cracks - transversely isotropic case. *Journal of Physics of the Earth* 30 331-347.
- NOLTE, B., FRAZER, N.L. 1994. Vertical seismic profile inversion with genetic algorithms. *Geophysical Journal International* 117 162-178.
- PEREYA, V., LEE, W.H.K., KELLER, H.B. 1980. Solving two point seismic ray tracing in a heterogeneous medium, Part I: A general adaptive finite difference method. *Bulletin of the Seismological Society of America* 70, 79-99.
- POSTMA, G.W. 1955. Wave propagation in a stratified medium. *Geophysics* 20 (4) 780-806.
- PRESS, W.H., TEUKOLSKY, S.A., VETTERLING, W.T., FLANNERY, B.P. 1992. *Numerical Recipes in Fortran: The Art of Scientific Computing*. Cambridge University Press.
- QUEEN, J.H., LEFEUVRE, F., SINTON, J.B., COX, V.D., BULLER, P.L. 1992. Propagator analysis of multicomponent data from the Conoco borehole test facility. 5th International Workshop on Seismic Anisotropy, Banff. Abstract.
- QUEEN, J.H., RIZER W.D. 1990. An integrated study of seismic anisotropy and the natural fracture system at the Conoco Borehole Test Facility, Kay County, Oklahoma. *Journal of Geophysical Research*. 95 (B7) 11255-11273.
- RATHORE, J., FJÆR, E., HOLT, R.M., RENLIE, L. 1992. Experimental and theoretical acoustic anisotropy in controlled cracked synthetic rocks. 5th International Workshop on Seismic Anisotropy, Banff. Abstract.
- SAMBRIDGE, M., DRIJKONINGEN, G. 1992 Genetic algorithms in seismic waveform inversion. *Geophysical Journal International* 109 323-342.
- SAYERS, C. M. 1988. Inversion of ultrasonic wave velocity measurements to obtain the microcrack orientation distribution function in rocks. *Ultrasonics* 26 73-77.
- SCHOENBERG, M., DOUMA, J., 1988. Elastic wave propagation in media with parallel fractures and aligned cracks. *Geophysical Prospecting*. 36 571-590.
- SCHOENBERG, M., MUIR, F. 1989. A calculus for finely layered anisotropic media. *Geophysics*. 54 (5) 581-589.
- SEN, M.K., STOFFA, P.L. 1992. Rapid sampling of model space using genetic algorithms: examples from seismic waveform inversion. *Geophysical Journal*

International 108 281-292.

- SHERIFF, R.E. 1984. Encyclopedic dictionary of exploration geophysics. Society of Exploration Geophysicists, Tulsa.
- SHUCK, E.L., BENSON, R.D., DAVIS, T.L. 1993. Analysis of shear-wave polarizations from a nine-component 3-D dataset, Cedar Hill, New Mexico. 63rd SEG meeting, Washington, Expanded Abstracts 271-274.
- SMITH, M.L., SCALES, J.A., FISCHER, T.L. 1992. Global search and genetic algorithms. *Geophysics: The Leading Edge of Exploration*. 22-26.
- STOFFA, P.L., SEN, M.K. 1991. Nonlinear multiparameter optimization using genetic algorithms: Inversion of plane-wave seismograms. *Geophysics* 56 (11) 1794-1810.
- STOFFA, P.L., SEN, M.K., VARELA, C., CHUNDURU, R.K. 1994 Geophysical applications of global optimization methods. 56th EAEG meeting, Vienna. P134.
- TARANTOLA, A. 1987. *Inverse Problem Theory : Methods for Data Fitting and Model Parameter Estimation*. Elsevier, Amsterdam.
- TATHAM, R.H. and McCORMACK, M.D. 1991. Multicomponent seismology in petroleum exploration. Society of Exploration Geophysicists, Tulsa, Oklahoma.
- TAYLOR, D.B. 1990. ANISEIS manual, version 4.5, Applied Geophysical Software, Houston.
- THILL, R.E., WILLARD, R.J., BUR, T.R. 1969. Correlation of longitudinal velocity variation with rock fabric. *Journal of Geophysical Research* 74 (20) 4897-4909.
- THOMSEN, L. 1986. Weak elastic anisotropy. *Geophysics* 51 (10) 1954-1966.
- THOMSEN, L. 1989. Comparison of anisotropic modelling codes: Anisotropic Modelling Collaboration, Res. Workshop, Recording and processing vector data, Snowbird, Utah, Society of Exploration Geophysicists, Technical Abstracts, 4.
- THOMSEN, L. 1991. Elastic anisotropy due to aligned cracks in porous rock. 53rd EAEG meeting, Florence. 244 - 245.
- YARDLEY, G. 1994 Identification and Characterization of Fractured Reservoirs by Analysis of Shear-wave Anisotropy. Ph.D. Thesis. University of Edinburgh.

- YARDLEY, G., CRAMPIN, S. 1990 Automatic determination of anisotropic parameters from shear-wave splitting in the Lost Hills VSP. 60th SEG meeting, San Fransisco, Expanded Abstracts 1424-1426.
- ZENG, X., MACBETH, C. 1993 Algebraic processing techniques for estimating shear-wave splitting in zero-offset VSPs - theory. *Geophysical Prospecting*, 41, 1033-1066.
- ZHOU, S., HILLIS, R., SANDIFORD, M. 1994. A study of inclined wellbores with regard to both mechanical stability and fracture intersection, and its application to the Australian north west shelf. *Journal of Applied Geophysics* 32 293-304.
- ZOBACK, M.L., ZOBACK, M. 1980 State of stress in the conterminous United States, *Journal of Geophysical Research*, 85, 6113-6156.

From: CBS%UK.AC.NERC-SWINDON.MAIL::COM.DELPHI::MARCHD  
4-JUN-1995 13:40:11.76

To: e\_sah

Subj: Publishing permission

Via: UK.AC.NERC-SWINDON.MAIL; Sun, 4 Jun 95 13:40 GMT

Received: from bos1g.delphi.com by mail.nerc-swindon.ac.uk with SMTP (PP)  
id <22318-0@mail.nerc-swindon.ac.uk>; Sun, 4 Jun 1995 13:35:52  
+0100

Received: from delphi.com by delphi.com (PMDF V4.3-9 #7804)  
id <01HRAVPFAXPG9FOD5Q@delphi.com>;  
Sun, 04 Jun 1995 08:37:45 -0400 (EDT)

Date: Sun, 04 Jun 1995 08:37:45 -0400 (EDT)

From: MARCHD@com.delphi

Subject: Publishing permission

To: e\_sah@uk.ac.nerc-murchison.vaxa

Message-id: <01HRAVPFAXPI9FOD5Q@delphi.com>  
X-VMS-To: IN%"e\_sah@va.nmh.ac.uk"  
X-VMS-Cc: MARCHD  
MIME-version: 1.0

Content-type: TEXT/PLAIN; CHARSET=US-ASCII  
Content-transfer-encoding: 7BIT

Thanks for your letter of the 22nd May. The Association has no objection to you using your paper as part of the thesis as long as you acknowledge the source.

D.W.March  
Publications Officer  
marchd@delphi.com

# Inversion for seismic anisotropy using genetic algorithms<sup>1</sup>

Steve Horne<sup>2, 3</sup> and Colin MacBeth<sup>2</sup>

## Abstract

A general inversion scheme based on a genetic algorithm is developed to invert seismic observations for anisotropic parameters. The technique is applied to the inversion of shear-wave observations from two azimuthal VSP data sets from the Conoco test site in Oklahoma. Horizontal polarizations and time-delays are inverted for hexagonal and orthorhombic symmetries. The model solutions are consistent with previous studies using trial and error matching of full waveform synthetics. The shear-wave splitting observations suggest the presence of a shear-wave line singularity and are consistent with a dipping fracture system which is known to exist at the test site. Application of the inversion scheme prior to full waveform modelling demonstrates that a considerable saving in time is possible whilst retaining the same degree of accuracy.

## Introduction

For an anisotropic material, the shear-wave phase velocity surface is no longer represented as a single continuous sheet, as is the case for isotropic materials, but as two separate sheets which may touch or intersect at singularities. Therefore, in anisotropic materials it is generally the case that three body waves may propagate: these are the quasi-compressional ( $qP$ ) and the faster ( $qS1$ ) and the slower quasi ( $qS2$ ) shear waves each of which propagate with polarizations and velocities fixed

---

<sup>1</sup> Received February 1994, revision accepted July 1994.

<sup>2</sup> Edinburgh Anisotropy Project, British Geological Survey, Murchison House, West Mains Road, Edinburgh, EH9 3LA, Scotland, U.K.

<sup>3</sup> Department of Geology and Geophysics, University of Edinburgh, West Mains Road, Edinburgh, Scotland, U.K.

by the direction of propagation. A seismic source may therefore excite two shear waves and a  $qP$  wave each with distinct polarizations and velocities. These continue to propagate through the medium leading to a time-delay between the fast and the slow shear waves, this phenomenon is known as shear-wave splitting. The  $qS2$ – $qS1$  time-delay is proportional to the distance travelled through the anisotropic medium, inversely proportional to the shear-wave velocity anisotropy, and is therefore a cumulative measure of the anisotropy sampled along the raypath. The recorded shear-wave polarizations depend on the relative amounts of anisotropy sampled along the raypath. Complications can arise if the split shear waves impinge on another different anisotropic region since further splitting may occur producing a wave train that is difficult to interpret. Shear-wave splitting is commonly measured in terms of the time-delay between the split shear waves and the polarization direction of the  $qS1$  arrival, since other quantities such as the differential shear-wave attenuation are difficult to estimate from field records although processing techniques have been developed which permit such measurements.

Intrinsically anisotropic materials are not thought to be the most common cause of observed anisotropy in the earth. One alternative explanation for seismic anisotropy is presented by the effective averaging that occurs when finely-layered isotropic materials are sampled by seismic energy with wavelengths greater than the thickness of the layers (Backus 1962; Folstad and Schoenberg 1993). In most cases where the layering is sub-horizontal, the resultant symmetry is transversely isotropic with a vertical (TIV) axis of symmetry (azimuthally isotropic). Aligned fractures and cracks embedded in an isotropic solid can also produce an effective anisotropic medium, which for vertical cracks gives a transversely isotropic medium with a horizontal (TIH) axis of symmetry (azimuthally anisotropic). It is possible that an effectively anisotropic medium may be produced by a combination of aligned cracks embedded in a fine layering sequence, such a symmetry system is orthorhombic if the cracks are orthogonal to the bedding planes or monoclinic, otherwise. It is useful to be able to know the symmetry, orientation and degree of these equivalent anisotropic media as this helps to identify the underlying physical cause. This knowledge is of value in resolving the heterogeneities which control the characteristics of the reservoir.

Inversion schemes for shear-wave anisotropy have been largely neglected due to the non-linearity of the problem. Chapman and Pratt (1992) suggested that the mean shear-wave arrival times could be inverted for a weak anisotropic medium by using degenerate perturbation theory to linearize the problem. Arts, Helbig and Rasolofosaon (1991) have used a localized inversion scheme based on a gradient method to invert for phase velocity measurements from laboratory experiments. However, the anisotropic model space is probably multi-modal and the use of a gradient-based technique is likely to be very dependent on the initial model. MacBeth (1991) attempted to invert shear-wave observations using a systematic search of a precalculated database of shear-wave attributes corresponding to the discretized anisotropic model space. The drawback to this type of approach is the

necessity of constructing the database prior to the inversion. For realistic model spaces this becomes computationally impractical because of the massive initial calculations required, subsequent storage of the database and access speeds to the database during the search. What is required is an efficient search mechanism which can be applied to very large, multimodal, non-linear model spaces. A solution to this problem is offered by genetic algorithms which may be considered an efficient directed Monte Carlo search.

## Genetic algorithms

Genetic algorithms (GA), which are thought to be non-linear global optimization schemes (Goldberg 1989), are receiving increasing attention due to their robustness, efficiency and suitability to many different problem domains (Stoffa and Sen 1991; Smith, Scales and Fischer 1992; Sambridge and Drijkoningen 1992). GAs can be classed alongside simulated annealing, since both are considered as directed searches guided by random processes and both attempt to model natural processes. In the case of simulated annealing the scheme mimics the energy minimization process that accompanies crystallization, whilst GAs attempt to simulate evolution. GAs achieve this by using genetic operations to manipulate individuals (chromosomes), each representing a model, and the set of these define a population. The operators are applied to the current population so that a new population is created with new individuals which, on average, are 'fitter', that is, nearer the optimal solution. The crucial factor underlying the GA's operation lies in the coding of model parameters in the chromosome. It is these codings that the GA manipulates in the optimization process by a passive search for similarities in the 'more' successful models, known as schemata. There are many choices available for the coding but the usual choice for the representation is a single string (haploid) with individual parameters linearly mapped to binary substrings which are then concatenated. For example, a model could be represented by the following coding, 0011|001|1000|000, where the vertical bar indicates a partition between adjacent parameters and is not a feature of the coding. If this is coded so that the most significant bit is to the left of each partition then the coding represents the values 3|1|8|0. These would then map directly to the actual model parameter values. Thus each model in the population is represented as a binary string. The simplest implementation of a GA uses only three genetic operations (the crossover and mutation operators are shown schematically in Fig. 1).

1. **Reproduction:** Two models are selected at random from the current population, with a probability proportional to the quantity being optimized.
2. **Crossover:** The models exchange portions of their codings at a point selected at random along the length of the string. This operator is applied with a fixed probability,  $P_c$ , to the two models selected by the reproduction step.

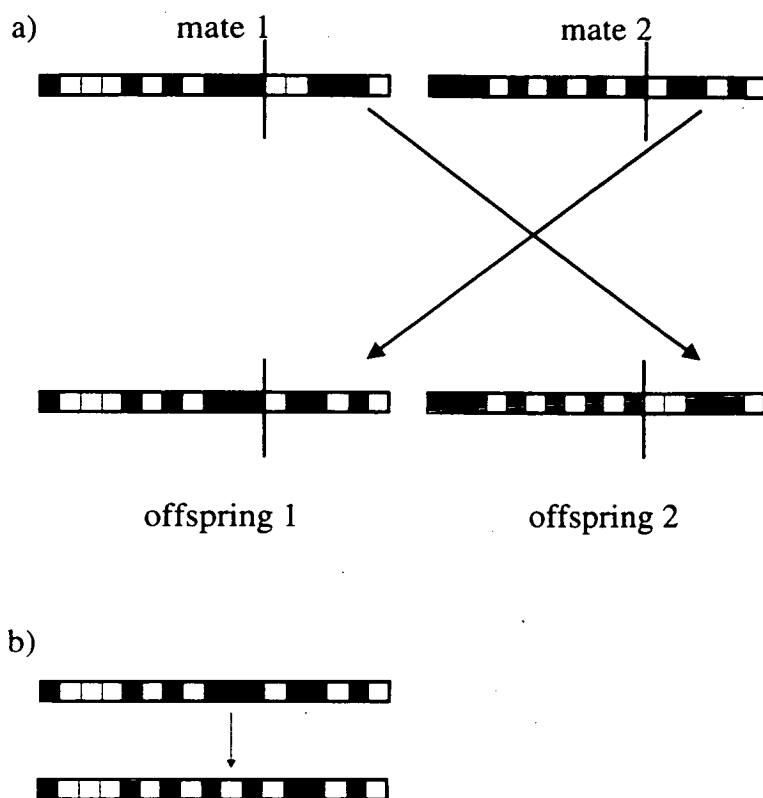


**Figure 1.** A schematic illustration of the operators employed by the genetic algorithm. The lines of black and white boxes represent a binary coding of a single model in the population. The crossover operator is illustrated in (a) where the two parent strings previously selected in the reproduction step exchange parts of their coding to produce two new offspring. In (b) the mutation operator is shown operating on a single bit in a models binary representation selected at random.

3. Mutation: A single bit is selected at random along the string and its value changed. This is a background operation applied with a small fixed probability,  $P_m$ , and is included to prevent the permanent loss of any genetic information.

A schematic illustration of a GA operation is shown in Fig. 2 in comparison to other commonly used optimization techniques. The first frame of Fig. 2a shows the initially random distribution of solutions in a 2D model space corresponding to the initial population of models. As the genetic operators are applied, the model distribution becomes denser around both the local and global optima although some solutions still occupy 'poor' regions, as shown in the second and third frames of Fig. 2a. The last frame of Fig. 2a shows the final population with most solutions clustered around the global optimum with several solutions approaching the optimal value. The behaviour of a simpler Monte Carlo search is shown in Fig. 2b and it can be seen that within each frame the models are randomly distributed over the entire model space. A local gradient technique is illustrated in Fig. 2c with four initial solutions chosen randomly as shown in the first frame converging in the final frame to three local minima and the global optimum. The potential disadvantage in using GAs is that many models need to be evaluated before convergence and their



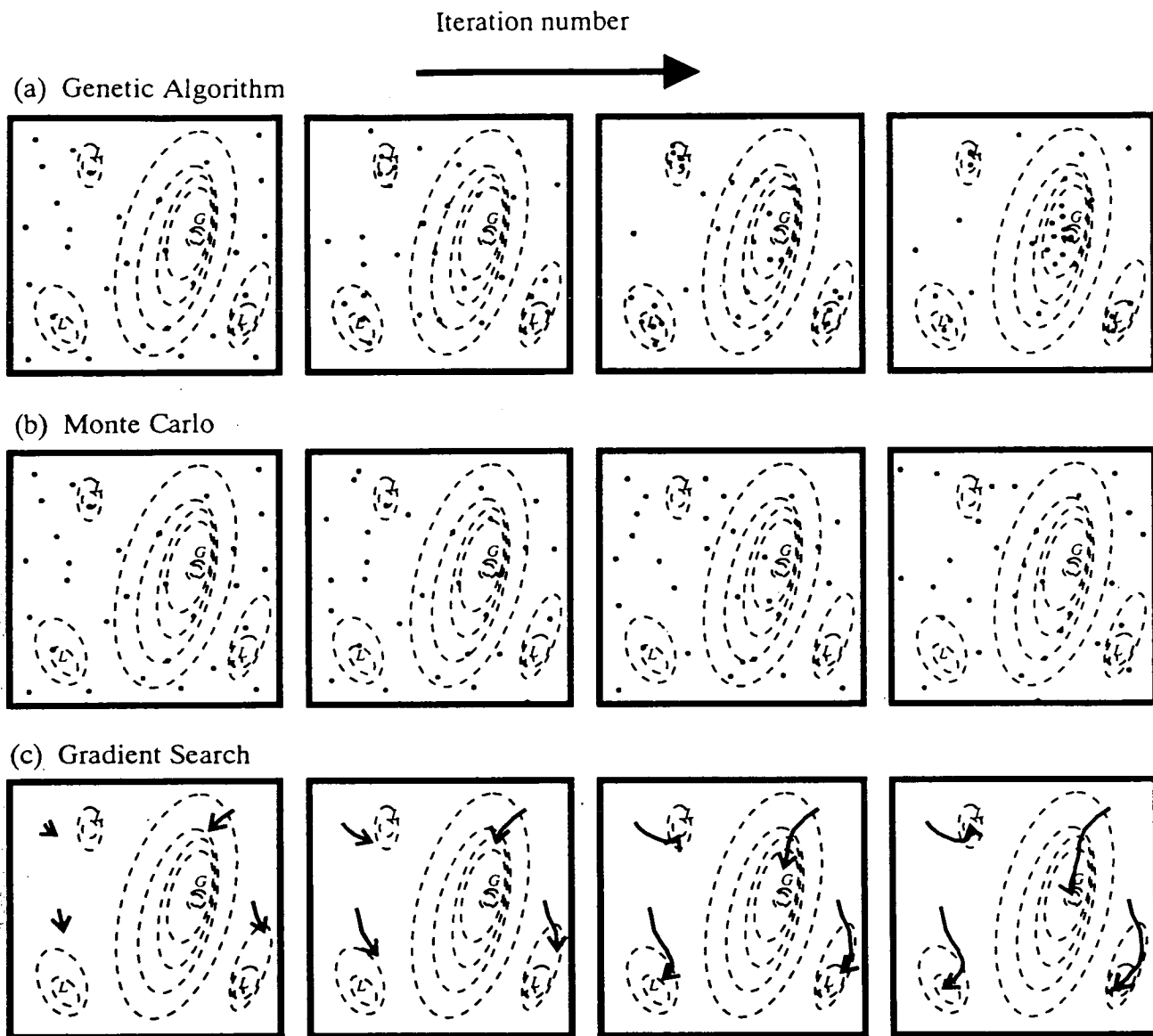


**Figure 2.** Schematic illustration of (a) a GA, (b) simple Monte Carlo and (c) local gradient searches for the optimization of a multimodal function in two dimensions during the iteration of the various methods. The Ls denote local optima and Gs the global optimum. For (a) and (b) the black dots indicate solutions sampled by the algorithms and for (c) the arrowed paths indicate the search directions from various starting models.

use may not be practical for problems where the forward modelling requirement is computationally expensive. As a further indication of a GA performance we show convergence curves in Fig. 3 for both a GA and a Monte Carlo search applied in a minimization role for synthetic data. This diagram shows behaviour typical of a GA with most of the minimization occurring at the beginning of the GA operation.

Our implementation of a GA is based on the three basic operations of reproduction, crossover and mutation but we also include more advanced methods (such as sharing and 'inversion' which is described in detail by Goldberg (1989)). Also included is a local search operator based on a steepest gradient method so that our

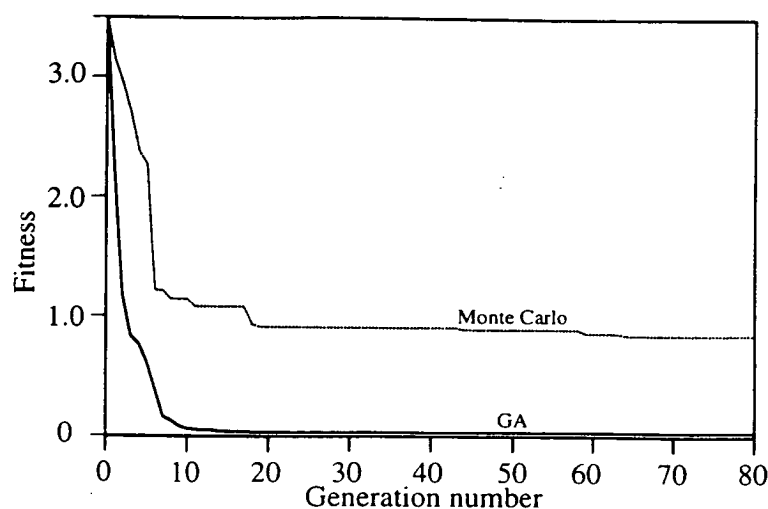


**Figure 3.** Comparison of a GA inversion scheme and a simple Monte Carlo search for seismic anisotropic parameters applied to synthetic data. The convergence of the GA and Monte Carlo searches are shown as solid and dotted lines, respectively.

scheme is a hybrid of both global and local search strategies. This has the advantage that the global search performed by the GA is enhanced by the local search to improve convergent behaviour.

### Application of the genetic algorithm to seismic anisotropic inversion

Most inversion schemes dealing with seismic anisotropy have concentrated on the inversion of  $qP$ -wave travel-times. This is because the  $qP$ -wave velocity sheet does not exhibit any singular behaviour so that linearization can be readily applied (Chapman and Pratt 1992). Shear-wave surveys have been largely neglected because the associated technology of multicomponent geophones and shear-wave sources are only a relatively recent advance in seismology and an understanding of their utility in the exploration and production industry is still developing (Tatham and McCormack 1991). Aside from the practical problems of obtaining estimates of the shear-wave attributes from the seismic traces is the inversion itself. Unlike the  $qP$ -wave velocity, the shear-wave velocities cannot be conveniently linearized owing to kiss, line and point singularities and the deviation of the group and phase velocity surfaces. However, it has been suggested that it is the shear waves that are most sensitive to the anisotropy caused by aligned thin cracks and consequently reveal more information on crack and fracture parameters than  $qP$ -wave observations (Crampin 1985).

The anisotropic model space can be parametrized using several different representations such as the elastic constants, the anisotropic parameters of Thomsen (1986), or parameters defining aligned isolated micro-cracks (Hudson 1991). The parametrization chosen for this inversion is the long wavelength equivalent medium for microcracks formulated by Hudson (1986) since these allow a physically intuitive interpretation for the anisotropy, which is not readily obtained from

the inspection of elastic constants. The disadvantage of this approach is that the elastic constants are restricted to the anisotropic systems defined by this model. The model consists of a single homogeneous layer with an embedded fracture system which can be represented as an equivalent anisotropic system. The model space for a single set of sub-vertical cracks is parametrized in terms of five parameters, the first three of these defining the crack properties and the remaining two the orientation of the crack system.

1. Crack Density ( $CD_1$ ): This is a dimensionless quantity defined by the following equation

$$CD_1 = \frac{N\langle a^3 \rangle}{v},$$

where  $N$  is the number of cracks in a volume  $v$  and  $\langle a^3 \rangle$  is the average of the crack radius cubed. A  $CD_1$  of zero implies an isotropic solid.  $CD_1$  ranges from 0.0 to 0.15 in 32 increments giving a five-bit string.

2. Aspect Ratio ( $AR_1$ ): The ratio of the crack thickness to its diameter.  $AR_1$  ranges from 0.001 to 0.3 in 32 increments, again giving a five-bit string.

3. Content ( $CT_1$ ): The content of the cracks is either wet (water-filled) or dry (gas-filled), represented by a single bit.

4. Direction of the crack strike in the horizontal plane ( $AZI$ ) ranging from 0 to  $180^\circ$  in 64 increments, giving a string length of 6 bits.

5. Direction of the crack dip measured from the vertical axis ( $DIP$ ) ranging from  $-32^\circ$  to  $+32^\circ$  in 32 increments, again giving a five-bit string.

The anisotropy is calculated for microcracks originally vertical and aligned along the horizontal  $y$ -axis (we use a right-handed co-ordinate system with  $z$  down and  $x$  pointing north). The system is then subjected to a rotation in the vertical  $x-z$  plane about the  $y$ -axis by an angle  $DIP$ , followed by rotation by an angle  $AZI$  in the horizontal  $x-y$  plane about the  $z$ -axis. On both the  $CD_1$  and  $AR_1$  parameters, upper limits of 0.15 and 0.3 must be imposed, respectively (Douma 1988), due to the limitations of Hudson's theory. For zero dip the cracks are vertically oriented with the direction of the symmetry axis given by the  $AZI$  parameter; such a system is TIH. Horizontally oriented cracks with a dip of  $90^\circ$  give rise to a TIV medium. For the inversion of orthorhombic symmetry, a second set of crack parameters is introduced which are orthogonal to the first set. This second crack set may model the effect of fine-layering. This gives an extra three parameters of  $CD_2$ ,  $AR_2$  and  $CT_2$ , with these cracks initially constrained to lie in the horizontal plane and then this combined dual crack system is rotated as before. Inversions for a hexagonal system with a horizontal symmetry axis requires a string of length 17 bits, an arbitrarily oriented symmetry axis requires 22 bits, and an arbitrarily oriented orthorhombic system requires 33 bits.

The forward modelling requirement is to calculate a set of predictions for the shear-wave attributes corresponding to any of the crack models (chromosomes) in

the population. To do this we compute the corresponding elastic constants for these crack parameters, and the phase velocities and polarizations for a range of propagation directions using the Kelvin-Christoffel equation (Musgrave 1970). These phase velocities and polarizations are then used to construct the corresponding group velocities and polarizations. This can be achieved by constructing a wave surface, equivalent to the group-velocity surface, derived from the envelope of wavefronts (Musgrave 1970). It is important to use these group, rather than the phase, attributes since it is these quantities that are observed. In practice only a quadrant of up- or down-going waves need to be calculated for orthorhombic or higher symmetry systems, since the remaining directional variations can be found by exploiting mirror symmetries.

Once the predicted group velocities and polarizations have been calculated, a misfit function between the predicted and observed estimates can be calculated. This misfit function takes the form

$$f(\mathbf{M}, \boldsymbol{\tau}^0, \mathbf{p}^0) = \frac{1}{2N} \left( \sum_{i=1}^N \frac{(\tau_i^0 - \tau_i^m)^2}{\delta\tau_i^2} \right)^{1/2} + \frac{1}{2N} \left( \sum_{i=1}^N \frac{(p_i^0 - p_i^m)^2}{\delta p_i^2} \right)^{1/2},$$

where  $\tau_i^0$  is a component of the vector of the observed  $qS2 - qS1$  time-delays,  $\tau_i^m$  is a component of the vector of model estimates for the  $qS2 - qS1$  time-delay. Similarly  $p_i^0$  is a component of the vector of the observed  $qS1$ -wave polarization,  $p_i^m$  is a component of the vector of model estimates for  $qS1$ -wave polarization.  $\delta\tau_i$  and  $\delta p_i$  are the estimated errors for the  $i$ th observation for the time-delays and the  $qS1$ -wave polarizations respectively. The summations are over the number of polarization and time-delay observations  $N$ . Each observation  $i$  represents a raypath from source to receiver. More specifically, the vector of model parameters  $\mathbf{M}$  is a set of crack and orientation values corresponding to one of the chromosomes in the GA's population. A misfit value of less than one implies that all observations are, on average, within the estimated errors. The GA is then applied in the minimization of the least-squares misfit function between the predictions and the observed estimates. The typical CPU time required for convergence is approximately 40 minutes on a VAX 4000/400 (Specmark 22.3).

## Application to field data sets

### *Experimental configuration for azimuthal VSP (AVSP)*

An example of the inversion procedure is presented here from an azimuthal VSP (AVSP) shot by Conoco in 1986, at the Conoco Borehole Test Facility (CBTF), Kay County, Oklahoma. The results from this survey have been previously published (Queen and Rizer 1990) as part of an extensive study of the natural fracturing occurring at the site. The AVSP was one of a number of experiments including surface fracture mapping, point load tests on oriented core samples, dip-

meter data and borehole televiewers (BHTV), which attempted to characterize the fractures at the CBTF.

The geology of the test site is sufficiently simple to neglect any significant ray bending or complications due to irregular interfaces. Ray tracing through a velocity structure derived from sonic logs indicates that the rays follow an essentially straight line between the source and receiver (Fig. 4) with no critical refractions lying outside the internal shear-wave window as defined by Liu and Crampin (1990). This study is useful because of the abundance of diverse and independent fracture-related information allowing verification of any hypothesis relating seismic anisotropy to cracks or fractures, such as that proposed by Crampin (1987). The AVSP consisted of nine shotpoints surveyed at  $15^\circ$  intervals lying on an offset arc of radius 290 m about well 33-1 (Fig. 5). Recordings were made using a three-component sonde at five levels with the shallowest at a depth of 582 m and equispaced at 10 m intervals thereafter. In-line and cross-line shear and compressional vibroseis sweeps were used in the experiment with frequency sweeps from 7 to 46 Hz and 18 to 96 Hz for the shear and compressional vibrators, respectively.

#### *Processing and wavefield parametrization*

After conventional seismic processing of the data, which includes cross-correlation, stacking and correction for sonde rotation using gyro data, two automatic estimation techniques, the dual-source cumulative technique (DCT) (Zeng and MacBeth

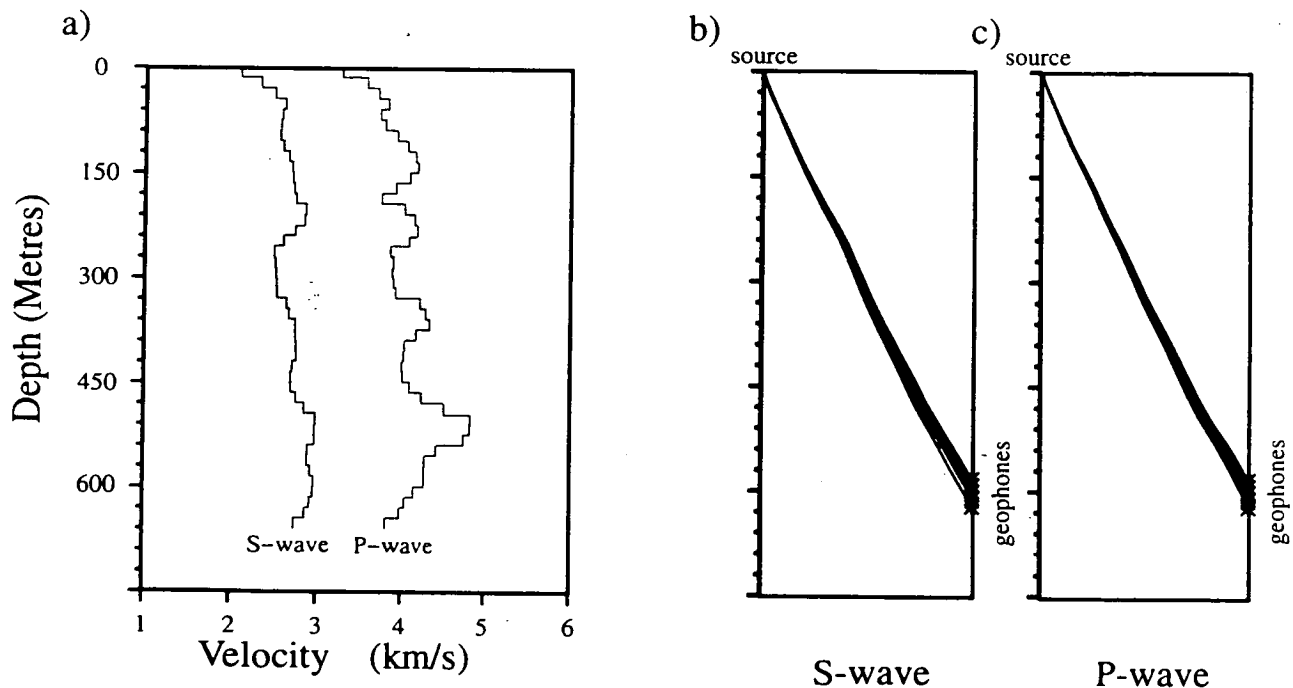


**Figure 4.** The velocity structure at the CBTF for both P- and S-waves as derived from sonic logs obtained in well 33-1. Isotropic ray tracing for both P- and shear-waves are shown in (b) and (c) for source and geophone positions corresponding to the azimuthal VSP geometry.

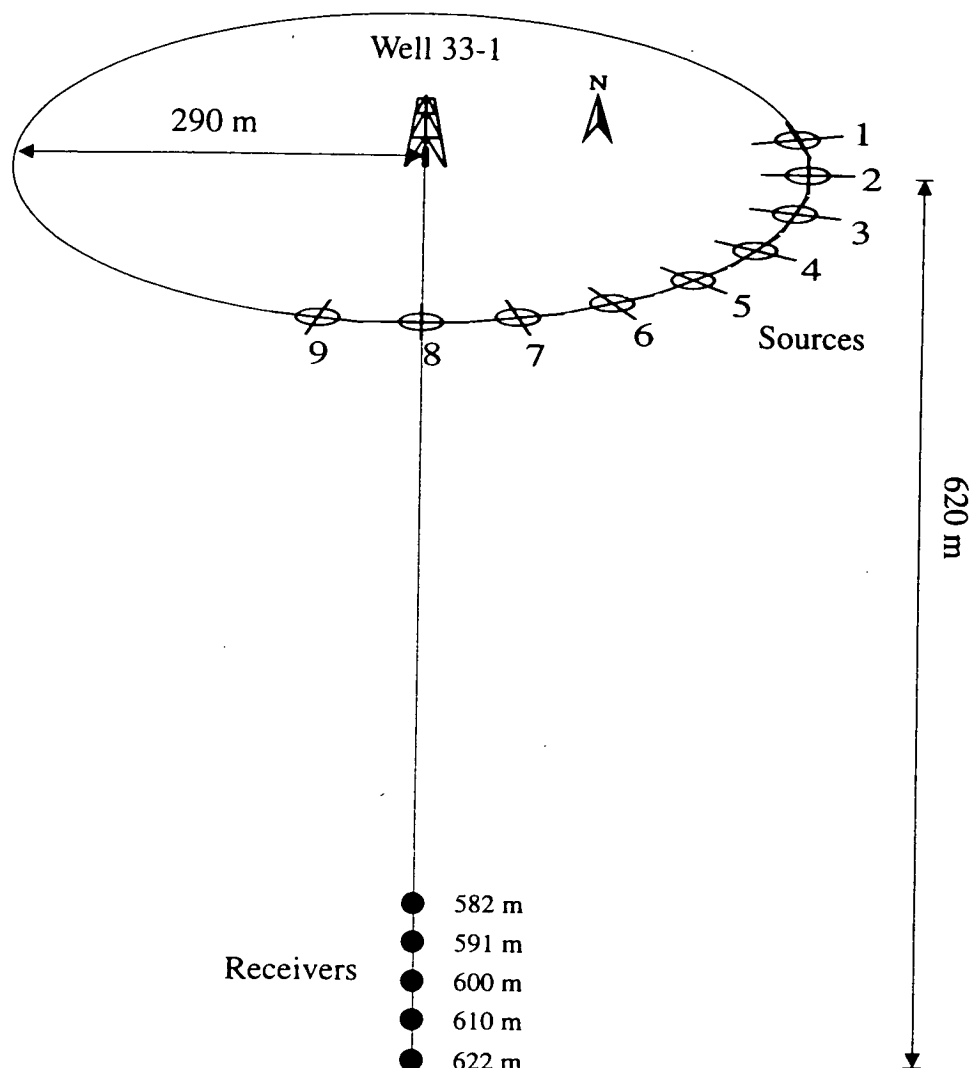


**Figure 5.** Schematic illustration of the acquisition geometry used for the azimuthal VSP showing the vibroseis source positions, as indicated by the crossed circles, and the three-component geophone positions indicated by the filled circles.

1993) and the linear transform technique (LTT) (Li and Crampin 1993), were applied to the shear-wave traces in order to estimate the  $qS1$ -wave polarization direction and the  $qS2 - qS1$  time-delay. These results agree with those published by Queen and Rizer (1990) which were obtained using a numerical rotation analysis (Alford 1986), suggesting a consistent processing sequence. The lateral uniformity of the geology around the test site and the constant source offset reduce any variation of the traveltimes due to ray bending, so that any change in the traveltimes is likely to be due to the effects of anisotropic wave propagation. Thus the anisotropic shear-wavefield is parametrized in terms of the  $qS1$ -wave polarization azimuth in the horizontal plane and the  $qS2 - qS1$  time-delay. The measured observations are shown in Figs 6 and 7a with an estimated error envelope given by Queen and Rizer (1990) for the time-delays. Using these values we set  $\delta\tau_i$  to be a constant 4 ms for  $qS2 - qS1$  time-delays and  $\delta p_i$  to be  $15^\circ$  for the  $qS1$ -wave polarizations.

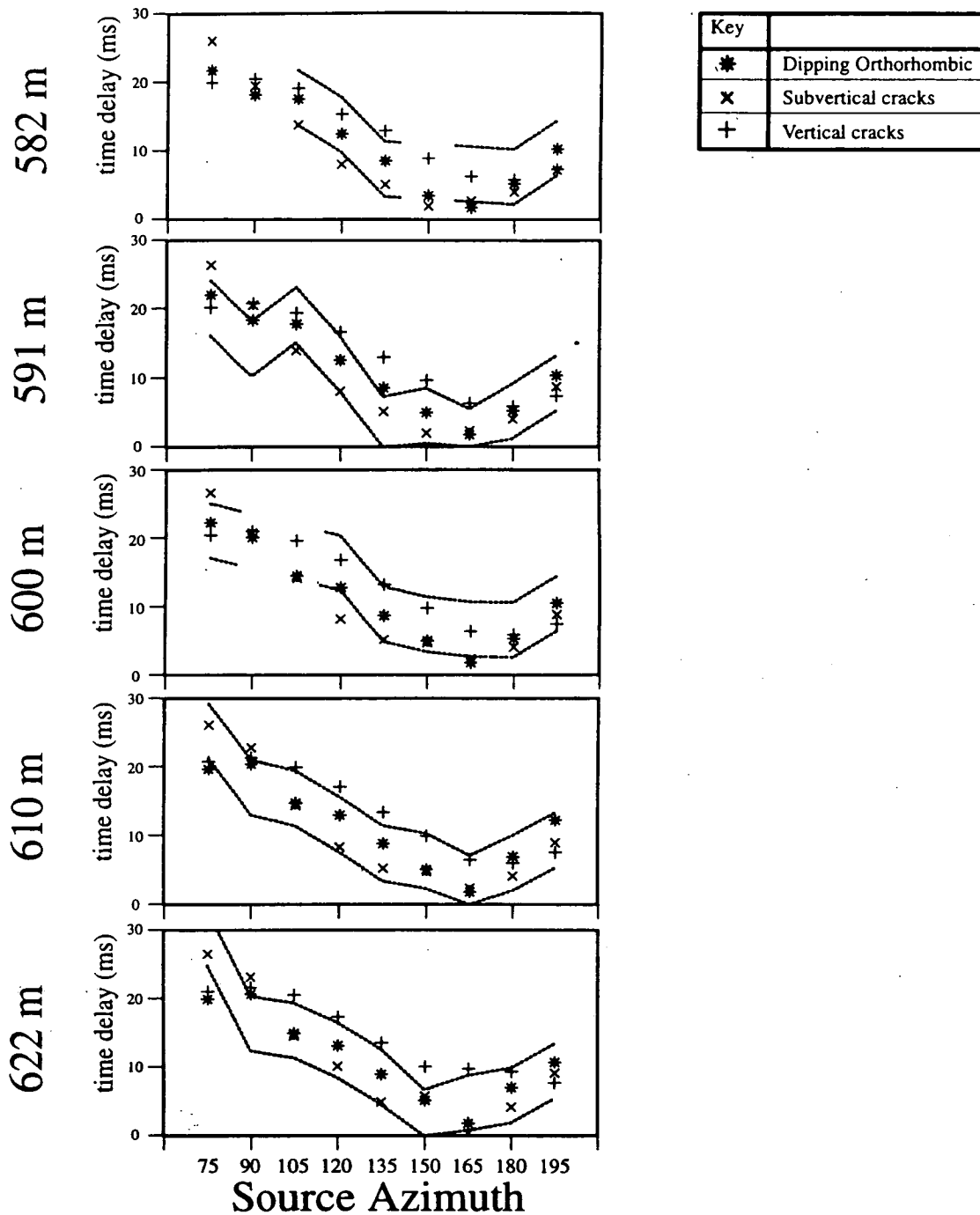


**Figure 6.** Time-delays between the fast and slow split shear waves corresponding to the optimal models found by the GA for different parametrizations. The dashed lines indicate the upper and lower estimated error bounds for the observed time-delays. Breaks in the dashed lines indicate that no data was available.

#### *Inversion of field data from the azimuthal VSP*

Inversions were attempted with several anisotropic symmetry systems. These results are summarized in Table 1 and Figs 6, 7b, c and d.

The simplest anisotropic model used in the inversion is a TIH system. Although the time-delays can be adequately explained in terms of such a system, the

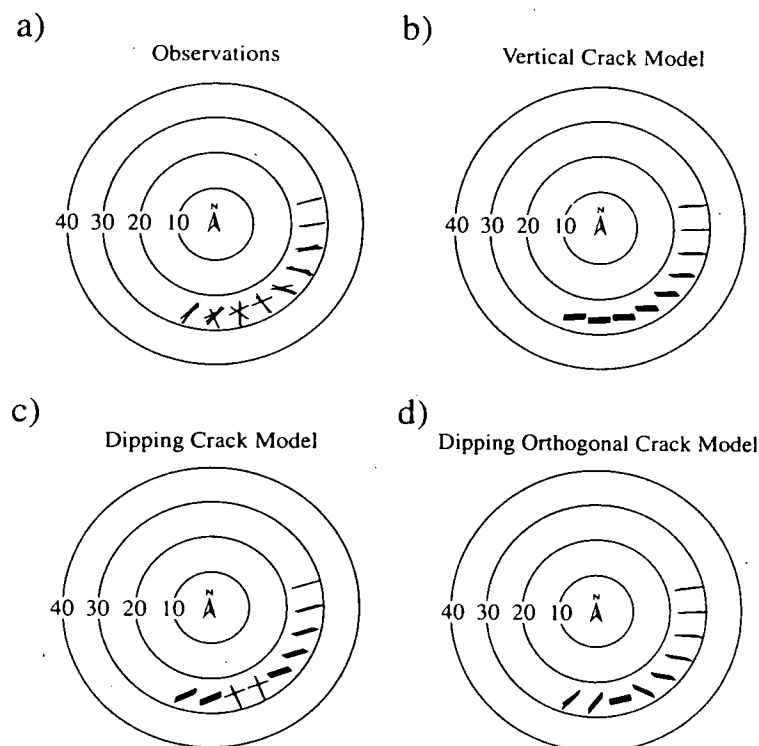


**Figure 7.** Polarization of the  $qS1$ -wave plotted on a lower hemisphere equal area projection corresponding to (a) the observations recorded using the AVSP geometry and (b)–(d) the optimal model observations obtained from the GA for different parametrizations. The  $qS1$  polarizations are plotted for the optimal (b) vertical crack model, (c) dipping crack model and (d) dipping orthogonal crack model. Each circle represents equi-incident angle propagation with the outermost representing propagation at  $40^\circ$  to the vertical.

observed  $qS1$ -wave polarizations are inconsistent with a single vertical crack model [Queen and Rizer (1990) found that a wet crack system striking at  $N75^\circ E$  with a crack density of 0.04 could model all but a few of the observations]. The GA inversion for the observed  $qS1$ -wave polarizations and time-delays using this TIH system finds a best-fit model similar to that given by Queen and Rizer (1990) with wet cracks striking at  $N87^\circ E$ , with  $CD_1 = 0.05$ ,  $AR_1 = 0.02$  and a misfit of 3.5. This crack strike is only just within the acceptable range suggested by *a priori* information determined from BHTV and geological measurements. The poor estimation of the crack strike is thought to be due to the averaging of the azimuthal variation of the observed  $qS1$ -wave polarization estimates to give an average crack strike direction, since for a single vertical crack set there is a broad band of horizontal  $qS1$ -wave polarizations parallel to the crack strike. This is confirmed if the residual is decomposed into the time-delay and polarization contributions, showing that the large residual is largely due to a poor fit of the polarization observations.

The second system that could account for such azimuthal anisotropy is a dipping crack system. The symmetry class is identical to that for vertically aligned cracks but an additional degree of freedom is required to specify the orientation of the symmetry axis since it is no longer constrained to the horizontal plane. Previous studies (Queen and Rizer 1990; Liu, Crampin and Queen 1991) in the area indicate



**Table 1.** Summary of the inversion results for the AVSP. The first two columns indicate the parameters included in the inversion. For 'dipping cracks' a parameter, *DIP*, was included defining the orientation of the cracks from the horizontal plane. For the orthorhombic inversion a second crack set (sub-horizontal) orthogonal to the first (sub-vertical) was included requiring an additional three crack parameters. This second set is shown on the second line in the appropriate columns. The crack and orientation parameters shown are those corresponding to the optimal model found by the GA with the corresponding misfit value shown in the last column. *AZI* is measured in degrees from north in a clockwise direction.

	OPTIMAL MODEL										misfit
	Hudson Cracks			Orientation		Elastic Constants					
	<i>CD</i>	<i>AR</i>	<i>CT</i>	<i>AZI</i>	<i>DIP</i>	<i>C</i> <sub>11</sub>	<i>C</i> <sub>22</sub>	<i>C</i> <sub>44</sub>	<i>C</i> <sub>55</sub>	<i>C</i> <sub>12</sub>	
Vertical cracks	0.05	0.02	w	87.0	n/a	30.41	31.60	8.00	7.19	15.21	3.5
Dipping cracks	0.06	0.07	w	69.0	10.0	27.43	30.86	8.00	7.04	13.72	1.8
Orthorhombic	(0.03	0.12	d	75.0	7.0						1.4
	0.04	0.01	w)								

that dipping fractures are present at shallow depths rotated  $20^\circ$  from the vertical to the south-east. Evidence from dipmeter and BHTV measurements also suggest the presence of dipping fractures. So in the second inversion a parameter is included specifying the dip of the cracks from the vertical axis, spanning a range from  $+32^\circ$  to  $-32^\circ$ . The remaining crack parameters were identical to those used for the vertical crack inversion described above. The best-fit model obtained from this inversion was a wet crack model with cracks striking at  $N69^\circ E$  and rotated  $10^\circ$  from the vertical to the south-east with  $CD_1 = 0.06$  and  $AR_1 = 0.07$ . The residual value for this model was almost half that obtained for the vertical crack set.

There are several interesting points to note from this inversion. Firstly, the introduction of crack dip allows an estimation of the crack strike which is more consistent with the *a priori* information. Secondly, the abrupt swings in the  $qS_1$ -wave polarizations observed at azimuths 6 through to 8 are reproduced in the crack model as can be seen on examining Fig. 7c. These polarization swings in the optimal crack model observation set are due to the presence of a line singularity.

The next lowest symmetry class to be inverted, after hexagonal, is orthorhombic, which can be represented as two orthogonally intersecting crack sets. For the orthorhombic inversion, three additional horizontal crack parameters were included describing the second orthogonal horizontal crack set. As before the first crack set is initially restricted to be vertical. As before the resulting system was then rotated by the *AZI* and *DIP* parameters. Results from the inversion gave a best-fit model with a misfit of 1.4 and crack parameters as indicated in Table 1. The orientation of the symmetry axis is consistent with previous versions and indicates a crack strike of  $N75^\circ E$  rotated by  $7^\circ$  from the vertical to the south-east. The decrease in the misfit function is not surprising since horizontal cracks introduce three additional degrees of freedom. It is not then surprising that an orthorhombic system simulated by two dipping intersecting orthogonal crack sets gives the lowest overall misfit of 1.3.

Although Queen and Rizer (1990) suggested the presence of two non-orthogonal crack sets as a possible explanation for the results obtained from the AVSP based on other observations, there is insufficient azimuthal coverage to warrant further inversions with even lower symmetries.

### *Experimental configuration for azimuthal RVSP (ARVSP)*

Reverse vertical seismic profiles (RVSP) have also been shot at the CBTF, centred around a shallow borehole GW3 located approximately 135 m to the south of well 33-1. The experimental configuration is shown in Fig. 8. Ten three-component surface geophones were located on an arc of radius 7.2 m extending from  $N358^\circ E$  to  $N160^\circ E$  with an azimuthal spacing of approximately  $18^\circ$ . The Conoco rotary downhole source was used to generate horizontally and vertically polarized shear waves at depths between 1.5 and 38.4 m at intervals of approximately 0.6 m. Shear-wave polarizations corresponding to sources located at 10, 15 and 25 m were used

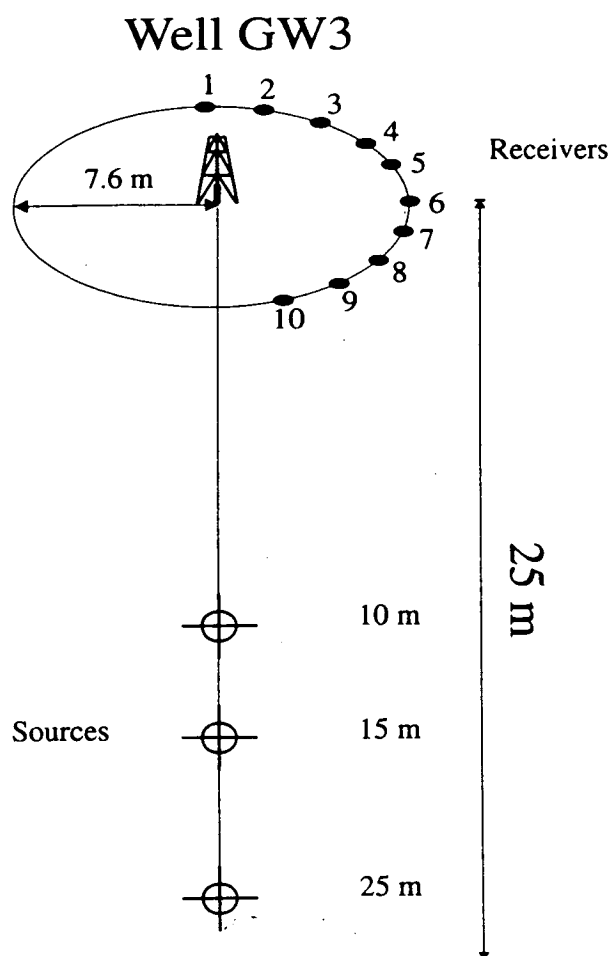


**Figure 8.** Schematic illustration of the acquisition geometry used for the azimuthal RVSP showing the Conoco rotary source and three-component surface geophone positions, shown as crossed circles and filled circles, respectively.

in the inversion providing a more extensive coverage of incident angles than that given by the AVSP. Time-delays were not inverted as the estimates were scattered and thought to be unreliable (Liu, personal communication). The polarization estimates have been published previously by Liu, Crampin and Queen (1991).

#### *Inversion of field data for azimuthal RVSP*

As for the AVSP, several inversions were carried out with different anisotropic symmetries as summarized in Table 2 and Fig. 9.

The first entry in Table 2 describes the results using a simple vertical crack system. The inversion results indicate a highly anisotropic region of crack density 0.10 with wet cracks striking at N81°E, although the crack density is unlikely to be well resolved with the absence of time-delay observation estimates. As with the vertical crack inversion for the AVSP, the orientation of the crack set is only just within the acceptable bounds given by *a priori* information. There is a considerable difference in the inverted CD's for the ARVSP and the AVSP which is not unexpected since the ARVSP extends over a shallow depth range of only 50 m where

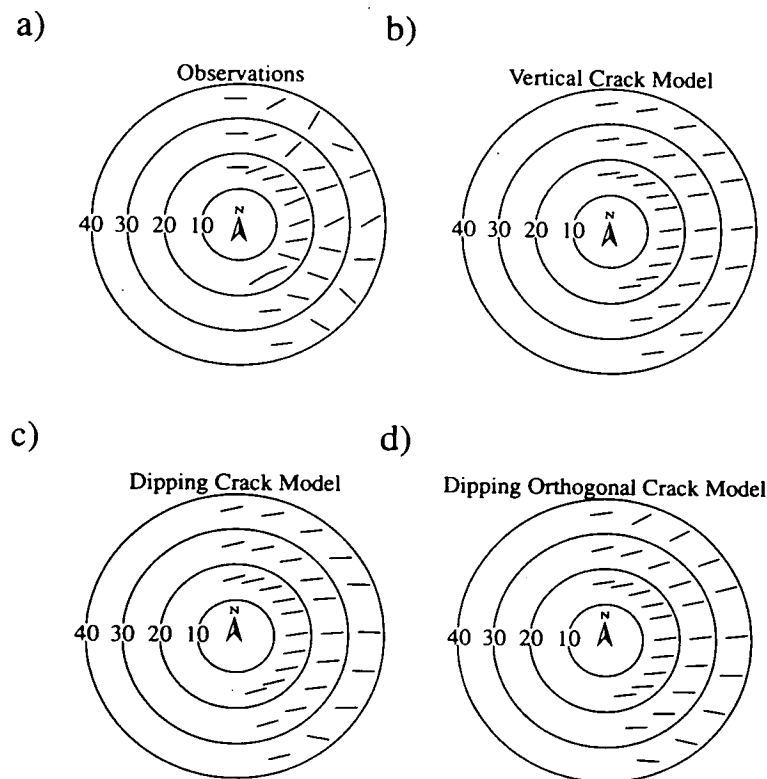


**Figure 9.** Polarization of the  $qS1$  shear wave plotted on an upper hemisphere equal area projection corresponding to (a) the observations recorded using the ARVSP geometry and (b)–(d) the optimal model observations obtained from the GA for different parametrizations. The  $qS1$  polarizations are plotted for the optimal (b) vertical crack model, (c) dipping crack model and (d) dipping orthogonal crack model. Each circle represents equi-incident angle propagation with the outermost representing propagation at  $40^\circ$  to the vertical.

high crack densities may be expected in the near surface. Liu, Crampin and Queen (1991) found that the ARVSP results could be adequately modelled using a  $CD_1$  of 0.12 which is similar to the  $CD_1$  obtained by the inversion.

The inversion results for the dipping crack system suggest dry cracks striking  $N76^\circ E$  and rotated  $26^\circ$  from the vertical to the south-east. This result agrees almost exactly with that obtained by Liu, Crampin and Queen (1991), who modelled the ARVSP using a crack set striking at  $N75^\circ E$  and rotated  $20^\circ$  from the vertical to the south-east.

### *Synthetic modelling for the AVSP*

Based on the results obtained from the GA inversion, full waveform modelling was attempted for the AVSP. The isotropic velocity structure at the CBTF was modelled using 17 layers and a lower half-space with velocities and densities based on logs from well 33-1.

The purpose of this modelling was to verify the results obtained from the inversion and to examine the effect of replacing the homogeneous half-space used in the

**Table 2.** Summary of the inversion results for the ARVSP. The format of this table follows that of Table 1.

	OPTIMAL MODEL										misfit
	Hudson Cracks			Orientation		Elastic Constants					
	<i>CD</i>	<i>AR</i>	<i>CT</i>	<i>AZI</i>	<i>DIP</i>	$C_{11}$	$C_{22}$	$C_{44}$	$C_{55}$	$C_{12}$	
Vertical cracks	0.10	0.13	w	81.3	n/a	22.78	29.69	8.00	6.46	11.39	2.2
Dipping cracks	0.08	0.11	d	75.5	25.9	20.01	29.00	8.00	6.74	10.01	2.0
Orthorhombic	(0.07 0.13	0.10 0.09	d w)	81.3	0.5						1.3

GA forward modelling step with a depth-dependent velocity structure. The synthetic seismograms produced were analysed by application of the same automatic techniques with the same time windows as had been used to extract the shear-wave attributes from the field data.

Synthetic seismograms were generated using the ANISEIS (Taylor 1990) modelling package which generates full-wave seismograms using the reflectivity method. The multi-azimuthal nature of the survey combined with propagation passing near to a line singularity required an integration over azimuthal as well as vertical slowness, so that the resulting forward modelling problem is time consuming, requiring 9 hours CPU on a VAX 4000/400 (Specmark 22.3).

The model which reproduced the observed shear-wave polarizations and time-delays most accurately was a wet crack model with cracks of  $AR_1$  equal to 0.07 striking  $N74^\circ E$  and rotated  $17^\circ$  from the vertical to the south-east. The predicted shear-wave polarizations and  $qS2 - qS1$  time-delays for this model are plotted in Figs 10a and 11a, respectively. In order to model the time-delays, a high  $CD_1$  of 0.12 was required in the top 130 m of the model and below this a  $CD_1$  of 0.065 was used. This high crack density agrees well with the GA inversion results for the ARVSP and also with full wave modelling conducted by Liu, Crampin and Queen (1991). The  $qS1$ -wave polarizations were found to be adequately modelled with the abrupt swings observed in the field data being reproduced in the synthetic model due to propagation through a line singularity. As expected, the position of the line singularity was extremely sensitive to the crack orientation and rotations as small as  $0.25^\circ$  could significantly affect the shear-wave polarizations. The discrepancy between the dip of the cracks obtained from matching full waveform synthetics and that obtained from the GA inversion is most probably due to the introduction of a laterally uniform velocity structure leading to ray bending.

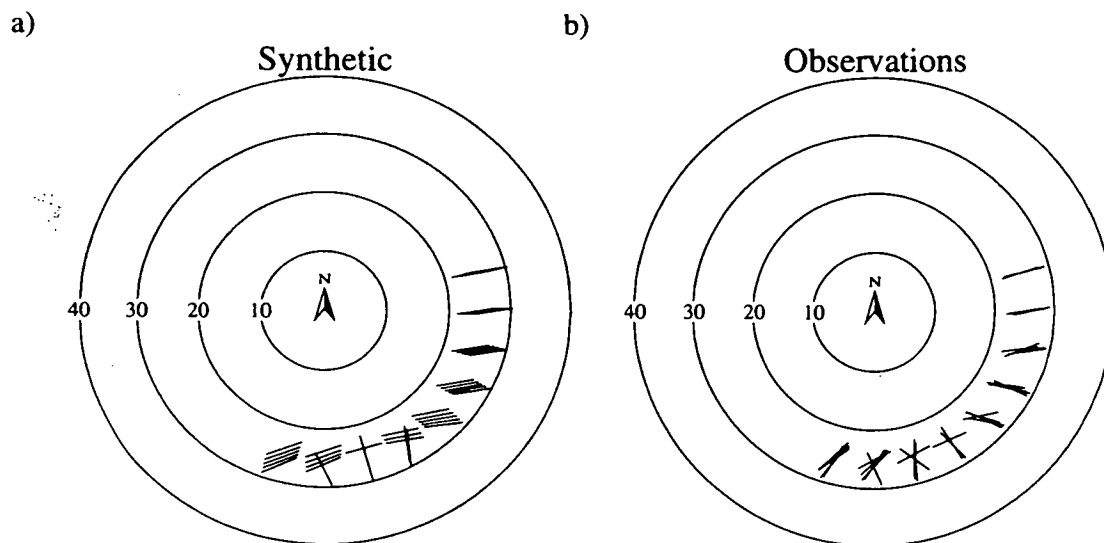


**Figure 10.** Polarization of the  $qS1$  shear waves measured from north for (a) the synthetic model observations and (b) the field observations plotted on a lower hemisphere equal area plot.

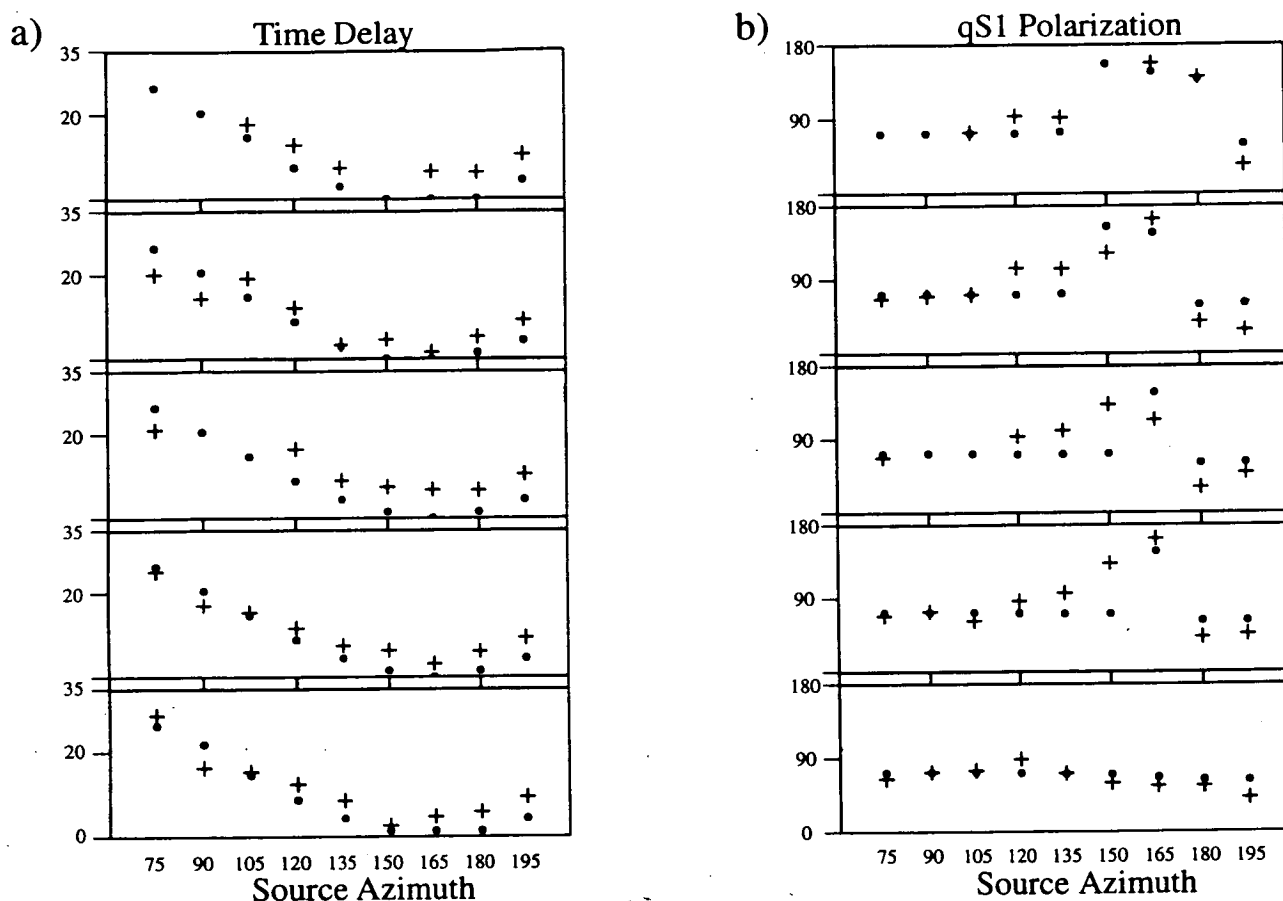


**Figure 11.** Estimation results showing (a) the time-delay between the fast and slow split shear waves and (b) the  $qS1$  polarization in the horizontal plane for the synthetic model observations and field observations. Results are plotted as a function of the source azimuth. Figures 10a and b show the same  $qS1$  polarizations but plotted on an equal area plot.

The final model derived by full waveform synthetics is similar to that obtained by GA inversion techniques. This similarity is encouraging, considering the relatively small CPU requirement of a GA inversion compared to the full wave modelling. However, the GA inversion should be regarded as an initial step before, rather than a substitute for, full waveform synthetic modelling.

## Discussion and conclusions

The inversion results that have been presented here for both the AVSP and the ARVSP have been found to be consistent with previous geological and numerical studies of the observed shear-wave anisotropy. In both cases the results appear to suggest that the presence of dipping fractures at the CBTF can be detected from the horizontal projections of the shear-wave polarizations from offset VSP data. The disturbance in the shear-wave polarizations measured at azimuths 6 to 8 with the AVSP was found to be modelled by using a line singularity. To identify the line singularity positively, it would be necessary to choose a field geometry that

would cross the line singularity where an abrupt change in shear-wave polarizations and zero time-delays would be observed.

The most significant problem with this work is the simplification of the forward modelling from what is in reality a 3D structure to an anisotropic homogeneous half-space. This approach is justified firstly by the prohibitive computational complexity and intensity of the forward modelling requirements that would be required in dealing with a more realistic anisotropic earth model. Secondly, it is unlikely that there are any significant changes in the crack orientation with depth (although there may be some rotation of crack direction to the vertical with depth due to the increase in the overburden) so that the polarizations measured at the geophones will correspond to the local anisotropy. Problems arise for the inversion of the time-delays since these are proportional to the shear-wave velocity which are not constant with depth. In this case the inverted time-delays will effectively average the shear-wave velocities sampled along the raypaths. Since time-delays are also proportional to the crack density, the inversion result will refer to a weighted average crack density over the region. Despite these limitations the GA appears to produce consistent results so that it would appear that these assumptions are valid. It should be emphasized that these limitations are related to the computational complexity of the forward modelling problem and not the nature of the inverse problem structure for the GA.

As with previous studies (Stoffa and Sen 1991; Sambridge and Drijkoningen 1992), the GA has been found to perform very efficiently when applied to the search of large non-linear model spaces. The main limitation with the GA is the dependence on the speed with which the fitness functions can be evaluated since many models need to be generated before convergence. However, for large multi-modal model spaces where the implementation of a Monte-Carlo process is considered impractical due to the slow convergence rate, the GA presents an attractive alternative. GAs are also very flexible and may be applied to different problem domains by replacing the evaluation routine by the relevant forward modelling problem. More fundamental problems exist with GAs but it appears that in most cases these schemes are robust and efficient and are likely to find increasing use within the exploration industry.

We have shown that an inversion scheme based on a GA can be used to invert shear-wave observations in the presence of seismic anisotropy and in future studies we intend to extend the GA approach to the inversion of guided wave dispersion in anisotropic waveguides.

### **Acknowledgements**

S. Horne thanks Elf UK for their financial support of this work and also colleagues at the British Geological Survey for their support, advice and friendship. This work was supported by the Edinburgh Anisotropy Project and the Natural



Environment Research Council, and is published with the approval of the Director of the British Geological Survey (NERC).

## References

- Alford R.M. 1986. Shear data in the presence of azimuthal anisotropy: Dilley, Texas. 56th SEG meeting, Houston, Expanded Abstracts, 476–479.
- Arts R.J., Helbig K. and Rasolofosaon P.N.J. 1991. Complete inversion of the anisotropic elastic tensor in rocks: Experiment and theory. 61st SEG meeting, Houston, Expanded Abstracts, 1538–1541.
- Backus G.E. 1962. Long-wave elastic anisotropy produced by horizontal layering. *Journal of Geophysical Research* 66, 4427–4440.
- Chapman C.H. and Pratt R.G. 1992. Traveltime tomography in anisotropic media – I. Theory. *Geophysical Journal International* 109, 1 – 19.
- Crampin S. 1985. Evaluation of anisotropy by shear-wave splitting. *Geophysics* 50, 42–152.
- Crampin S. 1987. Geological and industrial implications of extensive-dilatancy anisotropy. *Nature* 328, 491–496.
- Douma J. 1988. The effect of the aspect ratio on crack-induced anisotropy. *Geophysical Prospecting* 36, 614–632.
- Folstad P.G. and Schoenberg M. 1993. Scattering from a set of anisotropic layers to second order in frequency. 55th EAGE meeting, Stavanger, Norway, Expanded Abstracts, p. 105.
- Goldberg D.E. 1989. *Genetic Algorithms in Search Optimization and Machine Learning*. Addison-Wesley Pub. Co.
- Hudson J.A. 1986. A higher order approximation to the wave propagation constants for a cracked solid. *Geophysical Journal of the Royal astronomical Society* 87, 265–274.
- Hudson J.A., 1991. Crack distributions which account for a given seismic anisotropy. *Geophysical Journal International* 104, 517–521.
- Li X.Y. and Crampin S. 1993. Linear-transform techniques for processing shear-wave anisotropy in four-component seismic data. *Geophysics* 58, 240–256.
- Liu E. and Crampin S. 1990. Effects of the internal shear-wave window: comparison with anisotropy induced splitting. *Journal of Geophysical Research* 95, 11275–11281.
- Liu E., Crampin S. and Queen J.H. 1991. Fracture detection using cross-hole surveys and reverse vertical seismic profiles at the Conoco Borehole Test Facility, Oklahoma. *Geophysical Journal International* 107, 449–463.
- MacBeth C. 1991. Inverting shear-wave polarizations for anisotropy using three component offset VSP's: synthetic seismograms. *Geophysical Journal International* 107, 571–583.
- Musgrave M.J. 1970. *Crystal Acoustics*. Holden-Day Inc.
- Queen J.H. and Rizer W.D. 1990. An integrated study of seismic anisotropy and the natural fracture system at the Conoco Borehole Test Facility, Kay County, Oklahoma. *Journal of Geophysical Research* 95, 11255–11273.
- Sambridge M. and Drijkoningen G. 1992. Genetic algorithms in seismic waveform inversion. *Geophysical Journal International* 109, 323–342.
- Smith M.L., Scales J.A. and Fischer T.L. 1992. Global search and genetic algorithms. *The Leading Edge of Exploration* 11, 22–26.
- Stoffa P.L. and Sen M.K. 1991. Nonlinear multiparameter optimization using genetic algorithms: inversion of plane wave seismograms. *Geophysics* 56, 1794–1810.

- Tatham R.B. and McCormack M.D. 1991. Multicomponent seismology in petroleum exploration. In: *Investigations in Geophysics*, No. 6. (eds). E.B. Neitzel and D.F. Winterstein SEG.
- Taylor D.B. 1990. ANISEIS manual: version 4.5: Applied Geophysical Software Inc., Houston.
- Thomsen L. 1986. Weak elastic anisotropy. *Geophysics* 51, 1954 – 1966.
- Zeng X. and MacBeth C. 1993. Algebraic processing techniques theory. *Geophysical Prospecting* 41, 1033 – 1066.